Soft biomaterials for applications as local drug delivery systems for use in the brain

A thesis submitted in accordance with the conditions governing candidates for the degree of Philosophiae Doctor in Cardiff University

by

Yu Wang

March 2025

Cardiff School of Pharmacy and Pharmaceutical Sciences

Cardiff University

ABSTRACT

Glioblastoma is the most malignant brain tumour with less than two years median survival time after the first diagnosis. The current treatment strategy is based on the Stupp protocol established in 2005, which consists of surgery, radiotherapy, and temozolomide. The choice of chemotherapeutics is limited to lipophilic alkylating agents due to their ability to pass the blood-brain barrier. However, temozolomide might only have activity in O^6-methylguanine-DNA methyltransferase (MGMT) promoter-methylated tumours. So, glioblastoma is an unmet medical need, and it is urgent to develop effective, safe, and long-lasting treatment approaches. Drug repurposing is a strategy that repositions existing drugs for new medications, stimulating drug discovery by reducing drug development time and investment. This strategy also avoids the chemoresistance of glioblastoma to alkylating agents. Tumour recurrence is another intractable issue for glioblastoma treatment, and the standard of care has not been well defined. However, most recurrences occur close to the margin of surgery or radiotherapy, providing a critical rationale for local treatment. Local drug delivery could also bypass the blood-brain barrier, reach higher drug concentrations, and reduce systemic adverse effects. In this project, I focus on the local treatment strategies against glioblastoma and commit to resolving the key problems including mechanical properties of the materials, chemoresistance, and sustained long-term drug release.

First, publications about injectable drug delivery systems for glioblastoma local treatment were systematically searched. The *meta*-analysis results of these preclinical studies showed that injectable drug delivery devices improved efficacy compared to systemic or local administration of free drugs. The first objective of this project was to create cylindrical-shaped cryogels as an implant to deliver clemastine to a mouse glioblastoma resection model. The mechanical properties of this spongy-like cryogel approximately matched the soft brain tissue. Cryogels showed good *in vitro* cytocompatibility and *in vivo* biocompatibility. However, the variability in the extent of surgical resection may act as a confounding factor, affecting the clemastine treatment efficacy. In the second objective, microscale cryogels, termed cryogel microcarriers, were designed to be an injectable local drug delivery system flexibly administered to tumour resection cavities with various sizes. The drug loading efficiency and drug release profiles were investigated with four model drugs, doxorubicin, venetoclax, brexpiprazole, and vortioxetine. *In vitro* antitumor efficacy studies were performed with brexpiprazole microcarriers due to the best *in vitro* drug loading efficiency and release patterns. The results showed that brexpiprazole microcarriers effectively reduced cell viability both on 2D and 3D

cell culture models. The third objective aimed to create poly lactic-co-glycolic acid (PLGA) microsphere delivery systems to resolve the rapid release of vortioxetine microcarriers. A novel methodology was developed to create monodisperse and highly reproducible PLGA microspheres by droplet-based microfluidics. Vortioxetine microspheres achieved one month of sustained drug release without burst release. Empty PLGA microspheres had good cytocompatibility on primary human astrocytes, suggesting the water-free emulsion system did not introduce any toxic reagents into the final product. Vortioxetine microspheres reduced glioblastoma cell viability in a dose-dependent and time-dependent manner.

In summary, I developed cylindrical cryogel, cryogel microcarriers, and PLGA microspheres as local drug delivery systems for glioblastoma treatment. Repurposed drugs, clemastine, brexpiprazole, and vortioxetine showed a therapeutic window that effectively killed the tumour cells while being safe for astrocytes. Together strategies of novel local drug delivery systems and repurposed drugs provide promising approaches against glioblastoma.

ACKNOWLEDGEMENTS

Words cannot express my sincere gratitude to my supervisor, Dr. Benjamin Newland, for his invaluable guidance, patience, and feedback. He has provided me with a steadfast belief in my capabilities and academic potential and encouraged me to persevere in this journey.

I would like to express my gratitude to my colleagues, Dr. Majed Alghamdi and Dr. Abrar Hakami for teaching me the fundamental experiments at the beginning of my research.

I extend my deepest appreciation to Dr. Vadim Le Joncour, Professor Pirjo Laakkonen and their group at the University of Helsinki for welcoming me into their lab and collaborating on animal studies.

The appreciation is also extended to Dorit Siebzehnruebl and Dr. Florian Siebzehnrubl for generously providing glioblastoma cell line sources and advice on cell studies.

I would also like to express my gratitude to fellow researchers, Dr. Chiara Bastiancich, Dr. Tobias Weiss, Dr. Marcella Bassetto, Duncan Muir who contributed insights, offered support and collaborated on my project.

Special thanks to my parents for encouraging and supporting me in committing to my research.

Finally, I would like to acknowledge Cardiff University, China Scholarship Council, and Cardiff Cancer Research Hub for providing financial support. Without their contributions, this work would not have been possible.

LIST OF ABBREVIATIONS

2D	Two-dimensional
3D	Three-dimensional
ALL	Acute lymphoblastic leukaemia
ARTX	Alpha thalassemia/mental retardation syndrome X-linked
BBB	Blood-brain barrier
BCL-2	B-cell lymphoma-2
BRE	Brexpiprazole
BSA	Bovine serum albumin
BTICs	brain tumour-initiating cells
CED	Convection-enhanced delivery
CI	Confidence interval
CLE	Clemastine
CLL	Chronic lymphocytic leukaemia
CNS	Central nervous system
COC	Cyclic olefin copolymer
DDS	Drug delivery system
DMSO	Dimethyl sulfoxide
DOX	Doxorubicin
EDTA	ethylenediaminetetraacetic acid
EGFR	Epidermal growth factor receptor
EtOH	Absolute ethanol
FBS	Fetal bovine serum
FDA	Food and Drug Administration
FGF2-G3	Recombinant human fibroblast growth factor 2-G3
FTIR	Fourier transform infrared spectroscopy
GBM	Glioblastoma
GFAP	Glial fibrillary acidic protein
HMPP	2-Hydroxy-2-methylpropiophenone
IBA1	Ionized calcium-binding adapter molecule 1
IDH	Isocitrate dehydrogenase
IHC	Immunohistochemistry
IP	Intraperitoneal injection
LAP	Lithium phenyl(2,4,6-trimethylbenzoyl) phosphinate

MC	Cryogel microcarrier
MGMT	O^6-methylguanine-DNA methyltransferase
MRI	Magnetic resonance imaging
MS	Median survival
O/O	Oil-in-oil
O/W	Oil-in-water
PBAE	Poly(beta-amino ester)s
PBS	Phosphate-buffered saline
PDA	Photo diode array
PDMS	Poly(dimethylsiloxane)
PEG	Polyethylene glycol
PEGDA700	Poly(ethylene glycol) diacrylate 700
PFO	1H,1H,2H,2H-perfluoro-1-octanol
PFPE-PEG-PFPE	Perfluoropolyether-poly(ethylene glycol)-perfluoropolyether
PI	Photoinitiator
PLGA	Poly lactic-co-glycolic acid
PTX	Paclitaxel
rhEGF	Recombinant human epidermal growth factor
SEM	Scan electron microscope
SPA	3-Sulfopropyl acrylate potassium salt
TERT	Telomerase reverse transcriptase
TMZ	Temozolomide
TPN	Transferrin-putrescine-sodium selenite
TTF	Tumour treating fields
UV	Ultraviolet-visible
VBS	Sodium 4-vinylbenzenesulfonate
VOR	Vortioxetine
W/O/W	Water-in-oil-in-water
WHO	World Health Organization

Table of Contents

INDEX OF FIGURES

INDEX OF TABLES

Chapter 1: General introduction

Part of the work in this chapter has been published as a review paper.

Yu Wang, Chiara Bastiancich, and Ben Newland. Injectable local drug delivery systems for glioblastoma: a systematic review and *meta*-analysis of progress to date, Biomater Sci, 11 (2023) 1553-1566 (PMID: 36655634).

1. Glioblastoma (GBM)

Isocitrate dehydrogenase (IDH) wild-type 1 glioblastoma (GBM) is the most malignant primary brain tumour of the central nervous system (CNS), which is associated with poor clinical outcomes and high mortality.(1) At present, GBM is still incurable. The overall median survival is only 14.6 to 16.7 months after diagnosis, and only around 5-10% of GBM patients survive over five years.(2) Meanwhile, patients suffer from a decline in the quality of their life and loss of cognitive function.(3) GBM makes up around 57% of all gliomas and 48% of all primary malignant CNS tumours.(4) The classification of CNS tumours has undergone major changes after the World Health Organization (WHO) revised 4th and 5th editions of the classification of tumours of the CNS.(5, 6) CNS tumours are mainly classified by histological tumour typing and several molecular markers. The most relevant molecular characteristics of GBM include IDH wild type, telomerase reverse transcriptase (TERT) promoter mutant, epidermal growth factor receptor (EGFR) gene amplified, and gain of chromosome 7 combined with loss of chromosome 10 (**Figure 1-1**).(7) Although O^6-methylguanine-DNA methyltransferase (MGMT) promoter methylation is not used for the diagnosis of GBM, this marker is important to predict the success of chemotherapy with alkylating agents.(8)

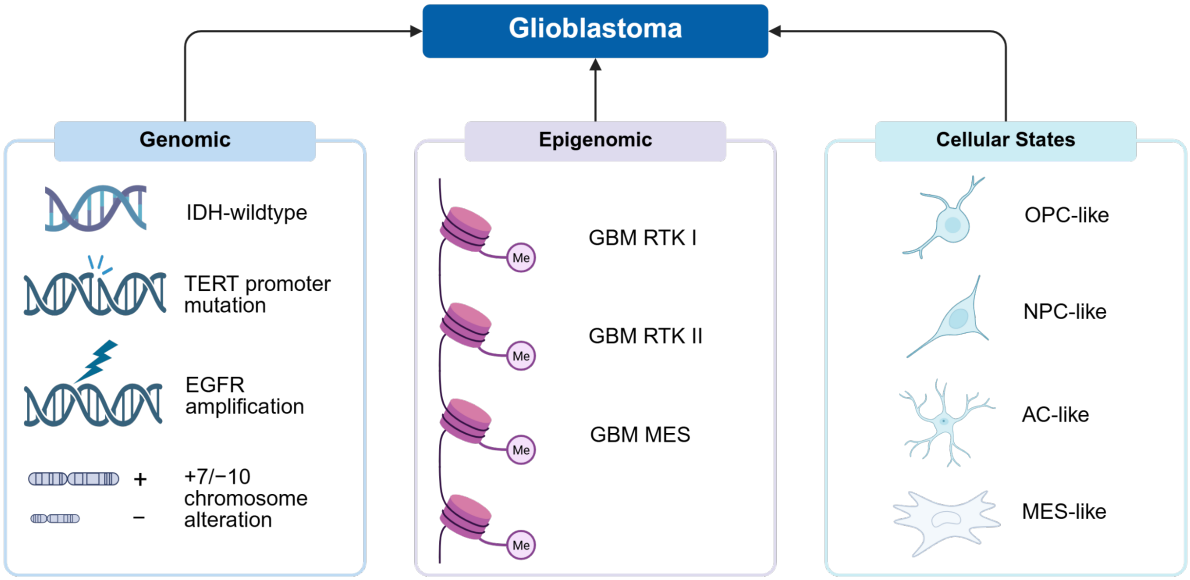

Figure 1-1 Schematic illustration represents the genomic and epigenomic subtype classifiers of GBM and the major GBM cellular states.

Abbreviation: RTK I and RTK II: receptor tyrosine kinase I and II; MES: mesenchymal; OPC-like: oligodendrocyte-progenitor-like; NPC-liken: neural-progenitor-like; AC-like: astrocyte-like; MES-like: mesenchymal-like. This figure is generated with Biorender.com.

In 2005, a series of clinical trials were published and the results showed an improvement in median survival after temozolomide (TMZ) combined with radiotherapy treatment, which shifted the paradigm of GBM treatment to a more aggressive combined-modality therapy (**Figure 1-2**).(9-11) At present, the gold standard therapy for GBM is maximum surgical resection followed by chemoradiotherapy and adjuvant chemotherapy. The therapeutic target is to resect the tumour tissue as much as possible, meanwhile avoiding compromising neurological function. Surgery can effectively reduce the tumour mass and surgical resection of 98% or more of the GBM volume could achieve a longer survival time.(12) However, because of the strong infiltrating nature of GBM cells into the normal surrounding tissue, it is impossible to resect the tumour completely.(13) Even a single cell can develop into a new tumour, resulting in multi-focal tumours.(14) It should be kept in mind that approximately 20-30% of GBM patients are unsuitable for surgical resection, either due to the lesion or site of the GBM (e.g. more than one lobe) or for reasons such as age, care status, or hospital capabilities.(15, 16) Although GBM is frequently confined to only one lobe, approximately 30% of GBM involves more than one lobe leading to a lower chance of undergoing surgery.(15, 17)

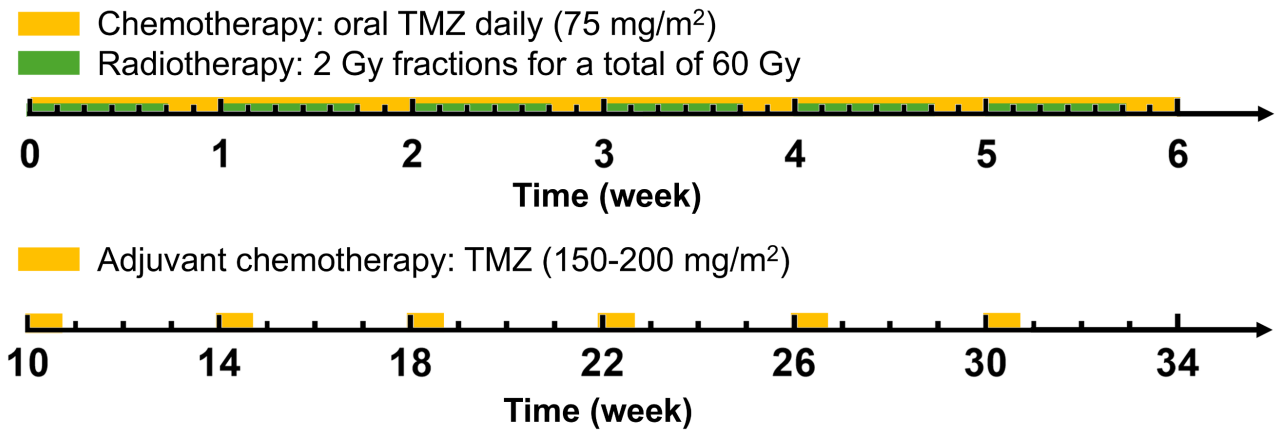

Figure 1-2 Illustration of the timeline of the standard of care for GBM treatment (Stupp protocol).

To attempt to eradicate the remaining tumour cells, surgical resection should be followed by a six-week radiotherapy combined with daily TMZ treatment and then six months of adjuvant TMZ. Radiotherapy is recommended to start between three to five weeks after the surgery.(18) GBM patients are commonly administered at 50-60 Gy divided into 1.8-2 Gy per day. The standard dose for TMZ treatment is 75 mg/m^2 daily throughout radiotherapy and 150-200 mg/m^2 5 days every 4 weeks for 6 cycles.

Notably, radiotherapy and chemotherapy still face many challenges. Even when treated with a high radiation dose, the recurrence was observed in some GBM patients, indicating that the tumour has radioresistance and cannot be eliminated completely by radiotherapy.(19) The expression signature dominated by *HOX* genes, which comprises Prominin-1 (CD133), might be the reason for the radioresistance of cancer stem cells.(20) On the other hand, the MGMT inhibits alkylating agents from killing GBM cells.(21) This protein can rapidly remove alkyl groups from the O^6 position of guanine, which is a crucial target site for alkylating agents. GBM patients with MGMT promoter methylation had better responsiveness to alkylating agents.(22) Elderly GBM patients without MGMT promoter methylation treated with radiotherapy plus temozolomide only had minor overall survival benefits without statistical differences compared to radiotherapy alone (median survival time, 10.0 months *vs* 7.9 months, p=0.055).(23)

After this gold standard treatment, most patients still suffer from recurrence within two years.(24) However, there are no established standard-of-care treatments for recurrent GBM patients. Treatment strategies are considered based on previous treatments, patients' age, and MGMT promoter methylation. Only a minority of patients are suitable to undergo a re-operation, which could significantly improve the median survival period to 36 weeks.(25) Although re-irradiation is basically possible for the treatment of recurrent GBM, it can only be a treatment approach for selected patients and severe cognitive side effects should also be considered. Moreover, the survival benefit of re-irradiation has not been proved by randomized trials. On the other hand, there is no clearly established chemotherapy regimen for the treatment of recurrent GBM after the prior chemotherapy, and investigational clinical protocols are still the best choice.(26) For example, chemotherapeutics such as procarabine and lomustine may achieve an antitumor effect.(27, 28)

However, because these drugs also function as alkylating agents and therefore have a similar mechanism to TMZ, their effectiveness is limited.

Some clinical trials showed that bevacizumab (with or without irinotecan) was well tolerated and had anticancer activity in recurrent GBM.(29, 30) Bevacizumab could prolong progression-free survival; however, it remains unclear how bevacizumab affects the life quality and overall survival benefit for patients.(31) Bevacizumab also failed to show overall survival benefit when it was combined with lomustine in comparison to lomustine alone.(32)

Tumour Treating Fields (TTF) are alternating electric fields with low-intensity and intermediate frequencies that inhibit cell growth by blocking mitosis.(33) Based on a randomized phase III trial, TTF was approved by the Food and Drug Administration (FDA) for the treatment of recurrent GBM.(34) A *post hoc* analysis showed that treatment with TTF plus chemotherapy improved the overall survival compared with chemotherapy alone at first recurrence.(35) However, drawbacks such as the high cost, patient compliance, and skin toxicity limit the use of TTF in the clinic, and TTF is not necessarily the best choice for physicians.(36)

Another obstacle to successful therapy is the heterogeneity of GBM tumours. The genetically unstable nature of GBM results in cells with diverse biological behaviours. For example, studies have shown that intratumoral heterogeneity exists within the same tumour.(37, 38) Thus, the entire tumour may not be represented by a single biopsy specimen, which is a reason for disappointing results from tailored treatments.(39)

GBM progression is significantly influenced by the interaction with the surrounding neural environment. The GBM tumour microenvironment is a complex system comprising various cell types, including immune cells, glial cells, and neurons.(40) Recent study revealed that the progression of high-grade gliomas was affected by the electrical and synaptic integration into neural circuits, and pharmacological or genetic blockade of these interactions inhibited the tumour growth.(41) Neuroligin-3 (NLGN3), a synaptic protein secreted in response to neuronal activity, promotes GBM proliferation through the PI3K-mTOR pathway and induces transcriptional changes in GBM cells.(42, 43) Targeting the tumour microenvironment components and their interactions with GBM cells may offer promising approaches for improving GBM treatment outcomes.

In the absence of pathology, the BBB protects the CNS by preventing the non-selective crossing of substances into the cerebrospinal fluid; however, it also limits the effective delivery of drugs to the CNS.(44) It is estimated that more than 98% of small molecular drugs and nearly 100% of large molecular drugs cannot pass the BBB.(45) For chemotherapeutics, only small hydrophobic drugs such as alkylating agents can cross the BBB. Meanwhile, a drug administrated systematically may be cleared or non-specifically absorbed by other tissues before arriving at the GBM site. This can lead to toxicity for other organs such as the liver and kidney. Local tumour treatment is another strategy that could be employed to deliver drugs accurately to the target site and circumvent the BBB. A wider range of chemotherapeutic agents, which cannot penetrate the BBB, can be used for local delivery. Local delivery could achieve a high concentration of drug at the tumour tissue while simultaneously avoiding systemic side effects and reducing the toxicity for normal brain tissue. Additionally, GBM is not a metastatic cancer, and only 0.4-0.5% of GBM patients suffer from extracranial metastasis, which makes GBM suitable for local treatment.(46)

One means of achieving local drug delivery is to implant a solid therapeutic into the surgical resection cavity. A drug delivery system (DDS) aiming to sustain the release of the drug is usually used in this strategy to suppress the growth of GBM cells which cannot be resected.(47) It is worth noting that most recurrences of GBM occur within two centimetres of the resection cavity.(48) For these reasons, delivering drugs to the resection cavity could maximize the anticancer effect and minimize systemic side effects.

The Gliadel® wafer is the only locally implantable DDS approved by the FDA for brain tumours. This wafer contains 7.7 mg of carmustine and 192.3 mg of biodegradable copolymer which consists of 1,3-bis-(p-carboxyphenoxy)propane (pCPP) and sebacic acid (SA) in a ratio of 20:80.(49) The results of clinical trials showed that patients treated with Gliadel® improved their median survival by around two months compared with placebo-treated patients.(48, 50, 51) Recently, several clinical trials were conducted to evaluate the effectiveness of Gliadel® combined with radiotherapy followed by TMZ. L.S. Ashby *et al*. conducted a systematic review of such clinical trials, which showed that the weighted mean of median overall survival of patients who received Gliadel® plus radiotherapy and TMZ was 18.2 months from ten included trials.(52) Compared with the median overall survival for Gliadel® plus radiotherapy (13.9 months)(48) and radiotherapy plus TMZ (14.6

months)(11) from previous clinical trials, Gliadel® plus radiotherapy and TMZ improved the median overall survival by around 3-4 months. Meanwhile, this combination therapy did not enhance toxicity. Whilst Gliadel® wafers show a modest improvement in therapeutic outcomes, their clinical use is still limited. Its rigid structure can lead to a mechanical mismatch between the stiff wafer and soft brain tissue causing side effects.(53) Moreover, the amount of drug that can be administered depends on the size of the cavity (8 wafers need to be placed to ensure therapeutic dose of carmustine) and the drug release profile is sub-optimal.(48, 54, 55) Whilst an array of local DDS is being developed to overcome these drawbacks,(56) there is still no clinically approved DDS designed for stereotactic injection directly into non-resectionable tumours.

Bypassing the BBB via direct intratumoral administration would not only facilitate a high local concentration of a drug to be achieved at the target site but also allow a wider range of therapeutics to be investigated. These factors allow a reduction in dose-limiting systemic toxicity whilst opening possibilities for re-purposing existing anti-cancer therapeutics, previously unsuitable due to BBB impermeability.

Stereotactic injections may allow delivery directly to deep, multi-sited, or highly irregular tumours that are otherwise unsuitable for surgery. Convection-enhanced delivery (CED) is another means of delivering injectable DDS. Due to the external pressure gradient, CED allows drugs to penetrate deeper than conventional injection without requiring higher doses.(57) One advantage of using local injection/CED is that a wide range of therapeutics (e.g., chemotherapeutics, monoclonal antibodies, and proteins) can be administered as these techniques bypass the BBB. Many injectable delivery systems such as colloid suspensions, liposomes, and hydrogels may be suitable for administration both directly to a tumour or to the resection cavity, making them highly versatile whilst avoiding mechanical mismatch with the host tissue. However, to date, there is no systematic overview of the current state of these delivery systems nor a *meta*-analysis of their efficacy in improving MS in GBM animal models.

I aimed to undertake a systematic review of the pre-clinical literature to tabulate injectable DDS that has been developed for GBM therapies. Furthermore, I aimed to analyse whether injectable DDS directly administered intratumorally in animals bearing GBM tumours showed therapeutic efficacy compared to negative controls (no treatment or vehicle-only controls). I also analysed the

role that the delivery system plays in comparison to the direct injection of a free drug. Finally, I sought to compare local drug administration with systemic administration.

1.2. Methods

1.2.1 Search strategy

Three databases (PubMed, Web of Science and Scopus) were used in this review to systemically search articles which were relevant to the topic. The search for this review was completed on 9th June 2022.

The three search strategies were as follows:

Pubmed: ((glioblastoma[Title/Abstract] OR "brain tumo*" [Title/Abstract] OR glioma [Title/Abstract] OR gliosarcoma[Title/Abstract]) AND ("local delivery" [Title/Abstract] OR "drug delivery system" [Title/Abstract] OR "sustained release" [Title/Abstract] OR microsphere*[Title/Abstract] OR microparticle*[Title/Abstract] OR "convection enhanced delivery" [Title/Abstract] OR CED [Title/Abstract] OR hydrogel* [Title/Abstract])) AND ("in vivo" [Title/Abstract] OR "pre-clinical" [Title/Abstract] OR intracranial [Title/Abstract] OR resection[Title/Abstract])

Wed of science: TI=(glioblastoma OR “brain tumo*” OR glioma OR gliosarcoma) AND AB=(“local delivery” OR “drug delivery system” OR “sustained release” OR microsphere* OR microparticle* OR “convection enhanced delivery” OR CED OR hydrogel*) AND AB=(“in vivo” OR “pre-clinical” OR intracranial OR resection)

Scopus: TITLE-ABS (glioblastoma OR “brain tumo*” OR glioma OR gliosarcoma) AND TITLE-ABS (“local delivery” OR “drug delivery system” OR “sustained release” OR microsphere* OR microparticle* OR “convection enhanced delivery” OR CED OR hydrogel*) AND TITLE-ABS (“in vivo” OR “pre-clinical” OR intracranial OR resection)

1.2.2 Inclusion and exclusion criteria

After the search, the results of all databases were downloaded to a Microsoft Excel file (Home and Student 2019). Duplicate results from the three databases were removed before screening. The

following inclusion and exclusion criteria were used to create a selection framework that was used whilst analysing titles/abstracts and full-text manuscripts.

The inclusion criteria were as follows:

- Original research articles written in the English language.
- Articles had at least one *in vivo* antitumor efficacy study using an orthotopic GBM tumour model without resection of the tumour prior to treatment administration.
- The study had to analyse the local delivery of anticancer agents in comparison to negative control of either untreated animals or a vehicle solution.
- The drug preparations used were injectable. The DDS could be drug-loaded nano/macro-carriers or scaffolds loaded with either free drugs or nanomedicines.
- Studies must have had quantitative results in terms of MS.

The exclusion criteria were as follows:

- Articles that were not available in English.
- Review articles, book chapters, and conference proceedings where the methodology was insufficient for the correct evaluation of the results.
- Articles that had only *in vitro* studies, clinical studies, or did not have a preclinical *in vivo* antitumor efficacy study.
- Articles that used either gene therapy, monoclonal antibodies, or genetically engineered cells as an antitumor treatment.
- Articles that did not use the orthotopic GBM tumour model in *in vivo* antitumor efficacy study (e.g., they used a subcutaneous tumour).
- Studies that used a GBM tumour model with resection of the tumour prior to administration of treatment.
- Studies that delivered uninjectable preparations (e.g., wafers), or only delivered liquid formulations of drugs that were not incorporated into a DDS.
- Articles that did not have an appropriate negative control group of either no treatment or empty vehicle control group in *in vivo* antitumor efficacy study.
- Articles that only researched radiotherapy or only had studies combined with radiotherapy.

- Articles that did not use MS to evaluate *in vivo* antitumor efficacy.

1.2.3 Data extraction

Data from the included articles was extracted and entered into tables with different categories. The extracted data included the year of publication, first author, drug used, delivery vehicle, cancer model, and MS for each relevant treatment group. The results were listed in the table by *in vivo* antitumor efficacy studies rather than articles. Many articles had more than one *in vivo* efficacy study, and all data from different studies that met the inclusion criteria were extracted. Different studies in the same article meant that studies had at least one difference in drug used, delivery vehicle or cancer model. Different drug dosages, times of treatment, or injection sites were regarded as too similar to represent separately. If two or more of the same studies were in one article, the most appropriate study was chosen and listed in the table according to the design of the *in vivo* antitumor efficacy study or the optimized study which was focused upon by the authors. Meanwhile, if two different drugs or single drug *vs* double drug combination were in one study, the study was listed separately by drug used.

For MS, some data was explicitly written in the article text or tables. However, in some cases, the MS data had to be calculated from the Kaplan-Meier survival curves. To achieve this, figures were extracted into Microsoft PowerPoint (Home and Student 2019) and scaled appropriately to calculate the medium survival of the relevant experimental groups.

The percentage change in MS between the no-treatment group (negative control) and the treatment group was also calculated. If the study did not have a no-treatment group, the empty vehicle group was used instead as the negative control.

$$\%\ Change\ MS = \frac{MS_{Treatment} - MS_{Control}}{MS_{Control}} * 100\%$$

Equation 1-1. *% Change MS* means the percentage change in median survival time, $MS_{Treatment}$ means median survival time in the treatment group, $MS_{Control}$ means median survival time in the negative control group.

1.2.4 Statistical Analysis

Review Manager software (version: 5.4.1) was used to conduct the *meta*-analysis to compare the antitumor efficacy between locally administrated DDS and the most appropriate negative control group, locally administrated DDS and locally injected free drug, locally administrated DDS, and systemic administration of either the free drug or the DDS. The MS ratio was used to summarize the MS data.(58) It was used as a method being consistent with the hazard ratio method.(59) The survival time ratio was calculated by the following equation 2-2. It was log-transformed to give the normal distribution and make the scale symmetric.(60, 61) The log-transformed MS ratio, the standard deviation (or standard error), and the group size were used as inputs for the *meta*-analysis. Due to the high heterogeneity (I^2 >50%), the random model was used in the *meta*-analysis.

$$survival\ time\ ratio = \frac{Survival\ time\ of\ an\ animal}{MS_{Control}}$$

Equation 1-2. $MS_{Control}$ means median survival time in the negative control group.

1.2.5 Quality assessment

The quality of each included article was assessed by a 12-point checklist described previously by Hirst et al.(58) One point was allocated to each item and the final score was the sum of all points. The 12-point checklist included: (1) peer-reviewed publication, (2) sample size calculation, (3) random allocation to groups, (4) blinded assessment of outcome, (5) compliance with animal welfare regulations, (6) statement of potential conflict of interests, (7) uniform volume or number of cells inoculated, (8) consistent site of tumour implantation, (9) reported number of animals in which the tumour did not grow, (10) stated number of excluded animals, and given reasons for exclusion, including anomalies, (11) explanation of tumour model used, or multiple glioma models used and (12) presentation of evidence that the chemotherapeutic agent acts directly against tumour.

1.3. Results and discussion

1.3.1 Results of the systematic search as a bibliographic screening of literature data

Since TMZ was adopted as the gold standard therapy of GBM in 2005, the number of papers related to the development of DDS for GBM has increased considerably. To select the papers that

could answer the scientific questions addressed in this review, we performed a systematic search using three search engines and defined inclusions and exclusion criteria.

The PRISMA diagram (**Figure 1-3 (A)**) shows the screening process conducted in this review. A total of 1854 articles were searched through three databases. 1038 duplicate articles were removed, and 816 articles remained. 520 articles were excluded during the title and abstract screen due to lacking primary data (e.g., review articles), being irrelevant, or clearly failing to meet the inclusion criteria. The remaining 296 articles were subject to analysis of the full text. Among these articles, the full text of two articles could not be accessed and no reply was received when the authors were contacted. Finally, 36 articles met all inclusion criteria for a total of 44 individual *in vivo* antitumor efficacy studies were eligible. These studies were classified into three categories according to what comparison groups were used as follows: 1- local DDS *vs* negative controls (no treatment or vehicle only); 2- local DDS *vs* locally administered free drug; 3- local DDS *vs* systemic administration of either the free drug or DDS. For all studies, a negative control group receiving either no intervention or vehicle solution only was required from which the percentage change in MS could be calculated. Data from these studies was extracted and entered into **Tables 1-1**, **1-2**, and **1-3**. **Figure 1-3 (B)** shows the quantity distribution by the publication year of all included articles in this review. Only two eligible articles were published before the establishment of the Stupp protocol in 2005.(62, 63) However, most of the included articles were published after 2008, which indicates an increasing trend of interest in more effective and safer DDS for anti-GBM use.

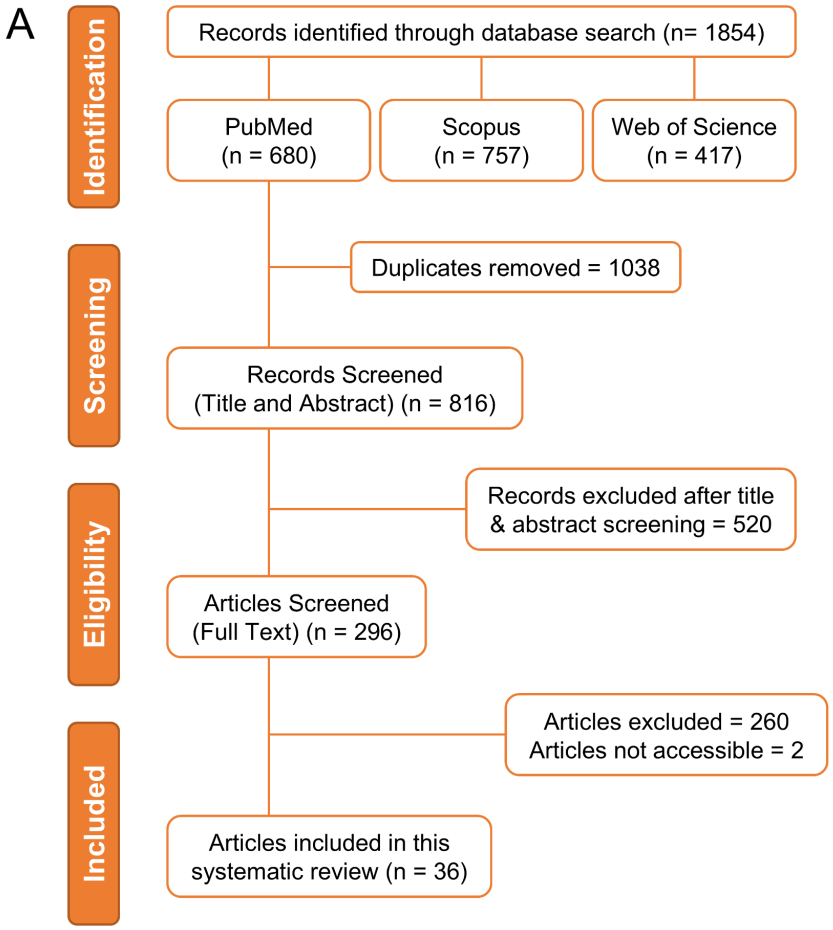

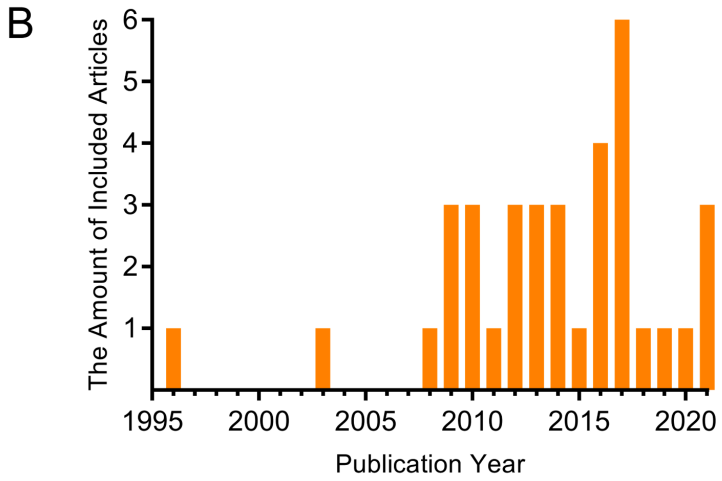

Figure 1-3 Summary of the workflow of the publication screening process.

(A) PRISMA diagram showing the screening process of this systematic review. **(B)** The quantity distribution by publication year of included articles.

At this point, the data was split into three subcategories as outlined via the research questions below. While all the studies that met the inclusion criteria are described in the tables, a general discussion of selected papers was carried out to answer the subcategory questions. These are then

followed by a *meta*-analysis of the data and a general discussion on the state of current research in this field.

1.3.2 Can the MS be improved by administering a DDS directly to the tumour tissue?

All the included studies had a no treatment or vehicle alone negative control group, but 19 of 44 studies had no comparison with local injection of the free drug or systemic administrations. The antitumor effect in these 19 studies, where the DDS was directly injected into the tumour, was variable (**Table 1-1**). Five studies prolonged the MS by more than 100% compared to the no-treatment or vehicle control group,(64-68) whilst others barely showed an increase. In addition, two studies did not reach a significant difference between the local DDS treatment group and the control group.(69)

Local drug delivery widens the drug choice for the treatment of brain tumours, allowing drug repurposing of drugs that have never been exploited for this therapeutic purpose but need to be rationally conceived to effectively result in improved therapeutic outcomes and clinical translation. For example, delivering drugs via nano-sized DDSs can increase the therapeutic efficacy and safety of active molecules for GBM.

Nanomedicines, which are commonly used for cancer diagnosis, therapeutic, and monitoring, can target and reach tumour tissues by passive targeting (enhanced permeability and retention effect) or active targeting (via ligand-receptor or antigen-antibody mechanisms). Singleton et al. designed a water-soluble poloxamer 407 micelle formulation loaded with the pan-histone deacetylase inhibitor Panobinostat.(65) The results showed that F98-bearing Fischer344 rats treated with the micelles by CED significantly prolonged the MS compared to untreated rats, and all treated animals survived until the endpoint of the experiment (60 days). This study demonstrated a novel method of delivering a poorly water-soluble drug to a brain tumour in a syngeneic infiltrative rat GBM model. In addition, the results of the *in vivo* toxicity study showed no adverse response after acute striatal infusion of unloaded micelles in healthy rats, showing the safety of this DDS.

Cancer theranostics represents a combined therapeutic and diagnosis approach that can be achieved using nanomedicines, to reduce delays in treatment and ease the subsequent treatment after diagnosis. Bernal et al. prepared a versatile nanoparticle formulation loaded with TMZ.(70)

This multifunctional platform contained superparamagnetic iron oxide in the shell, which allowed the nanoparticles to be imaged *in vivo* by magnetic resonance imaging (MRI), and the surface of the nanoparticles was tagged with a fluorescent agent. Even though theranostic agents are often tested following systemic administration, the authors specifically conceived their system for a local administration (< 100 nm diameter NPs with negative surface charge, to maximize convection through the extracellular space of brain parenchyma). Then, they exploited the theranostic properties of their nanomedicine to visualize by MRI their distribution in the brain following CED administration distance to the injection site. Moreover, the results of their antitumor efficacy study in the U87 MG xenograft model showed that nanoparticles significantly prolonged the MS of mice by 47% compared to the untreated group.

Stephen et al. designed a multifunctional magnetic nanoparticle to deliver O^6-benzylguanine by CED thus improving its biodistribution and efficacy.(66) This DDS consisted of an iron oxide core which could be used to image the nanoparticles by MRI and evaluate the brain diffusion via CED. The chitosan shell of the nanoparticle contained sulfhydryl groups which were sensitive to a redox environment for localized drug delivery within the cells. The chlorotoxin peptide was linked to the PEG surface for active targeting of GBM cells via MMP2 and Annexin A2 binding. Following CED administration, this DDS produced an excellent volume of distribution within the brain. The results of the antitumor efficacy study in the GBM6-Luc xenograft model showed that the mice treated with this DDS combined with oral TMZ significantly prolonged the MS compared to the untreated mice (p<0.001). Of note, in this study, the author defined the first treatment day as Day 0, which was 26 days after tumour inoculation, therefore affecting the percentage change in MS. If the tumour inoculation day was defined as Day 0 just as the other studies, the MS would have been 29 days (control group) and 35 days (treatment group), meaning that the percentage change in MS would have been 21%.

In another study, the BT4Ca glioma model was used to evaluate the antitumor efficacy of doxorubicin (DOX) microspheres and irinotecan microspheres administered intratumorally.(69) The results showed that the MS was only prolonged by 5% and 11% respectively compared to the no-treatment group, and both treatment groups did not reach a statistically significant difference (p=0.85, 0.33, respectively). The results of another study in this article showed that rats treated

with unloaded microspheres or saline boosted tumour growth.(69) The authors speculated that this might have been due to microsphere injection occurring too soon (three days) after tumour inoculation, though clearly more research is needed for a better understanding of this. This negative result shows how the time of treatment impacts therapeutic benefits in GBM preclinical orthotopic models. Indeed, following the grafting of cells in the brain, it is important to wait for them to form a tumour mass before treating it intratumorally. This will avoid further changes in the tissue architecture and the spreading of tumour cells from the injection site when administering liquids by CED, which would result in more infiltrated tumours and faster tumour growth.

Kikuchi et al. used two different xenograft tumour models to evaluate the antitumor efficacy of DOX liposomes.(71) For the U251 MG tumour model, nude rats treated with DOX liposomes had a significantly prolonged MS by 51%. However, for the U87 MG tumour model, nude rats that received DOX liposomes showed an improvement of MS by only 10%, which still had a significant difference (p=0.016) but minimal therapeutic benefit. This difference in efficacies displayed using these two tumour models might be due - among other factors - to the difference in tumour size at the time of treatment, the life span of animals within each model, or the different cellular sensitivity to DOX in these two cell lines. The MS of untreated rats inoculated with U251 MG cells was 42.7 days while that of rats inoculated with U87 MG cells was just 15.4 days. In this experimental set-up, the life span of the U87 MG model was rather short, perhaps limiting the evaluation of therapeutic efficacy in this experimental setting.

OncoGel is a paclitaxel (PTX) loaded thermosensitive and biodegradable hydrogel. Betty et al. evaluated the efficacy of OncoGel via direct intratumoural injection using the 9L rat model of glioma.(68) OncoGel significantly increased the survival in rats when the drug was administered on Day 0, the day of tumour cell implantation. However, OncoGel failed to prolong the rat survival time if the administration was performed on Day 5 compared to the no treatment control. The dose used in this study might not be enough to arrest an established tumour, even for the higher concentration formulation that was the maximum amount of PTX capable to be loaded into the OncoGel, suggesting the importance of the drug loading capacity in the local DDS. In the combination therapy (with radiotherapy) study, OncoGel (Day 0) combined with radiotherapy

further improved the efficacy compared to no treatment group, empty hydrogel control group, and radiotherapy only group, but if the start of the treatment was postponed to Day 5, the survival time in OncoGel plus radiotherapy treatment group did not reach a significant difference compared to the radiotherapy only group. This result confirmed that a higher PTX dose was required to supress the growth of the established tumour. In another study, Ananth et al. investigated the anti-GBM efficacy of the combination of OncoGel with oral or local TMZ using the 9L model.(67) The median survival time was significantly increased for rats treated with OncoGel plus radiotherapy and oral or local TMZ compared to radiotherapy with oral TMZ treatment. However, this study used a rodent GBM cell line, which might not accurately represent human GBM characteristics. Another limitation of this study was that the administration of OncoGel and the local treatment of TMZ was at different times, which might not be feasible in clinical trials.

Tetsuya et al. found that the combination of surgical tumour resection and implantation of a hydrogel containing camptothecin-loaded PLGA microspheres was an effective treatment for GBM in a C6 rat model.(72) The PLGA microspheres showed better retention at the injection site when incorporated in the thermoreversible gelation polymer hydrogel, whilst PLGA microspheres flowed back away from the injection site if injected alone. The results of the *in vivo* study showed that camptothecin hydrogel local treatment significantly prolonged the median survival time with or without surgical intervention compared to no treatment control. Their previous research showed that PLGA microspheres dispersed in the hydrogel had better therapeutic effects than the administration of PLGA microspheres alone, suggesting that the retention of the DDS at the injection site improved the targeting efficiency.(73)

Christopher et al. developed a gemcitabine and DOX loaded peptide functionalized hyaluronic acid-based hydrogel with the ability to be tuned to match the mechanical properties of the brain tissue.(74) Two GBM models from distinct fragments in the same tumour, A25 M with stiffer structure and grown as large and nodular tumour masses from the margin of the tumour and A25C with softer mechanical properties and grown as a diffuse tumour spreading throughout the brain from the tumour core, were used to evaluate the anti-GBM efficacy of gemcitabine and DOX combined therapy. Drug loaded hydrogel treatment showed a survival advantage compared to the no treatment control and empty hydrogel treatment in both tumour models. However, this study

lacks the investigation on how the stiffness of the hydrogel affects the bioavailability of the drugs and the therapeutic efficacy.

Table 1-1 Summary of direct injection studies with no drug comparison controls

Year	Drug used	Delivery vehicle	Cancer model	Treatment time (days) after tumour implantation	Number of implanted cells	Drug release pattern[a)]	MS no treatment (days)	MS vehicle alone (days)	MS Local delivery *via* DDS (days)	% Change MS (Local DDS *vs* control)[b)]	Ref.
2021	DOX and GEM	Hydrogel	A25 M cells - female NOD SCID mice	14	100,000	Rapid	N/A	61.5	79.5	54%	(74)
2021	DOX and GEM	Hydrogel	A25C cells - female NOD SCID mice	14	100,000	Rapid	N/A	54.5	82.5	51%	(74)
2020	CPT	Polymeric drug	GL261/fluc-DsRed glioma cells - unspecified gender NCr nu/nu mice	7	N/A	Prolonged	21.5[c)]	N/A	28.5[c)]	33%[d)]	(75)
2019	EPI	Nanoparticles	U87MG Lu cells - male nu/nu mice	2 doses: 5, 12	100,000	Prolonged	N/A	27	>60	122%	(64)
2017	$Cu(DDC)_2$	Liposomes	F98 cells - male Fischer rats	10	10,000	N/A	N/A	20.5	25	22%	(76)
2017	Panobinostat	Micelles	F98 cells - unspecified gender Wistar rats	10	100,000	N/A	24.5	N/A	>60	145%	(65)
2016	SN-38	Micelles	U87MG cells - male F344/NJcl-rnu/rnu (nude) rats	5	200,000	N/A	N/A	21	28	33%	(77)
2014	BG	Nanoparticles	GBM6-luc cells - unspecified gender nude athymic mice	4 doses: 26, 29, 34, 36	20,000	Rapid	3	N/A	9	200%	(66)
2014	TMZ	Nanoparticles	U87 cells - male athymic nude mice	2 doses: 4, 7	500,000	Rapid	19.0[c)]	N/A	28.0[c)]	47%[d)]	(70)
2013	PTX	Hydrogel	9L cells - female Fischer 344 rats	0	RP	N/A	15	N/A	33	120%	(67)
2013	Digoxin	Nanoparticles	BCSCs cells - unspecified gender nude rats	N/A	N/A	Prolonged	114.5[c)]	N/A	124.0[c)]	8%[d)]	(78)

2012	DOX	Microspheres	BT4Ca cells - male and female BD IX rats	3	8,000	N/A	19	N/A	20	5%	(69)
2012	Irinotecan	Microspheres	BT4Ca cells - male and female BD IX rats	3	8,000	N/A	19	N/A	21	11%	(69)
2012	CPT	Hydrogel	C6 rat glioma cells - male Sprague-Dawley rats	7	1,000,000	RP	18	N/A	26	44%	(72)
2010	Fc-diOH	Lipid nanocapsules	9L cells - female Fischer 344 rats	6	1,000	N/A	N/A	25	27	8%	(79)
2010	PTX	Hydrogel	9L cells - female Fischer 344 rats	0	100,000	RP	13	N/A	31	138%	(68)
2009	TPT and GD	Liposomes	U87MG cells - male nude rats	2 doses: 5, 8	500,000	N/A	20	N/A	33	65%	(80)
2008	DOX	Liposomes	U251MG cells - male nude (rnu/rnu, homozygous) rats	7	500,000	N/A	N/A	42.7	64.5[c)]	51%[d)]	(71)
2008	DOX	Liposomes	U87MG cells - male Fischer 344/ NJc1-rnu/rnu (nude) rats	7	500,000	N/A	N/A	15.4	17.0[c)]	10%[d)]	(71)

Abbreviations: MS: median survival time; DDS: drug delivery system; Ref.: Reference; GEM: Gemcitabine; CPT: Camptothecin; EPI: Epirubicin; $Cu(DDC)_2$: Copper diethyldithiocarbamate; BG: O6-benzylguanine; TMZ: temozolomide; PTX: Paclitaxel; DOX: Doxorubicin; Fc-diOH: Ferrociphenol; TPT: Topotecan; GD: gadodiamide; RP: referred to a previous protocol. Legend: [a)]: The drug release pattern was defined from the results of *in vitro* drug release studies. The prolonged release was defined as the DDS could release more than 10% of loaded drugs after the first two days. Studies that did not have drug release data after day two, or the cumulative drug release from day two to the end of the experiment did not exceed 10% would be regarded as the rapid release. [b)]: No treatment group was chosen as the negative control group to calculate the percentage change of MS. If the study did not have a no treatment group, the empty vehicle group would be used instead. [c)]: the MS data was measured and calculated from the Kaplan-Meier survival curves (not directly stated in the article). [d)]: the calculation of the percentage change in the MS data used at least one MS data not directly stated in the article.

1.3.3 Does using a DDS improve the efficacy of a locally administered drug?

Similarly to the studies outlined in **Table 1-1**, a further nineteen studies analysed the direct injection of a DDS into a tumour model, but this time with the addition of a locally injected free drug comparison group. The separation of these studies (shown in **Table 1-2**) allows us to analyse whether the DDS confers any therapeutic benefit compared to the same drug administered without a delivery system. However, first, it should be noted that the percentage change in MS between the local DDS treatment group and the control group was highly variable, confirming the findings from **Table 1-1**.

For 89% of the studies, the animals treated locally with a DDS showed an improvement in MS compared to animals treated locally with free drugs by the same administration approach. Injecting free drugs intratumorally did not prolong the MS in two studies compared to the control group.(77, 81) By contrast, in a few studies, local free drug administration prolonged the MS greatly.(82-84) However, except for two studies,(82, 85) local DDS treatment was more effective than local free drug treatment.(62, 63, 77, 78, 81, 83, 84, 86-93)

Zhou et al. designed a brain-penetrating PLGA nanoparticle DDS to overcome the infiltrative and heterogeneous nature of GBM and chemotherapy resistance.(78) The surface of the nanoparticles could be modified by [^{18}F]NPB4, which allowed the DDS to be tracked by PET imaging. The antitumor efficacy of PTX-loaded brain-penetrating nanoparticles was evaluated in the U87 MG model. The results showed that the MS of rats treated with PTX-loaded nanoparticles was significantly longer than the one of animals treated with free PTX or without treatment. However, the authors were aware of the limitations of the model, including the fact that the U87 MG cells are not infiltrative and therefore do not properly mimic human GBMs. Hence, the GS5 cell line - a well-characterized brain cancer stem cell (BCSC) line - which could recapitulate the histopathology of human GBM, was used in subsequent studies. Around 2000 FDA-approved compounds were screened to identify drugs that could inhibit the growth of GS5 cells by the thiazolyl blue tetrazolium bromide (MTT) assay. *In vitro* analysis showed that dithiazanine iodide, an anti-helminthic cyanine dye, effectively inhibited the proliferation of GS5 cells. The authors next evaluated the antitumor efficacy of dithiazanine iodide-loaded brain-penetrating nanoparticles *in*

vivo. Rats treated with dithiazanine iodide-loaded nanoparticles by CED significantly prolonged the MS compared to untreated rats and rats treated with the free drug by CED.

Chen et al. developed an injectable phospholipid-based gel to deliver PTX locally.(87) The viscosity of drug-loaded gel was less than 100cp, which was suitable for injection (for injection, the viscosity should be less than 300cp).(94) The gel was added into the dialysis bag and incubated in the artificial cerebrospinal fluid to evaluate the drug release profile *in vitro*. The results showed that PTX release could be sustained over 30 days. The *in vivo* efficacy study showed that C6-bearing mice treated with PTX gel significantly prolonged the MS compared to mice treated with saline (p<0.01) and mice treated with local free PTX (p<0.05). On the other hand, a different study showed a totally opposite result. Barth et al. used the fifth-generation polyamidoamine dendrimer to conjugate cisplatin and cetuximab.(82) Compared with the control group, local free cisplatin prolonged the MS of rats by 262%, while the DDS slightly reduced the MS by 10% in the F98EGFR model. The *in vitro* results also showed that the DDS were devoid of cytotoxicity perhaps indicating that the cisplatin failed to be released from the bioconjugates.

Bandita et al. embedded the first line drug, TMZ, into the hydrogel and evaluated the anti-GBM efficacy in the orthotopic model using a patient derived cell line.(88) The result showed that TMZ hydrogel treatment significantly prolonged the mice survival time compared to local treatment of the free TMZ. The reason of this improvement might be that the hydrogel formulation provides better drug release profiles than the free drug.

In summary, a wide range of delivery systems have been analysed in a variety of rodent models of GBM. It is therefore unsurprising that a broad range of outcomes has been observed, leading us to undertake a *meta*-analysis of the data as described later on.

Table 1-2 Summary of direct injection studies with local free drug control

Year	Drug used	Delivery vehicle	Cancer model	Treatment time (days) after tumour implantation	Number of implanted cells	Drug release pattern[a)]	MS no treatment (days)	MS vehicle alone (days)	MS Local free drug delivery (days)	MS Local delivery *via* DDS (days)	% Change MS (local free drug *vs* control)[b)]	% Change MS (Local DDS *vs* control)[b)]	Ref.
2021	Chlorogenic acid	Gel	C6 cells - male Kunming mice	2	600,000	Prolonged	N/A	14.5	15	18.5	3%	28%	(93)
2021	MIT	Nanoparticles	Luci^{+} GL261^{R132H} cells - unspecified gender C57BL/6J mice	12	150,000	Rapid	23.0[c)]	N/A	36.0[c)]	97.0[c)]	57%[d)]	322%[d)]	(84)
2017	TMZ	Liposomes	CNS-1 cells - male Lewis rats	5	500,000	N/A	N/A	11.0[c)]	15.8	19.2	44%[d)]	75%[d)]	(86)
2017	TMZ	Hydrogel	GBM001 cells - unspecified gender nu/nu mice	7	20,000	N/A	N/A	20	28	38	40%	90%	(88)
2017	PTX	Gel	C6 cells - male Balb/c mice	3	500,000	Prolonged	N/A	15.5	18	26.5	16%	71%	(87)
2016	DTX	Cloudy suspension	C6 cells - male Sprague-Dawley rats	7	1,000,000	Rapid	N/A	23.8	33.4	70.2	40%	195%	(89)
2016	SN-38	Micelles	9L cells - male Fischer 344 rats	5	10,000	N/A	N/A	29	28	42	-3%	45%	(77)
2016	SQ-Gem	Nanoparticles	RG2 cells - male Fischer 344 rats	4	250,000	N/A	N/A	12	13.0[c)]	19.0[c)]	8%[d)]	58%[d)]	(90)
2016	Cisplatin	Polymeric drug	F98EGFR cells - unspecified gender Fischer rats	14	1,000	N/A	21	N/A	76	19	262%	-10%	(82)
2015	PTX	Lipid nanocapsules	GL261 cells - female C57BL/6J mice	12	10,000	N/A	N/A	28	28	34	0%	21%	(81)

2014	DOX	Nanodiamonds	U251MG-Luc cells - unspecified gender NIH-RNU nude rats	14	RP	N/A	N/A	28.4	46.6	64.6	64%	127%	(83)
2014	DOX	Nanodiamonds	C6-Luc cells - male Fischer 344 rats	7	RP	N/A	N/A	31.0[c)]	43.8	78.2	41%[d)]	152%[d)]	(83)
2013	DI	Nanoparticles	GS5 cells - unspecified gender nude rats	10	500,000	Prolonged	147	N/A	177	>280	20%	90%	(78)
2013	PTX	Nanoparticles	U87MG cells - unspecified gender nude rats	7	500,000	Prolonged	27	N/A	30	46	11%	70%	(78)
2010	Am80	Micelles	U87MG cells - male Fischer 344 nude rats	7	500,000	RP	N/A	14.0[c)]	15.0[c)]	15.0[c)]	7%[d)]	7%[d)]	(85)
2009	BCNU	Nanoparticles	C6 cells - male Sprague–Dawley rats	5	1,000,000	Prolonged	12.9	N/A	14.7	22.0[c)]	14%	71%[d)]	(91)
2009	DOX	Micelles	9L cells - male Fischer 344 rats	7	500,000	N/A	N/A	16.9	19.6	36	16%	113%	(92)
2003	5-FU	Microspheres	F98 cells - female Fischer F344 rats	7	1,000	Prolonged	22.7	23.8	26.5	34.1	17%	50%	(63)
1996	5-FU	Microspheres	C6 cells - female Sprague-Dawley rats	7	200,000	RP	24.0[c)]	N/A	30.5[c)]	39.5[c)]	27%[d)]	65%[d)]	(62)

Abbreviations: MS: median survival time; DDS: drug delivery system; Ref.: Reference; MIT: Mitoxantrone; TMZ: Temozolomide; PTX: Paclitaxel; DTX: Docetaxel; SQ-Gem: Squalenoyl-gemcitabine; DOX: Doxorubicin; DI: Dithiazanine iodide; BCNU: carmustine; 5-FU: 5-fluorouracil; RP: referred to a previous protocol. Legend: [a)]: The drug release pattern was defined from the results of *in vitro* drug release studies. The prolonged release was defined as the DDS could release more than 10% of loaded drugs after the first two days. Studies that did not have drug release data after day two, or the cumulative drug release from day two to the end of the experiment did not exceed 10% would be regarded as the rapid release. [b)]: No treatment group was chosen as the negative control group to calculate the percentage change of MS. If the study did not have a no treatment group, the empty vehicle group would be used instead. [c)]: the MS data was measured and calculated from the Kaplan-Meier survival curves (not directly stated in the article). [d)]: the calculation of the percentage change in the MS data used at least one MS data not directly stated in the article.

1.3.4 Can local drug administration give higher efficacy than systemic delivery?

Of all the eligible studies included in this review, only six of them compared systemic *vs* intratumoral administration of the same drug. In all these studies, outlined in **Table 1-3**, the systemic treatment group improved the MS by less than 50% compared to untreated controls, while animals treated with local DDS showed a prolonged MS of more than 100% in four of six studies.(95-98) Except for one study,(99) local DDSs showed a better antitumor effect than the systemic administration of the same drug.

Chen et al. compared the antitumor efficacy of irinotecan liposomes by different routes of delivery.(97) Two different types of GBM xenograft models which use cells derived from primary human GBM tissues were used to evaluate the *in vivo* antitumor efficacy of this DDS. GBM43 cells were shown to be radioresistant and SF7796 cells were derived from a recurrent tumour. The results showed that local delivery of irinotecan liposomes by CED significantly enhanced the antitumor efficacy in both models compared to systemic administration by tail vein (p<0.001 in the GBM43 model and p=0.048 in the SF7796 model). Laine et al. developed an active targeting strategy to deliver ferrociphenol.(99) NFL-TBS.40–63 peptide (cell-penetrating peptide) was inserted onto the surface of lipid nanocapsules. The results of the *in vivo* study in the 9L model showed that the intratumoral delivery by CED significantly reduced the MS, while animals treated with intracarotid administration had increased MS. While this study showed the beneficial effect of active targeting in intracarotid treatment, it also showed that CED administration of ferrociphenol lipid nanocapsules was not safe in this experimental setting leading to severe side effects.

Chiara et al. found that local delivery of lauroyl-gemcitabine lipid nanocapsule based hydrogel prolonged the mice survival compared to intratumoral injection of the free drug in the orthotopic GBM model.(96) However, in the GBM resection model, the survival time did not show significant difference between hydrogel implantation group and free drug local administration group. The reasons of these conflicting results might be the difference of the tumour microenvironment with or without resection, the immunostimulatory capacities of the drug, and different humoral adaptive and innate immune response of the animals. This comparative experiment also revealed that the tumour resection attenuated the effect of using the DDS. As less tumour cells remained in

the brain, the targeting capacity of the DDS towards the monocytic-myeloid derived suppressor cells could not lead to a significant benefit of the treatment.(100)

As stated earlier, the current standard of care therapy for GBM is surgical resection followed by the Stupp protocol. TMZ is an alkylating agent able to pass the BBB following oral administration, so it is a good drug candidate to assess whether local delivery can outperform systemic delivery. Lin et al. delivered TMZ-loaded liposomes directly into the tumour by CED.(95) The U87 MG-bearing mice treated twice with local TMZ liposomes had a significantly longer MS compared with the control group, while mice treated three times with oral TMZ had no significant improvement in survival. Zhang et al. implanted TMZ poly (d,l-lactide-co-glycolide) (PLGA) microparticles on the surface of the tumour tissue to evaluate the antitumor effect in the C6 glioma model.(98) Rats treated with TMZ microparticles locally had a significantly longer MS than rats treated with TMZ orally (p=0.002). These studies demonstrate that local delivery can enhance the antitumor effect and reduce systemic toxicities by decreasing the TMZ concentration in circulating blood.

Table 1-3 Summary of direct injection studies with systemic direct control

Year	Drug used	Delivery vehicle	Cancer model	Treatment time (days) after tumour implantation	Number of implanted cells	Drug release pattern[a)]	MS no treatment (days)	MS vehicle alone (days)	MS Systemic delivery (days)	MS Local delivery *via* DDS (days)	% Change MS (systemic *vs* control)[b)]	% Change MS (local DDS *vs* control) [b)]	Ref.
2018	TMZ	Liposomes	U87MG cells - male nu/nu mice	2 doses: 10, 17	100,000	Prolonged	25	N/A	28.5	50	14%	100%	(95)
2017	$GemC_{12}$	Hydrogel	U87MG cells - female NMRI nude mice	15	30,000	RP	24	28	36	49	50%	104%	(96)
2013	Irinotecan	Liposomes	GBM43 cells - female athymic mice	2 doses: 5, 8	300,000	N/A	19.0[c)]	N/A	27.0[c)]	55.0[c)]	42%[d)]	189%[d)]	(97)
2013	Irinotecan	Liposomes	SF7796 cells - female athymic mice	20	300,000	N/A	41.0[c)]	N/A	48.0[c)]	58.5[c)]	17%[d)]	43%[d)]	(97)
2012	Fc-diOH	Lipid nanocapsules	9L cells - female Fischer F344 rats	6	100,000	N/A	25	N/A	26.5[c)]	11	6%[d)]	-56%	(99)
2011	TMZ	Microspheres	C6 cells - male Sprague–Dawley rats	6	2,000,000	RP	19.5	N/A	27	46.5	38%	138%	(98)

Abbreviations: MS: median survival time; DDS: drug delivery system; Ref.: Reference; TMZ: Temozolomide; GemC12: Lauroyl-gemcitabine; Fc-diOH: Ferrociphenol; RP: referred to a previous protocol. Legend: [a)]: The drug release pattern was defined from the results of *in vitro* drug release studies. The prolonged release was defined as the DDS could release more than 10% of loaded drugs after the first two days. Studies that did not have drug release data after day two, or the cumulative drug release from day two to the end of the experiment did not exceed 10% would be regarded as the rapid release. [b)]: No treatment group was chosen as the negative control group to calculate the percentage change of MS. If the study did not have a no treatment group, the empty vehicle group was used instead. [c)]: the MS data was measured and calculated from the Kaplan-Meier survival curves (not directly stated in the article). [d)]: the calculation of the percentage change in the MS data used at least one MS data not directly stated in the article.

1.3.5 *Meta*-analyses

Meta-analyses of the included studies were carried out to determine the overall effect size for the questions posed previously. Two eligible studies were excluded from the *meta*-analysis as the survival time of each animal was not available.(81, 82) A *meta*-analysis that compared locally administrated injectable DDS with negative control groups across 42 studies was conducted firstly to analyse whether a DDS directly administrated into the tumour tissue could improve the MS via the hazard ratio method.(59) For the purpose of this study, the hazard ratio-based "time to event" methodology was used, which gives the MS ratio between the intervention of the local DDS *vs* no DDS treatment controls. The diamond in the forest plot (**Figure 1-5**) showed that the total MS ratio (indicated as hazard ratio) was 1.68 (95% confidence interval (CI), 1.63-1.73), which reached a significant difference (p<0.00001). This result indicated that local administration of injectable DDS was beneficial for the survival time of animals. The heterogeneity in this *meta*-analysis was at a high degree (I^2=100%). The reason for this is probably because studies used different model drugs, delivery vehicles, tumour cells, animal models, and administration methods. According to **Tables 1-1, 1-2** and **1-3**, the time of tumour incubation prior to the treatment varied from the same day of implantation to 26 days after implantation; the number of implanted cells varied from 1,000 to 2,000,000. These experiment settings obviously affected the tumour size when starting the treatment, and the survival time of animals without treatment or animals in treatment groups, which would further affect the value of the MS ratio. Only 16 of the 44 studies had *in vitro* drug release results included in the study. Some studies showed that a DDS with a rapid release pattern could prolong the MS of animals treated with the DDS by more than 100% compared with that in the control group,(66, 84, 89) while a sustained-release DDS only slightly increased the MS by less than 30% in some studies.(78, 93) It might indicate that a sustained-release pattern does not necessarily mean a better antitumor efficacy.

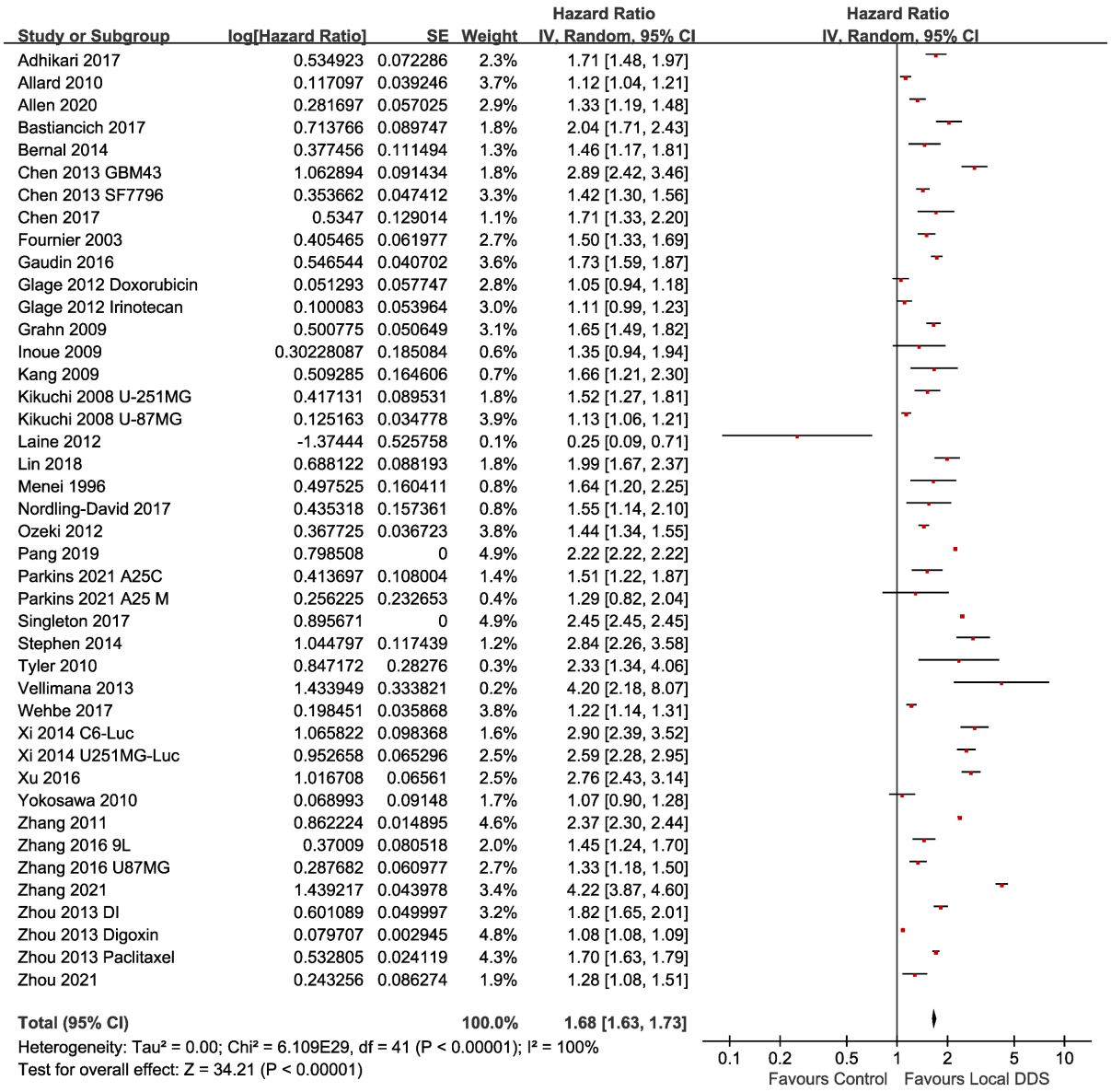

Figure 1-4 A forest plot of the hazard ratio shows the antitumor efficacy of locally administered injectable DDSs compared with control groups.

The table shows the median survival ratio (hazard ratio), the standard error (SE) and 95% confidence intervals (CI) of each study.

Another *meta*-analysis across seventeen studies was conducted to analyse whether using a DDS improved the efficacy of a locally administered drug. In this case, as a direct comparison was carried out between two therapeutic interventions, the mean difference method was used. Despite a large amount of heterogeneity (I^2=75%), **Figure 1-6** shows that local administration of injectable DDS could enhance the antitumor efficacy significantly (mean difference=0.17; 95% CI, 0.13-0.21; p<0.00001) compared with locally administrated free drugs.

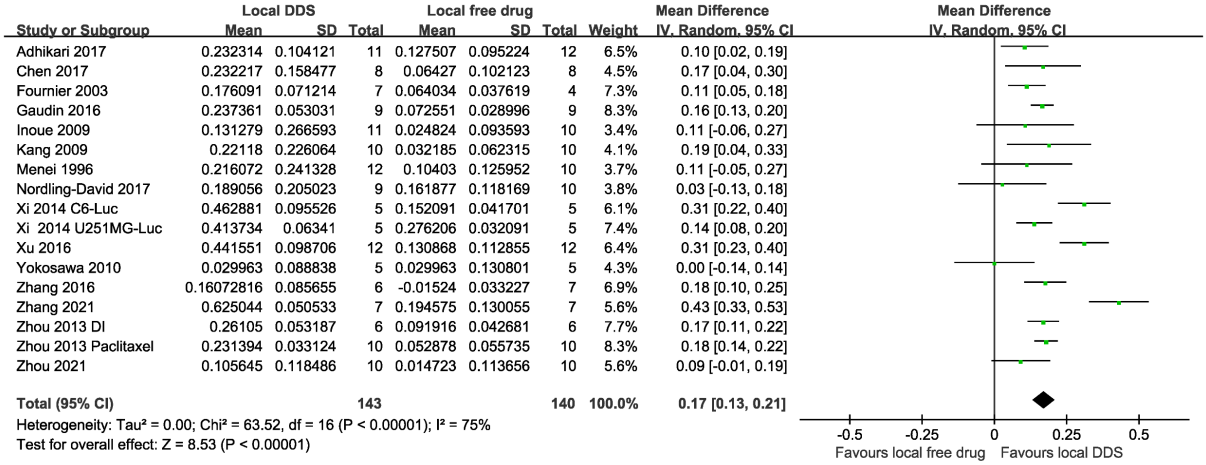

Figure 1-5 A forest plot shows the antitumor efficacy of locally administered injectable DDSs compared with locally injected free drugs.

The table shows the log-transformed data of the median survival ratio (Mean), the standard deviation (SD) and the number of animals in each group (Total). The mean difference shows the 95% confidence interval of each study.

Six of all the eligible studies had a systemic treatment group using the same drug as in the local administration. A *meta*-analysis was conducted across these studies to compare the antitumor efficacy between systemic treatment and local treatment. As shown in **Figure 1-7**, animals locally treated with DDS had a significantly prolonged MS compared with animals systemically treated with either the free drug or the DDS (mean difference=0.17; 95% CI, 0.07–0.26; p=0.0007).

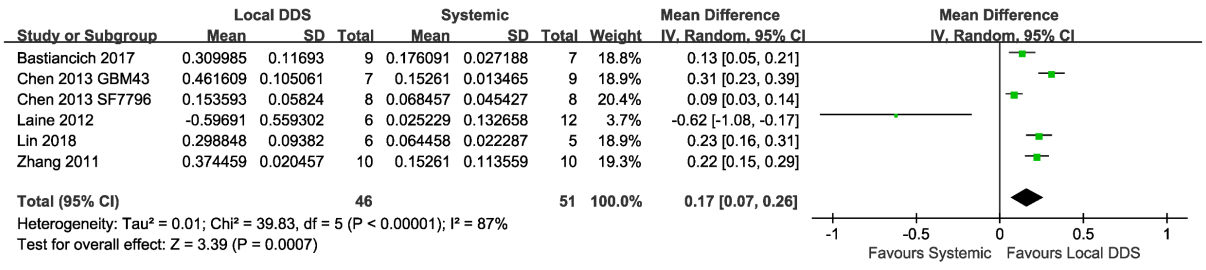

Figure 1-6 A forest plot shows the antitumor efficacy of locally administered injectable DDSs compared with systemic administration of either the free drug or the DDS.

The table shows the log-transformed data of the median survival ratio (Mean), the standard deviation (SD) and the number of animals in each group (Total). The mean difference shows the 95% confidence interval of each study.

1.3.6 Quality assessment of the included articles

Study quality was assessed by the 12-point checklist in all 36 included articles. **Table 1-4** shows the full breakdown score of the quality assessment. Except for one article, all articles were peer-reviewed publications. None of them mentioned how to calculate the sample size. Most of the articles stated the accurate site and the number of inoculated tumour cells for the establishment of a cancer model. Only three articles reported the number of animals in which the tumour did not grow, and two articles used a blinded assessment for *in vivo* studies. For greater research transparency and reproducibility, we think that the points on this checklist are important for researchers of future studies to consider. In particular, the blinded assessment of outcomes is a simple way to remove biases in the study.

Table 1-4 The specifics of quality assessment scores allocated to each included article

Year	1st Author	1	2	3	4	5	6	7	8	9	10	11	12	Total	Ref.
2021	Parkins	1	0	1	0	1	1	1	1	0	1	1	0	8	(74)
2021	Zhou	1	0	1	0	1	1	1	0	0	0	0	0	5	(93)
2021	Zhang	1	0	1	0	1	1	1	1	0	1	0	1	8	(84)
2020	Allen	1	0	1	0	1	0	0	0	0	NDS	1	1	5	(75)
2019	Pang	1	0	1	0	1	1	1	1	1	NDS	0	1	8	(64)
2018	Lin	1	0	0	0	1	1	1	1	1	0	0	0	6	(95)
2017	Wehbe	1	0	0	0	1	1	1	1	0	0	1	0	6	(76)
2017	Singleton	1	0	1	1	1	1	1	RP	0	NDS	1	1	8	(65)
2017	Nordling-David	1	0	0	0	1	1	1	1	0	1	1	1	8	(86)
2017	Adhikari	1	0	0	0	1	1	1	1	0	NDS	0	1	6	(88)
2017	Chen	1	0	1	0	1	1	1	1	0	NDS	1	0	7	(87)
2017	Bastiancich	1	0	1	0	1	1	1	1	1	1	1	1	10	(96)
2016	Zhang	1	0	1	0	1	1	1	1	0	NDS	0	0	6	(77)
2016	Xu	1	0	1	0	1	1	1	1	0	NDS	0	1	7	(89)
2016	Gaudin	1	0	0	0	1	1	1	1	0	NDS	1	0	6	(90)
2016	Barth	1	0	1	0	1	1	1	RP	0	NDS	1	1	7	(82)
2015	Lollo	1	0	0	0	1	0	1	1	0	0	1	1	6	(81)
2014	Stephen	1	0	0	0	1	0	1	1	0	NDS	1	0	5	(66)
2014	Bernal	1	0	1	0	1	1	1	RP	0	NDS	0	0	5	(70)
2014	Xi	1	0	0	0	1	1	RP	RP	0	NDS	0	1	4	(83)

2013	Vellimana	1	0	0	0	1	0	RP	RP	0	NDS	0	0	2	(67)
2013	Zhou	0	0	0	0	1	1	1	1	0	NDS	1	0	5	(78)
2013	Chen	1	0	0	0	1	1	1	RP	0	NDS	1	1	6	(97)
2012	Ozeki	1	0	0	0	1	0	1	1	0	0	0	0	4	(72)
2012	Glage	1	0	1	1	1	1	1	1	0	0	0	1	8	(69)
2012	Laine	1	0	0	0	1	0	1	1	0	0	0	0	4	(99)
2011	Zhang	1	0	1	0	1	0	1	1	0	0	0	1	6	(98)
2010	Allard	1	0	1	0	1	0	1	1	0	NDS	0	0	5	(79)
2010	Tyler	1	0	1	0	0	1	1	1	0	0	0	0	5	(68)
2010	Yokosawa	1	0	1	0	1	0	1	1	0	NDS	0	1	6	(85)
2009	Grahn	1	0	1	0	1	0	1	1	0	0	0	1	6	(80)
2009	Kang	1	0	1	0	0	0	1	1	0	NDS	0	0	4	(91)
2009	Inoue	1	0	1	0	1	0	1	1	0	0	0	0	5	(92)
2008	Kikuchi	1	0	1	0	1	1	1	1	0	NDS	0	0	6	(71)
2003	Fournier	1	0	1	0	0	0	1	1	0	1	1	1	7	(63)
1996	Menei	1	0	1	0	0	0	1	1	0	1	1	1	7	(62)

Where: 1 = Peer-reviewed publication, 2 = sample size calculation, 3 = random allocation to groups, 4 = blinded assessment of outcome, 5 = compliance with animal welfare regulations, 6 = statement of potential conflict of interests, 7 = uniform volume or number of cells inoculated, 8 = consistent site of tumour implantation, 9 = reported number of animals in which the tumour did not grow, 10 = stated number of excluded animals, and given reasons for exclusion, including anomalies, 11 = explanation of tumour model used, or multiple glioma models used, 12 = presentation of evidence that the chemotherapeutic agent acts directly against tumour. Abbreviations: RP: referred to a previous protocol, NDS: not directly stated, but all animals accounted for, Ref.: Reference.

1.4. Conclusions

Overall, the results of this study show that local drug delivery within the tumour mass is a promising approach to overcome the intrinsic GBM therapeutic challenges. Bypassing the BBB allows researchers to increase the number of active molecules that can be explored to defeat this devastating tumour and achieve high local drug concentrations thus maximizing their therapeutic effect. While the number of articles describing the use of local treatments for GBM in preclinical models has increased exponentially since Gliadel®'s approval, the clinical trials have been limited leading to no new local treatments approved for GBM since 1997.(53) Indeed, the development of local treatments for GBM is challenging, especially for non-resectable tumours where no cavity

exists for implantation. Several parameters need to be considered to properly achieve the therapeutic goal. These include a DDS design and formulation development which considers the GBM physiopathology and unique microenvironment, adapted properties for a local application in the brain, and a careful characterization of its *in vivo* safety and efficacy using appropriate preclinical models.(101)

The goal of this systematic review and *meta*-analysis was to evaluate the therapeutic efficacy of DDS intratumorally delivered via injection in unresected GBM preclinical models. In addition, we asked whether the DDS itself plays a role in outcomes by comparison to locally injected free drugs. The *meta*-analyses showed that whilst there was a high degree of variability across studies, local injection of delivery systems resulted in an improvement of MS compared to control groups and local injection of free drugs. This study also showed that local drug administration via a DDS could outperform systemic administration of free drugs. These results indicate that local delivery still holds promise for this scope, but efforts should be made to standardize the methods used to test such systems to compare their efficacy.

Indeed, the therapeutic effect observed following intratumoral administration can be subject to many variables and biases. For example, the GBM model chosen for the study can directly impact the outcome as less infiltrative cell lines are likely to respond better to local treatment compared to more aggressive models. Also, the volume injected, the injection rate, the drug dose, and the time of administration – which vary between studies – can make it very difficult to compare data between different groups (or between different investigators working in the same group). Moreover, the tumour size at the time of treatment is not always measured and/or reported so it is difficult to replicate the studies and understand the real impact of the treatment in the long-term.

Most of the papers reported in this review used xenograft models using established GBM cell lines to test the efficacy of local treatments. While these models lead to reproducible and reliable experiments with high engraftment and growth rates - and some of them have shown to still mimic the true biological nature of GBM (102) - cells are injected into the brain of immunodeficient animals. In recent years, the crosstalk between glial cells and immune cells (brain resident macrophages as well as immune cells recruited from the periphery) has been demonstrated to impact tumour cell behaviour. Testing local treatments on several models could help our understanding of the real therapeutic efficacy and potential long-term impact, thus partially filling the preclinical-clinical gap.

Whilst the prognosis for GBM is universally poor, there is no local intervention for non-resectable tumours. Stiff wafers such as Gliadel® are not only unsuitable but suffer from rapid release of monotherapy. The studies in this review show promise in this regard (soft hydrogels and injectable formulations) though it is likely that delivery of multiple drugs acting via differing mechanisms would be beneficial. Key considerations moving forward will be the evaluation of drug penetration to residual GBM cells proliferating deeper into the brain parenchyma,(103) obtaining optimal drug release profiles *in vivo*,(53) and multifaceted modes of therapeutic action. However, to date, the *meta*-analysis conducted herein shows a clear rationale for the continued development of injectable local drug delivery devices for GBM therapeutics.

Injectable biomaterials for local drug delivery in GBM span a wide range of natural and synthetic polymers. For example, natural materials such as hyaluronic acid-based hydrogel(74) and soybean phospholipid-based gel(93) were investigated due to their biocompatibility. In contrast, synthetic polymers, including 3-ethyl-3-(hydroxymethyl)oxetane,(75) poloxamer 407,(65) poly(ethylene glycol)-poly(amino acid) co-polymer,(77) and poly(D,L-lactide-co-glycolide)-poly(ethylene glycol) triblock copolymer,(67) offer better control over degradation kinetics and drug release profiles and have been widely used to fabricate drug delivery vehicles such as hydrogels and micelles.

A variety of drug candidates have been tested for local treatment of GBM, not only due to their inability to pass the BBB, but also for their potential to overcome resistance to alkylating agents. While many of these candidates have demonstrated survival benefits in animal studies, a comprehensive screening of existing oncology and neuroactive drugs could further aid in identifying potent therapeutic molecules. Repurposing FDA-approved drugs may accelerate the development process by leveraging existing preclinical and clinical data.

2. Drug repurposing

At present, discovering novel therapeutics is becoming increasingly challenging in the pharmaceutical industry. The burden of investment to find next-generation chemotherapeutics is growing, fuelling the rationale for drug repurposing approaches.(104) By repurposing or repositioning existing drugs for new indications, the time and money invested per successful outcome can potentially be reduced.(105) Many reasons may facilitate this strategy, including drugs failing to show efficacy in the late stage of clinical trials but proven the safety in early stage of clinical trials, the economic benefit not being enough in a certain therapy area, and the mechanism of action found to effectively treat another disease during the development

process.(106) To develop a novel cancer drug, the median time and median cost were 7.3 years and $648 million, respectively.(107) However, drug repurposing can accelerate clinical trials by using existing data such as pharmacokinetic data, pharmacodynamic data, and safety data from previous clinical trials, which reduces the drug development time by 3-5 years and the investment by $300 million.(108, 109)

There are dozens of FDA-approved drugs that have proven activity in GBM models, with some of them being tested in clinical trials.(110-113) Losartan, used to treat high blood pressure, showed the effect of decompressing vessels to normalize the tumour microenvironment.(114) An open-label phase II clinical trial (NCT03951142) uses losartan for the treatment of newly diagnosed and recurrent GBM to assess the safety of losartan and the dose-response relationship. Atorvastatin used to prevent cardiovascular disease, could inhibit tumour cell proliferation and migration *in vitro*.(115) A single-arm phase II study (NCT02029573) used atorvastatin in combination with radiotherapy and TMZ to treat newly diagnosed GBM, whose results showed 19.9 months of median survival time.(116)

Chloroquine, an antimalarial medication, might be used as an adjuvant to the standard treatment (NCT04772846, NCT02378532). The results of a randomized, double-blind, placebo-controlled trial showed that although patients treated with chloroquine combined with carmustine and radiotherapy did not show significant median survival benefits compared to patients treated with placebo plus chemoradiotherapy, the rate of death was decreased.(117) Chlorpromazine, primarily used to treat schizophrenia, was investigated as a potential adjuvant during the temozolomide solely in the adjuvant phase of the standard treatment (NCT04224441).

Screening existing drugs for potential candidates for use in GBM has provided a variety of drug candidates, though drug permeability across the BBB is the crucial obstacle for drug selection. Systemic drug delivery requires high BBB permeability to achieve therapeutic concentration in GBM tissue, hence giving rationale for screening neuroactive drugs. Sohyon Lee *et al*. used an image-based *ex vivo* drug screening method, also called pharmacoscopy, to screen drug candidates through the effective reduction of tumour cell population relative to non-malignant cells in the tumour microenvironment.(118) 67 neuroactive drugs were tested across 27 GBM patient samples. The results showed that vortioxetine got the top mean score, which did not show anti-GBM efficacy before. Brexpiprazole also showed positive anti-GBM activity, and interestingly, male patient samples were more sensitive to it. Three repurposed drugs, clemastine, brexpiprazole, and vortioxetine, were investigated for their potential efficacy against GBM (**Figure 1-7**).

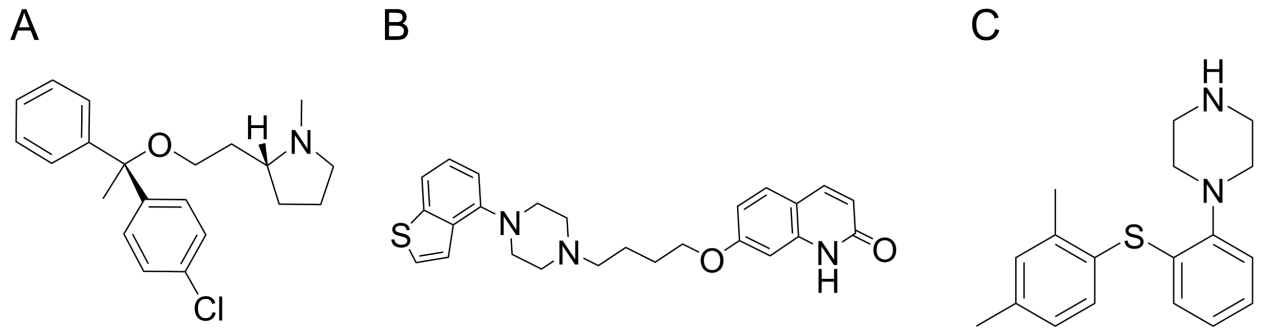

Figure 1-7 Structures of repurposed drugs.

(A): clemastine, **(B)**: brexpiprazole, **(C)**: vortioxetine.

2.1 Clemastine

Clemastine has been used for nearly 60 years in clinics as a first-generation antihistamine drug. It exhibits antagonist activity at the H1 histamine receptor,(119) used for allergic suppression such as allergic rhinitis and asthma.(120, 121) Histamine receptors are expressed in various types of cells such as nerve cells, immune cells, and smooth muscles, so antihistamines as well as clemastine have been researched as repurposed drugs on many indications.(122) GBM stem cells secreted histamine and promoted GBM progression by enhancing angiogenesis, and the antihistamine drug, diphenhydramine, inhibited GBM tumour growth.(123) Using siRNA or ciproxifan to inhibit the histamine receptor 3 significantly impeded the GBM tumour growth.(124) Moreover, clemastine treatment reduced the amount of invasive GBM cells and prolonged the mice's survival time.(125) So, I hypothesized that clemastine local treatment might achieve better therapeutic efficacy.

2.2 Brexpiprazole

Brexpiprazole is an atypical antipsychotic approved by the FDA in 2015. It is used to treat major depressive disorders and schizophrenia as an adjuvant. In 2023, it was approved by the FDA as the first and the only medication to treat agitation associated with dementia due to Alzheimer's disease.(126) Brexpiprazole acts with partial agonist activity at 5-hydroxytryptamine$_{1A}$ (5-HT$_{1A}$), dopamine D_2 and D_3 receptors, and antagonist activity at 5-HT$_{2A}$,5-HT$_{2B}$ and 5-HT$_7$ receptors.(127) More than 99% of Brexpiprazole is bound with serum albumin in the blood.(128) Typically, Brexpiprazole at a dosage of 2-4 mg/day showed effectiveness in the treatment of schizophrenia.(129-131) After 6 weeks of treatment, both young and old schizophrenia patients had a symptomatic response and functional response compared to placebo-treated patients.(132) Suzuki *et al*. found that Brexpiprazole downregulated the expression of an anti-apoptotic protein called survivin resulting in GBM stem cells being more sensitive to chemotherapeutic

reagents.(133) Brexpiprazole also reduced the stemness of cancer stem cells by downregulating the expression of CD133 and other stem cell markers.(133)

2.3 Vortioxetine

Vortioxetine, approved by the FDA in 2013, is used to treat major depressive disorders. It inhibits 5-HT reuptake and modulates key 5-HT receptors, which is an antagonist of 5-HT_3, 5-HT_7, and 5-HT_{1D} receptors, a partial agonist of 5-HT_{1B} receptor, an agonist of 5-HT_{1A} receptor and an inhibitor of serotonin transporter.(134, 135) The results of animal studies showed that vortioxetine could elevate the extracellular concentration of neurotransmitters such as noradrenaline, dopamine, acetylcholine, and histamine.(135, 136) The treatment effect of vortioxetine in the clinic was relevant to the dosage, and a higher dose could achieve a better treatment effect (5-20 mg/day).(137) A *meta*-analysis revealed that vortioxetine ranked in the top one-third both in efficacy and acceptability among 21 antidepressants.(138) Recent research demonstrated that vortioxetine upregulated AP-1 transcription factor further driving the expression of BTG 1 tumour suppressor and exerted anti-GBM efficacy in preclinical studies.(118)

As mentioned in Section 1, local drug delivery using a DDS within the tumour mass has demonstrated superior performance compared to both systemic administration and local delivery of the free drug, supporting the rationale for further development of novel DDS approaches. The mechanical mismatch is a critical limitation of the rigid Gliadel® wafer, so biomaterials with softer structures are appealing for the design of next-generation DDS used in the brain. Cryogels, which are similar to hydrogels, offer enhanced mechanical integrity, ease of handling, and high elasticity, making them a promising platform for intracranial drug delivery.

3. Cryogels

Cryogels are a type of three-dimensional (3D) hydrophilic network with interconnected macropores. They are prepared via a controlled freezing procedure before or during polymerization. In general, water-soluble monomers are used, and the prepolymer solution is frozen followed by crosslinking and thawing the ice crystals. The solvent used in cryogelation, water, makes the production process more economical and environmentally friendly than an organic solvent involved in preparing other polymer materials. The prepolymer solution is therefore concentrated around the ice crystalline arrangement. After polymerizing and defrosting, interconnected macropores are left behind in the cryogels. Other solvents such as 1,4-dioxane and dimethyl sulfoxide could be used if a higher freezing temperature is required.(139, 140)

Cryogels are similar to hydrogels but have some advantages for drug delivery applications. The interconnected macroporous structure enhances the viscoelastic property of cryogels and reduces physical deformation.(141) Cryogels can be dehydrated and rehydrated without losing mechanical integrity, whilst hydrogels typically lose their original shape when dehydrated. Cryogels also hold the advantage of possessing shape memory. The structure of the cryogels can be restored completely after being dried out and rehydrated. Meanwhile, cryogels have highly elastic properties. In a direct comparison, hydrogels could be only strained by around 20% before mechanical destruction, however, cryogels of the same polymer composition could be strained by more than 70%.(142) Moreover, the Young's modulus of cryogels is lower than that of hydrogels fabricated by the same composition (4 ± 2 kPa *vs* 42 ± 4 kPa).(143) It indicates that cryogels are a more suitable biomaterial for application in soft tissue. Combining the properties of elasticity and shape memory, cryogels can pass through pinholes that are much smaller than their size.(143, 144) Furthermore, they can be produced with customized shapes. Therefore, cryogels could be used as an injectable vehicle for irregularly shaped tissue cavities.(143, 145) In addition, cryogels can be autoclaved and remain intact, which is a basic requirement in clinical applications.(146) With these remarkable properties, cryogels have a wide range of applications in the fields of cell culture, bioseparation, tissue engineering, and drug delivery.(147-151)

Many methods can be employed for cryogelation, including free radical polymerization,(152) irradiation polymerization,(153) condensation polymerization,(154) enzymatic catalysis,(155) and self-assembly.(156) Free radical polymerization is a commonly used method for the fabrication of cryogels, which consists of three reaction stages: initiation, propagation, and termination.(157) The commonly used type I photoinitiators (e.g., 2-Hydroxy-2-methylpropiophenone (HMPP)(158) and lithium phenyl(2,4,6-trimethylbenzoyl) phosphinate (LAP)(159)) generate two free radicals by a cleavage reaction after absorbing the photon. These free radicals react with monomers to produce radical monomers to initiate polymerization. Monomers with free radicals further react with other monomers to propagate the chain. Termination usually happens when two chains with radicals merge into one longer chain. After the polymerization reaction, cryogels can be washed to remove the photoinitiators and unreacted monomers.

The physicochemical properties of cryogels, including pore size, stiffness, and porosity, can be controlled by altering the parameters of the prepolymer solution or in the process of freezing. For example, higher monomer concentration increases the number of cross-linkable groups, which results in a decrease in the pore size, with cryogels becoming stiffer.(160) On the other hand, the

crosslinking temperature and the cooling rate can affect the pore size considerably. A higher cooling rate at a lower freezing temperature can produce smaller pores.(161) This is based on the mechanism of the growth of ice crystals. Specifically, at a higher cooling rate, the rate of crystallization will increase, and more ice crystals will be formed.(162) For a certain volume of solvent, the quantity of ice crystals will increase whilst the size of ice crystals will become smaller. Therefore, more pores are generated in the cryogels, and the pore size becomes smaller. Meanwhile, with smaller and denser pores, the stiffness of the cryogels is enhanced.(163)

A variety of polymer materials can be used to create cryogels. Natural polymers including alginate,(164) silk,(165) gelatin,(166) and cellulose,(167) and synthetic polymers including polyethylene glycol (PEG),(168) poly(l-lactic) (PLLA),(169) and polyvinyl alcohol (PVA)(170) are widely utilized for the preparation of cryogels. PEG is generally inert and safe in biological environments and has extensive applications in medicine. PEG-modified with acrylate groups can be used for radical polymerization, which makes it possible to undergo chemical crosslinking. Additionally, the properties of PEG can be enhanced by copolymerization with other compounds(171). For example, N,N-dimethyl acrylamide (DMAAm) is used to prepare cationic cryogels,(172) 2-acrylamido-2-methyl-1-propan sulfonic acid (AMPS) is used as a functional group for anionic cryogel.(173)

It is worth noting that the PEG-based cryogel used in this study is a non-biodegradable material, meaning that it remains permanently in the brain following implantation. While PEG-based cryogels are generally biocompatible, potential long-term side effects in clinical applications must be considered, where such outcomes are difficult to assess in preclinical animal studies. In a clinical trial involving encapsulated cell biodelivery implants delivering nerve growth factor for Alzheimer's disease, polyurethane, a non-degradable material, was used as the tethering component.(174) These implants were successfully retrieved after 12 months with no evidence of inflammation or displacement, suggesting that non-biodegradable implants can be well-tolerated in the human brain. Nevertheless, for safety reasons, non-degradable systems may potentially need removing after completing drug release, which introduces additional surgical risk, especially for vulnerable GBM patients.

To prepare cryogels with well-defined dimensions, a template or mould is typically used to contain the precursor solution during the freezing and crosslinking process.(175) However, producing tens of thousands of microscale cryogels of uniform size using this method is both difficult and time-consuming. In contrast, droplet-based microfluidics enables the generation of monodisperse

emulsions with precise control over droplet size, offering potential for scalable production.(176) Additionally, microscale cryogels are suitable to be administered as the injection, expanding their applicability to both resectable and non-resectable forms of GBM.

4. Droplet-based microfluidics

Microfluidics is a technology that manipulates very small quantities of controllable fluids (10^{-9} to 10^{-18} L) in a microscale channel.(177) When the fluid dimension decreases to the microscale, the characteristic of the fluid remarkably changes due to the increase in the specific surface area, including highly efficient mass and heat transfer, mass transport dominated by viscous dissipation rather than inertial effects, and significant surface effects.(178) Droplet-based microfluidics is a branch of microfluidics techniques, which generates droplets by multiple immiscible flows in microchannels.

The design of microfluidic devices is distinguished as co-flow, cross-flow, and flow-focusing.(179) In the cross-flow geometry (**Figure 1-8 (A)**), two fluid flows meet at the junction with an angle. Orthogonal channel design is most used in this geometry, also known as a T-junction. Two flow phases are introduced into coaxial channels in a co-flow configuration (**Figure 1-8 (B)**), where the continuous phase envelops the dispersed phase. Flow-focusing geometry can be regarded as a specific case of co-flow geometry (**Figure 1-8 (C)**), in which two fluids are focused to go through a contraction region. The dispersed phase is symmetrically shared by the continuous phase, meaning the droplet generation is more controllable and stable.(180) The factors that affect the size of the droplets include the size of microchannels, flow rates of continuous and dispersed phases, interfacial tension, and the viscosities of the two phases.(181) All these factors can be controlled accurately, and the size of the droplets can be adjusted by changing the size of the microchannels or the flow rate ratio, which means that the droplet size is predictable.(182) According to different flow rates of the dispersed phase and continuous phase, the droplet generation regimes can be classified as squeezing, dripping, and jetting.(183, 184)

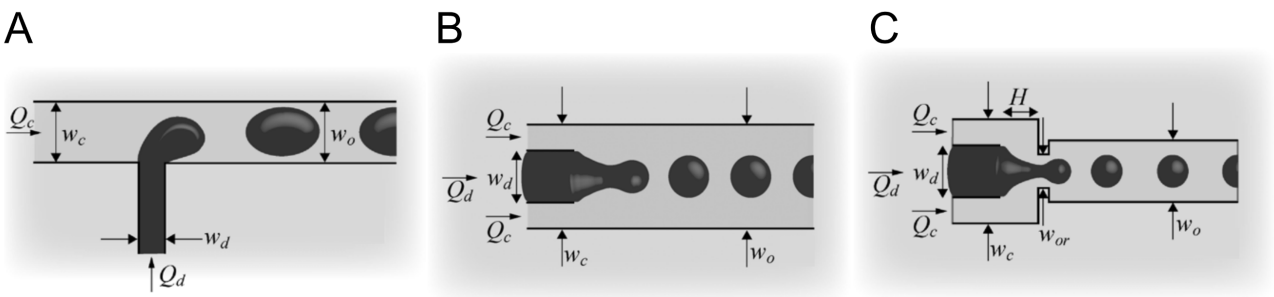

Figure 1-8 Illustration of the geometries of microfluidic devices.

(A): cross-flow geometry, **(B)**: co-flow geometry, **(C)**: flow-focusing geometry. This figure is adapted from (179).

Droplets are generated in the squeezing regime when the flow rate ratio of the dispersed phase to the continuous is high (**Figure 1-9 (A)**). The dispersed phase can fill the outlet channel and separate the continuous phase resulting in very large droplets. In contrast, the jetting regime occurs at a low flow rate ratio of dispersed phase to continuous phase (**Figure 1-9 (B)**). The dispersed phase is pulled away from the orifice, and droplets are generated downstream of the channel. The dripping regime requires a suitable flow rate ratio of two phases to keep the droplet generated at the orifice (**Figure 1-9 (C)**). When the shear force from the continuous phase is greater than the interfacial tension of the dispersed phase, the dispersed phase is broken up and droplets are generated one by one. Generally, droplets generated by the dripping regime have a uniform size than the jetting regime.(185) No droplets are generated in the threading regime when the flow rate of the dispersed phase is much higher than the flow rate of the continuous phase (**Figure 1-9 (D)**). In addition, the viscosity ratio of the two phases can affect the droplet generation regimes. The high viscosity of the dispersed phase reduces the options of flow rates to generate droplets in the dripping regime.(184)

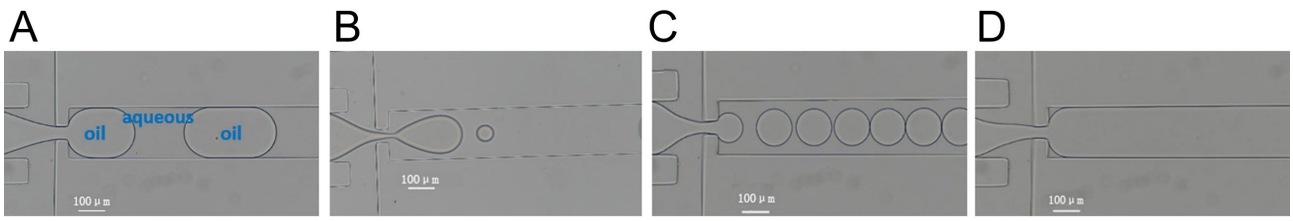

Figure 1-9 Illustration of droplet generation regimes.

(A): squeezing regime, **(B)**: jetting regime, **(C)**: dripping regime, **(D)**: threading regime. This figure is adapted from (184).

Many materials can be used to fabricate microfluidic chips, such as silicon,(186) poly(dimethylsiloxane) (PDMS),(187) glass,(188) poly(methyl methacrylate) (PMMA),(189) and cyclic olefin copolymer (COC).(190) Well-established soft lithography is usually used to fabricate versatile PDMS microfluidic chips.(191) PDMS materials have good light transmission and biocompatibility and allow gases such as oxygen and carbon dioxide to penetrate, which is suitable for cell culture.(192) However, limitations of PDMS such as swelling by organic solvents and the high elasticity which could change the geometry of microchannels indicate it is not always the ideal

material to generate monodisperse droplets.(193) Glass capillary microfluidic devices are widely used in laboratory research because they are easily assembled, low-cost, and have good chemical resistance.(194) This device is commonly used for poly lactic-co-glycolic acid (PLGA) microsphere preparation because the composition of the conventional oil in water emulsion (dichloromethane in water) can be directly adapted for glass devices.(195-197) However, manually fabricated glass capillary devices are not suitable for scale-up production. Meanwhile, manufacturing glass microfluidics chips is high-cost, time-consuming, and requires clean-room equipment.(198)

The flow rate of the dispersed phase is usually limited to a few millilitres per hour, so scale-up production by microfluidics could be an issue. Using multiple devices or microchannel array devices is a simple method to generate droplets simultaneously in hundreds or thousands of parallel microchannels or devices.(199, 200) However, it is worth noting that the variance of microchannels among microfluidics devices could affect the quality of the production. Polymer materials make it easy to fabricate microfluidics chips by moulding replication with lower costs becoming popular in microfluidics chip production.(201)

Droplet-based microfluidics has wide application in drug delivery because of the advantages of reproducibility, controlled size, narrow size distribution, and simple operation. Chen *et al*. used a glass capillary device to prepare 2-[[(4-phenoxyphenyl)sulfonyl]methyl]-thiirane-loaded PLGA microcapsules.(195) PLGA microcapsules had a narrow size distribution within a range of 56.03-64.48 μm with a golf ball-featured surface. Yang *et al*. tested the chemical resistance of four polymer materials to chloroform and chose phenol formaldehyde resin as the material of microfluidics chips to prepare PLGA microspheres.(202) PLGA microspheres with narrow size distribution (49.4 ± 3.3 μm) were prepared when the flow rates of the two phases were the same (0.2 mL/min). Oe *et al*. compared the testosterone-loaded PLGA microspheres prepared by microfluidics with conventional paddle mixers.(203) The results showed that microspheres prepared by microfluidics *in vivo* released drugs faster than microspheres prepared by a mixer, although *in vitro* drug release profiles were similar, which suggested that the removal rate of the organic solvent might affect the drug distribution inside microspheres. Wu *et al*. prepared PLGA-alginate core-shell microspheres through an O/W/O double emulsion template using a glass capillary device.(204) This research found that increasing the size of PLGA microspheres could postpone the peak of drug release and the alginate shell could regulate the release pattern to a near zero-order release.

Aim of the project:

Currently, the standard treatment of GBM has not changed since the Stupp protocol was established in 2005, and the prognosis of newly diagnosed GBM is still poor. It is urgent to develop new treatment strategies against GBM.

This project aimed to create soft biomaterials as an implantable or injectable platform for delivering chemotherapeutic agents or repurposed drugs and develop a local drug delivery system to achieve long-term sustained drug release.

The hypothesis:

1. Cryogel delivery systems can be created with mechanical properties similar to that of brain tissue, whilst remaining robust enough to handle/load with drugs/analyse *in vitro* and *in vivo*.

2. Negatively charged cryogels should load with positively charged drugs by the unspecific electrostatic interactions, which would mean they can be used as a universal platform to deliver cationic drug molecules.

3. Leveraging the advantage of microfluidics to generate monodispersed emulsion, microscale cryogel, cryogel microcarriers (MCs), and PLGA microspheres can be created with narrow size distribution and high reproducibility.

Objective 1 (Chapter 2): To create a cylindrical cryogel that fits the biopsy resection cavity in the tumour-bearing mouse model of GBM and evaluates the anti-GBM efficacy of clemastine-loaded cryogels and the biocompatibility of the implantation. The 3D printed template that was used to create cryogels should tightly control the size. The swelling of the cryogel and the brain tissue after the resection surgery was considered for the design of the template. The mechanical properties of the cryogel were investigated. The *in vivo* anti-GBM efficacy was evaluated in an orthotopic GBM tumour resection mouse model. Immunohistochemistry was performed to analyse the tumour cell invasion and the biocompatibility of cryogel implantation.

Objective 2 (Chapter 3): To create negatively charged MCs by microfluidics and evaluate the drug loading efficiency and drug release profiles. MCs were microscale cryogels, which was suitable for direct injection into the tumour site or implantation into small or irregular shape GBM resection cavities. One chemotherapeutic agent (doxorubicin, DOX), one targeted cancer drug (venetoclax) and two repurposed drugs (brexpiprazole and vortioxetine) should theoretically be loaded into the MCs as they were all positively charged drugs. The cytocompatibility of MCs was evaluated using

primary human astrocytes, and the *in vitro* anti-GBM efficacy of brexpiprazole MCs was investigated using human GBM cell lines.

Objective 3 (Chapter 4): To establish a novel method for the preparation of monodisperse PLGA microspheres and achieve sustained drug release for vortioxetine microspheres. The traditional emulsion solvent evaporation method for PLGA microsphere preparation could not precisely control the size distribution. In this chapter, a novel method was developed to create monodisperse PLGA microspheres by droplet-based microfluidics. Because vortioxetine MCs released drugs too fast via electrostatic interactions, the drug release profiles should be improved by encapsulating vortioxetine into PLGA microspheres. Primary human astrocytes were used for the evaluation of the cytocompatibility of PLGA microspheres. *In vitro,* the anti-GBM efficacy of vortioxetine microspheres was investigated on a 2D cell culture model and a 3D cell culture model.

Chapter 2: Soft sponge-like cryogel as an implant to deliver therapeutics to glioblastoma

Part of the work in this chapter was carried out via project collaborators. *In vivo* animal study and immunohistochemistry were carried out by Dr. Vadim Le Joncour at the University of Helsinki.

1. Introduction

Glioblastoma (GBM) is a primary malignant brain tumour of the central nervous system, characterized by poor clinical outcomes and high mortality.(1) Surgical intervention remains the cornerstone of GBM treatment, as it reduces tumour volume, alleviates symptoms, and provides tissue samples for diagnosis. Additionally, achieving maximum safe resection has a significant therapeutic impact, contributing to improving overall survival time.(205) However, due to the invasive nature of GBM cells infiltrating surrounding tissues, tumour debulking alone is insufficient to prevent recurrence.(13) Notably, most GBM recurrences occur within two centimetres of the resection cavity.(48) GBM is therefore an unmet medical need, and finding effective, safe, and long-lasting therapeutic approaches is urgently required.

Local drug delivery directly to the tumour tissue or the surgical resection cavity has been proposed to bypass the blood-brain barrier (BBB). This strategy potentially facilitates higher drug concentrations at the tumour site and reduces systemic side effects that often limit systemic chemotherapy. One means of achieving local drug delivery is to implant a solid therapeutic into the surgical resection cavity. Up to now, only Gliadel® has been approved by the Food and Drug Administration for the local treatment of GBM. However, its rigid structure can lead to a mechanical mismatch between the stiff wafer and the soft brain tissue causing side effects, which limit its use in the clinic.(53, 206) Therefore, there is an urgent need to develop soft biomaterials for local drug delivery to the brain. Cryogels, with their soft and porous structure, potentially offer an alternative means of safe delivery of therapeutics to the resection cavity.

Cryogels are a type of 3D hydrophilic network with interconnected macropores. Their production typically involves water as the solvent, making the process economical and eco-friendly. The cryogelation occurs below the freezing point of the solvent, and an interconnected macropore structure is formed after a freeze-thawing cycle.(207) The spongy structure of cryogels contributes to a highly elastic and robust property. The stiffness of a cryogel has been shown to be approximately only one-third that of a hydrogel with the same chemical composition, yet was still robust enough to be handled with forceps.(208) The pore size and the thickness/density of the pore walls are critical for the property of cryogels, which can be controlled by adjusting the content of monomers, the types of crosslinkers, the cooling rate, or the polymerization temperature.(209, 210) Additionally, the use of different monomers enables the synthesis of cationic(211) and anionic(212) cryogels.

Polyethylene glycol (PEG) is generally inert and safe in biological environments and has extensive medical applications. Its properties can be enhanced through copolymerization with other compounds.(171) Poly(ethylene glycol) diacrylate 700 (PEGDA700) is a PEG variant modified with acrylate groups, suitable for radical polymerization. 3-sulfopropyl acrylate potassium salt (SPA) has an acrylate group and a sulfonic acid group which is negatively charged at neutral pH. The electron-withdrawing carbonyl group connecting to the vinyl group on both above-mentioned monomers is essential for radical polymerization. The PEGDA-co-SPA polymer material is ideal for loading positively charged drugs by electrostatic interaction, such as Doxorubicin (DOX, a chemotherapeutic agent) and clemastine (a neuroactive repurposed drug).

Doxorubicin (DOX) has the function of inhibiting topoisomerase II, a critical enzyme involved in DNA strand relaxation during replication.(213) DOX intercalates into the DNA strand and inhibits the topoisomerase II to re-ligate the broken DNA, which ultimately causes DNA damage.(214) It is approved to treat various types of cancers in the clinic, such as metastatic breast cancer and small-cell lung cancer.(215) However, DOX causes severe side effects especially cardiomyopathy limiting its use in clinical practice.(216) Although the mechanism of DOX-induced cardiomyopathy remains unclear, DOX disrupts the normal mitochondrial function which might be the key factor causing cardiomyopathy.(217-219)

Doxil®, a liposomal formulation of DOX, targets tumours passively through enhanced retention and permeation, reducing off-target toxicity and cardiotoxicity compared to free DOX.(220) However, because only selected small hydrophobic molecules can pass the BBB, systemic administration neither free DOX nor Doxil® can reach the brain. Local administration of DOX offers a promising strategy to bypass the BBB and avoid the chemoresistance of GBM.

Clemastine, an H1 histamine antagonist, has been used in clinics for allergy relief for around 60 years. In recent years, a novel strategy to treat GBM has been proposed in which cationic amphiphilic antihistamines induced GBM cell death while sparing healthy cells.(221) However, the mechanism of action of clemastine to kill GBM cells is still unclear. Cationic amphiphilic antihistamines have a proven ability to provoke lysosomal membrane permeabilization.(222) Losing lysosomal membrane integrity leads to the release of lysosomal hydrolases into the cytosol, resulting in cell apoptosis.(223) A preclinical study has shown that clemastine not only induces GBM cell death *in vitro* but also extends survival in an orthotopic GBM mouse model.(125) Furthermore, clemastine suppressed tumour growth and promoted the differentiation of brain tumour-initiating cells (BTICs), which might be another mechanism used to treat GBM.(224) BTICs,

a type of cell capable of self-renewal and tumour initiation, are highly resistant to chemotherapy and radiotherapy and contribute to intratumoral heterogeneity and GBM recurrence.(225, 226) Local drug delivery holds the advantage of starting the treatment immediately after the surgery, bridging the gap for waiting the recovery from the surgery. However, up to now, there is no local implant to deliver clemastine into the brain.

Aims

The work in this chapter aims to create a cryogel delivery system which is soft, non-toxic and capable of delivering both doxorubicin and clemastine. This chapter focuses on designing 3D printed templates for cryogel preparation tailored to fit the biopsy resection cavity in orthotopic GBM tumour resection mouse models. The objectives include creating soft cylindrical cryogels that could match the stiffness of the brain tissue, assessing the drug loading capacity of two model drugs (DOX and clemastine), analysing drug release profiles, investigating *in vitro* cell toxicity of clemastine loaded cryogels, evaluating the *in vivo* antitumor efficacy of clemastine loaded cryogel as a local drug delivery device in an orthotopic GBM tumour resection mice model. We hypothesize that the interconnected macropore structure in the cryogel could provide very soft but robust properties, the PEG-based polymeric network would exhibit biocompatibility and non-toxicity, and SPA branches could theoretically bind with drug molecules to reach a 1:1 molar ratio and allow controlled drug release.

2. Materials and methods

2.1 Chemicals and Materials

The chemicals and materials used in this chapter are shown in **Table 2-1**. Chemicals were used without any further purification. **Table 2-2** shows the equipment used in this chapter.

Table 2-1 List of chemicals and materials

Chemicals and Materials	Company	Catalog number
Poly(ethylene glycol) diacrylate 700 (PEGDA700)	Sigma	455008
3-sulfopropyl acrylate potassium salt (SPA)	Sigma	251631
2-hydroxy-2-methylpropiophenone (HMPP)	Sigma	405655
Phosphate-buffered saline (PBS)	Gibco	2339177
Dimethyl sulfoxide (DMSO)	Sigma	D2650
Absolute ethanol (EtOH)	Fisher Chemical	E/0600DF/15
Isopropanol	Sigma	24137-M
iFluor® 647	AAT Bioquest	1065
Doxorubicin (DOX)	LC-Laboratories	D-4000
Clemastine fumarate salt	Sigma	SML0445

Eosin Y	Sigma	E6003
Sodium acetate trihydrate	Sigma	32318
Acetic acid	Sigma	27225
Bovine serum albumin (BSA)	Sigma	SLCD6757
Primary human astrocytes	ScienCell	1800
DMEM/F12, Glutamax	Gibco	10565-042
DMEM/F12 (1:1)	Gibco	21331-046
Astrocyte medium	ScienCell	1801
Fetal Bovine Serum (FBS)	Sigma	F7524
Penicillin-Streptomycin	Sigma	P4333
0.25% Trypsin-ethylenediaminetetraacetic acid (EDTA) solution	Sigma	T4049
Poly-L-lysine	Sigma	P6282
MycoZap Plus-CL	Lonza	VZA-2011
Transferrin	Sigma	T8158
Putrescine	Sigma	P5780
Sodium selenite	Sigma	S5261
Progesteron	Sigma	P8783
Insulin	Sigma	I5500
Hydrochloric acid solution	Sigma	H9892
Heparin	Sigma	H4784
Recombinant human fibroblast growth factor 2-G3 (FGF2-G3)	Qkine	Qk053
Accutase	Thermo Fisher	00-4555-56
Geltrex basement membrane matrix	Thermo Fisher	A1413202
Absolute ethanol (EtOH)	Fisher Chemical	E/0600DF/15
PrestoBlue	Invitrogen	A13261
Recombinant human epidermal growth factor (rhEGF)	Peprotech	AF-100-15
Monoclonal anti-vimentin−Cy3 antibody	Sigma	C9080
Rat monoclonal antibody against podocalyxin	R&D Systems	MAB1556
Goat monoclonal antibody against GFAP	Abcam	ab302644
Goat monoclonal antibody against IBA1	Abcam	ab289874
Donkey anti-goat IgG (Alexa Fluor® 647)	Abcam	ab150135
Donkey anti-rat IgG (Alexa Fluor® 488)	Abcam	ab150153
Donkey anti-goat IgG (Alexa Fluor® 488)	Abcam	ab150129
Paraformaldehyde	Sigma	158127
Triton X-100	Thermo Fisher	HFH10
DAPI	Thermo Fisher	D1306
Mowiol	Sigma	81381
PlasWhite V2 resin	Asiga	PN/00931

Table 2-2 List of equipment

Equipment	Company	Catalog number
Freezer	Fryka	B30-20
Plasma cleaner	Harrick plasma	PDC-002-CE
UV hand lamp	Koehler	UV-30L
InfiniteRX plate reader	Tecan	
EVOS imaging system	Thermo Fisher	M7000
Orbital Shanker-incubator	Grant-bio	ES-20
MAX X27 3D printer	Asiga	
Ultraviolet radiation lamp	Asiga	DR-301C

Zeiss Sigam HD Field Emission Gun Scanning Electron Microscope	Zeiss	
BIO-RAD SC500 sputter coater	Quorum Technologies	
IRSpirit FTIR Spectrometer	Shimadzu	
Confocal microscope	Leica	TCS SP5
Material testing machine	Zwick	0.5TS
Cryostat	Leica	CM3050

2.2 Preparation of cylindrical cryogels

The precursor solution of PEGDA700 and SPA (molar ratio: 5:95), with 10% (molar proportion) HMPP as photoinitiator (PI) was prepared at an 8% (wt/v) solid content concentration. Briefly, the precursor solution was prepared by dissolving 54.8 mg PEGDA700, 345.2 mg SPA, and 23.9 µL HMPP in 5 mL deionized water. The solution was stored at 4°C in the absence of light.

3D printed template for pilot studies was designed by Dr. Ben Newland and fabricated at the Leibniz-Institut für Polymerforschung, Dresden using an Asiga Pro 4K 3D printer (Alexandria, Australia). The size of this template was 1.6 mm in diameter and 2.5 mm in height. Dr. Chiara Bastiancich kindly provided the predicted dimensions of biopsy resection cavities in rat and mouse models based on this research.(227) 3D printed templates for animal studies therefore were modified from the template for pilot studies with Autodesk Inventor Professional (2022) and printed in our lab using an Asiga MAX X27 3D printer (Alexandria, Australia) with Asiga PlasWhite V2 resin. 3D printed templates with sizes of 1.31 mm in diameter and 1.75 mm in height; 0.94 mm in diameter and 1.56 mm in height were used to create cryogels for rat or mouse models, respectively. After the printing, templates were washed with isopropanol to remove the unpolymerized and excess resin and post-cured with UV light (DR-301C, Asiga) for 30 minutes.

To produce cylindrical cryogels, one side of each template hole was sealed with tape. The templates were treated with a plasma cleaner (Harrick Plasma, USA) for five minutes to enhance surface hydrophilicity. Then, the precursor solution was added into the holes and frozen for one hour at -20°C. A UV hand lamp at 365 nm (2*15W, Koehler, Germany) was used to crosslink the monomers for 2 minutes on each side of the template. After the ice crystals were thawed, the cryogels were removed from the template and washed with ethanol three times. The cryogels were stored in their dry state long-term at room temperature.

2.3 Morphological characterization of the cryogels

2.3.1 Bright field microscopy images

The EVOS imaging system was used to observe the morphology and measure the size of the cryogels. Dehydrated cryogels were put into 96-well plates and bright field images were taken. 50 µL PBS was added to rehydrate cryogels and their images were taken. ImageJ software was used to measure the size of dehydrated and rehydrated cryogels, and the size expansion ratio of rehydrated cryogels to the hole in the template was calculated.

2.3.2 Scanning electron microscope (SEM)

The macroporous structure of the cryogels was visualized via a Zeiss Sigam HD Field Emission Gun Scanning Electron Microscope (Zeiss, Germany). Due to the non-conducting property of cryogels, dehydrated cryogels were coated by AuPd using a BIO-RAD SC500 sputter coater (Quorum Technologies, UK), which was uniformly covered with a thick layer of AuPd around 10-20 nm. A beam energy of 5 kV with a 30 µm diameter final aperture was used for imaging cryogels by an Everhart-Thornley detector.

2.3.3 Confocal microscopy

To prepare fluorescently labelled cryogels, 5 µg/mL iFluor® 647 was added to the precursor solution. Samples were imaged with a Leica TCS SP5 confocal microscope using a 633 nm laser, and a 3D series ("z stack") with 1 µm section thickness was captured to visualize the inner structure of cryogels. The entire 3D series was compressed into one 2D representative image by average projection. ImageJ was used to measure the length and width of pores.

2.4 Fourier transform infrared spectroscopy (FTIR)

Infrared spectra of monomers and cryogels were scanned using an IRAffinity-1S FTIR Spectrometer (Shimadzu, Japan). The background signal was scanned before running each sample to subtract any residual peaks from the instrument and the environment. FTIR spectra were scanned by transmittance mode from 500 cm^{-1} to 2500 cm^{-1} with a resolution of 0.9. Cryogels were dried completely to avoid any interference.

2.5 Characterization of the cryogel stiffness

Disc-shape cryogels with 16 mm diameter and 3 mm height were prepared to test the mechanical properties. The cryogels were placed between two parallel steel plates of the tensile test machine (Zwick, Germany) and compressed at 1 mm/min. The Young's modulus of cryogels was calculated

from the initial compression stage when the macroporous structure of cryogels was compressed (the first part of the stress-strain curve before the inflection point) by equation 2-1.

$$E = \frac{\sigma}{\varepsilon}$$

Equation 2-1. Where *E* is Young's modulus (kPa), σ is stress (kPa), and ε is strain.

2.6 Detection and quantification of the concentration of the drugs

2.6.1 DOX

The calibration curve method was used to calculate the drug concentrations. DOX was detected by the absorbance at 506 nm or by the fluorescence at 488 nm for excitation and 550 nm for emission using an InfiniteRX plate reader (Tecan, Switzerland). The calibration curve was built by serial dilution from the starting concentration of 200 to 0.1953 μg/mL. The absorbance method was used for concentrations from 200 to 6.25 μg/mL, and the fluorescence method was used for concentrations from 6.25 to 0.1953 μg/mL.

2.6.2 Clemastine

A fluorescence quenching method was used to determine the clemastine concentration because the absorbance peak of clemastine was below the UV cut-off wavelength of the polyethylene material of 96-well plates.(228) The tertiary amine group of clemastine can be protonated under acidic conditions, which non-specifically binds with eosin Y. The fluorescence of eosin Y was measured at the excitation wavelength of 306 nm and the emission wavelength of 539 nm. The clemastine-eosin Y complex formation resulted in the quenching of eosin Y's fluorescence, allowing the determination of clemastine concentration by monitoring changes in fluorescence intensity. The 5 mg/mL clemastine stock solution in DMSO was diluted with deionized water at 0, 1.5, 3, 6, 12, 18, 24, 30, 37.5, and 45 mg/mL to build the calibration curve. 0.3 mL clemastine sample, 0.3 mL eosin solution (0.15 mg/mL), and 0.3 mL acetate buffer (0.2 M, pH 3.7) were added into a 2 mL centrifuge tube. A vortex mixer was used to mix this solution, and the fluorescence intensity was read immediately.

2.7 Measuring drug loading to the cryogels

2.7.1 Loading large amounts of drugs

DOX stock solution (200 mg/mL in pure DMSO) was diluted using deionized water or PBS and clemastine stock solution (5 mg/mL in pure DMSO) was diluted using deionized water to prepare the loading solutions. Dehydrated cryogels were put into 500 μL drug solutions in a 2 mL centrifuge

tube. Cryogels were incubated at room temperature for three days (in the absence of light for DOX studies). After the incubation, the drug concentration in the supernatant was determined, and the drug loading efficiency was calculated by Equation 2-2.

$$\%\ of\ loaded\ drug = \frac{c_1 - c_2}{c_1} * 100\%$$

Equation 2-2. where c_1 is the drug concentration before incubation, c_2 is the drug concentration in the supernatant.

2.7.2 Loading small amounts of drugs

To load a small amount of DOX, 5 µL DOX solution at 1 mg/mL was directly injected into dehydrated cryogels. After 10 minutes, cryogels were washed with PBS three times to remove the unloaded drugs. The DOX concentration in supernatant from the first-time wash was determined to calculate drug loading efficiency.

2.8 Evaluation of *in vitro* drug release profiles

The drug release profiles of DOX and clemastine cryogels were investigated. PBS containing 0.3 mg/mL BSA was used as the release medium for DOX cryogels release studies, which was intended to mimic the protein concentration in the cerebrospinal fluid.(229) Pure PBS was used as the release medium for clemastine cryogels release studies, as BSA had positive charges below pH 4.5, which caused interference in the determination.(230) Cryogels were incubated in 1 mL release medium at 37°C with an 80 rpm gentle shake (in the absence of light for DOX). At each time point, 900 µL supernatant was removed and replaced by fresh release medium. Samples were stored at -20°C for further investigation. At the end of the experiment, the drug concentration in all samples was detected. The cumulative amount of drug released was calculated by the following equation 2-3.

$$m_n = \begin{cases} c_n * V_{Total} & (n = 1) \\ c_n * V_{Total} + V_{Replaced} * \sum_{i=1}^{n-1} c_i & (n > 1) \end{cases}$$

Equation 2-3. where m_n is the cumulative release amount of the nth time point (µg). c_n is the drug concentration of the nth time point (µg/mL). V_{Total} is the total volume of the release medium. $V_{Replaced}$ is the volume of the removed and replaced medium at each time point.

2.9 Cell culture

2.9.1 Preparation of cell culture medium for patient-derived GBM stem cells

N2 medium was prepared by adding 1 mL of MycoZap Plus-CL and 500 µL each of transferrin-putrescine-sodium selenite (TPN), insulin, and progesterone to 497.5 mL DMEM/F12 (Glutamax). TPN was prepared by dissolving 500 mg of transferrin and 81 mg of putrescine in deionized water and adding 25 µL of sodium selenite stock solution (10.5 mg sodium selenite was dissolved in 10 mL deionized water) to a final volume of 5 mL. Insulin solution was prepared by dissolving 25 mg insulin in 5 mL 0.1 M HCl. 6.3 mg progesterone was dissolved in 10 mL absolute ethanol to prepare the stock solution, and 50 µL stock solution was diluted to a 5 mL solution with deionized water to get the final progesterone solution. TPN, insulin, and progesterone solutions were filter-sterilized and stored at -20°C. The feeding solution to support the growth of cells contained 400 ng/mL rhEGF, 60 ng/mL thermostable FGF2 G3, and 40 µg/mL heparin. When culturing hGBM cells, 50 µL feeding solutions were added in N2 medium to get 1 mL complete medium.

2.9.2 Patient-derived GBM stem cells

Patients-derived GBM stem cell lines (hGBM L0, L1, and L2) were cultured as previously reported.(231, 232) Briefly, hGBM L0, L1, and L2 were grown as suspension cells in N2 medium with 20 ng/mL rhEGF and 3 ng/mL thermostable rhFGF2 G3 in a 37^{o}C, 5% CO_2 incubator. Typically, cells were subcultured every week based on their growth situation. Cells were transferred from the cell culture flask to a 15 mL centrifuge tube and spun down for 5 minutes at 300 g. The supernatant medium was removed, and the cell pellets were resuspended in 100 µL accutase. A 200 µL pipette was used to break the cell pellets by gently going up and down. Then, cells were incubated for 3 minutes at 37°C and a 200 µL pipette was used to completely break the cell pellets. 10 mL PBS was added into the centrifuge tube, and cells were spun down for 5 minutes at 300 g. The supernatant PBS was removed, and cell pellets were resuspended in 200 µL N2 medium. After the cell pellets were separated into single cells, 800 µL N2 medium was added, and the number of cells was counted using a Beckman Coulter Z2 (Beckman Coulter Inc., USA). The cells were plated at a density of 50,000 cells/mL.

2.9.3 Primary human astrocytes

Primary human astrocytes, isolated from the cerebral cortex, were purchased from ScienCell Ltd (USA). Cells were cultured as instructed by the manufacturer but with a slight modification, in which 10% FBS in DMEM/F12 was used instead of the trypsin/EDTA neutralization solution available from the manufacturer. Briefly, primary human astrocytes were cultured in the astrocyte

medium (1801, ScienCell Ltd., USA) in a 37°C, 5% CO_2 incubator. Cell culture flasks were coated with 2 µg/cm^2 poly-L-lysine. The cell culture medium was changed every 2 or 3 days until the confluency reached 90-95%. Cells were dissociated using 0.025% trypsin-EDTA solution at room temperature. Cells were transferred into a 50 mL centrifuge tube containing 5 mL FBS after all cells round up. The empty flasks were placed in the incubator for another minute, and the remaining cells were transferred into the centrifuge tube using DMEM/F12 containing 10% FBS. Cells were plated at a density of 5,000 cells/cm^2.

2.9.4 Cell freezing and thawing

To freeze the hGBM cells, after removing the supernatant PBS in the subculturing process, the cells were resuspended in the N2 medium containing 10% DMSO at a concentration of around 1 million cells/mL. The cell suspension was transferred into cryovials. The cells were frozen in a freezing container overnight in a -80°C freezer at a cooling rate of -1°C/minute and were transferred to liquid nitrogen for long-term storage. To thaw the frozen hGBM cells, the cryovials were immediately put into a 37°C water bath after taking it out from the liquid nitrogen. The cells were transferred into 10 mL of prewarmed N2 medium when there was only a small piece of ice in the cryovial. The cells were spun down for 5 minutes at 300 g, and the supernatant was removed. Then, cells were resuspended in the fresh N2 medium, plated in the cell culture flask, and grew in the CO_2 incubator.

2.10 Analysing the cytocompatibility of the empty cryogel

The cytocompatibility of empty cryogel was evaluated using primary human astrocytes. Cells were seeded in poly-L-lysine coated 48-well plates (Costar, 3548) at a density of 4,800 cells/well. After one day of incubation, an empty cryogel was added to the primary human astrocytes in culture. Images of the cells were taken via a microscope camera (A35180U3, OMAX Microscope, South Korea) and the cell viability was tested using the PrestoBlue assay 1, 4, and 7 days after adding cryogels and normalizing to untreated control cells (background fluorescence was subtracted from experimental wells). Cells were incubated in PrestoBlue for 2 hours and the fluorescence intensity was read with an excitation wavelength of 560 nm and an emission wavelength of 590 nm by the bottom reading model.(233)

2.11 Cytotoxicity of free clemastine

To investigate the cytotoxicity of free clemastine, primary human astrocytes were plated in poly-L-lysine coated 96-well plates (Costar, 3595) at a density of 1,600 cells/well, and hGBM cells were

plated in Geltrex-coated 96-well plates at a density of 5,000 cells/well. After one day of incubation, clemastine solution was added, which was prepared by serial dilution from 5 mg/mL stock solution in pure DMSO using the complete culture medium. The cell viability was tested using the PrestoBlue assay 1, 4, and 7 days after adding the drug to the cells.

2.12 *In vitro* anti-GBM efficacy of clemastine cryogel

The hGBM L0, L1, and L2 cells were cultured in 48-well plates as suspension cells to investigate the *in vitro* anti-GBM efficacy. Cells at a density of 15,000 cells/well were cultured for two days, and then cryogels loaded with 3.125, 6.25, 12.5, 25, and 50 µg clemastine were added. The empty cryogel was used as a negative control and 5 µg/mL free clemastine was used as a positive control. 1, 4, or 7 days after adding the cryogels/drug, the cells were imaged, and the cell viability was analysed using the PrestoBlue assay.

2.13 *In vivo* antitumour efficacy study

Animal experiments were approved by the Committee for Animal Experiments of the District of Southern Finland (ESAVI/10262/2022). Six-week-old immunocompromised nude mice were housed in a 12 h light/12 h dark cycle and had free access to food and water. Patient-derived BT-12 GBM cells were cultured in DMEM/F12 medium supplemented with 2 mM L-glutamine, 2% B27-supplement, 0.01 µg/mL recombinant human fibroblast growth factor-basic, 0.02 µg/mL recombinant human epidermal growth factor, 15 mM HEPES-buffer, 100 U/mL penicillin and 100 µg/mL streptomycin. To implant GBM cells, mice were anaesthetized by isoflurane, and 100,000 BT-12 GBM cells were engrafted intracerebrally by the stereotaxic injector. 15 days after tumour implantation, mice were randomly allocated to four treatment groups (tumour resection only, n=5; tumour resection plus empty cryogel implantation, n=4; tumour resection, empty cryogel implantation plus intraperitoneal injection (IP) of clemastine, n=6; tumour resection plus clemastine cryogel implantation (10 µg/animal, n=9) and the tumour was resected by biopsy punch (2 mm). Cryogels were implanted into the surgical resection cavity and the skin was sutured. The intraperitoneal administration of clemastine started 4 days after the tumour resection (50 mg/kg per day for 10 days). The body weight and behaviour of mice were monitored regularly. After 14 days of the tumour resection, all animals were euthanized, and their brains were collected and stored at -80°C for further studies.

2.14 Fluorescent immunohistochemistry (IHC)

The mouse brains were cryosectioned to 9 µm coronal sections at an object temperature -24°C and cryostat temperature -22°C using Leica CM3050 Cryostat. The IHC slides were stored at -20°C before the staining.

The slides were fixed with 4% paraformaldehyde in PBS for 7 minutes and then washed with PBS 3 times for 5 minutes. 0.3% triton X-100 in PBS was used to permeabilize the cellular membrane for 7 minutes. After washing 3 times with PBS, the slides were incubated in the blocking solution (10% FBS, 0.03% triton X-100 in PBS) for 30 minutes. The slides were incubated with the primary antibody solution (1:800 dilution) overnight at 4°C. After the incubation, the slides were washed with PBS 4 times for 5 minutes. The slides were incubated in the secondary antibody solution (1:500 dilution) for 120 minutes at room temperature in the absence of light. Then, the slides were washed with PBS 4 times for 5 minutes and incubated with DAPI solution (1 µg/mL in water) for 7 minutes. After the incubation, the slides were rinsed with distilled water. Finally, the slides were mounted with Moviol and stored at 4°C.

2.15 Data analysis of fluorescence immunohistochemistry

2.15.1 Tumour cell analysis

Three brain sections were selected from each IHC slide for tumour cell analysis. The lateral ventricle was used to localize brain sections to ensure that selected medial sections were at a similar position. The distance between each two connecting brain sections was around 380 µm. The tumour cell analysis was performed manually in Sliderviewer (v2.6) software. First, the primary tumour was marked, and the size was measured. Brain sections without primary tumours were excluded from the tumour cell analysis. Single-cell invasion was defined as less than three tumour cells invading together. The total number of single invasive cells was counted, and the shortest distance between each single invasive cell and the primary tumour was measured. On the other hand, more than two tumour cells migrated together were regarded as a tumour cell cluster. Three parameters were analysed including the shortest distance between each tumour cell cluster and the primary tumour, the total number of tumour cells, and the area of the tumour cell clusters.

2.15.2 Glial fibrillary acidic protein (GFAP) and ionized calcium-binding adapter molecule 1 (IBA1) expression analysis

A semi-quantitative method was used to investigate the host response to the tumour and cryogel in terms of GFAP and IBA1 protein expressions. Four brain sections were selected from each IHC

slide to analyse GFAP and IBA1 expressions (two anterior sections and two sections within the surgical resection cavity). A blinded experiment was performed to analyse GFAP expression. Snapshots with the whole coronal brain section were taken in Sliderviewer. Fiji ImageJ was used to analyse the fluorescence intensity. The medial longitudinal fissure was used as a mark to separate the mouse brain into two regions of interest. The ipsilateral side was the hemisphere with the resection cavity, and the other hemisphere was the contralateral side. The edge of the brain sections that showed autofluorescence was excluded from the analysis. Images were converted to black and white pixels (8-bit type). The threshold function (red background) was used to select the positive GFAP or IBA1 staining area. The minimum threshold value was manually adjusted to find a suitable value that avoided selecting the background noise signals. The area fraction (the percentage of the area where the grey value was above the minimum threshold value in the region of interest, which meant protein expressions) of these two regions of interest were measured and the positive staining area ratio was calculated.

2.16 Statistical analysis

The statistical analysis was conducted using GraphPad Prism (8.4.3). First, the assumption of normality was checked by the Shapiro-Wilk test. To compare two groups of data, if both two groups passed the normality test, Student's t-test was used for the data without significantly different variances, and Welch's t-test was used for the data with significantly different variances. The Mann-Whitney U test was used to analyse the data without a normal distribution. To compare three or more groups of data, if all groups passed the normality test, the one-way ANOVA test was used for the data with homogeneity of variances (checked by Brown-Forsythe test), and the Welch's ANOVA test was used for the data with unequal variances. The Kruskal-Wallis test was used if at least one data group did not have a normal distribution. *Post hoc* tests (Tukey's multiple comparisons test for ordinary one-way ANOVA test, Dunnett's T3 multiple comparisons test for Welch's ANOVA test, and Dunn's multiple comparisons test for Kruskal-Wallis test) were performed if the results of the overall ANOVA test had significant difference to determine which specific group was significantly different from the other group. The two-way ANOVA test was used to compare the mean differences if there were two independent variables and Tukey's multiple comparisons test was used for the *post hoc* tests. p-value ≤ 0.05 was defined as a significant difference (ns, $p>0.05$; *, $p\leq0.05$; **, $p\leq0.01$; ***, $p\leq0.001$; ****, $p\leq0.0001$).

3. Results and discussion

3.1 Preparation of cylindrical cryogels

In this chapter, cylindrical-shaped bulk cryogels were created as soft biomaterials for local therapy of GBM. A template synthesis strategy was used to create cylindrical cryogels. The 3D printed template with certain size holes can tightly control the size and the shape of cryogels. A schematic representation of cryogel preparation and the polymerization reaction is shown in **Figure 2-1**.

In clinical settings, magnetic resonance imaging scans provide detailed information on GBM tumour size and volume, guiding surgical planning and enabling estimation of the resection volume. Based on these imaging results, a customised 3D printed template can be designed preoperatively to fabricate a bulk cryogel that matches the anticipated resection cavity. However, intraoperative challenges such as brain tissue swelling and anatomical variability may hinder the precise fitting of a single bulk cryogel. In contrast, the cylindrical cryogels developed in this study are significantly smaller than typical tumour resection cavities, allowing for the implantation of multiple units to fill the cavity effectively. This approach provides practical advantages, such as the preparation method being straightforward and scalable, and the amount of drug loading can easily be consistent across batches and each single cryogel. Moreover, drug dose can be flexibly adjusted by varying the number of drug-loaded cryogels and supplementing with unloaded cryogels as needed. Importantly, the cylindrical format serves as a practical starting point for preclinical studies, where consistent cavity volumes are created in animal models.

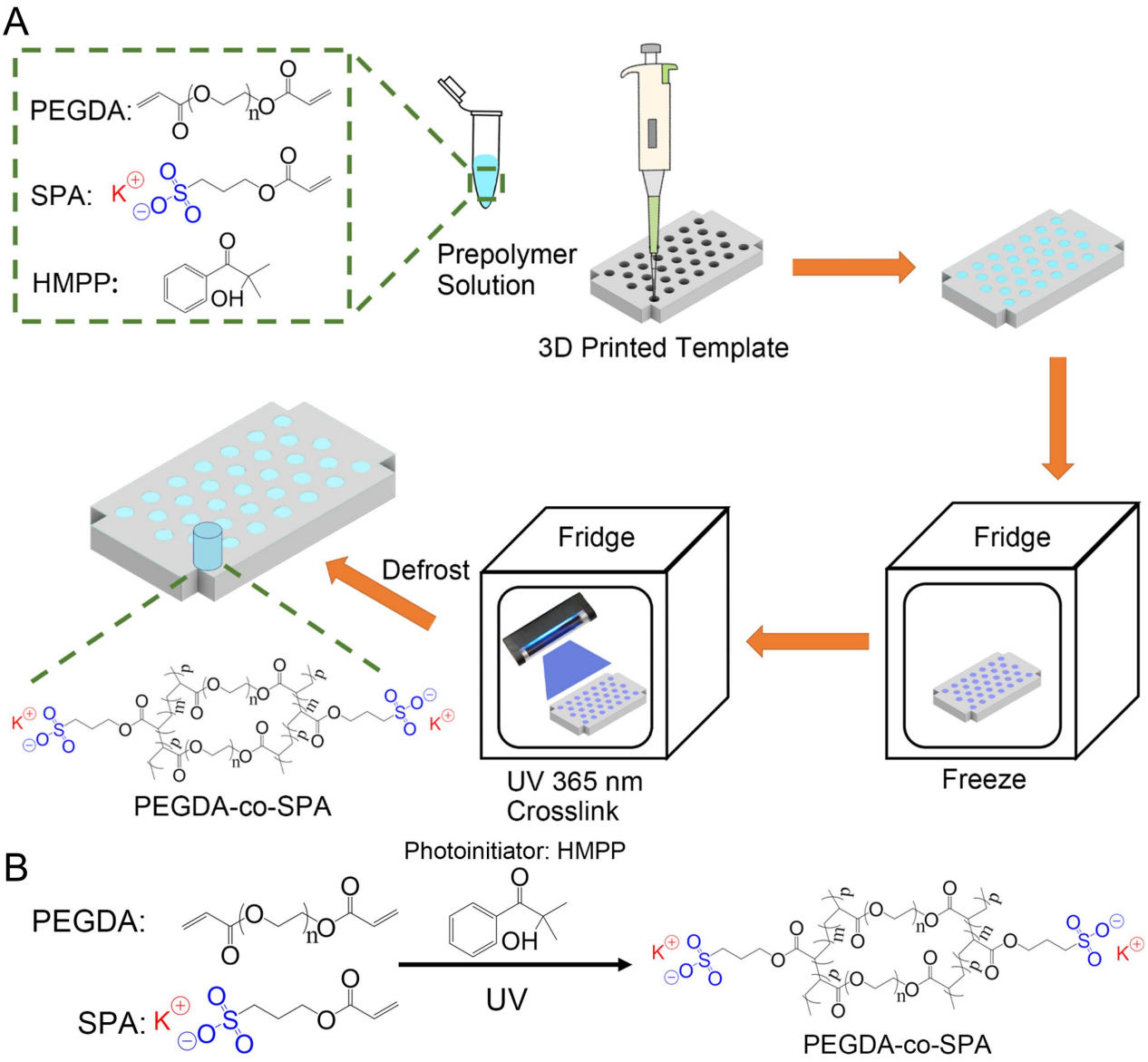

Figure 2-1 Schematic representation of cylindrical cryogel preparation.

(A) shows the workflow of the cryogel preparation. **(B)** shows the polymerization reaction. Abbreviation: PEGDA: Poly(ethylene glycol) diacrylate, Mn = 700; SPA: 3-sulfopropyl acrylate potassium salt; HMPP: 2-hydroxy-2-methylpropiophenone.

3.2 Morphological characterization of cryogels

After the cryogels were removed from the template, they would expand to a certain extent. To best match the size of the biopsy resection cavities, the size expansion ratio of cryogels needed to be considered. Therefore, the EVOS imaging system was used to take images for measuring the size of cryogels. Cylindrical cryogels with formulations of 8% (wt/v) solid content concentration and 10% to 95% SPA, or 95% SPA and 6-10% (wt/v) solid content concentration was prepared to investigate the size expansion ratio. **Figure 2-2 (A)** and **(B)** show the size of the cryogel with various

formulations made by the same template. As shown in **Figure 2-2 (C)**, the proportion of SPA and the size expansion ratio had a positive correlation. The size expansion ratio of cryogels with the same formulation was similar in height and diameter, which suggested that the expansion did not have a preferable orientation. 10SPA cryogel only expanded by 10%, whilst 95SPA cryogel expanded by 60% compared to the template size. Interestingly, the solid content concentration did not affect the size expansion ratio (**Figure 2-2 (D)**). The size expansion ratio might be controlled by the degree of crosslinking, as PEGDA consisted of the skeleton of the polymeric network and SPA only formed the branches. When increasing the proportion of PEGDA, more available monomers were crosslinked to form a network rather than a chain resulting in a higher-density polymeric network. Although cryogels can be compressed, we would not want to make placement into the resection cavity technically challenging. In the orthotopic GBM resection animal model, the brain parenchyma rapidly swells after tumour resection. Research showed that only 5 µL space could be used for the treatment when animals underwent surgical resection using a 2 mm diameter biopsy punch inserted 3 mm depth.(96) So, I redesigned the template to make the 95SPA cryogels best match the size of the resection cavity by taking into account the swelling of the brain parenchyma and the expansion ratio between the template sizes and the hydrated cryogel size. 3D printed templates with the size of 1.31 mm in diameter and 1.75 mm in height or 0.94 mm in diameter and 1.56 mm in height were made for the use of rat or mouse models, respectively.

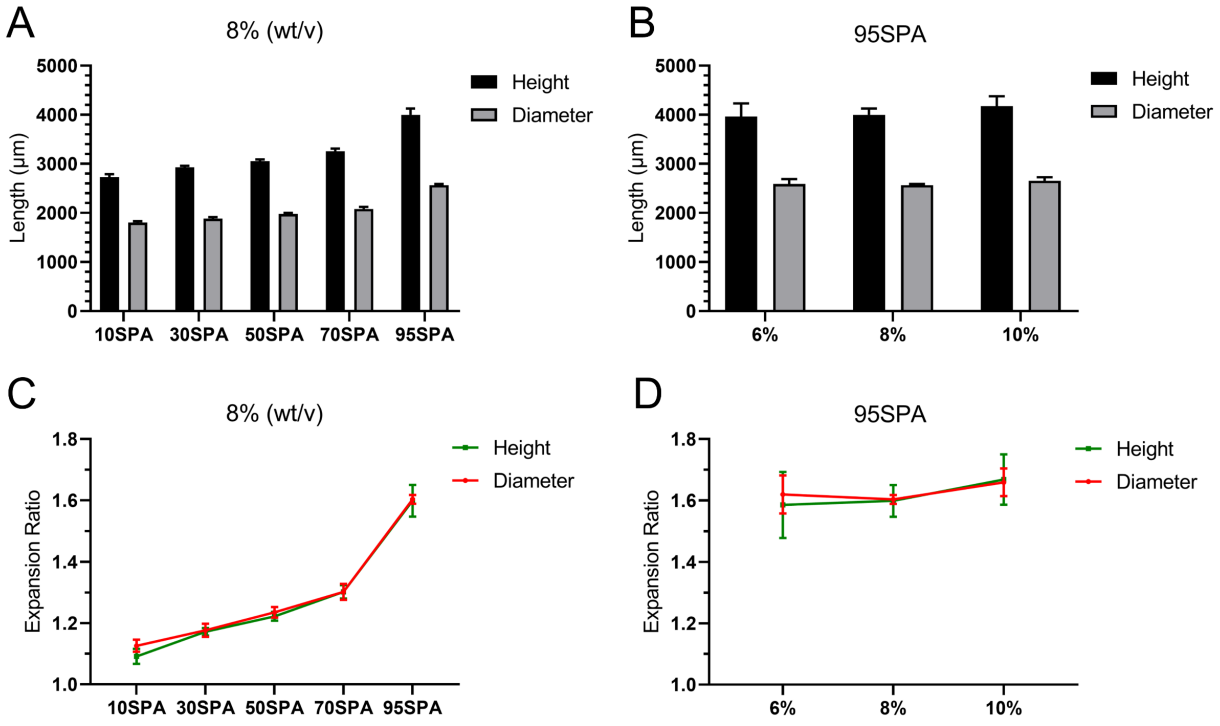

Figure 2-2 Cryogels swell larger than their template size.

(A) and **(B)** show the height and the diameter of the cryogels (10% to 95% of SPA monomer ratio and 8% (wt/v) to 10% (wt/v) of the solid content in precursors solution) rehydrated in PBS. **(C)** and **(D)** show the size expansion ratio of the rehydrated cryogel compared with the size of the template. **(A)** – **(D)**: n=10, error bars represent the mean ± SD; template size: height: 2.5 mm, diameter: 1.6 mm.

Figure 2-3 (A) and **(B)** show the representative EVOS photos of a dehydrated cryogel for a mouse model and the same cryogel rehydrated by PBS, respectively. The shape of the dehydrated cryogels was irregular but was completely restored after rehydration, which indicated that the cryogels maintained mechanical integrity after losing water. The average size of the cylindrical cryogels for the mouse model was 2516 µm in height and 1490 µm in diameter (**Figure 2-3 (C)**).

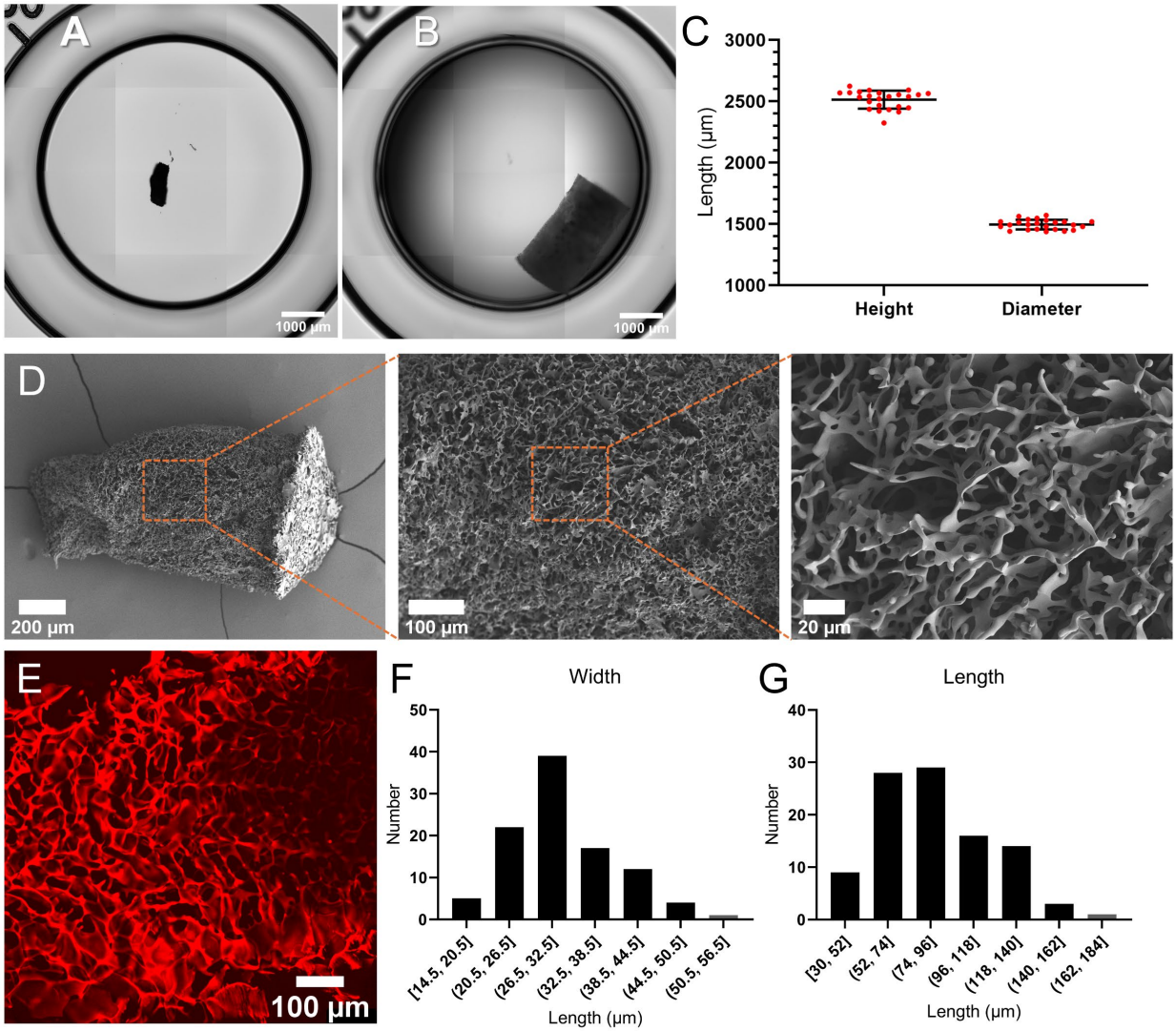

Figure 2-3 Morphological characterization of cylindrical cryogel.

Representative EVOS photos of **(A)** a dehydrated cryogel and **(B)** the same cryogel rehydrated in PBS. **(C)** shows the average size of rehydrated cryogels (n=24, error bars represent the mean ± SD).

(D) Representative SEM images show the pore structure of dehydrated cryogel. **(E)** Representative confocal microscopy image shows the pore structure of rehydrated cryogel. **(F)** and **(G)** show the pore size distribution. Pore size was measured from confocal microscopy images (n=100).

The interconnected macropore structure of the 95SPA cylindrical cryogel was observed under SEM (**Figure 2-3 (D)**). Although the size of the cryogel dramatically shrunk after dehydration, the macroporous structure was still clearly seen by SEM.

Because SEM images could not represent the real pore size in the rehydrated cryogel, fluorescently labelled cryogels were made for imaging under the confocal microscope. The huge interconnected rectangular pores in the cryogel are shown in **Figure 2-3 (E)**. **Figure 2-3 (F)** and **(G)** show the macropore size distribution, regarding macropores approximate to a rectangle shape. The macropore structure in 95SPA cryogels had an average size of 87 µm in length and 31 µm in width.

3.3 FTIR analysis confirms complete polymerization reaction

FTIR spectra (**Figure 2-4**) show that the peak of the vinyl group (C=C stretching) at 1638 cm^{-1} almost disappeared and the peaks of the sulfonate group (S=O stretching) at 1040 cm^{-1} and 1170 cm^{-1} were present after the crosslinking. In addition, the intensity of the C=O stretching at 1720 cm^{-1} and sulfonate group ($-SO_3^-$) at 1040 cm^{-1} and 1170 cm^{-1} was reduced after the crosslinking. FTIR spectra confirmed a successful polymerization reaction to incorporate the sulfonate groups into the cryogel and only some free vinyl groups left in the cryogel.

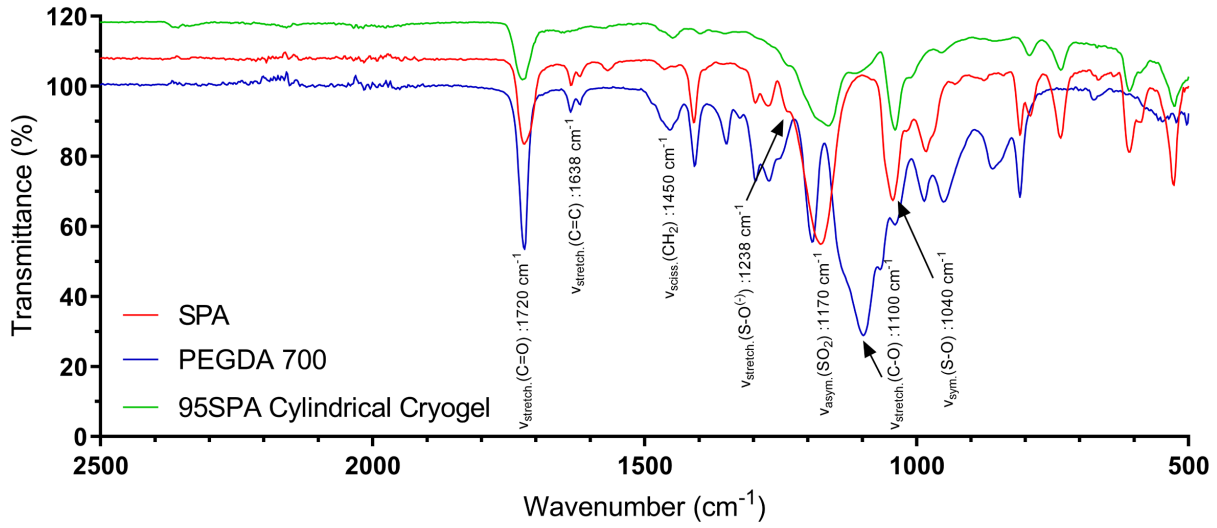

Figure 2-4 FTIR spectra confirm the complete photopolymerization.

3.4 The cryogels exhibit a soft compressible structure

The stiffness of the cryogels in compression was tested for the formulations of 95% SPA, 6-10% (wt/v) of solid content, and 8% (wt/v) solid content, 10-95% SPA. This experiment was performed in triplicate, and the stress-strain curves and Young's modulus of the cryogels with different formulations are shown in **Figure 2-5 (A - K)**. The Young's modulus is measured by the stress applied to an objective over the axial strain, representing the stiffness of materials. The results showed that the Young's modulus of cryogels increased with the increase in solid content or the decrease in the proportion of SPA. When increasing the solid content, the density of the polymeric network inside the cryogel also increased resulting in a stiffer cryogel. Because only PEGDA can form crosslinks between chains of the polymeric network, changing the ratio of SPA to PEGDA considerably impacted the crosslink density in the cryogel. The brain is an extremely soft tissue in the body, with a Young's modulus of only 3-10 kPa.(234) The results of mechanical tests showed that even the stiffest formulation was soft enough to avoid the mechanical mismatch when implanting the cryogel into the brain. 8% (wt/v), 95% SPA (Young's modulus: 1.57 ± 0.08 kPa) was chosen as the standard formulation in this chapter for the subsequent experiments because softer cryogel could be better as an implant to deliver drugs locally, but the cryogel was too soft to handle when the solid content was below 8%.

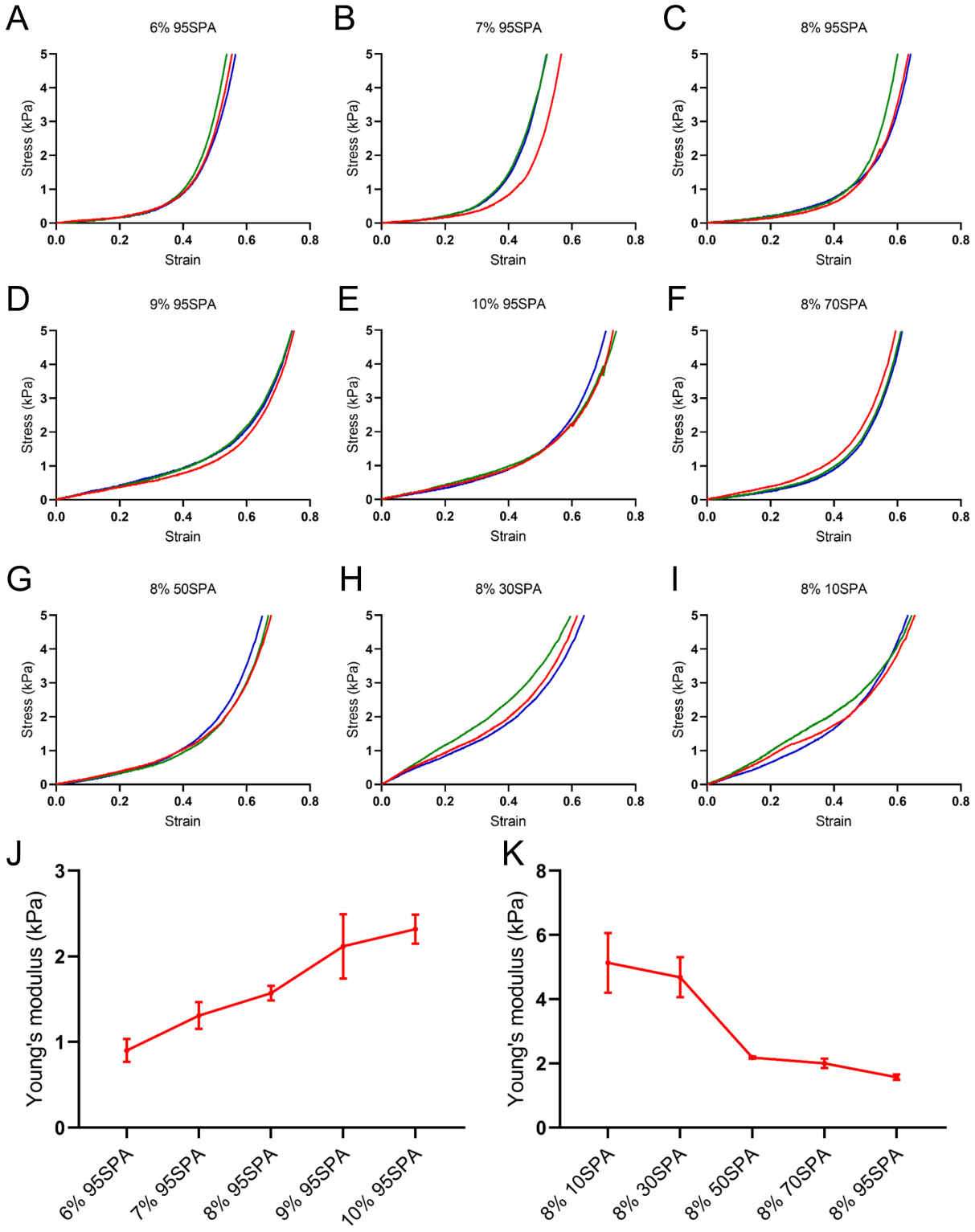

Figure 2-5 The cryogels exhibit a soft compressible structure.

(A) – **(I)** Stress-strain curves of cryogels with various formulations (solid content: 6-10% (wt/v); proportion of SPA: 10-95%). **(J)** and **(K)** showed Young's modulus of cryogels with various formulations calculated from the stress-strain curves (n=3, error bars represent the mean ± SD).

3.5 The cryogels effectively load DOX and clemastine

The principle of drug loading is based on the electrostatic interactions illustrated in **Figure 2-6**. The sulfonate group of SPA provides a negative charge, which allows positively charged drugs to bind with it. This nonspecific binding means that the SPA cryogel scaffold should theoretically be able to load a variety of drugs.

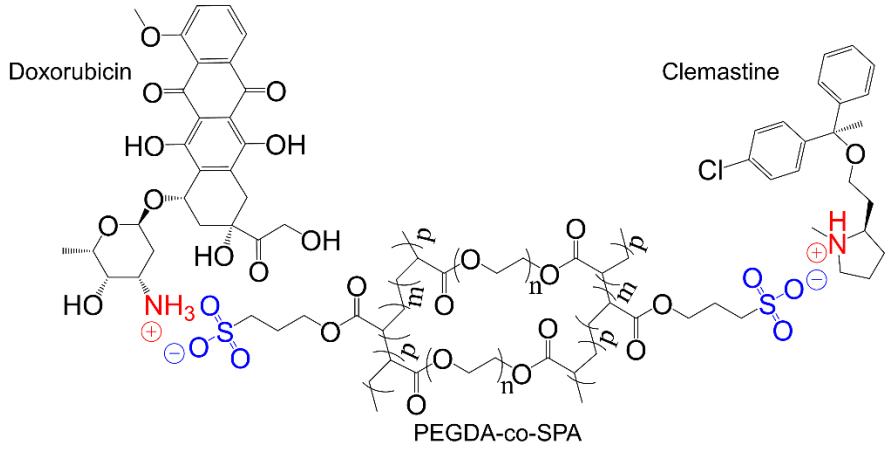

Figure 2-6 Illustration of the electrostatic interactions between the DOX or clemastine and the SPA.

95SPA cryogels created by the template for initial studies (1.6 mm in diameter, 2.5 mm in height) were used to evaluate the DOX loading capacity and the saturation point. The drug loading experiments were performed in two different media. **Figure 2-7 (A)** and **(B)** show the percentage and the amount of DOX loaded in an aqueous solution, respectively. After cryogels were incubated with 600 or 800 µg DOX for 24 hours, approximately 90% of DOX was loaded into the cryogels. The percentage of drug-loaded showed a slight increasing trend with incubation time, and it exceeded 95% after 72 hours. However, when incubated with 1000 or 1200 µg DOX, the highest DOX uptake was reached at 48 hours or 24 hours, respectively, which indicated the time when reached the saturation point.

At the saturation point, each cryogel was loaded with around 780 µg DOX, which meant the molar ratio of DOX to SPA was 2.07:1. As both DOX and SPA had one charged group, the excess of 1:1 loading ratio suggested that DOX was loaded into cryogels via mechanisms additional to electrostatic interactions. **Figure 2-7 (C)** and **(D)** show the results of DOX loading in PBS solution. The percentage of DOX loaded had an increasing trend in all concentrations of DOX solutions considered. Although incubation in 1200 µg DOX showed the highest DOX uptake, DOX precipitation was observed after 72 hours, which indicated that the amount of DOX loaded calculated by the DOX concentration in the supernatant was inaccurate. The highest DOX

concentration which would not precipitate after 72 hours incubation was 800 µg/mL (equal to 400 µg DOX samples). After incubation at this concentration for 72 hours, 380.7 ± 3.0 µg (95.2% ± 0.8%) DOX was loaded into the cryogels. For effective loading, DOX.HCl complex must be displaced by sulfonate-DOX complex. To load the DOX into the cryogel, the Cl^- must be displaced so that DOX can form a new complex with the sulfonate groups. This kind of ion exchange is involved in the DOX loading, where a more stable complex is formed between DOX and sulfonate groups. The drug-ion complexation is affected by the ionic strength and pH value. Comparing the deionized water and PBS, the higher ionic strength in PBS can screen electrostatic interactions, affecting how tightly DOX binds. Additionally, the slight difference in pH value affects the protonate state of the functional groups, thus changing the binding affinity. Therefore, the drug loading medium influences the DOX loading efficiency and capacity.

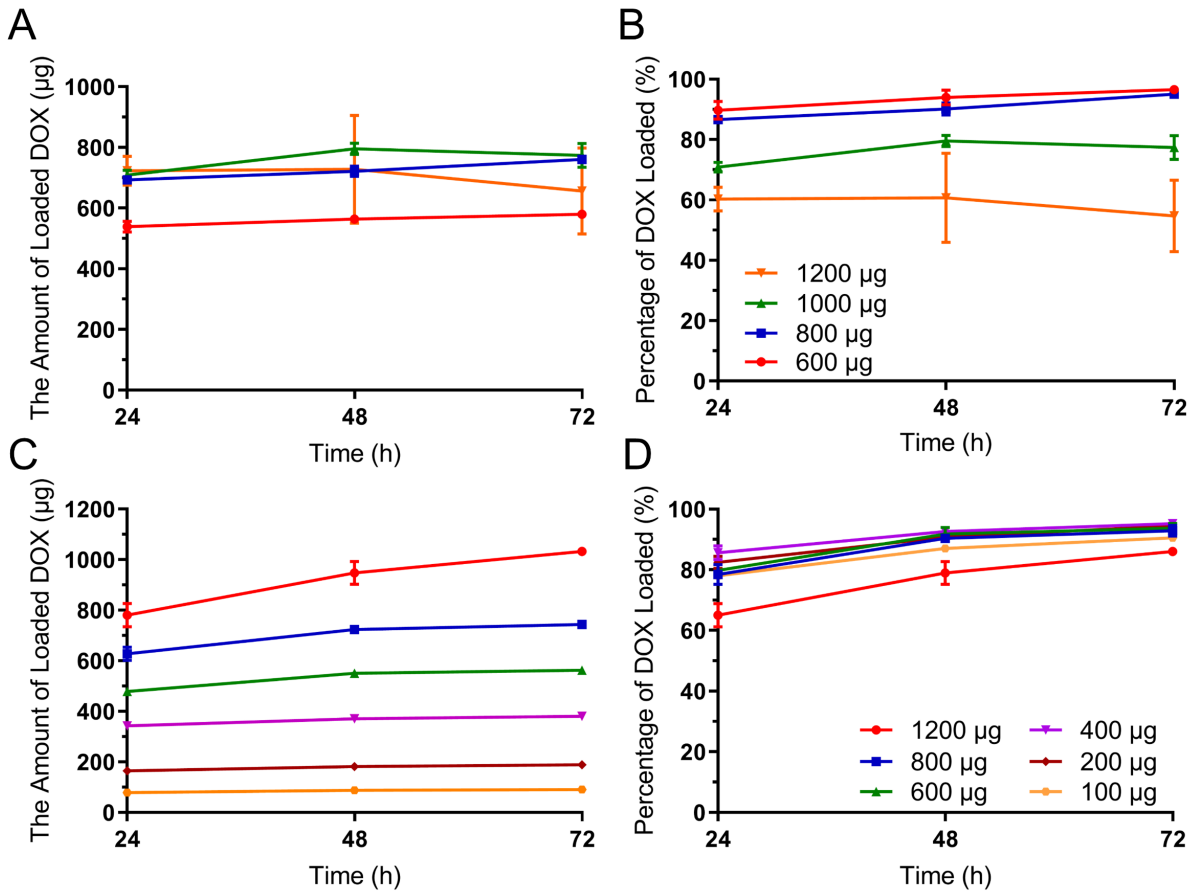

Figure 2-7 The cryogels have high DOX loading capacity and efficiency.

The cryogels were incubated in DOX solutions at various concentrations for different time periods. **(A)** and **(B)** show the amount and the percentage of DOX loaded for different incubation periods in an aqueous solution, respectively. **(C)** and **(D)** show the amount and the percentage of DOX loaded

at different times in the PBS solution, respectively. The legend showed the amount of DOX in the loading samples before incubation (n=3, error bars represent the mean ± SD).

Although the cryogel showed a high loading efficiency of a high amount of DOX, this dosage was too high for the animal study. According to the research about the local delivery of DOX, the maximum dosage for a rat model was only 5 μg per animal.(71, 83, 92) It is worth investigating the loading efficiency for a small amount of DOX, especially 5 μg to match the *in vivo* dosage. When the cryogels were incubated in DOX solution at a low concentration, the DOX loading efficiency decreased dramatically (**Figure 2-8 (A)** and **(B)**) which was less than 50% if the concentration was less than 10 μg/mL. Interestingly, the DOX concentration in the supernatant was maintained at a stable level after the incubation (approximately 13 μg/mL) when the DOX concentration was above 50 μg/mL before the loading (**Figure 2-8 (C)** and **(D)**). These results suggested that the electrostatic force-driven drug loading needed a concentration gradient to generate enough force to make the DOX bond with SPA. This stable level of DOX concentration after drug loading might indicate that the point of the equilibrium was reached, in which DOX bonded and dissociated with SPA. In addition, the π-π stacking among DOX molecules might dominate the drug-loading mechanism when the cryogel was loaded with a high amount of DOX.(235, 236) So, the reason why higher DOX concentrations resulted in higher loading efficiency might be because the equilibrium of electrostatic interactions was not relevant to the amount of available sulfonate groups, and π-π stacking was stronger than electrostatic interactions. Therefore, an alternative loading method is required to be discovered to load a small amount of DOX with high loading efficiency.

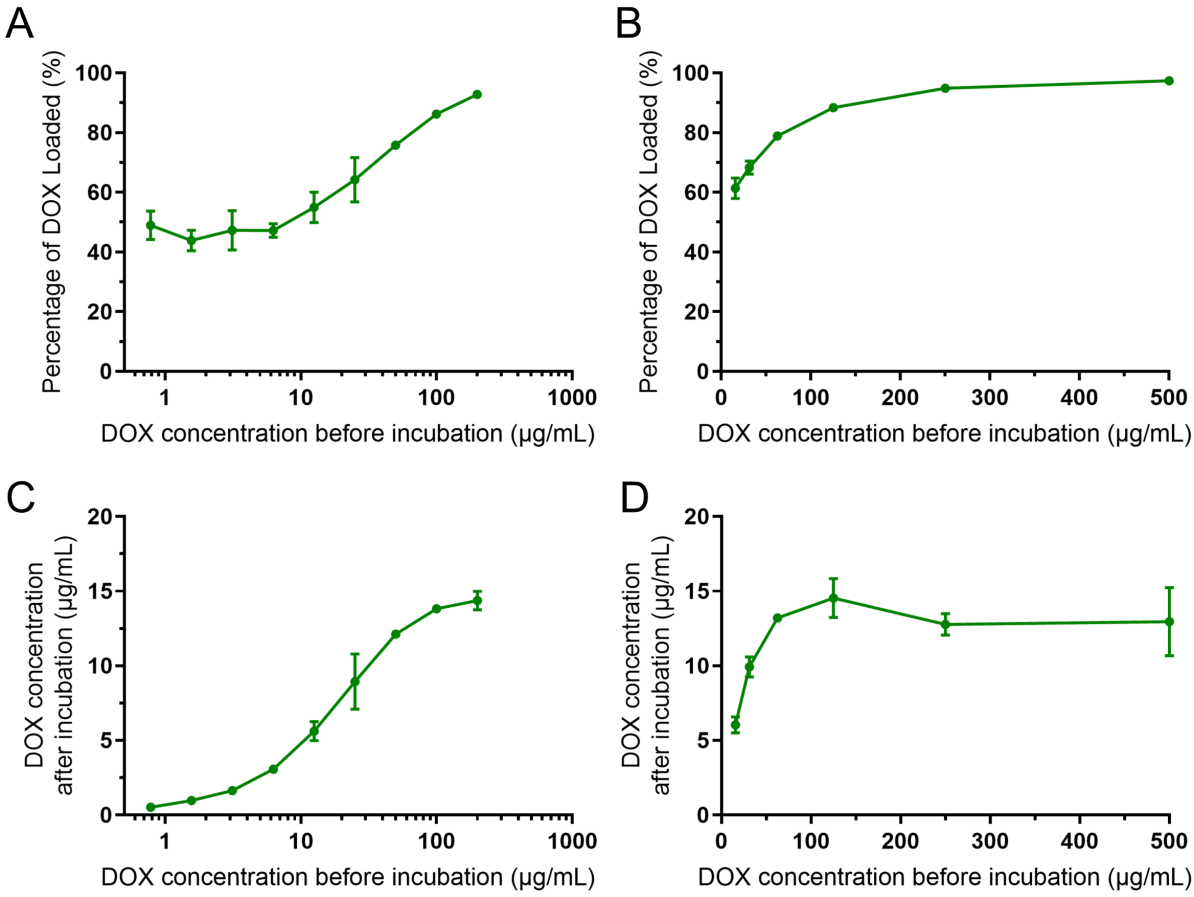

Figure 2-8 Low DOX concentration reduces the drug loading efficiency.

The DOX loading efficiency from two experiments was shown in **(A)** and **(B)**. 95SPA cryogels made by the template for the initial study were incubated in DOX solution for 24 h. The remaining DOX concentration was shown in **(C)** and **(D)**. **(A)** – **(D)**: DOX stock solution was diluted using deionized water; n=3, error bars represent the mean ± SD.

Taking advantage of high DOX concentration in the drug loading study, a direct injection method was decided upon, in which a small volume of DOX solution was injected into the dehydrated cryogel. The effect of the DOX concentration was investigated first, and the results showed that 100% drug was loaded into the cryogels within 10 minutes (**Figure 2-9 (A)**). This superb loading efficiency might be because DOX molecules had more chance to bind with SPA by electrostatic interactions or other DOX molecules by π-π stacking in such a small volume. Next, the drug loading efficiency was evaluated on cryogels with a SPA proportion from 10% to 95%. Because the size expansion ratio of cryogels was reduced with a lower SPA proportion, an injection volume of 2.5 μL of DOX solution (2 mg/mL) was selected for drug loading, which can be fully absorbed by 10SPA cryogels. The results of drug loading (**Figure 2-9 (B)**) showed that 100% DOX was loaded into the cryogels containing 50% or more SPA, while the DOX loading efficiency showed a decreasing trend

of 30% and 10% SPA cryogels, which indicated that the SPA proportion affected the loading efficiency. This simple drug loading method precisely controlled the amount of loaded drugs and met the requirements of dosage for animal study.

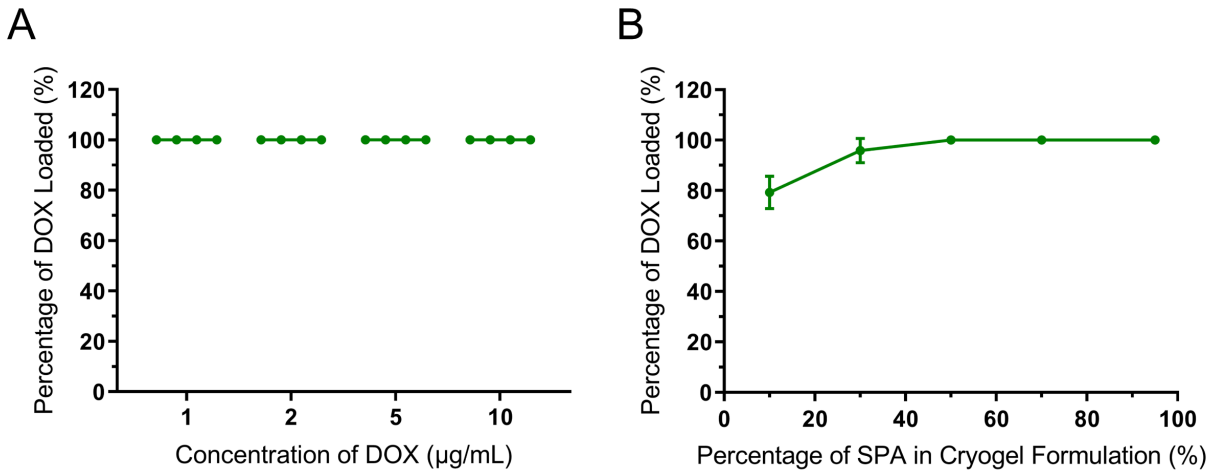

Figure 2-9 The direct injection method achieves high DOX loading efficiency for a small amount of drug (5 μg).

Cryogels for the rat model were used. DOX stock solution was diluted using deionized water. **(A)** shows the DOX loading efficiency when dehydrated 95SPA cryogels were directly injected with various concentrations of DOX solution. **(B)** shows the effect of the percentage of SPA in the cryogels for DOX loading efficiency (n=4, error bars represent the mean ± SD).

Next, the clemastine loading efficiency was investigated. Cryogels for the mouse tumour resection model were used in this study. Cryogels were incubated in clemastine solution at various concentrations for three days. As shown in **Figure 2-10**, cryogels incubated with 100 μg clemastine showed the highest loading efficiency, in which more than 95% of the drug was loaded into the cryogel. Increasing or decreasing the clemastine concentration caused a reduction in the loading efficiency. For the small amount of drugs, the decrease in the loading efficiency might be because the electrostatic interactions required a concentration gradient to maintain the binding equilibrium. The theoretical saturation point for clemastine was 137 μg. Cryogels cannot load more clemastine beyond the saturation point, which is different from DOX. Two phenyl rings in the clemastine are not in the same plane. This structure might have steric effects to reduce the π-π stacking force, so clemastine can only be loaded into cryogels via electrostatic interactions.

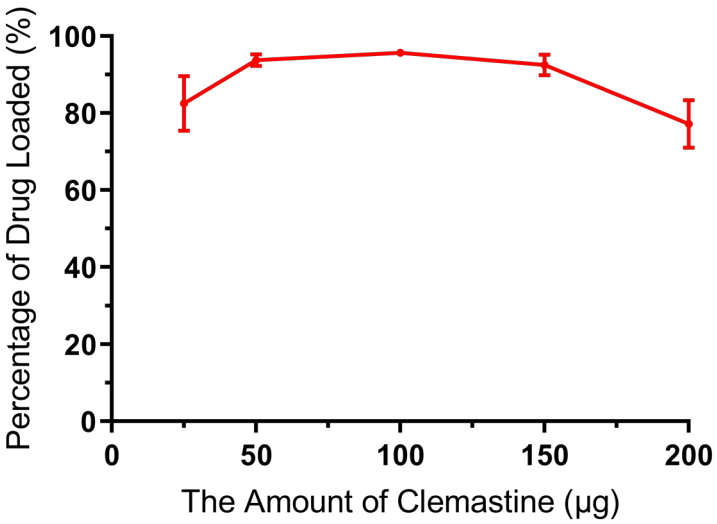

Figure 2-10 The cryogels have a high loading capacity and efficiency of clemastine.

Error bars represent the mean ± SD (n=4).

3.6 The amount of payload affects the release profiles

To evaluate the long-term DOX release profiles, cryogels made by the template for the initial study were loaded with different amounts of drugs. As shown in **Figure 2-11**, for 400 μg samples, after the burst release in the first week, DOX was released from cryogels at a nearly zero-order rate until Day 53. However, most of the drugs were released over the first four days from the cryogels loaded with 50 μg DOX. Then only an extra 7 μg DOX was released over the following 12 days. In addition, cryogels loaded with 10 μg DOX released all drugs in the first two days. These results indicated that loading more DOX into the cryogel improved the sustained release profiles. Intermolecular forces among DOX molecules such as π-π stacking might dominate the drug release and reduce the release rate.

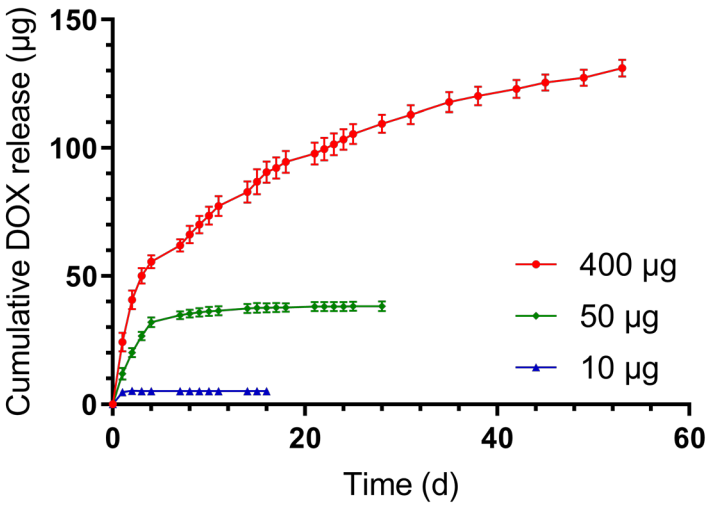

Figure 2-11 Cumulative release profiles of DOX from cryogels loaded with varying initial drug concentrations (10 µg, 50 µg, and 400 µg per cryogel).

The cryogels loaded with higher amounts of DOX extended the drug release period. DOX stock solution was diluted using PBS for drug loading. The legend showed the amount of loaded drugs (n=4, error bars represent the mean ± SD).

To further investigate the release profiles of cryogels loaded with a small amount of DOX, additional release studies were performed for the cryogels loaded with 5 µg DOX. This dosage should be better to reflect the *in vivo* release profiles. First, the effect of the concentration of DOX solution for drug loading was tested. According to the results shown in **Figure 2-12 (A)**, unfortunately, all payloads were released within two days even increasing the DOX concentration to 10 mg/mL. Using higher concentrations only slightly reduced the proportion of drugs released on the first day but failed to prolong the drug release period. Next, the effect of the SPA proportion was investigated. As shown in **Figure 2-12 (B)**, changing the SPA proportion also did not alter the release profiles. Almost all drugs were released within one day, followed by a small amount of DOX released from the 50SPA, 70SPA, and 95SPA cryogels on the second day. These results suggested that alerting the SPA proportion did not improve the release kinetics. 95SPA cryogels had the best release profile among these formulations, which might be because the high SPA proportion provided more chances for drugs to bind with SPA. Therefore, cryogels loaded with 5 µg DOX released payload in a rapid pattern, indicating the limitation of delivery of a small amount of drug.

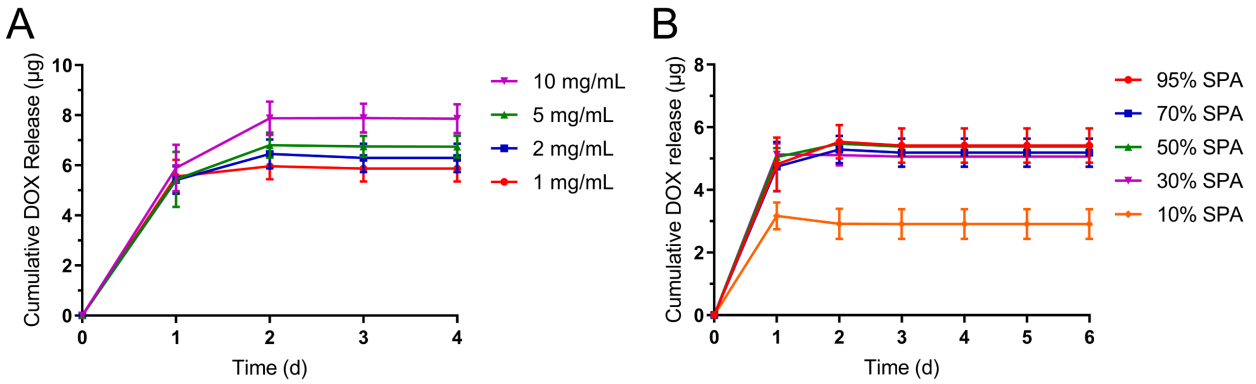

Figure 2-12 The cryogels loaded with a small amount of DOX (5 µg) show a rapid release pattern. **(A)** shows the cumulative drug release curves of the cryogels loaded by various DOX concentrations. **(B)** shows the cumulative drug release curves of the cryogels with different formulations of SPA ratio. **(A)** and **(B)**: DOX stock solution was diluted using deionized water for drug loading; n=4, error bars represent the mean ± SD.

The drug release profiles of clemastine cryogels were investigated. As shown in **Figure 2-13**, for the cryogels loaded with 100 µg or more clemastine, around 60% of the drugs were released on the first day, and another 20% of the drugs were released on the following days. After the burst release, less than 10% of the drug was sustained released. A slower release profile was observed for cryogels loaded with 50 µg drugs. Cryogels sustained released drugs after the burst release on Day 1 with almost zero order kinetics from Day 2 to Day 9. Only 40% of clemastine was released from cryogels loaded with 25 µg drugs in two weeks, which might be due to the limitation of the determination method (1.5 µg/mL). The drug concentration in the samples would be considered zero if it was below the limitation of the determination. The burst release could become the loading dose to reach a high drug concentration at the beginning of the therapy, and the small amount of sustained released drug could maintain the focal drug concentration, potentially benefiting the local treatment.

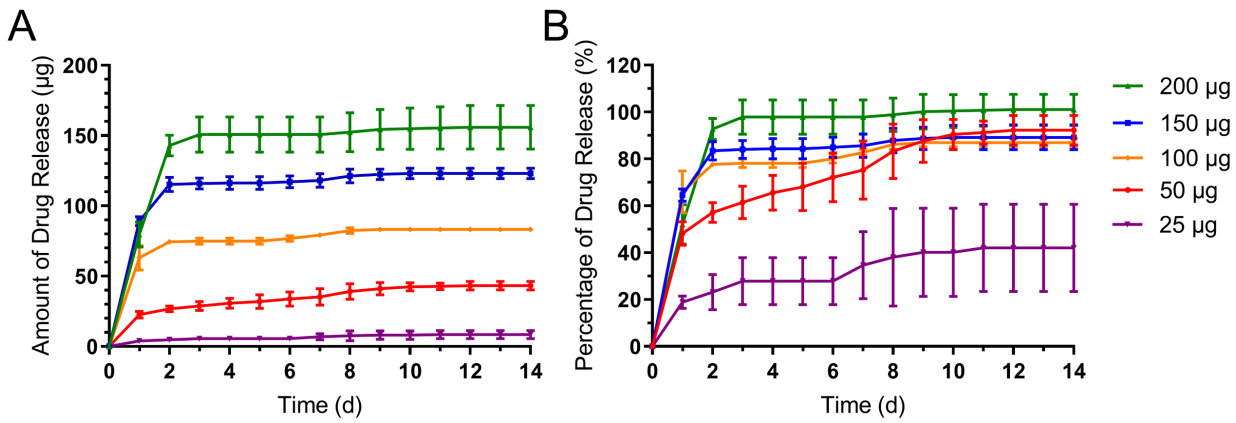

Figure 2-13 Drug release profiles of cryogels loaded with various amount of clemastine. **(A)** and **(B)** show the amount and the percentage of cumulative clemastine release in PBS, respectively. **(A)** and **(B)**: n=4, error bars represent the mean ± SD. Cryogels were made by template for mouse resection cavity.

3.7 Empty cryogels are not toxic to astrocytes

To evaluate the *in vitro* cytocompatibility of 95SPA empty cryogels, primary human astrocytes, the most abundant cell type in the CNS, were chosen as the cell model. Empty cryogels were added on Day 1 and incubated with hAstrocytes for 1, 4, or 7 days to test the cell viability. As shown in **Figure 2-14 (A)**, empty cryogels did not impact the morphology of hAstrocytes. The cell viability of hAstrocytes treated with empty cryogels had no significant difference with the untreated cells, indicating that empty cryogels were not toxic to healthy cells (**Figure 2-14 (B)**).

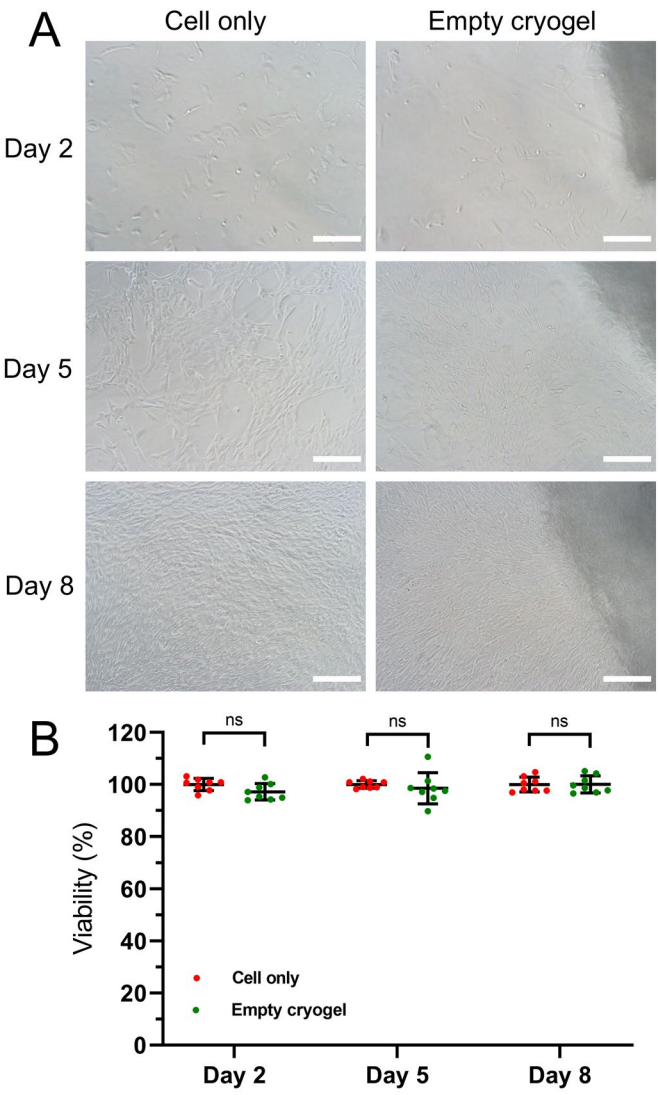

Figure 2-14 The empty cryogel has good cytocompatibility on primary human astrocytes.
(A) shows representative images of primary human astrocytes incubated with or without empty cryogel. Cryogels were added on Day 1. Images were taken on Day 2, 5, and 8 (Scale bar = 200 µm). **(B)** shows the cell viability after 1, 4 or 7 days of adding cryogel (n=8, error bars represent the mean ± SD). Unpaired t-test: Day 2 and Day 8, Welch's t-test: Day 5, ns = no significant difference.

3.8 Clemastine shows a therapeutic window and effectively kills GBM cells *in vitro*

Human GBM cell lines were cultured in a serum-free medium. Compared to the patient-derived GBM cells grown in the standard serum-contained medium (for example, 10% FBS in DMEM medium) from the same specimen, primary GBM cells grown in serum-free medium showed extraordinary similarity to normal neural stem cells including forming neurospheres, indefinite self-renewal potential, capacity to differentiate into glial and neuronal lineages, stable gene expression even after several passages, whilst GBM cells grew in serum contained medium lost clonogenicity

and tumorigenicity, gene expression profile changed, and failed to show the ability to self-renew and differentiate.(237) So, a serum-free medium can maintain primary GBM cells as cancer stem cells and be a more reliable model for *in vitro* drug screening.

First, the cytotoxicity of free clemastine was investigated on hGBM cell lines and hAstrocytes. According to the data shown in **Table 2-3** and **Figure 2-15**, IC_{50} values considerably decreased when the exposure time increased from 1 day to 4 days (drugs added on Day 1), which hGBM L2 cell line showed the highest percentage of the reduction in IC_{50} values. The IC_{50} values did not change too much if the exposure time was extended to 7 days on all cell lines. Despite hGBM L0 being the most resistant GBM cell lines to clemastine, the IC_{50} values of hGBM L0 were much smaller than that of hAstrocytes exposed to the drug for the same time, which suggested that there was a potential therapeutical window that the drug could kill the GBM cells while being safe for healthy cells.

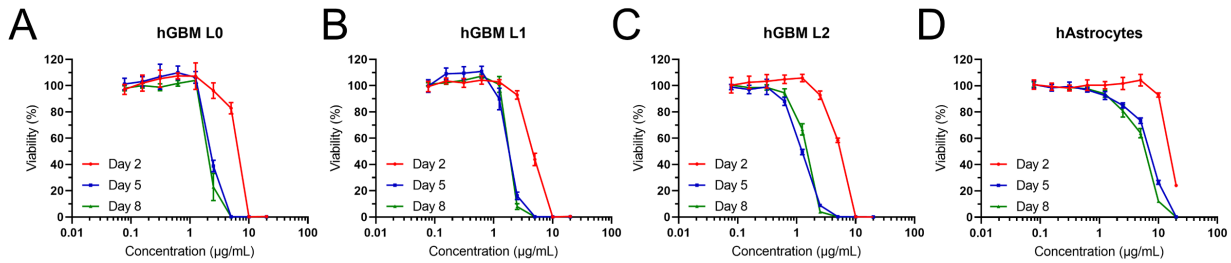

Figure 2-15 Clemastine is more toxic to GBM cells than astrocytes.

Dose-respond curves of free clemastine on hGBM cell lines and primary human astrocytes (n=6, error bars represent the mean ± SD).

Table 2-3 IC_{50} values of free clemastine on hGBM cell lines and hAstrocytes (μg/mL)

	hGBM L0		**hGBM L1**		**hGBM L2**		**hAstrocytes**	
	IC_{50}	SD	IC_{50}	SD	IC_{50}	SD	IC_{50}	SD
Day 2	5.78	0.93	4.63	0.16	5.29	0.22	16.20	0.61
Day 5	2.25	0.14	1.76	0.10	1.23	0.04	6.80	0.40
Day 8	2.00	0.18	1.89	0.12	1.42	0.03	5.54	0.34

The PrestoBlue assay used in this experiment is an indirect, metabolism-dependent assay in which viable cells reduce resazurin to a fluorescent resorufin product, allowing quantification of metabolic activity. A decrease in signal often correlates with cell death or cytotoxicity. After treatment with clemastine, a significant reduction in cell metabolic activity was observed, suggesting a potential cytotoxic effect. However, this assay does not distinguish between reduced

metabolic activity and actual cell death, meaning that a lower signal may result from metabolic suppression rather than cytotoxicity.

Three hGBM cell lines (L0, L1, and L2) were grown individually as multicellular spheres in a serum-free medium to evaluate the cytotoxicity of clemastine cryogels. Empty cryogels did not kill GBM cells and affect the cell morphology after 7 days of incubation (**Figure 2-16**). 50 µg clemastine cryogels killed all hGBM L0 cells after one day of adding cryogels. The cell viability of hGBM L0 cells on Day 3 treated with 25 µg clemastine cryogels had no significant difference compared to 5 µg/mL free drug treatment, suggesting the controlled drug release from cryogels. Clemastine released from 3.125, 6.25, or 12.5 µg samples was not sufficient to kill hGBM L0 cells. However, four days after adding the cryogels, even 3.125 µg clemastine cryogels nearly killed all hGBM L0 cells. Similar results were observed on hGBM L1 and hGBM L2 cell lines (**Figure 2-17** and **Figure 2-18**). The cell viability data on Day 3 revealed that hGBM L2 was the most sensitive GBM cell line to clemastine.

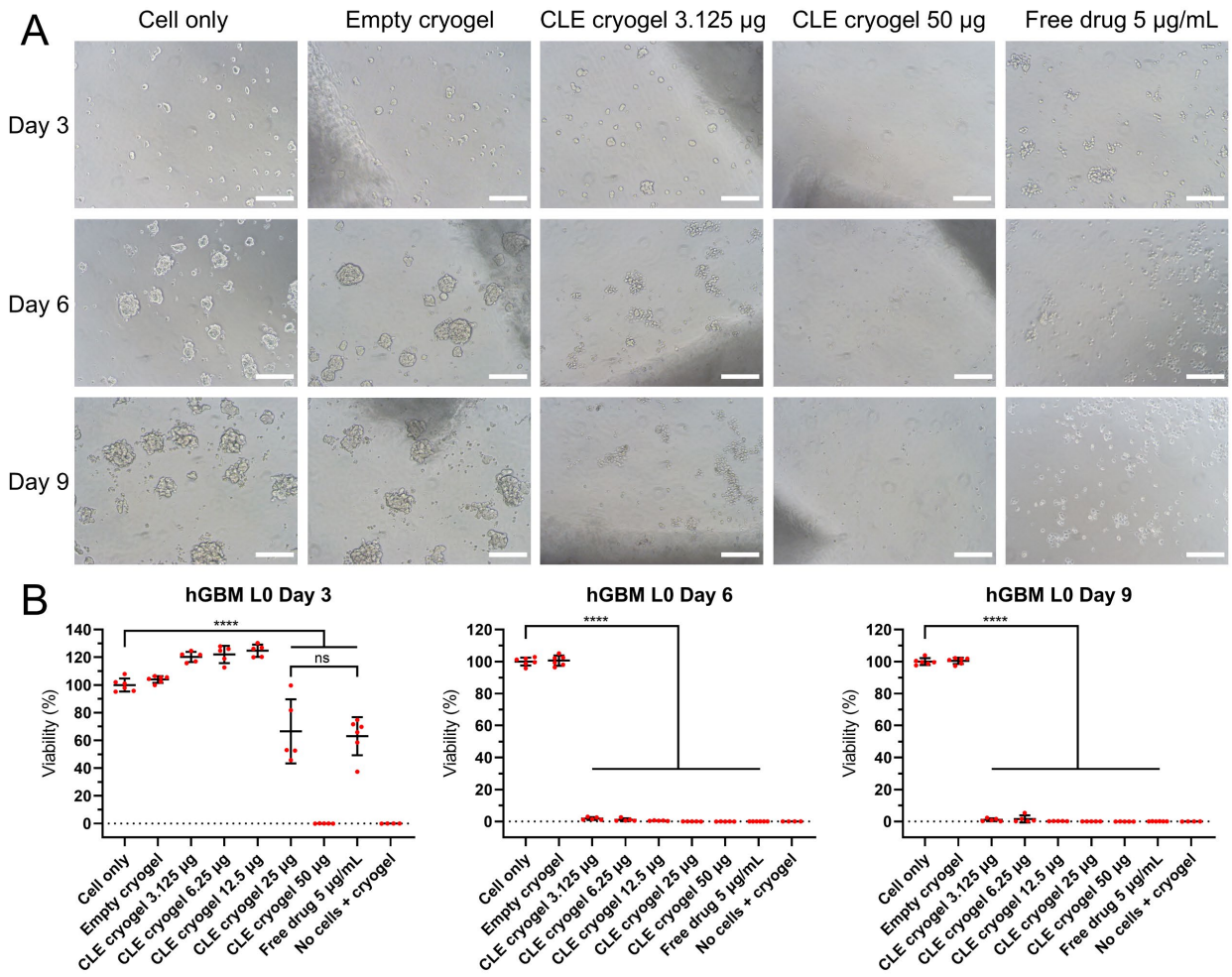

Figure 2-16 *In vitro* anti-GBM efficacy of clemastine cryogel on hGBM L0.

(A) shows representative bright field images of hGBM L0 cells incubated with culture medium only, empty cryogel, 3.125 or 50 µg clemastine cryogel, and 5 µg/mL free clemastine. The cryogels were added on Day 2. Images were taken on Day 3, 6, and 9 (Scale bar = 200 µm). **(B)** shows the cell viability on Day 3, 6, and 9 (Cell only, empty cryogel and free drug, n=6; clemastine cryogel groups, n=5; no cells + empty cryogel, n=4; error bars represent the mean ± SD. Ordinary one-way ANOVA test: Day 3 and Day 9, Welch ANOVA tests: Day 6, ns = no significant difference, for **** $p \leq 0.0001$). Abbreviation: CLE: clemastine.

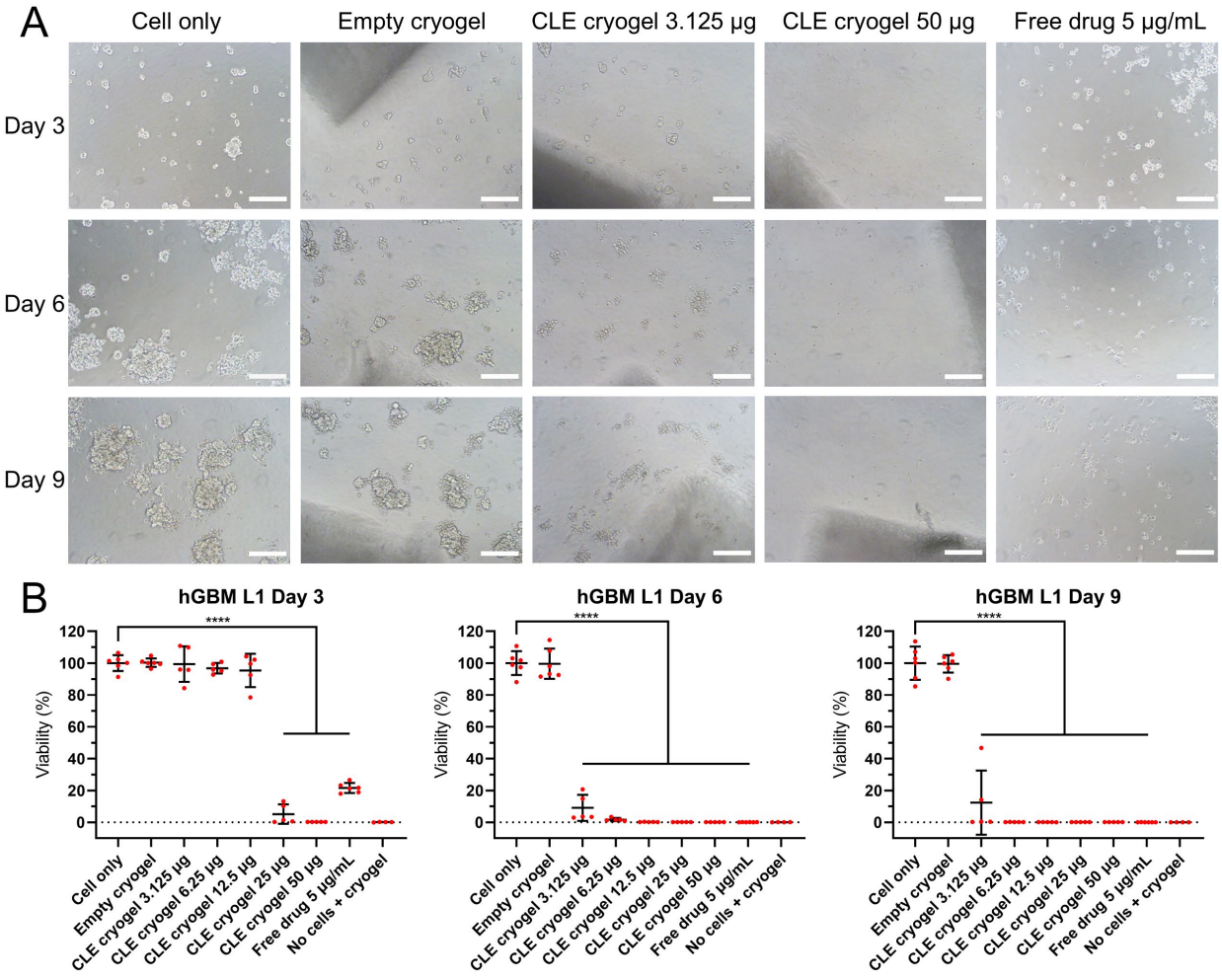

Figure 2-17 *In vitro* anti-GBM efficacy of clemastine cryogel on hGBM L1.

(A) shows representative bright field images of hGBM L1 cells incubated with culture medium only, empty cryogel, 3.125 or 50 µg clemastine cryogel, and 5 µg/mL free clemastine. The cryogels were added on Day 2. Images were taken on Day 3, 6, and 9 (Scale bar = 200 µm). **(B)** shows the cell viability on Day 3, 6, and 9 (Cell only, empty cryogel and free drug, n=6; clemastine cryogel groups, n=5; no cells + empty cryogel, n=4; error bars represent the mean ± SD. Ordinary one-way ANOVA test: Day 3 and Day 9, Welch ANOVA tests: Day 6, for **** $p \leq 0.0001$). Abbreviation: CLE: clemastine.

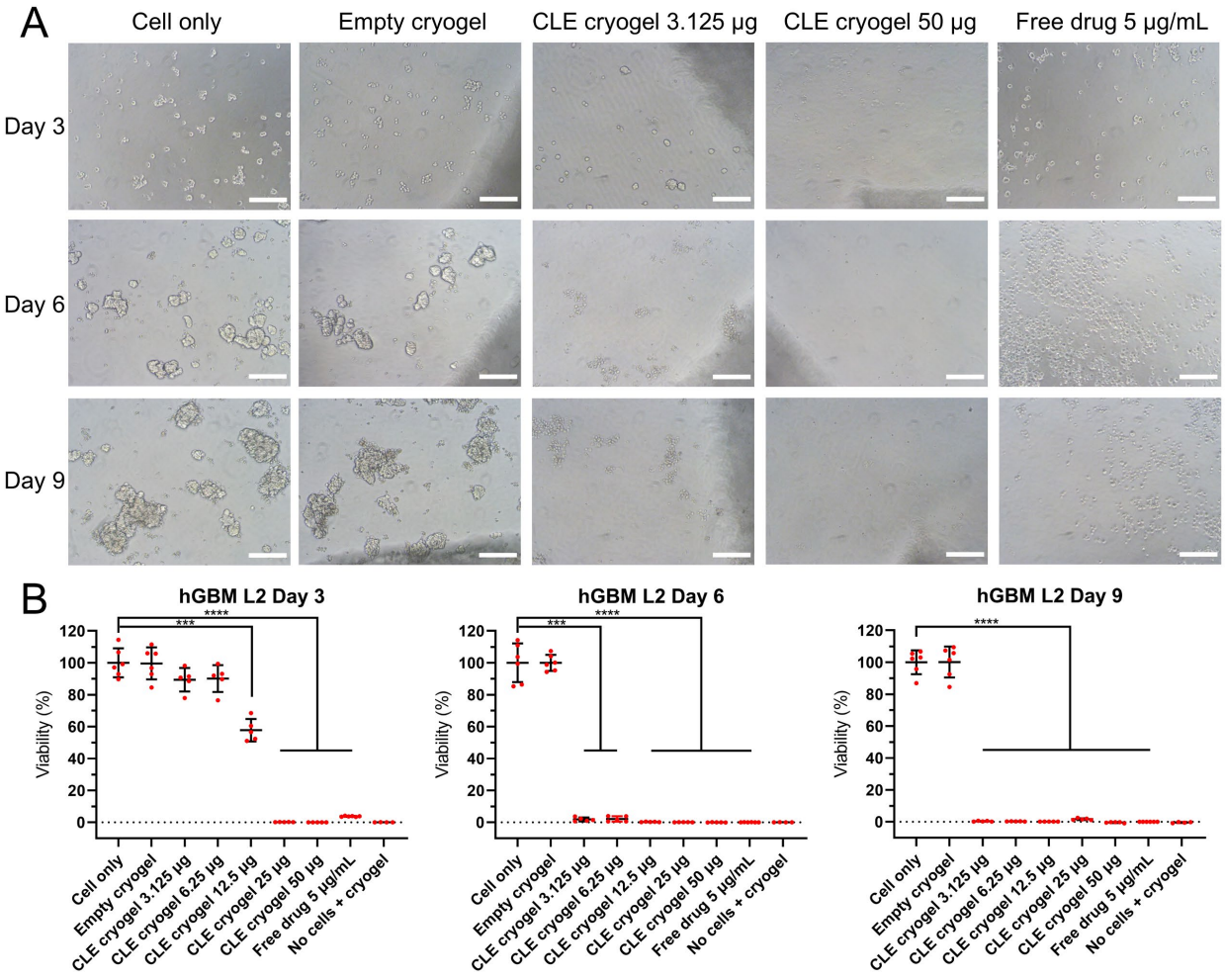

Figure 2-18 *In vitro* anti-GBM efficacy of clemastine cryogel on hGBM L2.

(A) shows representative bright field images of hGBM L2 cells incubated with culture medium only, empty cryogel, 3.125 or 50 µg clemastine cryogel, and 5 µg/mL free clemastine. The cryogels were added on Day 2. Images were taken on Day 3, 6, and 9 (Scale bar = 200 µm). **(B)** shows the cell viability after on Day 3, 6, and 9 (Cell only, empty cryogel and free drug, n=6; clemastine cryogel groups, n=5; no cells + empty cryogel, n=4; error bars represent the mean ± SD. Welch ANOVA tests for all figures, for *** $p \leq 0.001$, **** $p \leq 0.0001$). Abbreviation: CLE: clemastine.

3.9 The variability in the extent of surgical resection affects the clemastine treatment efficacy

A patient-derived GBM cell line (BT12) was used to establish the *in vivo* GBM model (**Figure 2-19**). This cell line had a growth pattern in the cells that would form a tumour bulk but still have individual cells and clusters invading other areas in the brain.(125) After 15 days of cell implantation, craniotomy was done to partially remove the tumour bulk and cryogels were implanted into the surgical resection cavities. Animals were randomly allocated into four treatment groups during the surgery. Five mice received only tumour resection, and their resection cavities

were left empty. 11 mice were implanted with empty cryogels, four days after surgery, six of them were intraperitoneally administered with clemastine (50 mg/kg per day for 10 days), while the other five mice did not receive additional treatment. Nine mice were implanted with the clemastine-loaded cryogel as the local treatment group (10 µg/animal).

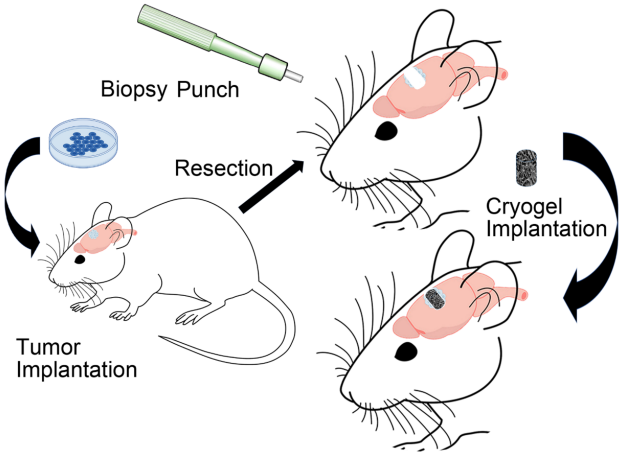

Figure 2-19 Schematic representation of the *in vivo* orthotopic GBM tumour model establishment and surgery procedure.

We first tried to locally administer 20 µg clemastine, but this animal died a few minutes after the surgery. So, we thought that 20 µg might be too high and cause toxicity to the animals. As the mice were weak after the craniotomy and local drug delivery achieved a much higher drug concentration than the systemic treatment, we reduced the dosage to 10 µg. As shown in **Figure 2-20 (A)**, all mice lost weight after the craniotomy but recovered from the surgery after 4-8 days. There were no significant difference in the body weight among the four treatment groups two weeks after the surgery (p=0.0764), which indicated the *in vivo* biocompatibility of the implanted cryogel. The mice's behaviour after the surgery was monitored to examine the brain injury and the biocompatibility of the cryogel. Two mice from the clemastine cryogel group showed hemiplegia after 8 and 10 days of surgery, and one mouse from the resection-only group showed the same symptom after 14 days of the surgery, which suggested that cryogel implantation only caused rare side effects.

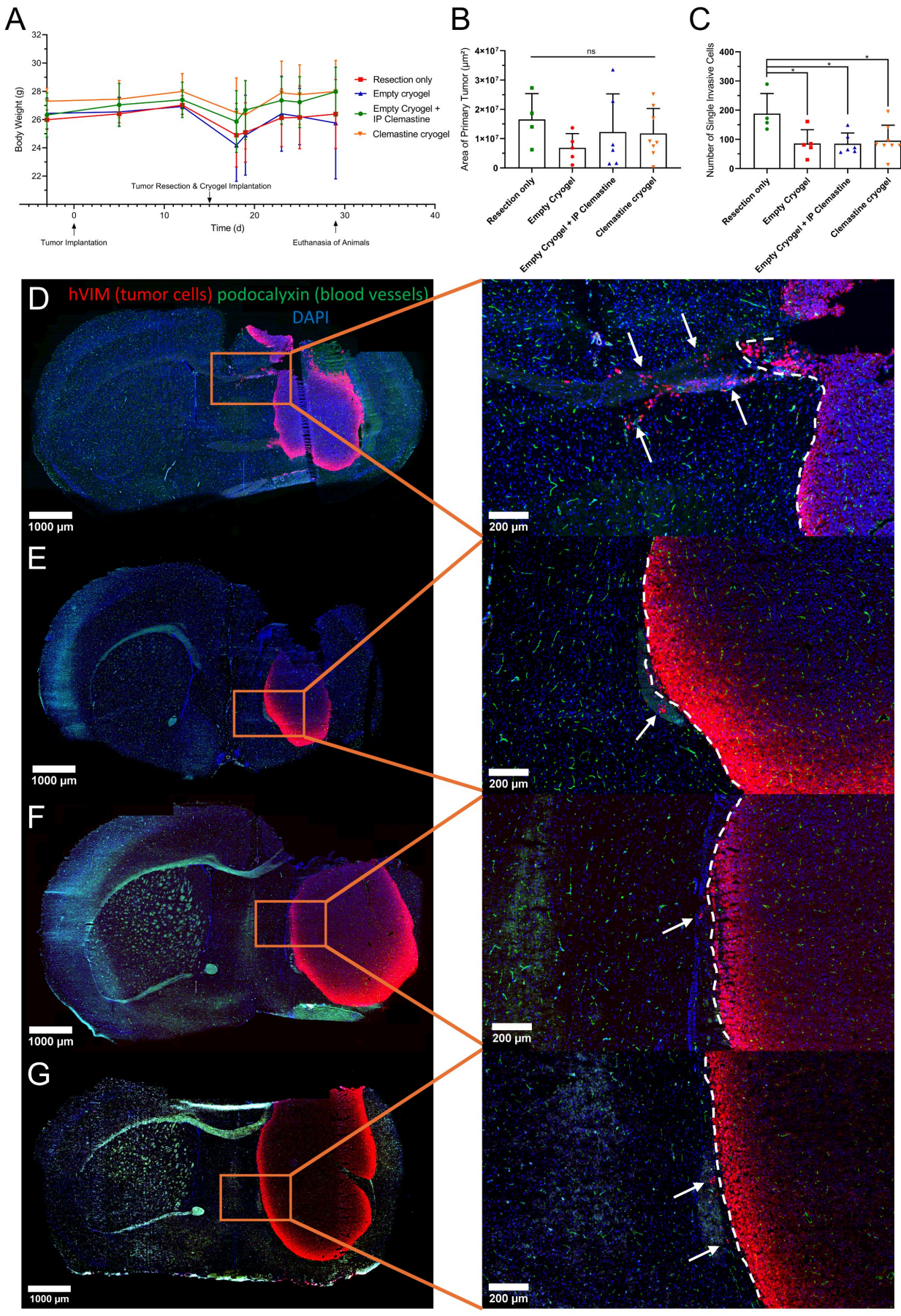

Figure 2-20 *In vivo* anti-GBM efficacy of clemastine cryogel.

(A) shows the changes in mouse body weight during the treatment (Resection only, n=5; Empty cryogel, n=5; Empty cryogel + IP clemastine, n=6; clemastine cryogel, n=9). **(B)** The size of the primary tumour after the treatment. **(C)** Quantification of the number of single invasive cells. **(B)** and **(C)**: The tumours of one animal from resection only group and one animal from the clemastine cryogel group were completely resected, and these two animals were excluded from tumour analysis. Error bars represent the mean ± SD. Ordinary one-way ANOVA test for **(B)** and **(C)** (ns = no significant difference, for * $p \leq 0.05$). Representative whole coronal sections of murine brain treated with **(D)** tumour resection only, **(E)** empty cryogel, **(F)** empty cryogel + IP clemastine, and **(G)** clemastine cryogel. Dashed lines separate the primary tumour mass and the normal brain in portion zoomed-in images. Arrows show the invasive GBM cells.

All mice were euthanized after 14 days of tumour resection, and their brains were collected for IHC analysis. Due to the limited number of available animals, it was not feasible to simultaneously conduct survival studies and IHC analyses only after a short period of the treatment. Given this constraint, IHC was prioritised as it offers more detailed and informative insights into tumour progression, tumour cell invasion, and host responses following cryogel implantation. To analyse the antitumor efficacy of clemastine cryogel, the size of the primary tumours, the number of single invasive tumour cells, the total size of the tumour cell clusters, the total number of tumour cells in tumour cell clusters, and the shortest distance between primary tumours and single invasive cells or tumour cell clusters were manually counted or measured in three sections for each animal. However, some animals only had a tiny primary tumour covering less than three sections. So, one mouse in the empty cryogel group was analysed for two brain sections and one mouse in the clemastine cryogel group was analysed for one brain section. Additionally, the primary tumours in two animals (one in the resection-only group and one in the clemastine cryogel group) were not observed, which might be due to the complete tumour resection. These two animals were excluded from the tumour analysis.

Due to the partial tumour resection, the primary tumours of most animals grew to a large bulk tumour after 14 days of surgery, whilst some animals underwent more successful surgery, and only a small primary tumour was observed. However, the size of primary tumours in the four treatment groups did not reach a significant difference (**Figure 2-20 (B)**, $p=0.5094$). The empty cryogel treatment group had the smallest average size of primary tumours, which was only 41.5% compared to resection-only treatment ($p=0.4383$). Additionally, regardless of systemic administration or local delivery, clemastine failed to suppress the growth of primary tumours after

the tumour resection surgery. Interestingly, mice treated with the empty cryogel, empty cryogel plus IP injection clemastine, or clemastine cryogel had significantly less total amount of single invasive cells (**Figure 2-20 (C)**). Although treatment with clemastine cryogels appeared to reduce the number of single invasive tumour cells compared to the surgery-only group, a similar reduction was also observed in the empty cryogel group. This suggests that the presence of the cryogel may influence cell invasion, potentially due to mechanical or immunological effects. Moreover, variability in the extent of surgical resection may act as a confounding factor, affecting the number of residual or invasive cells detected post-treatment. Representative whole coronal sections of the murine brain in each group are shown in **Figure 2-20 (D)** – **(G)**. Tumour cells were visualized by human vimentin protein, which is a structural cytoskeletal protein, and podocalyxin was used to visualize the blood vessels. A large primary tumour was formed in all groups after 14 days of tumour resection A small part of GBM cells were observed invading the surrounding tissues through nerve fibre tracts such as corpus callosum or blood vessels (**Figure 2-20 (D)**).

In tumour cell analysis, if more than two cells migrated together, these tumour cells were regarded as tumour cell clusters. **Figure 2-21 (A)** and **(B)** show that the total size of the tumour cell clusters and the total number of invasive tumour cells in tumour cell clusters did not have significant difference among the four treatment groups (p=0.3534 and p=0.2003, respectively). This indicates that the anti-GBM efficacy of clemastine treatment is limited. In the orthotopic BT12 mouse model without resection, systemic clemastine treatment significantly reduced the total number of invasive cells and the distance of invasion compared to the vehicle treatment control group.(125) However, as the surgery is the mainstay for GBM management, tumour resection might attenuate the efficacy of clemastine treatment. In addition, the invasion distance from the primary tumours also showed no significant difference both for single invasive cells (**Figure 2-21 (C)**, p=0.8829) and tumour cell clusters (**Figure 2-21 (D)**, p=0.1197) among the four treatment groups. However, the invasion distance measured in one brain section might not represent the shortest distance. Because of the 3D structure, the shortest distance might not be in the coronal plane. The huge variances in primary tumour size also impacted the measurement of invasion distance, as tumour cells did not have a large space to migrate if the primary tumour grew too large.

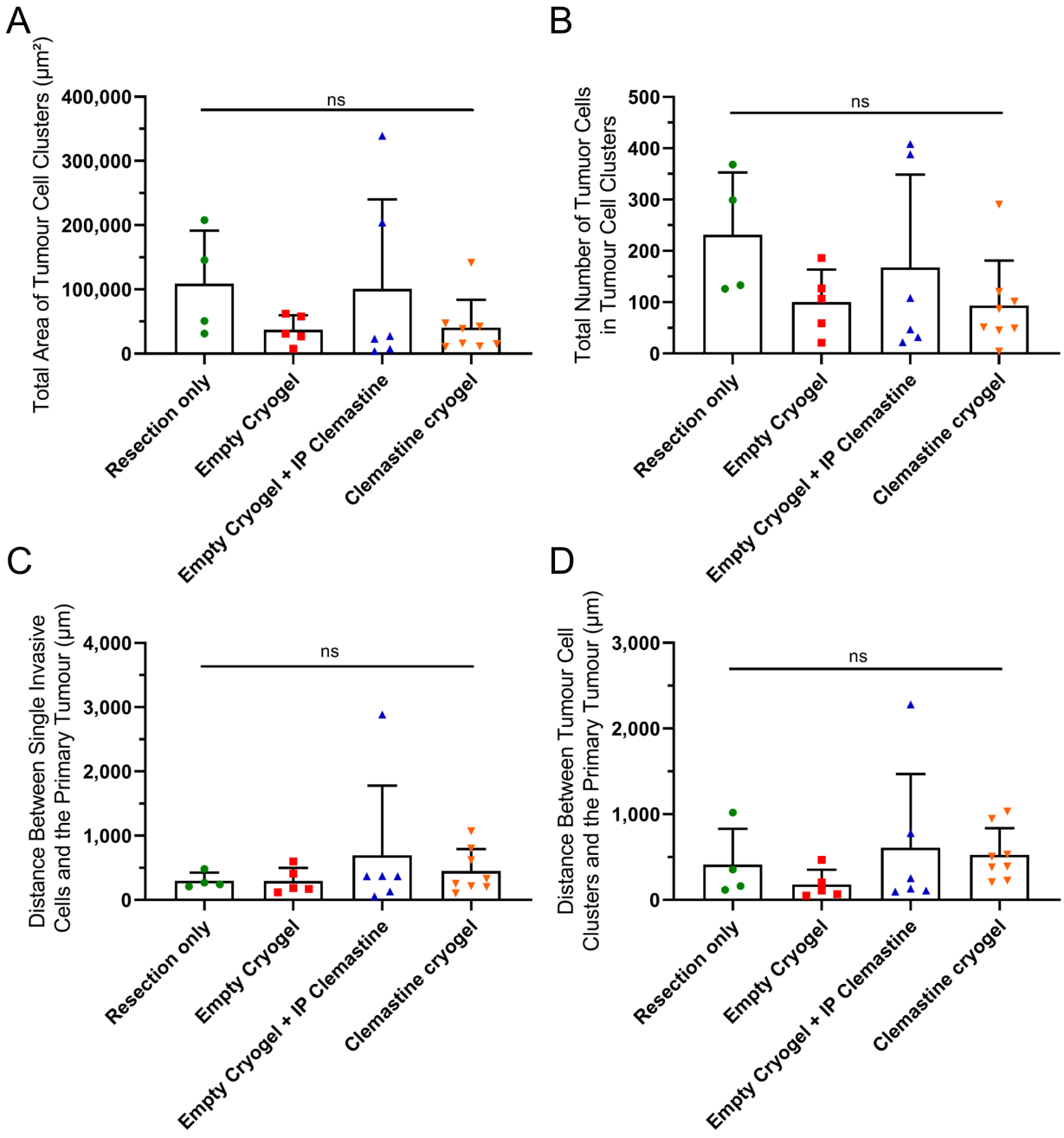

Figure 2-21 Analysis of the capability of GBM cell invasion.

(A) Total size of tumour cell clusters in three brain sections. **(B)** Total number of cells in tumour cell clusters. **(C)** The average shortage distance between single invasive cells and the primary tumour. **(D)** The average shortage distance between the tumour cell clusters and the primary tumour. Resection only, n=4; Empty cryogel, n=5; Empty cryogel + IP clemastine, n=6; clemastine cryogel, n=8. Error bars represent the mean ± SD. Nonparametric Kruskal-Wallis test for all figures, ns = no significant difference.

3.10 Cryogel implantation does not induce an inflammatory response

GFAP is expressed exclusively in astrocytes, which is used as a protein marker corresponding to severe neural damage.(238) Astrocytes did not actively secrete GFAP under physiological conditions, but intracerebral bleeding caused rapid release of GFAP.(239) GFAP expression level was commonly used to estimate the inflammatory response after implanting biomaterials.(240) Recent studies suggested that GFAP might also be used as a diagnostic biomarker of GBM.(241-243) However, the prognostic value of GFAP remains controversial. Some studies showed that high GFAP blood levels led to poorer survival times.(244, 245) Other studies noticed that blood GFAP levels could not help to predict the overall survival time and GBM recurrence.(246, 247)

Figure 2-22 (A) shows a representative coronal section stained with GFAP in the empty cryogel plus IP injection clemastine treatment group. The GFAP-positive staining area was concentrated in the primary tumour/surgical resection area. To analyse GFAP staining, the area fraction of positive GFAP staining area was measured as a semi-quantitative method. The ratio of the GFAP positive staining area fractions on the ipsilateral side versus the contralateral side was calculated for every coronal section, and the GFAP expression on the contralateral side was used as the standard level to normalize the fluorescence intensity among different brain sections. As shown in **Figure 2-22 (B)** and **(C)**, the ratio of the GFAP positive staining area fractions did not have significant difference among the four treatment groups neither in brain sections with resection cavity (p=0.5548) nor in anterior brain sections (p=0.6283). As the tumour progress was similar, these results indicated that cryogel implantation did not induce extra neural damage compared to mice treated with tumour resection only. The data of GFAP positive staining area fractions is shown in **Figure 2-23**.

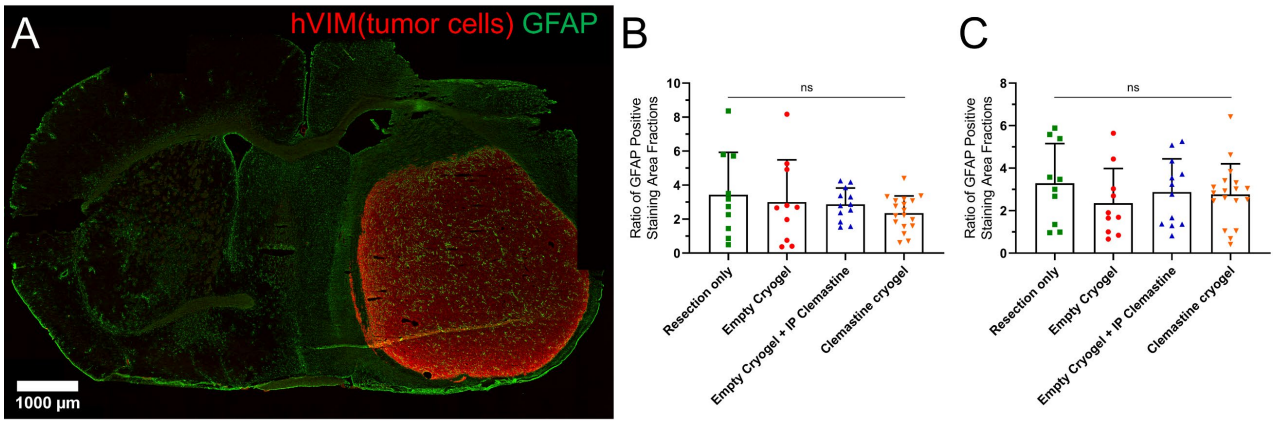

Figure 2-22 Cryogel implantation does not elevate the GFAP expression.

(A) Representative whole coronal section micrographs of murine brain treated by empty cryogel plus IP clemastine with GFAP staining. The ratio of the GFAP positive staining area fractions in the

ipsilateral side of the brain with surgical resection versus the contralateral side of the brain **(B)** for the sections with resection cavity, **(C)** for the anterior sections. Resection only, n=10; Empty cryogel, n=10; Empty cryogel + IP clemastine, n=12; clemastine cryogel, n=18; error bars represent the mean ± SD. Welch ANOVA tests: **(B)**, Ordinary one-way ANOVA test: **(C)**, ns = no significant difference.

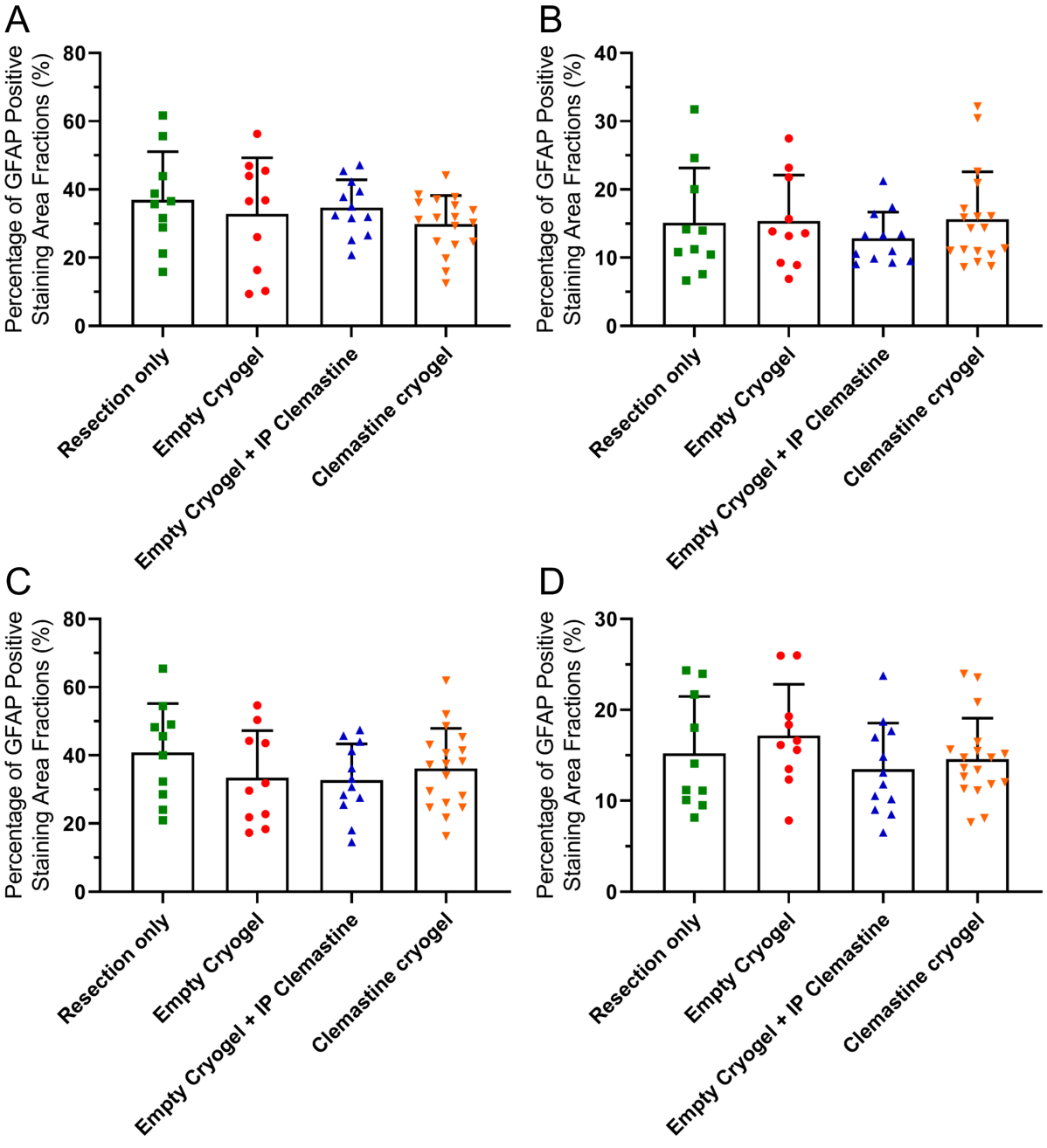

Figure 2-23 Data of GFAP positive staining area fractions.

GFAP positive staining area fractions of brain sections with resection cavity **(A)** in the ipsilateral side of the brain and **(B)** in the contralateral side of the brain. GFAP positive staining area fractions of anterior brain sections **(C)** in the ipsilateral side of the brain and **(D)** in the contralateral side of

the brain. Resection only, n=10; Empty cryogel, n=10; Empty cryogel + IP clemastine, n=12; clemastine cryogel, n=18. Error bars represent the mean ± SD.

IBA1 staining is used to evaluate the microglia activation.(248) IBA1 is localized in the cytoplasm and nucleus, which is relevant to the rearrangement of the actin cytoskeleton.(249, 250) Microglia activation is the process where microglia cells become activated due to infection or injury.(251) Although activated microglia cells can kill tumour cells, growth factors, and cytokines secreted by these cells, such as epidermal growth factor and interleukin 6, can also promote tumour growth and invasion, especially for GBM.(252, 253) Moreover, active microglia cells led to neuron cell death via coactivating of Toll-like receptor 4 and interferon-gamma or inducing neurotoxic reactive astrocyte formation.(254, 255) IBA1-positive microglia is used as a biomarker for analysing the inflammatory response.(256)

A representative coronal section stained with IBA1 from the empty cryogel treatment group is shown in **Figure 2-24 (A)**. The active microglia cells were concentrated around the surgical resection cavity. The microglia activation was mild in the contralateral side of the brain. The ratio of IBA1 positive staining area fraction after normalizing to the contralateral side did not have significant difference in brain sections with resection (**Figure 2-24 (B)**, p=0.4334) or anterior brain sections (**Figure 2-24 (C)**, p=0.8165). The cryogel did not stimulate the microglia activation over and above that of the mice with resected tumours only, which further confirmed the biocompatibility of the cryogel. **Figure 2-25** shows data of IBA1 positive staining area fractions in the ipsilateral side or the contralateral side of the brain.

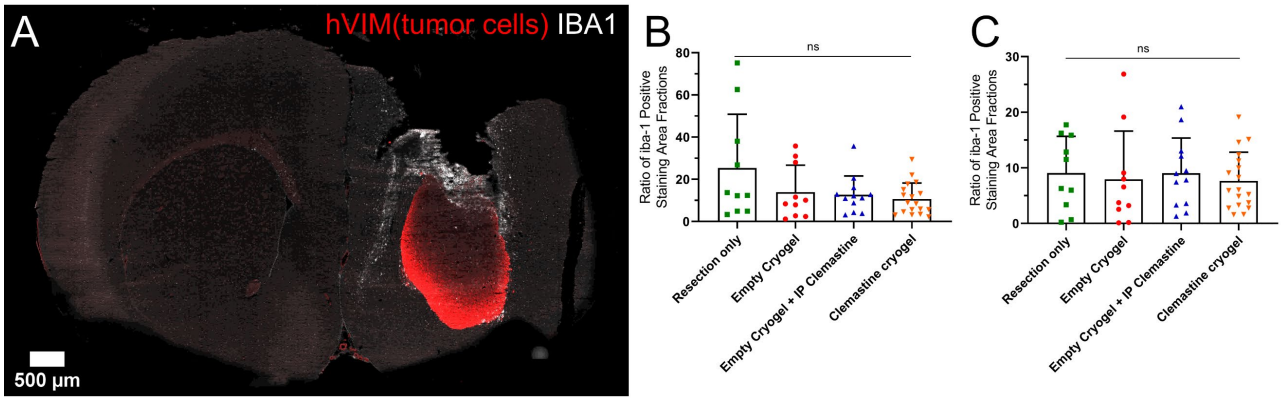

Figure 2-24 Cryogel implantation does not elevate the IBA1 expression.

(A) Representative whole coronal section micrographs of murine brain treated by empty cryogel with IBA1 staining. The ratio of the IBA1 positive staining area fractions in the ipsilateral side of the brain with surgical resection versus the contralateral side of the brain **(B)** for the sections with

resection cavity, **(C)** for the anterior sections. Resection only, n=10; Empty cryogel, n=10; Empty cryogel + IP clemastine, n=12; clemastine cryogel, n=18; error bars represent the mean ± SD. Nonparametric Kruskal-Wallis test: **(B)** and **(C)**, ns = no significant difference.

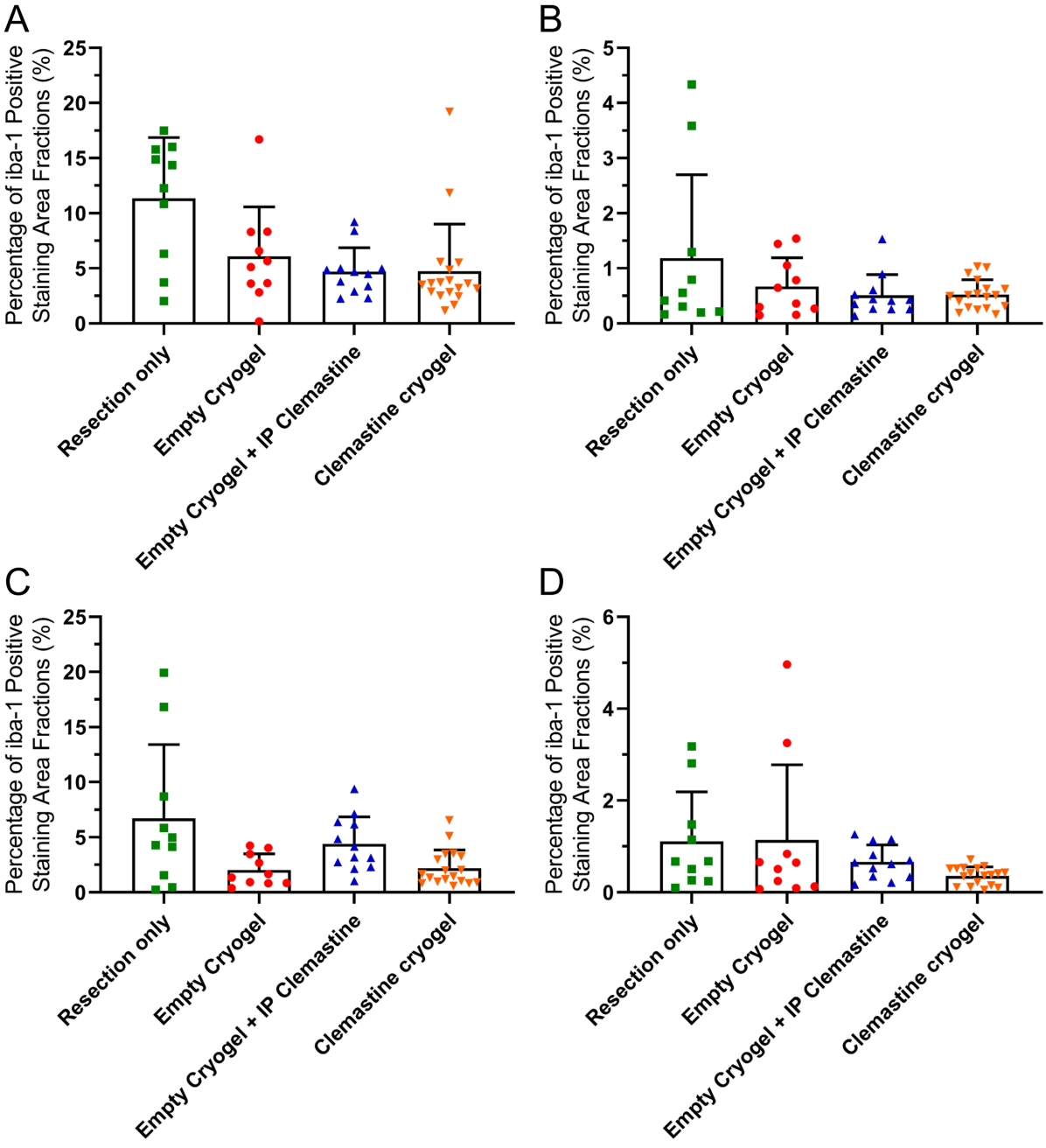

Figure 2-25 Data of IBA1 positive staining area fractions.

IBA1 positive staining area fractions of brain sections with resection cavity **(A)** in the ipsilateral side of the brain and **(B)** in the contralateral side of the brain. IBA1 positive staining area fractions of anterior brain sections **(C)** in the ipsilateral side of the brain and **(D)** in the contralateral side of the brain. Resection only, n=10; Empty cryogel, n=10; Empty cryogel + IP clemastine, n=12; clemastine cryogel, n=18. Error bars represent the mean ± SD.

This animal study mainly focused on the suppression of invasive GBM cells after clemastine local treatment and the host response to cryogel implantation. The large highly variable primary tumours formed after 14 days of the surgery, showing the common GBM recurrence. Despite clemastine treatment reducing the amount of single invasive tumour cells, it failed to suppress the growth of the bulk primary tumours. These results also suggest that the surgery might still dominate the therapeutic efficacy rather than the following clemastine treatment. So, a combined therapy for clemastine, such as a chemotherapeutic, might be needed to eradicate the residual tumour cells. On the other hand, the dosage of local treatment also limited the therapeutic efficacy. The animals cannot afford a high dosage of clemastine after the surgical tumour resection, which makes long-lasting therapeutic efficacy nearly impossible. However, the immediately started local treatment did not induce other adverse effects, and administrating a tiny amount of drugs locally got a similar tumour progress compared to the high-dosage systemic treatment, suggesting the importance of early treatment and high drug delivery efficiency. One advantage of the local treatment is bridging the gap of for waiting the wound to heal before starting the chemoradiotherapy.(257) If animals received the systemic treatment combined with local treatment, the therapeutic efficacy might be better. Additionally, the negatively charged SPA cryogel is a versatile drug delivery system able to bind various positively charged drugs and proteins. It is worth investigating delivering other therapeutics together, such as oncology drugs, repurposed drugs, or proteins for immunotherapy.

4. Conclusions

In this chapter, I designed 3D-printed templates for creating cylindrical cryogels used for rat/mouse tumour resection cavities. The size expansion ratio of cryogels with different formulations was determined to guide the design of the templates. The cryogels had a soft but robust structure, fitting the mechanical property of the brain tissue while being easy to handle. DOX and clemastine were loaded into the cryogels with high loading efficiency and loading capacity, suggesting the versatility of a drug delivery platform. Cryogels loaded with a high amount of DOX sustained released drugs for 53 days, but cryogels loaded with a small amount of DOX had a rapid release pattern. Clemastine cryogels showed a burst release in the first two days and a small part of the drugs were sustained released after that. Empty cryogels had good cytocompatibility and clemastine cryogel delayed killing hGBM cells. The results of the *in vivo* study confirmed the biocompatibility of the cryogel implantation by body weight monitoring and IHC analysis of GFAP staining and IBA1 staining. Empty cryogel, clemastine cryogel and systemic clemastine plus empty

cryogel implantation showed the similar reduction in the single invasive tumour cells. The variability in the extent of surgical resection may act as a confounding factor, affecting the number of the invasive GBM cells. Together with these results, although a potent therapeutic agent is required to be discovered, cryogel is a promising soft biomaterial for local drug delivery into the brain.

Chapter 3: Designing cryogel microcarriers as a drug delivery vehicle to locally treat glioblastoma

1. Introduction

Cryogels are a type of polymeric material with large, interconnected pores. The high porosity creates a high surface area to volume ratio for the interaction between the cryogel scaffold and surrounding molecules, allowing many potential applications in biomedical sciences such as cell culture,(258) tissue engineering,(259) bioreactors,(260) and wound healing.(261) Traditionally, particle crystallization or immiscible liquid droplets have been used as porogens to prepare macroporous networks.(262, 263) However, these methods encounter challenges in ensuring adequate interconnectivity and completely removing porogens.(264) Cryogelation is a process where polymeric materials are crosslinked around the ice crystals under semi-frozen conditions, which ice crystals serve as porogen in this scenario.(265) This process streamlines the production of interconnected macroporous polymer materials, making cryogels increasingly attractive in recent years.

One advantageous property of cryogels is their shape retention. Cryogels can be easily prepared as customized shapes and recover the shape after passing through a needle of much smaller diameter than the cryogel itself.(266) For example, a cylindrical shape cryogel (5 mm in diameter, 2 mm in height), or a rectangular shape cryogel (9*6*1.5 mm) could easily pass through a much smaller needle (16 gauge size, 1.194 mm inner diameter).(144) This property therefore allows more flexibility in the material design whilst still allowing injectability of the scaffold.(267) To prepare cryogels with well-defined dimensions, a template or mold is usually used to hold the precursor solution for freezing and crosslinking.(175) However, it is difficult and time-consuming to prepare tens of thousands of microscale cryogels of the same size by this method. Droplet-based microfluidics allows the generation of monodispersed emulsions.(176) The size of the droplets is tightly controlled by the design of the microfluidics device and the flow rate of the dispersed phase and continuous phase. Herein, we leveraged this technique to prepare cryogels on a microscale with a narrow size distribution, named cryogel microcarriers (MCs).

Conventional drug administration, systemic with repeat administration, usually results in a high proportion of off-target drugs and side effects.(268) Ideally, therapeutic agents could be delivered to tissues with control over time and space. Less frequent drug administration has been shown to enhance patient compliance, improve effectiveness, and potentially reduce adverse effects and healthcare costs.(269, 270) For intracranial drug delivery, it could also improve the applicability

and reduce the need for logistic support. So, it is crucial to develop a drug delivery system (DDS) with long-term sustained drug release for glioblastoma (GBM) local treatment.

Affinity-based DDS attenuates the diffusion of the therapeutics through the polymeric matrix and controls the release rate by reversible interactions between the therapeutics and a binding ligand.(271) The high surface area to volume ratio of the cryogel facilitates the affinity-based controlled release by providing a higher density of the binding ligand. Hydrophobic interactions, van der Waals forces, electrostatic interactions, and hydrogen bonding are the four main types of affinities utilized for affinity-based DDS.(272) For hydrophobic associations, cyclodextrin and π-π stacking interactions are used to incorporate the drugs into DDS.(235, 273) The π-π stacking interaction is the interaction between aromatic groups containing π bonds which includes edge-to-face stacked, edge-to-face stacked, and face-to-surface stacked.(274) Liu *et al*. loaded Doxorubicin (DOX) on PEG-functionalized single-walled carbon nanotubes by a π-π stacking interaction.(275) In another study, the π-π stacking interaction between DOX molecules was used to encapsulate free drugs and assemble the micelles.(276) Liang *et al*. utilized π-π stacking interaction to prepare DOX self-assembled polymeric micelles that the terminal of poly(ethylene glycol)-poly(lactic acid) was modified by cinnamic acid, 7-carboxymethoxy coumarin or chrysin.(235) The π-conjugated moieties modification improved the drug loading efficiency, slowed down the release rate, and enhanced the *in vivo* antitumor efficacy. On the other hand, electrostatic interactions are a simple way for molecular binding, depending on the different charges between the polymeric material surface and the drug molecules. This non-specific attraction allows simultaneous delivery of multiple drugs in one vehicle.(277) The sulfonic group in 3-sulfopropyl acrylate provides negative charges, and the cryogel made by this monomer is effectively loaded with positively charged proteins and dyes.(208, 278) We hypothesized that negatively charged MCs could be utilized as a universal drug delivery platform to deliver positively charged drugs. We selected two chemotherapeutics, venetoclax and DOX, and two repurposed drugs, brexpiprazole and vortioxetine, with potential anti-GBM efficacy,(118) which are all positively charged compounds, to investigate the loading efficiency and release profiles (**Figure 3-1**).

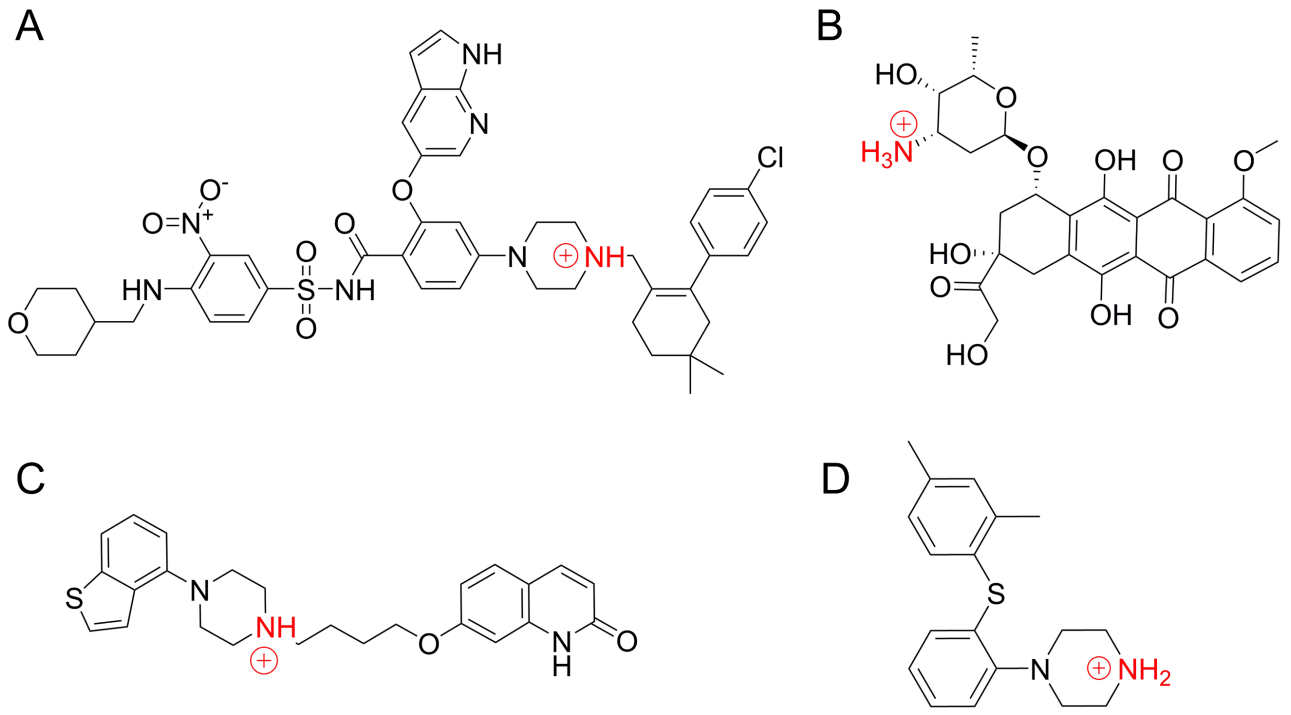

Figure 3-1 Structures of drug molecules with protonated amines under physiological conditions (pH 7.4).

(A): venetoclax, **(B)**: DOX, **(C)**: brexpiprazole, **(D)**: vortioxetine.

Brexpiprazole, vortioxetine and DOX are introduced in either Chapter 1 or Chapter 2. Venetoclax is a small molecular inhibitor targeting B-cell lymphoma-2 (BCL-2) for the treatment of chronic lymphocytic leukaemia (CLL).(279) The survival of CLL cells highly depended on the expression of BCL-2.(280) Venetoclax induced cell apoptosis via activating caspases-9 and caspases-3, meanwhile cleaving the caspase substrate and poly(ADP)ribose-polymerase.(281) Research showed that venetoclax had high activation in *TCF3-HLF*-positive acute lymphoblastic leukaemia (ALL), which suggested it could become an option for the treatment of paediatric ALL.(282) The results of a Phase II clinical trial showed that venetoclax had robust activity and good tolerability in CLL patients recurrent or refractory to ibrutinib and idelalisib.(283) One-year progress-free survival was 72% and overall survival was 90%. BCL-2 family protein (such as BCL-2, BCL-xL, and BCL-W) inhibitors demonstrated the ability to induce cell apoptosis in GBM cell lines, including LN229 and A172 treated with ABT-737 and ABT-263 (navitoclax),(284) and U87MG treated with ABT-263.(285) Rahman *et al*. found that radiation or TMZ exposure of GBM cells could induce selective vulnerability to BCL-2 inhibitors such as venetoclax.(286)

Aims:

This chapter aims to create negatively charged MCs by microfluidics, investigate the drug loading capacity and drug loading efficiency of four drugs (DOX, venetoclax, brexpiprazole and vortioxetine), evaluate the drug release patterns, test the cytocompatibility of empty MCs on primary human astrocytes and anti-GBM efficacy of brexpiprazole MCs. We hypothesize that drugs with a positive charge under normal physiological conditions (pH=7.4) could bind with the negatively charged sulfonate groups and the electrostatic interaction between the drug and the sulfonate groups could control the drug release.

2. Materials and methods

2.1 Chemicals and materials

The chemicals and materials used in this chapter are shown in **Table 3-1**. Chemicals were used without any further purification. **Table 3-2** shows the equipment used in this chapter.

Table 3-1 List of chemicals and materials

Chemicals and Materials	Company	Catalog number
Poly(ethylene glycol) diacrylate 700 (PEGDA700)	Sigma	455008
3-sulfopropyl acrylate potassium salt (SPA)	Sigma	251631
Sodium 4-vinylbenzenesulfonate (VBS)	Sigma	94904
Lithium Phenyl(2,4,6-trimethyl-benzoyl)phosphinate (LAP)	TCI	L0290
Phosphate-buffered saline (PBS)	Gibco	10010023
Bovine serum albumin (BSA)	Sigma	SLCD6757
Dimethyl sulfoxide (DMSO)	Sigma	D2650
Absolute ethanol	Fisher Chemical	E/0600DF/15
Acetone	Fisher Chemical	A/0600/17
HFE-7500 engineered fluid	3M	7100025016
1H,1H,2H,2H-perfluoro-1-octanol (PFO)	Sigma	370533
008 Fluoro Surfactant	RAN Biotechnologies	038-074
DOX	LC-Laboratories	D-4000
Venetoclax	MedChemexpress	HY-15531
Brexpiprazole	MedChemexpress	HY-15780
Vortioxetine	TargetMol	ABIN6574672
Tween 80	Sigma	P4780
Eosin Y	Sigma	E6003
Sodium acetate trihydrate	Sigma	32318
Acetic acid	Sigma	27225
iFluor® 647	AAT Bioquest	1065

Table 3-2 List of equipment

Equipment	Company	Catalog number
Microfluidic pump	Imprint Landgraf Laborsysteme HLL GmbH	LA30
Microscope Primovert	Zeiss	491206-0002-000
High-speed camera	Phantom	C110

Immersion cooler	Huber	TC100E
OmniCure UV Curing System	Excelitas	S1500
InfiniteRX plate reader	Tecan	
Vortex mixer	Scientific industries	G560E
Orbital Shanker-incubator	Grant-bio	ES-20
Zeiss Sigam HD Field Emission Gun Scanning Electron Microscope	Zeiss	
BIO-RAD SC500 sputter coater	Quorum Technologies	
IRSpirit	Shimadzu	
Confocal microscope	Leica	TCS SP5

2.2 Preparation of MCs

The preparation method of MCs was adapted from a previously published protocol (**Figure 3-2**).(278) Briefly, 2% 008 Fluoro Surfactant (wt/v) was dissolved in the HFE-7500 oil as the continuous phase, and the formulation of the dispersed phase was described in **Table 3-3**. The nozzle size of the droplet generator chip was 140 µm (Fluidic 163, 10000004, Microfluidic ChipShop, Germany). The water-in-oil (W/O) emulsion was prepared at a flow rate ratio of 1.5 (900 µL/h for continuous phase and 600 µL/h for dispersed phase driven by LA30 syringe pump, Imprint Landgraf Laborsysteme HLL GmbH, Germany). An inverted microscope (Zeiss, Germany) with a high-speed camera (C110, Phantom, USA) was used to monitor the droplet generation. The W/O emulsion was collected in the absence of light after the droplet generation was stable and then freezing for 17 hours at -60°C in a precooled ethanol bath. MCs were crosslinked using Omnicure S1500 UV lamp (Excelitas, USA) by relevant intensity mode at 50% power (11.5 W/cm^2) for 3 minutes under frozen conditions. MCs were purified after the ice crystals were thawed. 160 mg MCs were washed with 750 µL 20% (v/v) PFO in HFE oil 3 times to remove the Fluoro Surfactant, and 1 mL HFE oil 3 times to remove the excess PFO. Then, 1 mL of deionized water was added to resuspended MCs, and the remaining HFE oil was removed from the bottom after the solution layered. Next, MCs were washed with 3 mL acetone 3 times to completely remove the HFE oil and 3 mL ethanol 3 times. MCs were transferred into pre-weighed 2 mL centrifuge tubes and were ready to be used after complete drying in the vacuum oven at room temperature.

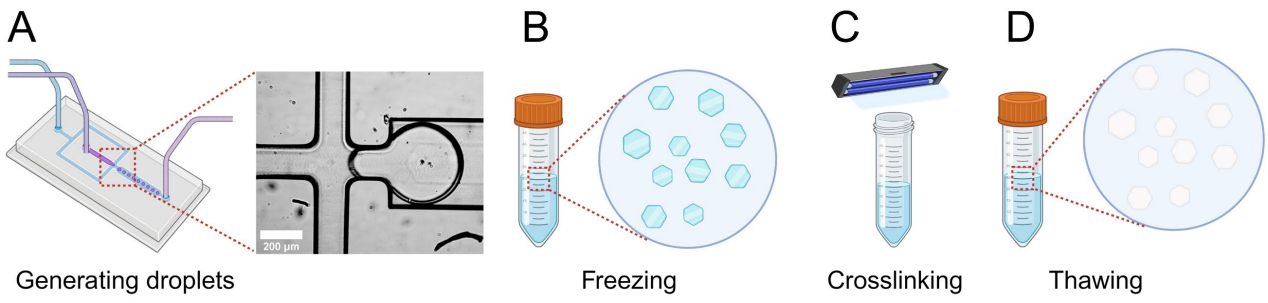

Figure 3-2 A schematic diagram shows the preparation of MCs by microfluidics.

(A) W/O emulsion is generated by microfluidics. **(B)** Ice crystals form inside the droplets. **(C)** Monomers are crosslinked under semi-frozen conditions. **(D)** Interconnected macropore structure is formed after ice crystals thaw. This figure was generated with Biorender.com.

Table 3-3 The formulation of the dispersed phase

Abbreviation	Formulation (molar ratio)	Solid content (wt/v)	PEGDA 700 (mg)	SPA (mg)	VBS (mg)	LAP (mg)	Volume of water (mL)
95SPA MCs	95% SPA / 5% PEGDA 700	8%	54.8	345.2		4.6	5
50SPA MCs	50% SPA / 50% PEGDA 700	8%	300.3	99.7		2.5	5
50VBS MCs	50% VBS / 50% PEGDA 700	8%	309.0		91.0	2.6	5

2.3 Morphological characterization of the MCs

The size distribution of MCs was evaluated using images captured through a light microscope. The microscope's scale was calibrated using a stage micrometre. Measurements of MC sizes were performed manually utilizing the ImageJ software.

Zeiss Sigam HD Field Emission Gun Scanning Electron Microscope (Zeiss, Germany) was used to visualize the structure of MCs. Completely dried MCs were coated with 10-20 nm AuPd by BIO-RAD SC500 sputter coater (Quorum Technologies, UK). Imaging of MCs was conducted using an Everhart-Thornley detector, with a beam energy of 5 kV and a final aperture diameter of 30 µm.

To prepare fluorescently labelled MCs, 5 µg/mL iFluor® 647 was added into the dispersed phase solution. Samples were scanned by TCS SP5 confocal microscope (Leica, Germany) using a 633 nm laser, and a 3D series (“z stack”) was captured. 3D pore structure was reconstructed in ImageJ.

Infrared spectra of monomers and MCs were scanned using an IRAffinity-1S FTIR Spectrometer (Shimadzu, Japan). The background signal was scanned before running each sample to subtract any residual peaks from the instrument and the environment. FTIR spectra were scanned by transmittance mode from 500 cm^{-1} to 2500 cm^{-1} with a resolution of 0.9. MCs were dried completely to avoid any interference.

2.4 Detection and quantification of drug concentrations

2.4.1 Venetoclax

Venetoclax was detected by ultraviolet-visible (UV) spectrophotometry at 424 nm. The calibration curve method was used to calculate the drug concentration in samples. The linear range of the calibration curve was from 6.25 to 400 µg/mL. Samples were diluted from the 5 mg/mL stock

solution in pure DMSO. The medium used for dilution contained 5% (wt/v) Tween 80 due to the low solubility of venetoclax in water.

2.4.2 Brexpiprazole

Brexpiprazole was quantified using UV spectrophotometry at a wavelength of 325 nm. Drug concentrations were determined based on a calibration curve within the linear range of 0.39 to 50 µg/mL. Samples for building the calibration curve were diluted from the 5 mg/mL stock solution in pure DMSO. The medium used for dilution contained 5% (wt/v) Tween 80 as a solubilizer.

2.4.3 Vortioxetine

A fluorescence quenching method was used for vortioxetine detection.(228) Eosin Y and weak basic compounds can form a complex under weak acid conditions resulting in fluorescence quenching of eosin Y, so the concentration of the weak basic compounds could be determined by the change in fluorescence value.(287) The linear range of the calibration curve was from 0.4 to 8 µg/mL. The samples used to build the calibration curve were diluted by 0.2 M acetic acid buffer at pH 3.7 from the stock solution of vortioxetine at 10 mg/mL in pure DMSO. 300 µL vortioxetine samples, 300 µL 0.15 mg/mL eosin Y and 300 µL extra blank medium (the same as the medium in the samples to be tested) were added into one 2 mL centrifuge tube and mixed well by vortex mixer. The fluorescence was read in a 96-well plate by InfiniteRX plate reader (Tecan, Switzerland) using excitation and emission wavelengths of 306/539 nm. For samples to be tested, 300 µL sample solution, 300 µL 0.15 mg/mL eosin Y and 300 µL 0.2 M acetic acid buffer at pH 3.7 were added into one 2 mL centrifuge tube and mixed well by vortex mixer. The drug concentration was calculated by the calibration curve.

2.5 Analysis of drug loading capacity and efficiency

Dried MCs were resuspended in deionized water at 5 mg/mL. DOX stock solution (200 mg/mL in pure DMSO) was then diluted using deionized water to a certain concentration. To prepare drug loading samples, 100 µL MCs solution and 400 µL DOX solution were put into a 2 mL centrifuge tube and mixed well. Positive control without MCs was prepared to monitor the degradation of DOX. DOX was loaded at room temperature for 3 days in the absence of light. After the incubation, the drug concentration in the supernatant was detected, and the loading efficiency was calculated by subtracting the unloaded drugs. MCs were washed by PBS 3 times to remove the unloaded drugs.

Venetoclax solution at 500 µg/mL was diluted from the stock solution (5 mg/mL in pure DMSO) by 5% (wt/v) Tween 80 in pH 3.7 acetic acid buffer (0.1 M). The loading sample was mixed using 100 µL MCs solution and 400 µL venetoclax solution in a 2 mL centrifuge tube. Venetoclax was loaded at room temperature for 3 days or at 37°C with a gentle shake (80 rpm) for 3 or 7 days. A positive control sample (containing 400 µL venetoclax solution and 100 µL deionized water) was used to monitor the stability of the drug in the loading medium. After the incubation, the drug concentration in the supernatant was detected, and the loading efficiency was calculated by subtracting the unloaded drugs. MCs were washed using PBS 3 times to remove the unloaded drugs, remove Tween 80 and bring up pH to 7.4.

A brexpiprazole stock solution (5 mg/mL in pure DMSO) was diluted using 1% (wt/v) Tween 80 in pH 3.7 acetic acid buffer (0.1 M). Drug loading samples were prepared by mixing the MCs solution and brexpiprazole solution at a volume ratio of 1:4. To investigate how the weight ratio of brexpiprazole to MCs affected the drug loading efficiency, brexpiprazole concentrations in drug loading samples were changed, but the amount of drugs and the concentration of MCs were kept constant. Detailed data on drug loading sample preparation is shown in **Table 3-4**. Next, the weight ratio of the drug to MCs was kept constant at 1:1, but the amount of drug was changed to investigate whether the volume of the loading medium would affect the drug loading efficiency. One control sample was prepared for each loading condition by adding the same volume of deionized water to replace the MC solution to monitor the stability of the drug solution. After incubating at 37°C for 3 days in an orbital shaker incubator (ES-20, Grant-bio, UK) with 80 rpm shaking, drug concentrations in the supernatant were detected, and the loading efficiency was calculated by subtracting the unloaded drugs. MCs were washed with PBS 3 times to remove the unloaded drugs, remove Tween 80, and bring up pH to 7.4.

Table 3-4 Detailed information on drug loading sample preparation

Weight ratio of drug to MCs	The amount of drugs (µg)	The amount of MCs (µg)	Drug concentration in loading medium (µg/mL)	Volume of drug loading medium (µL)	Volume of MCs solution (µL)	Volume of drug solution (µL)	Drug concentration in prepared solution (µg/mL)
1:5	100	500	200	500	100	400	250
2:5	100	250	400	250	50	200	500
3:5	100	167	600	167	33	134	750
4:5	100	125	800	125	25	100	1000
5:5 (1:1)	100	100	1000	100	20	80	1250
6:5	100	83.3	1200	83.3	16.7	66.7	1500
1:1	25	25	1000	25	5	20	1250
1:1	50	50	1000	50	10	40	1250

1:1	150	150	1000	150	30	120	1250
1:1	200	200	1000	200	40	160	1250

Vortioxetine stock solution (10 mg/mL in pure DMSO) was diluted to 500 µg/mL solution by pH 3.7 acetic acid buffer (0.1 M). 100 µL MCs solution and 400 µL drug solution were mixed in a 2 mL centrifuge tube to prepare drug-loading samples. Vortioxetine was loaded either at room temperature without shaking or at 37°C with a gentle shake (80 rpm). After the incubation, the drug concentration in the supernatant was detected, and the loading efficiency was calculated minus the unloaded drugs. MCs were washed by PBS 3 times to remove the unloaded drugs and bring up pH to 7.4.

2.6 Evaluation of *in vitro* drug release profiles

To evaluate drug release profiles, a certain volume of drug-loaded MCs was put into a 1.5 mL centrifuge tube and a release medium was added to reach up to 1 mL. PBS containing 0.3 mg/mL BSA was used as a release medium for DOX studies, which mimicked the protein concentration in the brain. 1% or 5% (wt/v) Tween 80 in PBS was used as a release medium for brexpiprazole studies and pure PBS was used as a release medium for vortioxetine studies. The samples were put into the incubator at 37°C with gentle shaking at 80 rpm (in the absence of light for DOX studies). At each time point, 900 µL supernatant was removed and replaced by fresh release medium. The samples were stored at -20°C for further investigation. At the end of the experiment, the concentration of drugs in all samples was detected. The amount of drug released is calculated by the following equation 3-1.

$$m_n = \begin{cases} c_n * V_{Total} & (n = 1) \\ c_n * V_{Total} + V_{Replaced} * \sum_{i=1}^{n-1} c_i & (n > 1) \end{cases}$$

Equation 3-1. Where, m_n is the cumulative release amount of the nth time point (µg). c_n is the drug concentration of the nth time point (µg/mL). V_{Total} is the total volume of the release medium. $V_{Replaced}$ is the volume of the removed and replaced medium at each time point.

2.7 Cell culture

Patient-derived GBM stem cell lines (hGBM L0, L1, and L2) and primary human astrocytes were cultured and maintained as described in Chapter 2 section 2.9.

2.8 Analysing the cytocompatibility of empty MCs

The cytocompatibility of empty MCs was evaluated using primary human astrocytes. Empty MCs were incubated at 37°C in pH 3.7 acetic acid buffer (0.1 M) with 1% (wt/v) Tween 80 at a concentration of 1000 µg/mL for 3 days to match the drug loading conditions. Primary human astrocytes were seeded in poly-L-lysine coated 48-well plates (Costar, 3548) at a density of 4800 cells/well. After one day of incubation, empty MCs were added at a final concentration of 100 µg/mL. Images of cells were taken by microscope camera during the incubation (E3ISPM, microscience Ltd., UK) and the cell viability was tested by the PrestoBlue assay after 1, 4, and 7 days of adding empty MCs and normalizing to untreated control cells (background fluorescence was subtracted from experimental wells). Cells were incubated in PrestoBlue for 2 hours and fluorescence intensity was read with 560 nm wavelength excitation and 590 nm wavelength emission.(233)

2.9 Cytotoxicity of free brexpiprazole

To investigate the cytotoxicity of free brexpiprazole, primary human astrocytes were plated in poly-L-lysine coated 96-well plates (Costar, 3595) at a density of 1,600 cells/well, and hGBM stem cells were plated in Geltrex coated 96-well plates at a density of 5,000 cells/well. After one day of incubation, brexpiprazole solution was added, which was prepared by serial dilution from 5 mg/mL stock solution in pure DMSO using the complete culture medium. The cell viability was tested using the PrestoBlue assay after 1, 4, and 7 days of adding drugs.

2.10 Anti-GBM efficacy of brexpiprazole MCs in 2D cell culture model

The *in vitro* anti-GBM efficacy of brexpiprazole MCs was first investigated on a 2D monolayer cell culture model. The hGBM L0, L1, and L2 cells were cultured in Geltrex-coated 48-well plates. GBM cells were seeded at a density of 15,000 cells/well, and drugs were added on the second day at a final concentration of 100 µg/mL for empty MCs; 2.5, 10, 25, 50, and 100 µg/mL for brexpiprazole MCs; and 2.5 µg/mL for free drug. The morphology of cells was imaged, and the cell viability was analysed by PrestoBlue assay on Day 2, 5, and 8.

2.11 Anti-GBM efficacy of brexpiprazole MCs in 3D spheroid model

A 3D spheroid cell culture model was established by using ultra-low attachment 96-well plates (Costar, 7007). Briefly, hGBM L2 cells were seeded at a density of 1,000 cells/well. Well plates were centrifuged at 300 g for 5 minutes to force cells into forming spheroids. Cell spheroids were cultured for 4 days before the treatment. Brexpiprazole MCs were added at 2.5, 10, 25, 50 µg/mL,

and 2.5 µg/mL free drug was used as a control group. The size of the spheroids was analysed by microscope images in ImageJ on Day 4, 5, 6, 7, 8, and 11. On Day 5, 8, and 11, additional cultures of the spheroids were incubated with PrestoBlue for 3 hours to test the cell viability before reading the fluorescence intensity.

2.12 Statistical analysis

Statistical analysis was conducted as described in Chapter 2 Section 2.16.

3. Results and discussion

3.1 Preparation and characterization of MCs

A W/O emulsion was generated by droplet-based microfluidics to serve as the template for MC preparation. **Figure 3-3 (A)** shows the morphology of the droplets whose size was around 270 µm. **Figure 3-3 (B)** shows the morphology of MCs after purification and resuspending in deionized water. MCs had a narrow size distribution of 482.4 ± 35.1 µm (**Figure 3-3 (C)**). The size of MCs increased compared to the droplets, because of the volume expended when water got converted to ice and the low proportion of PEG, which formed the skeleton of MCs. As shown in **Figure 3-3 (B)**, the texture of MCs converged at one point. Variations in greyscale within the MCs may reflect differences in pore density. This could be attributed to the temperature gradient during freezing, where a localized region exposed to lower temperatures experiences a faster freezing rate, leading to smaller pore sizes.(288)

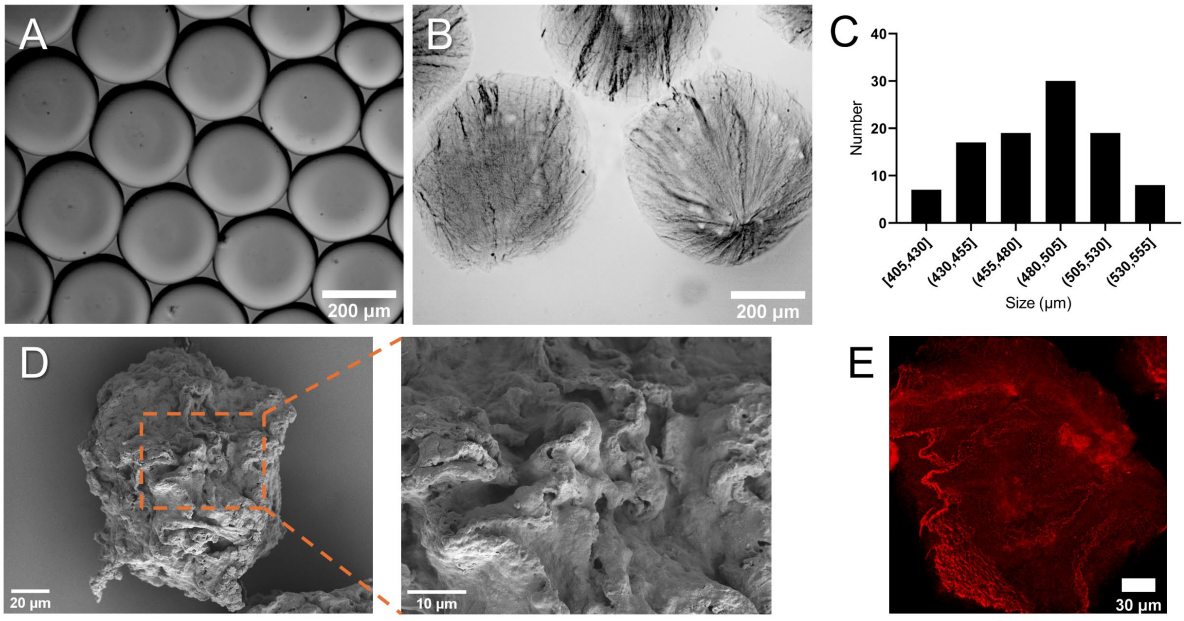

Figure 3-3 Morphological characteristics of MCs.

Representative bright field photos of **(A)** the droplets, and **(B)** the MCs after the crosslinking and purification. **(C)** shows the size distribution of MCs (n=100). **(D)** Representative SEM image and a component of the zoomed-in portion of a dehydrated MC. **(E)** Representative confocal microscope image of MCs shows the inner pore structure.

LAP was used as the photoinitiator for the synthesis of MCs, which has an absorbance peak at 375 nm and measurable absorbance in the visible light range from 400 nm to 420 nm.(289) Compared to the commonly used Irgacure 2959 photoinitiator, LAP catalysed the polymerization reaction ten times faster when using the same concentration of photoinitiator.(289) The higher molar extinction coefficient of LAP enables the usage of 365 nm UV light and 405 nm visible light in biomedical applications.(290) Despite LAP having good cytocompatibility, research showed that the cytotoxicity of LAP could be enhanced by exposure to 405 nm light, especially without a reactant, which might be because the generated free radicals interact with the cells.(291, 292) So, it is also crucial to remove the excess LAP after the cryogelation.

SEM images of MCs (**Figure 3-3 (D)**) show that the size of MCs shrunk to around 100 µm after dehydration. Due to the extremely low freezing temperature used for MC preparation, the resulting pore size was very small, rendering the macropore structure undetectable under SEM. Therefore, the hydrated MCs were visualized using a confocal microscope. **Figure 3-3 (E)** illustrates that the pore size was approximately 5-10 µm.

FTIR spectra confirmed a successful polymerization reaction, in which the sulfonate groups were incorporated in the MCs after the cryogelation. Specifically, **Figure 3-4** shows that the peak of the vinyl group at 1638 cm^{-1} (C=C stretching) almost disappeared and the peaks of the sulfonate group at 1040 cm^{-1} and 1170 cm^{-1} (S=O stretching) were present after the crosslinking. In addition, the intensity of the C=O stretching at 1720 cm^{-1}, SO_2 asymmetric stretching at 1040 cm^{-1}, and S-O symmetric stretching at 1170 cm^{-1} were reduced after the cryogelation.

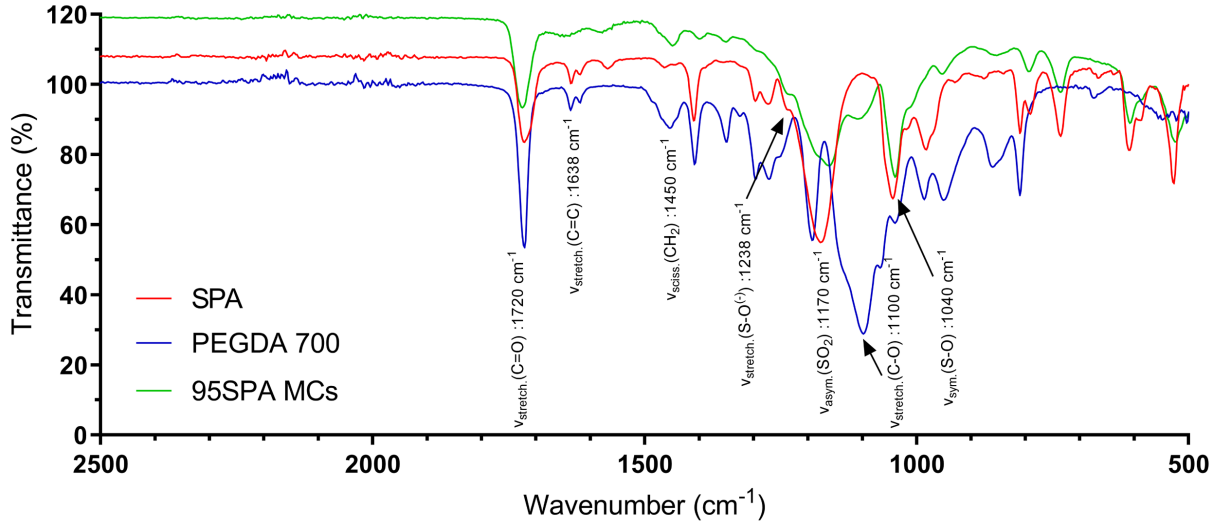

Figure 3-4 FTIR spectra confirm the complete polymerization reaction of 95SPA MCs.

3.2 Analysis of drug loading capacity and efficiency of MCs

3.2.1 High loading efficiency is achieved for DOX

The loading efficiency of DOX was tested by using 95SPA MCs, 50SPA MCs, and 50VBS MCs. The effect of MC concentration was investigated first on 95SPA MCs. As shown in **Figure 3-5 (A)**, the drug loading efficiency was almost the same when using 1 mg/mL or 2 mg/mL MCs to load the same amount of DOX. So, 1 mg/mL of MC concentration was chosen for the subsequent experiments because using a lower MC concentration achieved higher drug loading capacity.

Another monomer, VBS, was used to create MCs, and the results of DOX loading efficiency in VBS MCs are shown in **Figure 3-5 (B)**. The sulfonic group in VBS is covalently bonded to a phenyl group, which can stabilize the anion of the sulfonic group after losing the hydrogen ion (**Figure 3-5 (C)**). This stability improvement of sulfonic acid anion means the acidity of VBS is stronger than that of SPA. For the acrylate group in SPA, the vinyl group is covalently bonded to an ester group which can withdraw the electron of the vinyl group and make the vinyl group more sensitive to being attacked by the free radicals. Despite the vinyl group acting as an electron-donating group when it is covalently bonded to a phenyl group, this activity is very weak. Additionally, the sulfonic group in the para position withdraws the electron and transfers this effect through the conjugated system to the vinyl group, so VBS should be able to be polymerized via free radical reaction. However, MCs cannot be prepared using 95% VBS, which might be due to the lower chemical reactivity of the vinyl group than SPA. So, I decreased the proportion of VBS and successfully prepared 50VBS MCs, and 50SPA MCs were used as a comparison (**Figure 3-5 (D)**). For 50SPA MCs and 50VBS MCs, the density of negative charges was lower than 95SPA MCs, which meant a reduction in the loading

capacity and a lower DOX concentration was required. According to the results of DOX loading studies in the previous chapter, increasing the concentration of DOX benefited drug loading efficiency. So, to reduce the decreased range of DOX concentration in the loading medium, a higher MC concentration (2 mg/mL) was chosen to be used. The weight ratio of 1 to 4 of DOX to MCs (250 µg DOX and 1000 µg MCs) showed the highest loading efficiency both in 50SPA MCs and 50VBS MCs, which was selected for the subsequent experiments (**Figure 3-5 (B)**).

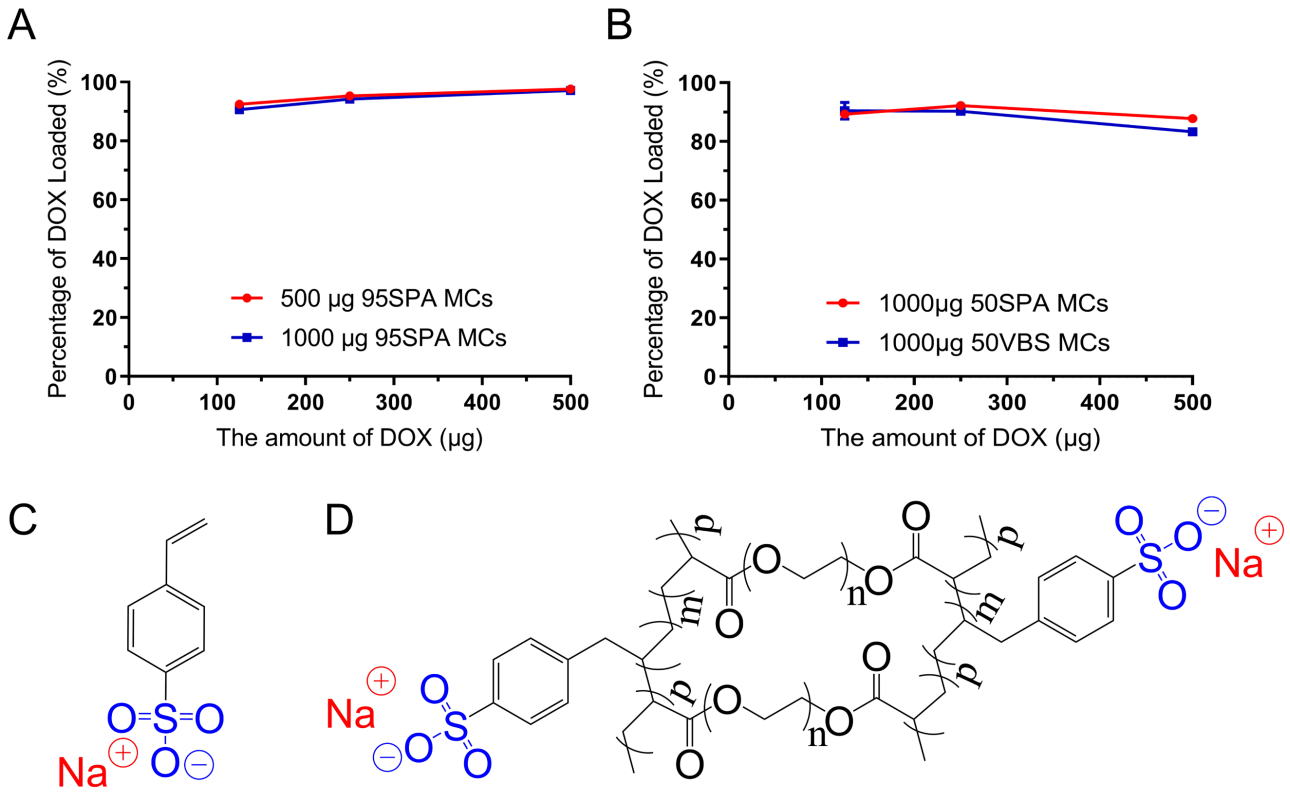

Figure 3-5 SPA MCs and VBS MCs effectively load DOX.

(A) shows the DOX loading efficiency in 95SPA MCs when altering the amount of DOX. **(B)** shows the DOX loading efficiency in 50SPA MCs and 50 VBS MCs when altering the amount of DOX. **(C)** The structure of VBS monomer. **(D)** The structure of PEGDA-co-VBS. **(A)** and **(B)**: n=3, error bars represent the mean ± SD.

3.2.2 The loading efficiency of venetoclax is limited

5% (wt/v) Tween 80 was added into the loading medium as a solubilizer due to the low solubility of venetoclax in PBS. Some pilot studies were done to test the loading efficiency of venetoclax in 95SPA MCs. As shown in **Figure 3-6**, venetoclax failed to be loaded into the 95SPA MCs in PBS (pH 7.4). I hypothesized that pH value could affect drug loading efficiency because only protonated drugs could bind with the negatively charged groups in the MCs, and more weak alkaline drugs could be protonated at lower pH values. 0.1 M acetic acid buffer was used to adjust the pH value of

the loading medium to 5.5 and 3.7. The results showed that pH 3.7 improved the drug loading efficiency by around 10% compared to pH 7.4 but failed to show significant difference. Next, the effect of temperature on drug loading was investigated. The higher temperature accelerates the thermal motion of the molecules, meaning higher chances for the drugs to bind with the negatively charged groups. Compared to the room temperature, the loading efficiency was significantly increased by around 13% at 37°C. Extending the loading period from 3 to 7 days increased the loading efficiency by around 9% without significant difference. However, even with the best conditions, less than 35% of venetoclax was loaded into the MCs. Because of this low loading efficiency, venetoclax was not taken forward for release studies.

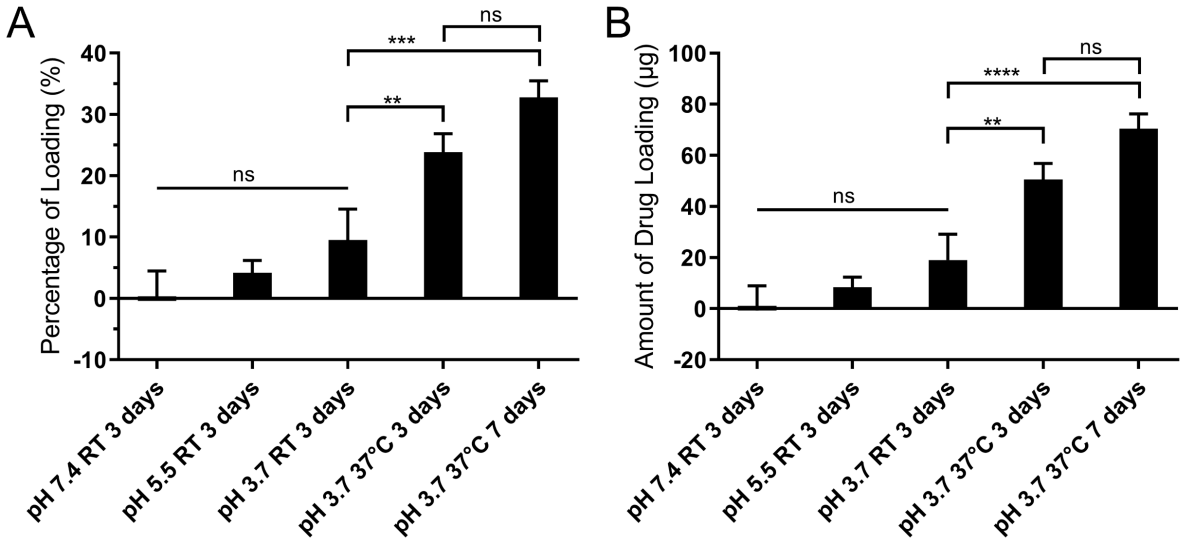

Figure 3-6 The loading efficiency of venetoclax in 95SPA MCs under various conditions.
(A) and **(B)** show the percentage and the amount of drug loading, respectively (n=3, error bars represent the mean ± SD. Ordinary one-way ANOVA test, ns = no significant difference, for ** $p \leq 0.01$, *** $p \leq 0.001$, **** $p \leq 0.0001$. Abbreviation: RT: room temperature).

3.2.3 MCs load brexpiprazole with high capacity and efficiency

The medium used for brexpiprazole loading was 1% Tween 80 in 0.1 M acetic acid buffer at pH 3.7. More protonated drug molecules existed under acidic conditions for weak alkaline compounds, which provided more chances for drug molecules to interact with sulfonate groups on the MCs. Furthermore, an increased proportion of ionic drug molecules enhanced the drug's solubility. To further augment solubility, 1% Tween 80 was employed as a solubilizer. However, adding too much solubilizer reduced the loading efficiency (92.2% ± 1.7% in 1% Tween 80 *vs* 83.6% ± 5.7% in 10% Tween 80). This might be because of the viscosity of the loading medium. A highly viscous solution could affect the thermal motion of the drug molecules. In addition, a higher concentration of

Tween 80 could mean more chances of Tween 80 molecules masking the sulfonate groups and interfering with the electrostatic interactions.

The drug loading capacity of MCs was investigated by changing the weight ratio of the drug to MCs, which was adjusted through the drug concentration in the loading medium while the MCs concentration was kept constant. As shown in **Figure 3-7 (A)**, drug loading efficiency rose by around 5% when the weight ratio increased from 1:5 to 2:5 (drug to MC). The loading efficiency remained stable at approximately 95% until the weight ratio reached 5:5 (1:1). However, the loading efficiency of 6:5 samples decreased to 81.4% ± 7.2%. For 100 µg MCs, the theoretical saturation point to load brexpiprazole was 161 µg. The reduction in loading efficiency was possibly due to the small volume of the drug loading medium (83.3 µL), which might limit the movement of MCs. The first increasing part of this curve suggested the limitation of drug loading via the electrostatic interactions mechanism. The equilibrium that positively charged drugs bound with the sulfonate groups in the MCs required a drug concentration gradient.

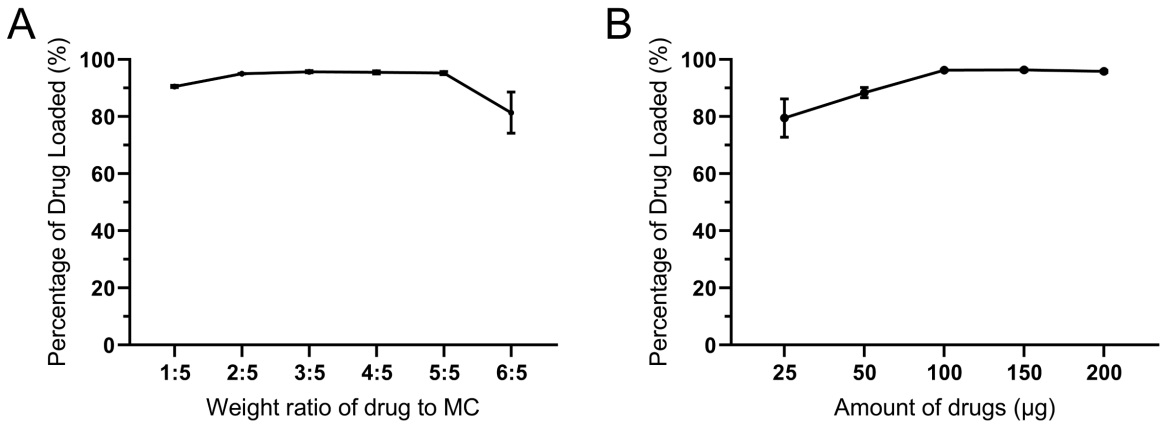

Figure 3-7 Brexpiprazole has high loading efficiency.

(A) shows the brexpiprazole loading efficiency with various weight ratios of drug to MCs from 1:5 to 6:5. Each sample contained 100 µg drug. **(B)** shows the brexpiprazole loading efficiency with various amount of the drug. The weight ratio of the drug to MCs was kept constant at 1:1. **(A)** and **(B)**: n=4, error bars represent the mean ± SD.

The weight ratio 5:5 (1:1) was selected for the next loading experiments because this weight ratio had both high loading efficiency and loading efficacy. A decrease in loading efficiency was observed when samples had less than 100 µg drug (100 µL loading medium, **Figure 3-7 (B)**). This experiment further confirmed that a small volume of loading medium affected the loading efficiency, and 100 µL loading medium might be the threshold.

3.2.4 Vortioxetine shows high loading efficiency

To load Vortioxetine, 0.1 M pH 3.7 acetic acid buffer without Tween 80 was used as the loading medium because I observed that Tween 80 affected drug detection (Eosin Y assay). The solubility of vortioxetine at pH 3.7 was 298.45 mg/mL (data calculated from Chemicalize), which was high enough for the drug loading and the drug solution under this condition was stable for at least 3 days. The results showed that around 95% of the drug was loaded into the 95SPA MCs, and the loading efficiency was not affected by the temperature (**Figure 3-8**).

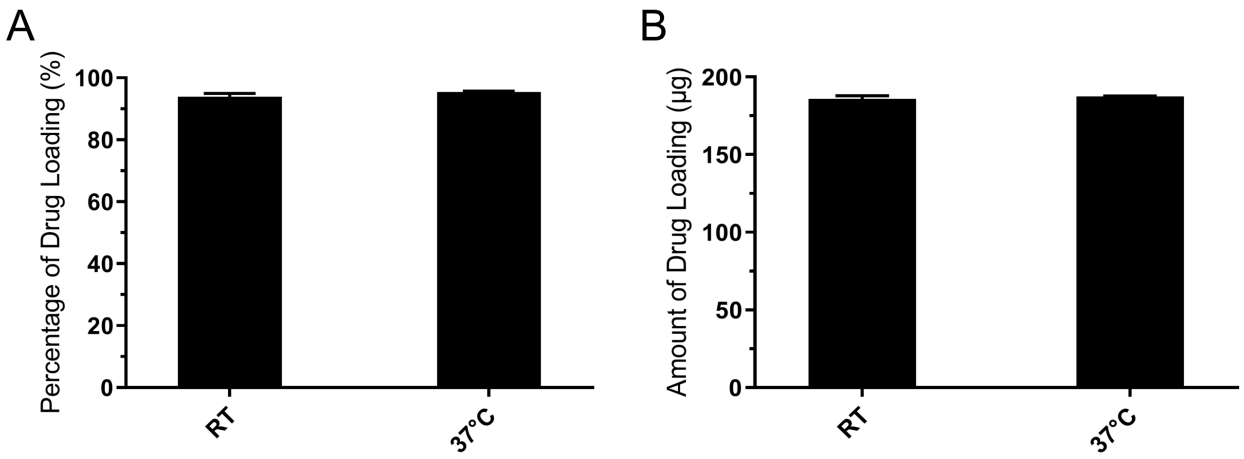

Figure 3-8 Vortioxetine has high loading efficiency in 95SPA MCs.

(A) and **(B)** show the percentage and the amount of drug loading, respectively (n=3, error bars represent the mean ± SD; abbreviation: RT: room temperature).

3.3 *In vitro* drug release profiles of drug-loaded MCs

3.3.1 MCs loaded with higher amount of DOX prolong the drug release period

To investigate the drug release profiles of DOX 95SPA MCs, the first drug release study was conducted with the MCs loaded with the different weight ratios of DOX, which were 1:2, 1:4, and 1:8. In this experiment, each sample contained 200 µg MCs. As shown in **Figure 3-9**, for the burst release in the first two days, 58.1% ± 2.2%, 38.8% ± 5.0%, and 23.7% ± 3.0% DOX were released from the MCs loaded with 25, 50 and 100 µg DOX, respectively, followed by a small part sustained released DOX. 25 and 50 µg samples stopped releasing on Day 5 and Day 12 respectively, while 100 µg samples continued releasing DOX until Day 14. This release pattern of DOX MCs matched that of DOX cylindrical cryogel in Chapter 2, in which the cryogel loaded with a higher amount of DOX sustained released drugs for a longer period. When MCs were loaded with less drugs, there were more available negatively charged groups in MCs, but MCs failed to retain the payload and slow down the release rate. The reason might be due to additional intermolecular forces among DOX

molecules such as π-π stacking. Only 37%-66% payloads were released from the MCs before no further drug release occurred. The remaining DOX might be precipitated/drug crystals generated during the drug loading. The release of this portion of the drugs is potentially controlled by the solubility equilibrium of DOX. These results suggest that a higher weight ratio of DOX to MCs prolongs the long-term sustained drug release, but the remaining unreleased DOX might be a hazardous factor to cause adverse effects. With that said, the release study *in vitro* only partially mimics in vivo conditions, so the true release extent in vivo is as of yet unknown.

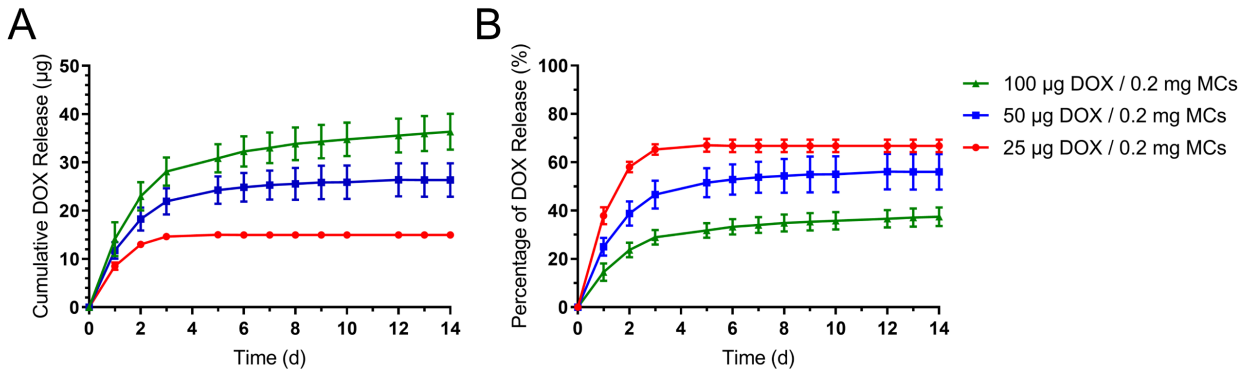

Figure 3-9 Increasing the weight ratio of DOX to MCs extends the DOX release period.
(A) and **(B)** show the amount and the percentage of cumulative DOX release, respectively (n=4, error bars represent the mean ± SD).

When the weight ratio of DOX to MCs increased to 1:1, the loading efficiency was maintained at a high level (over 95%). So, in the second experiment, the weight ratio of DOX to MCs was kept constant at 1:1 and samples containing various amounts of DOX from 5 to 100 μg were used to conduct a drug release study. Samples with more DOX cumulatively released a higher amount of the drug (**Figure 3-10 (A)**). However, as shown in **Figure 3-10 (B)**, the percentage of DOX release had a different pattern, in which the DOX release rate accelerated in samples with less drugs. 5 and 25 μg samples significantly released more proportion of payloads compared to 100 μg samples.

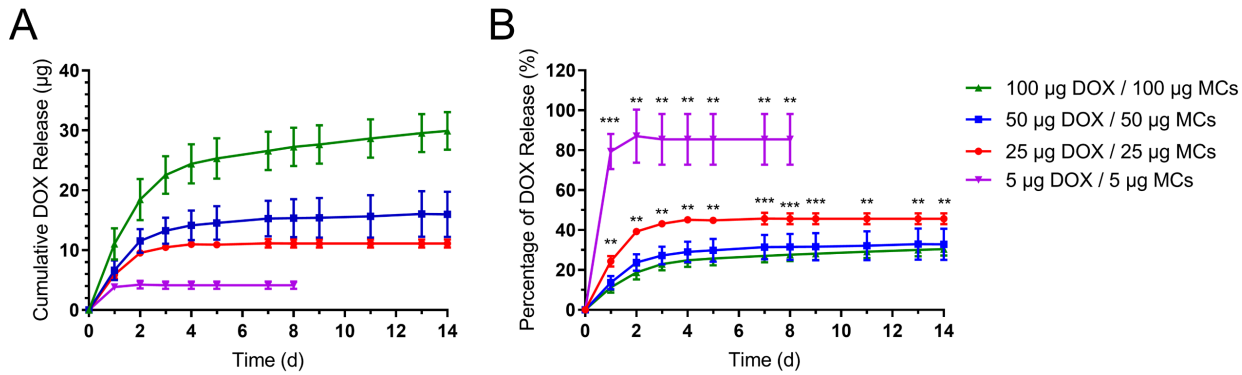

Figure 3-10 The amount of DOX in the release samples affects the drug release profiles. **(A)** and **(B)** show the amount and the percentage of cumulative DOX release, respectively (95SPA MCs loaded with 1:1 weight ratio of DOX; n=4, error bars represent the mean ± SD). Asterisks in **(B)** show the statistical significance of the percentage of DOX release compared to 100 μg DOX / 100 μg MCs samples (two-way ANOVA test).

The doses of DOX previously administered via local delivery in orthotopic GBM rat models ranged from 1-5 μg per animal.(69, 71, 83, 92) So, 5 μg samples were also selected for the evaluation of drug release profiles because 5 μg could represent a relevant dose for *in vivo* studies. However, for 5 μg samples, DOX was released very fast, and 79.3% ± 8.8% of DOX was released after only one day. These results revealed that the amount of DOX in the release samples affected the release rate. The solubility of DOX at pH 7.4 is 5.15 mg/mL (data from Chemicalize), meeting the requirements of sink conditions for 100 μg samples, which suggests that other factors play the key role to control the drug release. The difference of the concentration gradient generated by the released DOX might affect the intermolecular forces including electrostatic interactions and π-π stacking, which further controls the release rate. As mentioned-above, the precipitation/drug crystals of DOX in MCs generated during the drug loading at a high weight ratio should be easier to be released when the drug concentration is low in the medium. These might be the reasons of the rapid release pattern for 5 μg samples.

In the third DOX release study, release profiles were investigated on 50VBS MCs and 50SPA MCs. The phenyl group in VBS might provide π-π stacking interactions with DOX to increase the binding force and prolong the drug release. As shown in **Figure 3-11**, the release curves were nearly overlapping for 50SPA MCs and 50VBS MCs loaded with the same amount of DOX. Only the release from 100 μg samples on Day 1 had a significant difference, in which 27.0% ± 2.3% and 36.4% ± 1.8% DOX were released from 50VBS MCs and 50SPA MCs, respectively. For 5 μg samples, the drug release rate was still very fast, and 77.6% ± 9.7% of DOX were released from 50VBS MCs on Day 1. These results suggested that DOX release profiles did not improve by a slightly higher acidity of the monomer and the potential extra π-π stacking interactions.

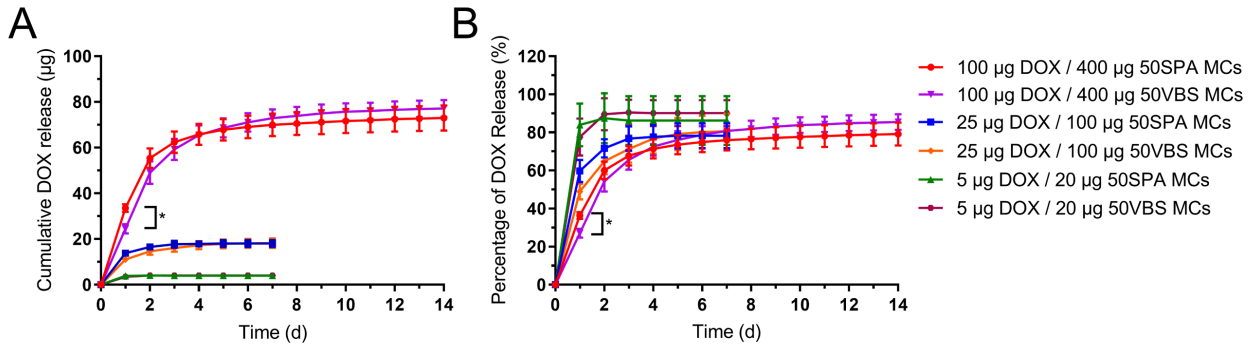

Figure 3-11 VBS MCs slightly improve the burst release of DOX.

(A) and **(B)** show the amount and the percentage of cumulative DOX release, respectively (n=4, error bars represent the mean ± SD; two-way ANOVA test, for * $p \leq 0.05$).

Because a higher weight ratio of drug to MCs improved the sustained release profiles and only a few micrograms of DOX could be administrated locally into the brain in animal studies, there might be some extra space in the resection cavity after implanting DOX MCs. Empty MCs could be used to fill the residual space of the resection cavity. So, in the fourth DOX release experiment, 5-45 µg empty MCs were added to the drug release samples. I hypothesized that the extra empty MCs might slow down the release rate because released DOX might bind with other MCs before becoming the free drug. However, results showed that most of the DOX was released within one day (**Figure 3-12**). Adding empty MCs did not decrease the release rate. It only resulted in the reduction of the total amount of released DOX, which might be because some of the released DOX were "reloaded" into the empty MCs, and they were never released again.

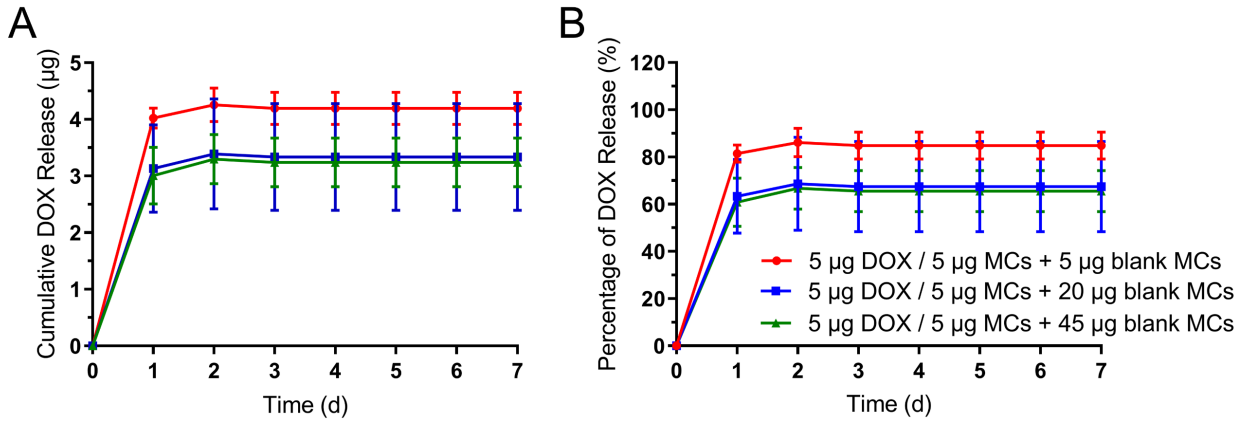

Figure 3-12 Adding blank MCs in the release samples results in the retention of DOX.

(A) and **(B)** show the amount and the percentage of cumulative DOX release, respectively (n=3, error bars represent the mean ± SD).

The total volume of cerebrospinal fluid in a rat is around 400-600 µL, and the production rate of cerebrospinal fluid is around 2.2 µL/min.(293, 294) So, the volume of release medium used in previous studies (1 mL) might not represent the real environment. In the fifth DOX release experiment, various volumes of release medium, from 100 to 1000 µL, were used to conduct the release study. As shown in **Figure 3-13**, changing the volume of the release medium only affected the total amount of DOX release, but did not alter the release pattern.

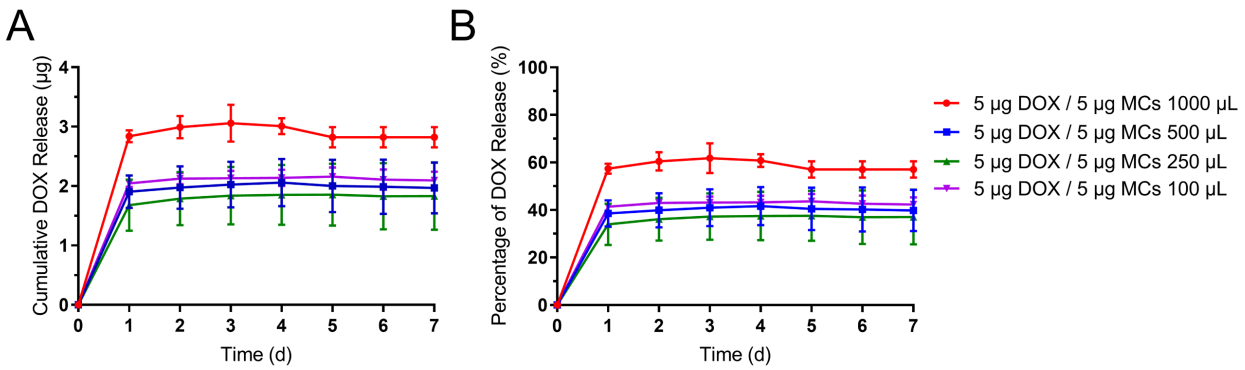

Figure 3-13 The volume of the release medium does not affect the DOX release profiles for MCs loaded with a small amount of DOX.

(A) and **(B)** show the amount and the percentage of cumulative DOX release, respectively (n=3, error bars represent the mean ± SD).

The effect of five parameters (weight ratio, amount of drug, type of monomer, blank MCs, volume of release medium) for the DOX release pattern was analysed. According to the results of the above experiments, sustained DOX release via electrostatic interactions only occurred when using a large amount of drugs, which was also proved by the previous publications in our group.(233, 295) However, the release pattern dramatically changed using a small amount of drugs (5 µg DOX), which was required for local treatment of GBM. The release profiles of MCs loaded with 5 µg DOX matched the finding in Chapter 2 **Figure 2-12** using bulk cryogel material, indicting a consistency in the drug release pattern regardless of the size of the cryogel material. MCs are a versatile delivery vehicle with the flexibility to fit into tumour resection cavities of various sizes and shapes, holding the advantage to be translated to the human condition. Interestingly, decreasing the amount of drug and the volume of release medium in equal proportion, (experiment 2: 50 µg sample in 1 mL release medium and experiment 5: 5 µg sample in 0.1 mL release medium) the release pattern was different, which might be because of the interaction efficiency between the release medium and MCs.

MCs settled down at the bottom of the centrifuge tube during the release experiments. One potential reason for the sustained DOX release in the samples with a large amount of drugs is the inefficient medium exchange. However, topping with an extra 45 μg blank MCs did not affect the release pattern of the 5 μg sample (experiment 4), suggesting that DOX release was controlled at the molecular level. Another potential reason causing this problem might be the DOX concentration. Specifically, the concentration gradients between the solution and MCs are different for samples with different amounts of DOX. The results of previous DOX loading studies (Chapter2, **Figure 2-8**) showed that a certain DOX concentration (approximately 13 μg/mL) was required to keep the equilibrium of binding via electrostatic interactions, which was not affected by the total amount of loaded DOX. So, on the contrary, a certain amount of DOX is needed to be released from the cryogel to raise the drug concentration high enough to reach the binding equilibrium, which also should not be relevant to the amount of DOX remaining in the MCs. So, the proportion of released DOX needs to be increased to reach the binding equilibrium whilst decreasing the total amount of DOX in the drug release samples. Another hypothesis is that DOX might become precipitation/drug crystals inside the MCs when loading at a high weight ratio of drug to MCs. The drug precipitation is difficult to be dissolved in the release medium, because the solubility of DOX in PBS is lower than in deionized water. These might be the reasons why DOX was released faster using less amount of drug in the samples. However, it should be kept in mind that *in vivo* conditions will inherently be different from *in vitro* drug release conditions. As the cerebrospinal fluid is always circulating, if the DOX concentration cannot reach the binding equilibrium of electrostatic interactions, even administering a high amount of DOX MCs, the drug release might be rapid.

3.3.2 MCs sustained release brexpiprazole

The drug release profiles of brexpiprazole MCs were first investigated for the effect of the weight ratio of the drug to MCs. All samples contained the same amount of drugs (100 μg) with a weight ratio from 1:5 to 6:5. Two types of release medium were used in this study (1% Tween 80 in PBS (**Figure 3-14 (A)** and **(B)**) and 5% Tween 80 in PBS (**Figure 3-14 (C)** and **(D)**). The release profiles of brexpiprazole MCs were significantly affected by the concentration of Tween 80. The release curves were like a first-order curve in 5% Tween 80 medium, whilst it became nearly a zero-order curve in 1% Tween 80 medium after the burst release. When using 1% Tween 80, the burst release in the first two hours was 17.02% ± 0.27% in 6:5 samples. 1:5 (27.07% ± 3.50%), 2:5 (24.98% ± 1.79%), 3:5 (24.57% ± 2.18%), and 5:5 (21.65% ± 1.66%) samples released significantly more

payloads compared to 6:5 samples in the first two hours. However, on Day 1 and Day 2, only 3:5 samples had significant difference of the percentage drug release compared to 6:5 samples. After the burst release, brexpiprazole was released at a nearly constant rate in 1% Tween 80 medium until the drug release stopped for all samples. So, the weight ratio of the drug to MCs only have limited effect on the release rate under this condition, and increasing the weight ratio extended the drug-releasing period. On the other hand, the drug release rate accelerated when using 5% Tween 80 medium, especially for samples with low weight ratio of drug to MCs. 1:5 samples released 50.2% ± 3.5% payload whilst 6:5 samples only released 19.28% ± 8.77% after two hours. 1:5 and 2:5 samples showed a significant difference compared to 6:5 samples at this time point. 3:5 samples reached the significant difference on Day 1 and Day 2, comparing to 6:5 samples. Most drugs were released within a week. 1:5 samples stopped drug release only after 3 days whilst 6:5 samples sustained released drugs for 10 days. These data revelled that increasing the weight ratio slowed down the drug release rate in the burst release and prolonged the drug release period. The release patterns of brexpiprazole MCs were tested in a pure PBS medium, but no drugs were detected (Data not shown).

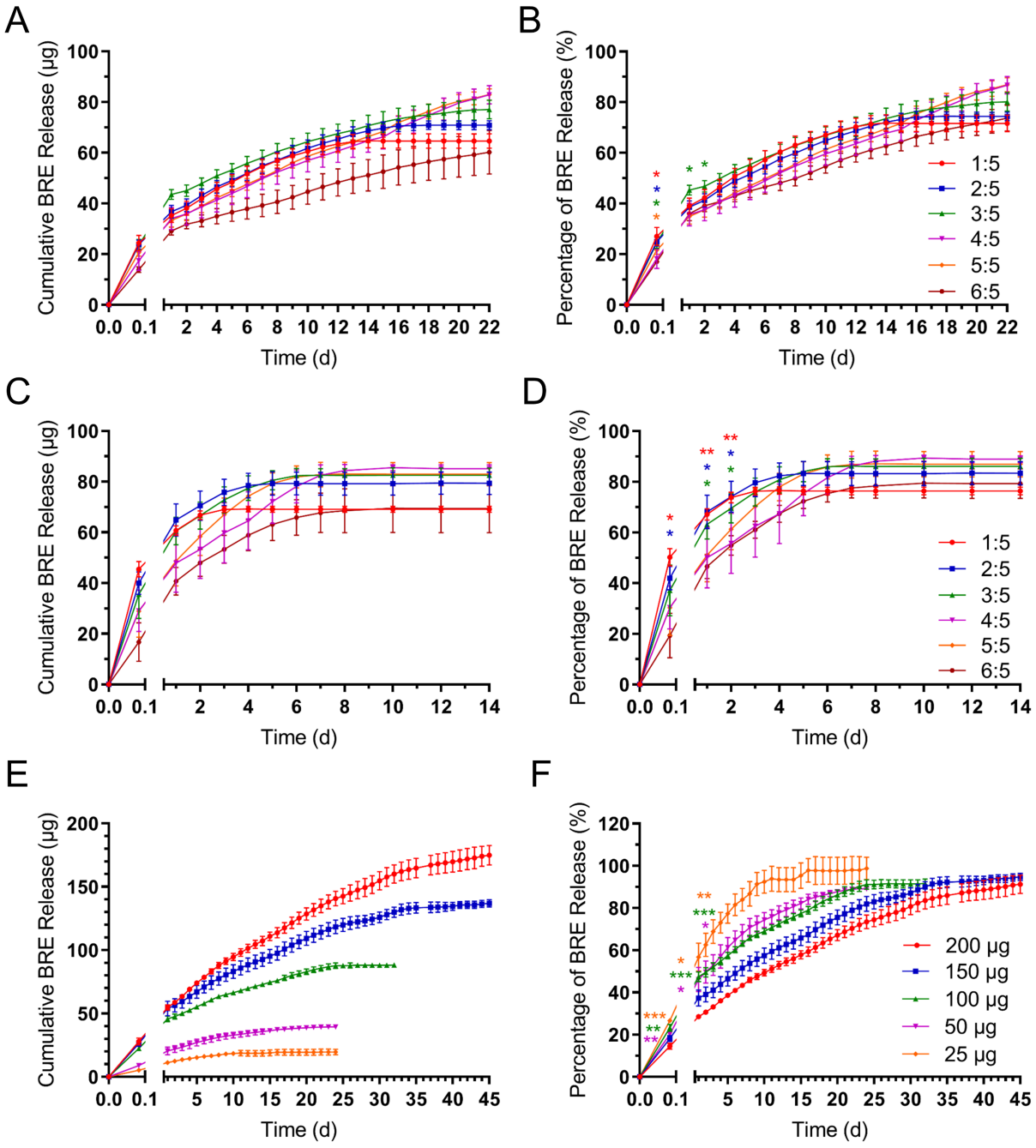

Figure 3-14 MCs sustained release brexpiprazole.

(A) and **(B)** show the amount and the percentage of cumulative drug release using 1% (wt/v) Tween 80 in PBS release medium, respectively. **(C)** and **(D)** show the amount and the percentage of cumulative drug release using 5% (wt/v) Tween 80 in PBS release medium, respectively. **(B)** and **(D):** Asterisks represent the significant difference compared to the 6:5 samples (the colour of the asterisks matches the figure keys; asterisks are marked for the first three time points, showing the difference of the drug release in the burst release stage). **(A)** – **(D)**: each sample contained 100 µg drug; the legend shows the weight ratio of drug to MCs. **(E)** and **(F)** show the amount and the percentage of cumulative drug release when changing the amount of drugs in the release samples,

respectively. 1% (wt/v) Tween 80 in PBS was used as the release medium. **(F):** Asterisks represent the significant difference compared to the 200 μg samples (the colour of the asterisks matches the figure keys; asterisks are marked for the first three time points, showing the difference of the drug release in the burst release stage). **(A)** – **(F)**: n=4, error bars represent the mean ± SD; abbreviation: BRE: brexpiprazole.

Increasing the weight ratio modestly improved the drug release profiles. The reason might be because drugs first bound with sulfonate groups on the surface of MCs and subsequently bound with sulfonate groups at the core of MCs. Drugs on the surface were vulnerable to release from MCs, whilst inner drug molecules needed to diffuse longer and might rebind with other sulfonate groups during the release.

The second brexpiprazole release study was performed to investigate the effect of the amount of drugs in release samples. The weight ratio of drugs to MCs was kept constant at 1:1. To increase the accuracy of the amount of drugs in release samples by avoiding pipetting MCs after the loading, each release sample was prepared from a single loading sample. The cumulative amount and percentage of released drugs are shown in **Figure 3-14 (E)** and **(F)**, respectively. Samples with more brexpiprazole showed an extended drug release period. Brexpiprazole was sustained released from MCs for 45 days in 200 μg samples, whilst 25 μg samples sustained released drugs for around 11 days. The burst release in the first two hours was 14.6% ± 1.4% and 26.7% ± 0.7% for 200 μg and 25 μg samples, respectively. After one day, 56.8% ± 6.6% brexpiprazole was released from 25 μg samples and 28.6% ± 1.1% brexpiprazole was released from 200 μg samples. 25 μg, 50 μg, and 100 μg samples released significantly more proportion of payloads compared to 200 μg samples in the initial release period (within two days). These results indicated that the amount of drugs (or the concentration of drugs) affected the drug release rate. Since electrostatic interactions are reversible, samples containing a smaller amount of drugs must release a higher proportion of the drug to achieve binding equilibrium.

3.3.3 Vortioxetine is rapidly released from MCs

The effect of the solubilizer on the release patterns of vortioxetine MCs was investigated. The solubility of vortioxetine at pH 7.4 is 0.097 mg/mL (data calculated from Chemicalize), which means pure PBS as a release medium could not meet the requirement of the sink conditions. Ethanol was used as the solubilizer instead of Tween 80 because Tween 80 interferes with the determination of vortioxetine. As shown in **Figure 3-15 (A)** and **(B)**, changing the proportion of ethanol in the release medium only affected the cumulative amount of drug release. The release

profiles were nearly the same when using 20% (v/v) ethanol, 10% (v/v) ethanol, or pure PBS. The drug release stopped only after two or three days. 99SPA (20%, wt/v) MCs were prepared as a formulation with a higher density of negative charges. However, compared with the standard 95SPA MCs, the drug release pattern was almost the same (**Figure 3-15 (C)** and **(D)**). The reduction of the cumulative amount of drug release when decreasing the usage of ethanol might be because some vortioxetine precipitated in the release medium. As the released drugs were detected from the supernatant of the release medium, the precipitated drugs were ignored. Moreover, the precipitation reduced the drug concentration in the release medium further promoting the release rate. These results indicated that vortioxetine MCs had a rapid drug release pattern. Therefore, vortioxetine MCs were not taken forward for cell studies.

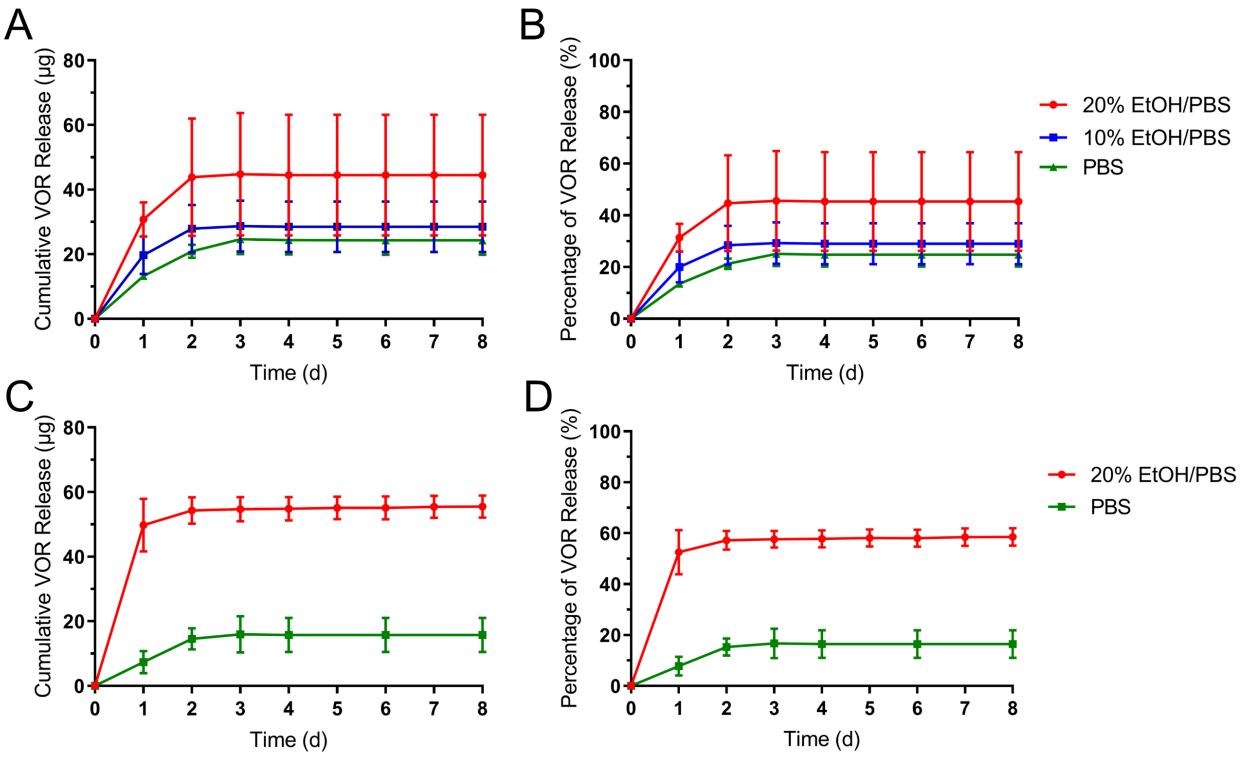

Figure 3-15 Vortioxetine MCs show a rapid drug release profile.

(A) and **(B)** show the amount and the percentage of cumulative vortioxetine release from 95SPA MCs, respectively. **(C)** and **(D)** show the amount and the percentage of cumulative vortioxetine release from 99SPA (20%, wt/v) MCs, respectively. **(A)** – **(D)**: n=4, error bars represent the mean ± SD.

3.4 Drug loading medium does not make empty MCs cytotoxic

The *in vitro* cytocompatibility of empty MCs was evaluated on primary human astrocytes. Empty MCs were incubated in the drug loading medium (1% Tween 80 in 0.1 M pH 3.7 acetic acid buffer)

for 3 days to evaluate whether the drug loading medium induced cytotoxicity. **Figure 3-16 (A)** shows that there were no morphological changes for cells incubated with empty MCs. As shown in **Figure 3-16 (B)**, there were no significant difference in cell viability between untreated cells and cells cultured with empty MCs. Together these results indicated that MCs had good cytocompatibility and confirmed that the drug-loading method would not cause potential toxicity.

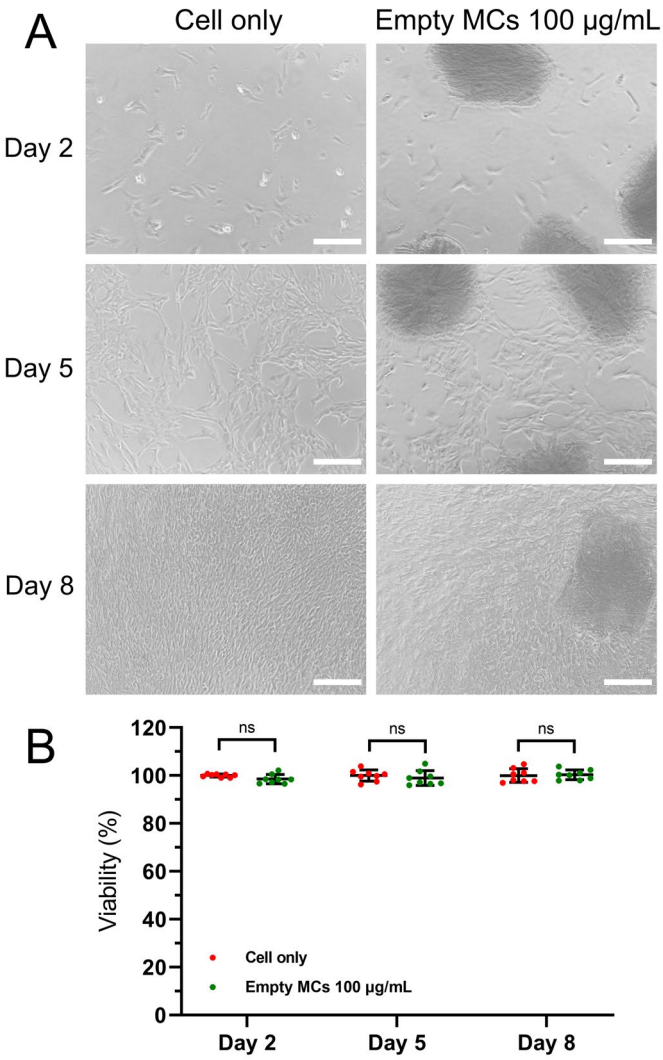

Figure 3-16 Empty MCs have good cytocompatibility on primary human astrocytes after being incubated in the drug-loading medium.

(A) shows representative images of primary human astrocytes incubated with or without 100 µg/mL empty MCs (Scale bar = 200 µm). MCs were added on Day 1. Images were taken on Day 2, 5, and 8. **(B)** shows the cell viability on Day 2, 5, and 8 (n=8, error bars represent the mean ± SD). Unpaired t-test: Day 5 and Day 8, Welch's t-test: Day 2, ns = no significant difference.

3.5 Free brexpiprazole is more toxic to GBM cells than astrocytes

Four drug candidates (DOX, venetoclax, brexpiprazole and vortioxetine) were investigated for the drug loading efficiency and release profiles in this chapter. However, three of the four above-mentioned drugs showed dissatisfactory results. Specifically, the loading efficiency of venetoclax was too low. DOX and vortioxetine were released rapidly at therapeutic concentrations. Only brexpiprazole MCs had both high loading efficiency and desirable release patterns. So, it is worth further investigating the potential of brexpiprazole MCs against GBM in cell studies.

Figure 3-17 shows the dose-respond curves of free brexpiprazole on three patient-derived hGBM stem cell lines and primary human astrocytes, and **Table 3-5** shows the IC_{50} values. hGBM L0 was the most resistant hGBM cell line to brexpiprazole, and the IC_{50} was 2.67 µg/mL on Day 5, two times higher than that of hGBM L1 and hGBM L2. However, the IC_{50} of hAstrocytes was 4.25 µg/mL, which was even higher than hGBM L0. It meant that the drug concentration between 2.67 and 4.25 µg/mL could selectively kill GBM cells. This therapeutic window suggested that brexpiprazole shows promise for repurposing as an anti-GBM drug.

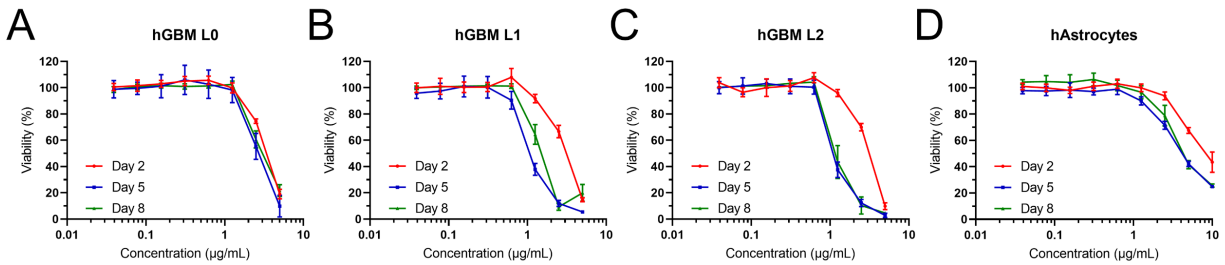

Figure 3-17 Dose-respond curves of free brexpiprazole.

(A) – **(C)** hGBM cell lines and **(D)** primary human astrocytes (n=6, error bars represent the mean ± SD).

Table 3-5 IC_{50} values of free brexpiprazole on hGBM cell lines and hAstrocytes (µg/mL)

	hGBM L0		**hGBM L1**		**hGBM L2**		**hAstrocytes**	
	IC_{50}	SD	IC_{50}	SD	IC_{50}	SD	IC_{50}	SD
Day 2	3.37	0.16	3.03	0.17	3.03	0.16	8.30	0.62
Day 5	2.67	0.22	1.12	0.07	1.15	0.06	4.25	0.28
Day 8	3.07	0.17	1.46	0.11	1.20	0.06	4.77	0.44

3.6 Brexpiprazole MCs reduce the viability of hGBM cells

The cytotoxicity of brexpiprazole MCs was first evaluated on a 2D monolayer cell culture model. Cell morphology was monitored during the experiments (**Figure 3-18 (A)**). Interestingly, brexpiprazole MCs were darker than the empty MCs under the microscope. With the drug release,

the colour of brexpiprazole MCs lightened. The bright field images also showed that some released drugs precipitated probably due to the low solubility of brexpiprazole.

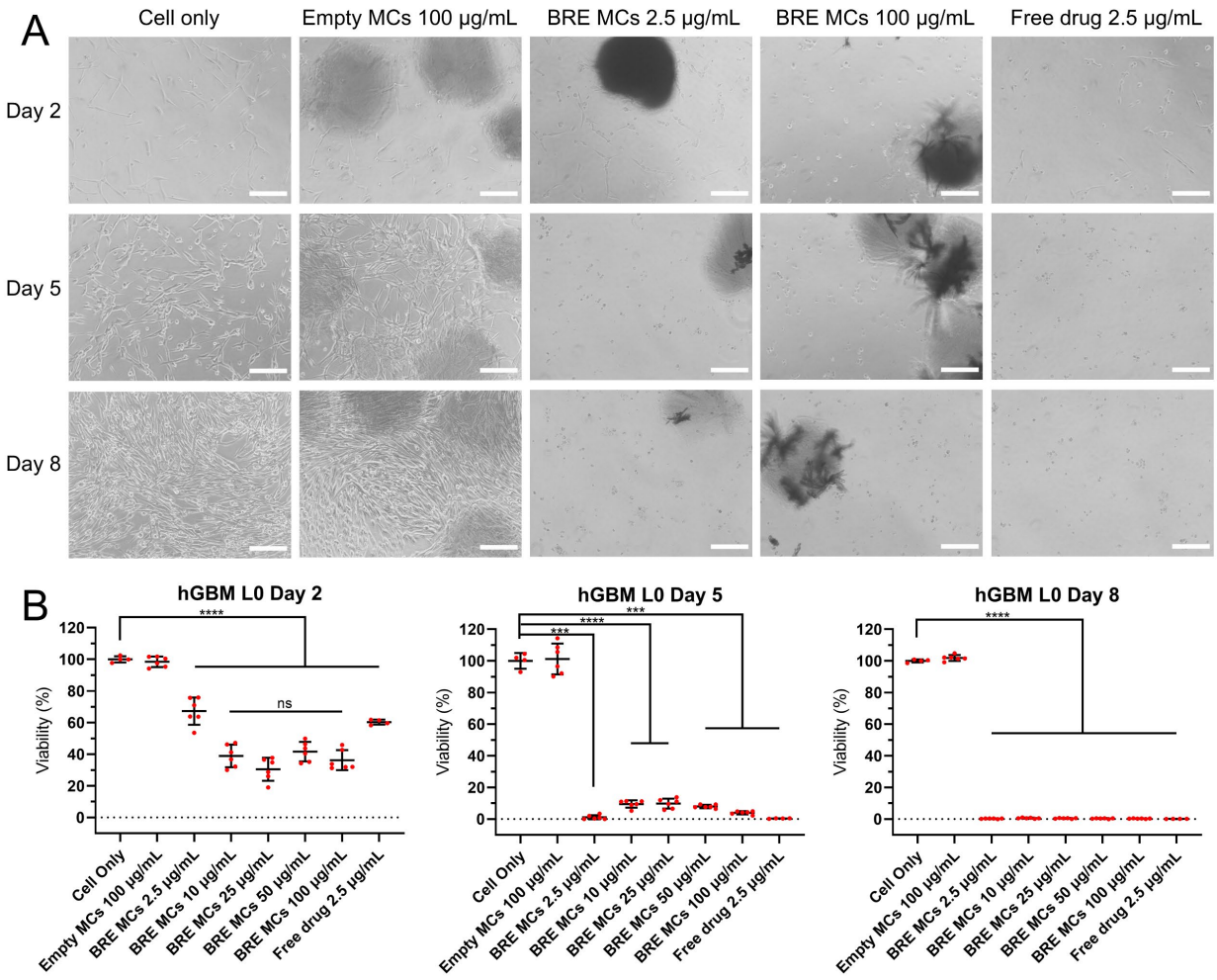

Figure 3-18 *In vitro* anti-tumour efficacy of brexpiprazole MCs against hGBM L0.

(A) shows representative bright field images of hGBM L0 cells incubated with cell culture medium only, 100 µg/mL empty MCs, 100 or 2.5 µg/mL brexpiprazole MCs, or 2.5 µg/mL free brexpiprazole (Scale bar = 200 µm). MCs were added on Day 1. Images were taken on Day 2, 5, and 8. **(B)** shows the cell viability on Day 2, 5, and 8 (Cell only and Free drug, n=4; Empty MCs and brexpiprazole MCs, n=6, error bars represent the mean ± SD). Ordinary one-way ANOVA test: Day 2, Welch ANOVA test: Day 5 and Day 8, ns = no significant difference, for *** $p \leq 0.001$, **** $p \leq 0.0001$. Abbreviation: BRE: brexpiprazole.

As shown in **Figure 3-18 (B)**, empty MCs did not reduce the cell viability of hGBM L0 until Day 8. The cell viability on Day 2 did not show significant difference among 10, 25, 50, and 100 µg/mL brexpiprazole MCs treatments. The cell viability of 2.5 µg/mL brexpiprazole MCs and 2.5 µg/mL free drugs treatment was significantly higher than the other four concentrations of brexpiprazole

MCs treatment, but cell viability did not show significant difference between these two groups. On day 5, all brexpiprazole MCs treated groups and the free drug treatment nearly eradicated all GBM cells. Similar results were observed on hGBM L1 and hGBM L2 (**Figure 3-19** and **3-20**). Specifically, there were no significant difference in cell viability among 10, 25, 100 µg/mL brexpiprazole MCs treatments on hGBM L1 for 1 day, and the cell viabilities of hGBM L2 exposed to 10, 25, 50, 100 µg/mL brexpiprazole MCs or 2.5 µg/mL free drug for 1 day had no significant difference. These results suggested that although the concentrations of brexpiprazole MCs were different, the cumulative amount of released drugs by 1 day was similar, which matched the results of *in vitro* drug release profiles that lower concentrations of brexpiprazole MCs released the drug faster. Although 100 µg/mL brexpiprazole MCs had the best release profile, the low IC_{50} values of free brexpiprazole mean it is impossible to observe the sustained drug release at such a high concentration in cell studies.

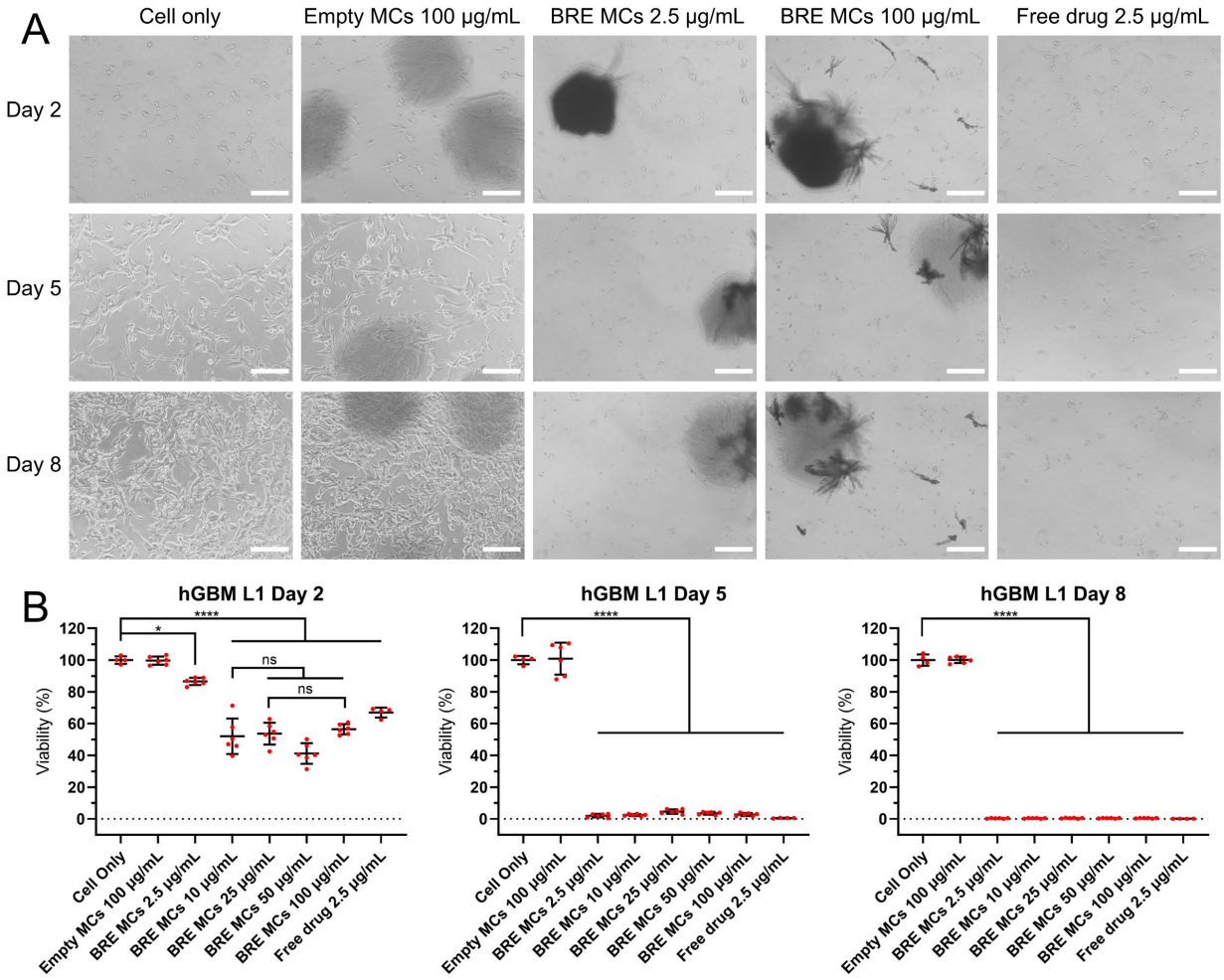

Figure 3-19 *In vitro* anti-tumour efficacy of brexpiprazole MCs against hGBM L1.

(A) shows representative bright field images of hGBM L1 cells incubated with cell culture medium only, 100 µg/mL empty MCs, 100 or 2.5 µg/mL brexpiprazole MCs, or 2.5 µg/mL free brexpiprazole

(Scale bar = 200 µm). MCs were added on Day 1. Images were taken on Day 2, 5, and 8. **(B)** shows the cell viability on Day 2, 5, and 8 (Cell only and Free drug, n=4; Empty MCs and brexpiprazole MCs, n=6, error bars represent the mean ± SD). Ordinary one-way ANOVA test: Day 2, Welch ANOVA test: Day 5 and Day 8, ns = no significant difference, for * $p \leq 0.05$, **** $p \leq 0.0001$. Abbreviation: BRE: brexpiprazole.

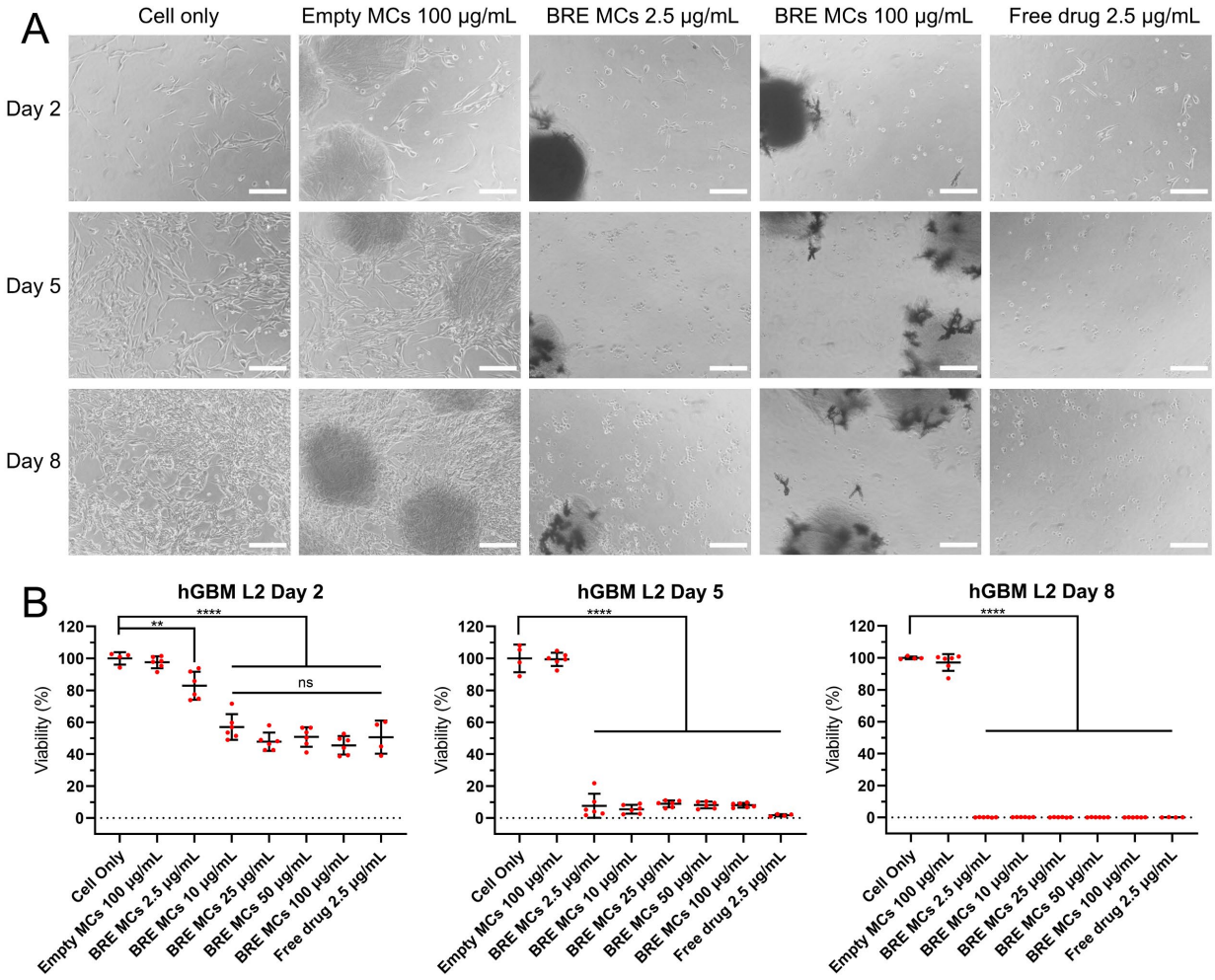

Figure 3-20 *In vitro* anti-tumour efficacy of brexpiprazole MCs against hGBM L2.

(A) shows representative bright field images of hGBM L2 cells incubated with cell culture medium only, 100 µg/mL empty MCs, 100 or 2.5 µg/mL brexpiprazole MCs, or 2.5 µg/mL free brexpiprazole (Scale bar = 200 µm). MCs were added on Day 1. Images were taken on Day 2, 5, and 8. **(B)** shows the cell viability Day 2, 5, and 8 (Cell only and Free drug, n=4; Empty MCs and brexpiprazole MCs, n=6, error bars represent the mean ± SD). Ordinary one-way ANOVA test: Day 2 and Day 5, Welch ANOVA test: Day 8, ns = no significant difference, for ** $p \leq 0.01$, **** $p \leq 0.0001$. Abbreviation: BRE: brexpiprazole.

3.7 Brexpiprazole MCs suppress the growth of hGBM L2 3D spheroids

The shortcomings of 2D monolayer cell cultures, such as lack of cell-cell interaction and different patterns of the distribution of nutrients, have probably been a reason for the contradiction between the results of *in vitro* drug candidate screening and *in vivo*/clinical models.(296, 297) In 3D cell culture models, cells grow in rounded shapes and form clusters, mimicking the *in vivo* tumour microenvironment including the hypoxia and acidity core in solid tumours.(298, 299) To further understand the *in vitro* anti-GBM efficacy of brexpiprazole MCs, we used the forced-floating method to form cell spheroids using non-adhesive well plates.

The average size of hGBM L2 3D spheroids was 65,380 μm^2 before the treatment (**Figure 3-21**). Untreated spheroids grew to an average of 505,206 μm^2 after a week. Despite the size of cell spheroids treated with 2.5 µg/mL brexpiprazole MCs showing no significant difference in comparison to negative control (**Figure 3-22 (A)**), the morphology of cell spheroids changed, and the edge became unclear and fuzzy, suggesting the effect on cell growth. Images of cell spheroids treated with 2.5 µg/mL free drug on Day 7 and 8 showed tumour cells on the surface of spheroids were killed first, which suggested that 3D cell culture reduced the drug penetration to more inward cells.

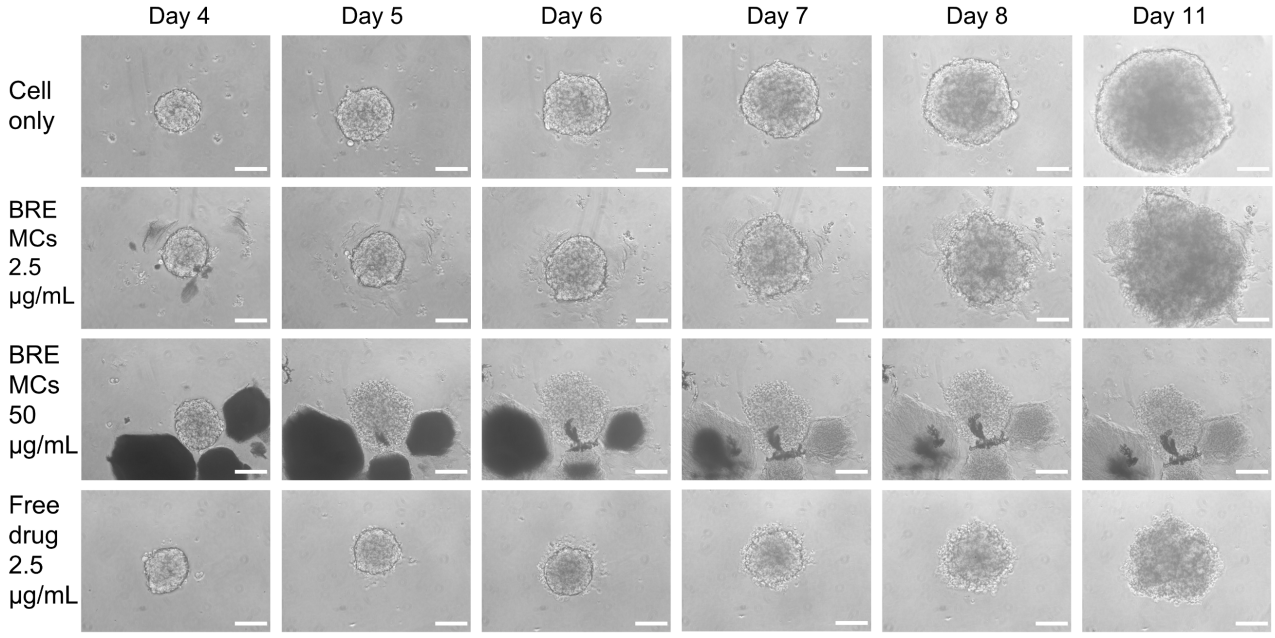

Figure 3-21 Images of hGBM L2 spheroids during the treatment.

Representative bright field images of hGBM L2 3D spheroids incubated with cell culture medium only, 2.5 or 50 µg/mL brexpiprazole MCs, or 1.25 µg/mL free brexpiprazole (Scale bar = 200 µm). MCs were added on Day 4. Abbreviation: BRE: brexpiprazole.

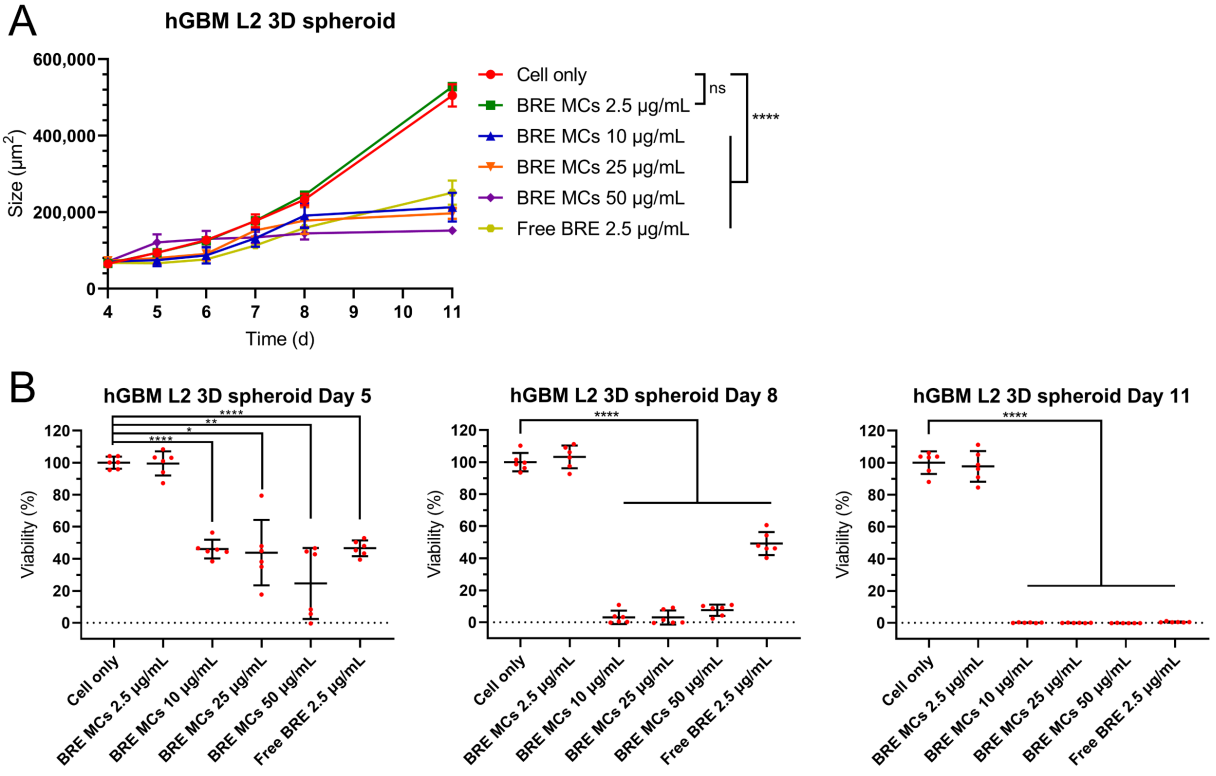

Figure 3-22 Brexpiprazole MCs reduce the viability and suppress the growth of hGBM L2 3D spheroids.

(A) shows the size changes of cell spheroids (n=6, error bars represent the mean ± SD). Two-way ANOVA test. Asterisks show statistically significant difference compared to cell only control. **(B)** shows the cell viability on Day 5, 8, and 11 (n=6, error bars represent the mean ± SD). Ordinary one-way ANOVA test: Day 4, Welch ANOVA test: Day 1 and Day 7, ns = no significant difference, for * $p \leq 0.05$, ** $p \leq 0.01$, **** $p \leq 0.0001$. Abbreviation: BRE: brexpiprazole.

Compared to untreated spheroids, the size of hGBM L2 spheroids treated with 10, 25, 100 μg/mL brexpiprazole MCs or 2.5 μg/mL free drug significantly decreased after seven days (**Figure 3-22 (A)**). The cell viability was considerably reduced after one day of being treated with 10, 25, and 100 μg/mL brexpiprazole MCs or 2.5 μg/mL free drug (**Figure 3-22 (B)**). After 4 days of exposure to 2.5 μg/mL free drug, the cell viability of hGBM L2 spheroids was 49.2% ± 7.2%, whilst 10, 25, or 100 μg/mL brexpiprazole MCs treatment nearly killed all cells. On Day 11, the cell viability decreased to zero when the spheroids were treated with 2.5 μg/mL free drug. The lowest concentration of brexpiprazole MCs treatment (2.5 μg/mL) did not decrease cell viability during the experiment. These data indicated that hGBM L2 spheroids exhibited less sensitivity in comparison to 2D monolayer culture. The innate resistance in 3D spheroids could better guide the transition from *in vitro* studies to *in vivo* studies.

4. Conclusions

In this chapter, I have successfully created negatively charged MCs with a narrow size distribution by droplet-based microfluidics. The drug loading efficiency was evaluated by DOX, venetoclax, brexpiprazole and vortioxetine, and results showed that three drugs had high loading efficiency, with the exception of venetoclax. Five drug release studies were conducted on DOX MCs to investigate the drug release profiles, especially for the dose corresponding to *in vivo* study. The results suggested that the amount of DOX in the release samples obviously affected the release profiles, and samples with a small amount of DOX had a rapid release pattern. Although the loading efficiency of vortioxetine was good, the rapid release pattern meant it was not suitable to be delivered by MCs. Brexpiprazole MCs showed both high loading efficiency and sustained drug release profiles, so the *in vitro* anti-GBM of this drug was further investigated. The results of cell studies showed that empty MCs had good cytocompatibility on primary human astrocytes, free brexpiprazole had a potential therapeutic window to kill GBM cells whilst being safe for non-malignant cells, and brexpiprazole-loaded MCs showed sustained release of the drug and kill GBM cells.

Chapter 4: Vortioxetine: a potential drug for repurposing for glioblastoma treatment via a microsphere local delivery system

The work in this chapter has been published as a research paper.

Yu Wang, Dorit Siebzehnrubl, Michael Weller, Tobias Weiss, Florian A. Siebzehnrubl, and Ben Newland. Vortioxetine: a potential drug for repurposing for glioblastoma treatment via a microsphere local delivery system, ACS Biomaterials Science & Engineering (PMID: 40167528).

1. Introduction

Glioblastoma (GBM) is the most malignant primary brain cancer, associated with poor clinical outcomes and high mortality.(1) The median survival time after the first diagnosis is less than two years.(300, 301) The standard of care, established in 2005, is still the routine treatment for GBM and includes maximal safe resection (when possible/practical) followed by radiotherapy plus adjuvant temozolomide chemotherapy.(11) However, half of GBM patients are resistant to temozolomide which has been linked to promoter methylation of O^6-methylguanine-DNA methyltransferase (MGMT), a DNA damage repair protein.(302) Bevacizumab was approved by the Food and Drug Administration (FDA) to treat recurrent GBM but has thus far failed to show a benefit in the overall survival time.(303, 304) Lomustine, an alternative chemotherapeutic has also not shown significant advantages over temozolomide when the drug was used alone in a randomized controlled trial.(305-307) There is therefore an urgent need to find effective, safe, and long-lasting therapeutic agents for GBM.

At present, synthesizing novel active ingredients is becoming increasingly challenging. The burden of investment to find the next generation of chemotherapeutics is growing, fuelling the rationale for drug repurposing approaches.(104) By repurposing or repositioning existing drugs for new indications, the time and money invested per successful outcome can potentially be reduced.(105) There are dozens of FDA-approved drugs that have proven activity in GBM models, with some of them being tested in clinical trials.(110-113)

Recently, Sohyon Lee *et al.* screened 67 repurposed neuroactive drugs in 27 *ex vivo* GBM patient samples.(118) The resulting pharmacoscopy score, which was quantified by measuring the changes in cell population fraction, showed vortioxetine scored highest, and had a high specificity for killing inter-tumour and intra-tumour heterogeneous GBM cells. In addition, vortioxetine also gave a significant survival benefit in comparison to the vehicle control in an orthotopic xenograft GBM mouse model and a comparable survival benefit to temozolomide treatment. Vortioxetine is a 5-hydroxytryptamine receptor antagonist to treat major depressive disorder, approved by the FDA in 2013.(308) It has a high fraction of plasma protein binding, with 99% of the drug being protein-bound, suggesting limited free drug availability for a therapeutic effect.(309) With little else known about its potential as a GBM therapeutic, I hypothesized that local delivery to the tumour may increase its anti-tumour efficacy.

Since surgical resection of the tumour is applicable to most GBM patients, local delivery into the resection cavity is an attractive strategy to circumvent the blood-brain barrier (BBB), achieve high drug concentrations at the residual tumour site, and reduce systemic side effects. The Gliadel® wafer is the only FDA-approved local treatment drug for GBM. However, the survival benefit for patients treated with Gliadel® has been modest.(48) A systematic review revealed that the median overall survival of patients that received Gliadel® plus radiotherapy and TMZ was 18.2 months,(52) compared to 14.6 months after the standard of care.(11) Additionally, the large stiff wafer needs a gross tumour debulking to get enough space for the implantation and has been associated with side effects occurring when dislodged.(206, 310) Injectable drug delivery systems offer additional flexibility in terms of application, either through use in uneven/small cavities, or via means such as convection-enhanced delivery to otherwise inoperable tumours.(311) Much research has focused on the development of hydrogel, nanoparticle, and microparticle delivery systems,(56) but the goal of a non-toxic, well-defined, and reproducible drug delivery system, suitable for regulatory approval with a slow drug release profile has thus far remained elusive.(312)

Microspheres, which are defined as particles with a size range between 1 and 1000 μm, can encapsulate drugs within their homogeneous matrix as single molecules or small clusters.(313) Microspheres smaller than 250 μm can be considered as injectable preparations depending on the cannula used.(314) Poly(D,L-lactide-co-glycolide) (PLGA) is a biocompatible and biodegradable lactic acid and glycolic acid copolymer approved by the FDA for clinical use.(315) PLGA was chosen over other polymers for simplicity in design with the controllable degradation properties and good solubility in numerous organic solvents, making it an attractive starting point for delivery system synthesis.(316)

Many methods can be used to prepare PLGA microspheres, including double or multiple emulsion solvent evaporation,(317, 318) cryogenic solvent extraction,(319) catalytic hydrolysis solvent removal,(320) non-solvent addition,(321) spray-drying,(322) supercritical fluids,(323) and membrane emulsification.(324) However, the size distribution of PLGA microspheres is typically very poor. For example, the commonly used emulsion solvent evaporation method, relies upon nonuniform mechanical forces to create droplets, resulting in high size dispersity.(325) Polydispersity reduces reproducibility and introduces variation as particle size affects factors such as drug release and degradation rate. Factors such as the drug molecular distribution in the microspheres, surface area to volume ratio, and porosity, all affect polymer hydrolysis and drug dissolution.(326, 327) Tight control over these factors is essential for producing reproducibly

efficacious and regulatory-approved therapeutics. A new approach to prepare monodisperse PLGA microspheres with a smooth surface (low porosity) and a regular round shape is therefore desirable.

Aims:

In this chapter, I aimed to validate vortioxetine as an anti-glioblastoma therapeutic, and to combine droplet-based microfluidics with a new emulsion formula, to create vortioxetine-loaded, monodispersed PLGA microspheres as a locally administered sustained therapeutic for GBM. Herein, free vortioxetine showed more toxicity towards patient-derived GBM cell lines than to primary human astrocytes, indicating a potential therapeutic window minimizing the side effects to healthy cells. Then a water-free oil-in-oil (O/O) emulsion was created in a microfluidic device to prepare empty and vortioxetine-loaded microspheres (termed vortioxetine microspheres) with high reproducibility and monodispersity. The cytocompatibility of the empty PLGA microspheres was demonstrated *in vitro* on primary human astrocytes, and sustained drug release from vortioxetine microspheres effectively killed patient-derived GBM cells both in 2D culture and in 3D tumour spheroids.

2. Materials and methods

2.1 Chemicals and materials

The chemicals and materials used in this chapter are shown in **Table 4-1**. Chemicals were used without any further purification. **Table 4-2** shows the equipment used in this chapter.

Table 4-1 List of chemicals and materials

Chemicals and Materials	Company	Catalog number
Resomer® RG 752 H, PLGA (L:G 75:25, Mw: 4,000-15,000)	Sigma	719919
Vortioxetine	TargetMol	ABIN6574672
HFE-7500 engineered fluid	3M	7100025016
008 Flouro Surfactant	RAN Biotechnologies	038-074
1H,1H,2H,2H-perfluoro-1-octanol (PFO)	Sigma	370533
Dimethyl sulfoxide (DMSO)	Sigma	D2650
Acetonitrile	Fisher Chemical	A/0632/PB15
Phosphate-buffered saline (PBS)	Gibco	10010023
Eosin Y	Sigma	E6003
Sodium acetate trihydrate	Sigma	32318
Acetic acid	Sigma	27225
Water with 0.1% Formic Acid (v/v)	Fisher Scientific	10229884
Acetonitrile with 0.1% Formic Acid (v/v)	Fisher Scientific	10678935

Table 4-2 List of equipment

Equipment	Company	Catalog number
Microfluidic pump	Imprint Landgraf Laborsysteme HLL GmbH	LA30
Vacuum oven	Gallenkamp	OVL-570-010J
Microscope Primovert	Zeiss	491206-0002-000
High-speed camera	Phantom	C110
InfiniteRX plate reader	Tecan	
Orbital Shanker-incubator	Grant-bio	
ACQUITY UPLC System	Waters	
IRSpirit	Shimadzu	
Zeiss Sigam HD Field Emission Gun Scanning Electron Microscope	Zeiss	

2.2 Preparation of PLGA microspheres

A droplet-based microfluidics technique was used to create PLGA microspheres. A cross-junction configuration microfluidic chip with 80 µm nozzle size was used (Microfluidic chip Fluidic 440, microfluidic ChipShop, Germany). The continuous phase contained 2% 008 Fluoro Surfactant in HFE-7500 oil. 100 mg/mL PLGA and 10 mg/mL vortioxetine were dissolved in acetonitrile as the disperse phase. To prepare empty PLGA microspheres, the dispersed phase contained 100 mg/mL PLGA only. The flow rate of the continuous phase and the disperse phase was set at 900 µL/h and 150 µL/h, respectively (driven by LA30 syringe pump, Imprint Landgraf Laborsysteme HLL GmbH, Germany). An inverted microscope (491206-0002-000, Zeiss, Germany) with a high-speed camera (C110, Vision Research Ltd., UK) was used to monitor the droplet generation. After the droplet generation was stable, droplets were collected in 2 mL centrifuge tubes. To purify PLGA microspheres, droplets were dried in a vacuum oven (OVL-570-010J, Gallenkamp, UK) at room temperature for 3 hours to remove the acetonitrile. The HFE oil was aspirated from the bottom of the tube. Microspheres were washed three times using 100 µL 20% (v/v) PFO in HFE and three times with 200 µL HFE oil. PLGA microspheres were dried in a vacuum oven at room temperature overnight to remove the remaining HFE oil.

2.3 Morphological characterization of PLGA microspheres

2.3.1 Bright field microscope images

Three batches of vortioxetine microspheres were prepared to evaluate reproducibility. Dried microspheres were resuspended in PBS. The size of 300 microspheres was analysed for each batch. The size of microspheres was measured by the particle analysis function in ImageJ, and the diameter of microspheres was calculated by the circle area formula.

2.3.2 Scanning electron microscope (SEM)

The morphology of microspheres was visualized by Zeiss Sigam HD Field Emission Gun Scanning Electron Microscope (Zeiss, Germany). To prepare the samples, microspheres were coated by AuPd using a BIO-RAD SC500 sputter coater (Quorum Technologies, UK). The microspheres were uniformly covered with a thick layer of AuPd around 10-20 nm. A beam energy of 5 kV with a 30 µm diameter final aperture was used and microspheres were imaged via an Everhart-Thornley detector.

2.4 Fourier transform infrared spectroscopy (FTIR)

Infrared spectra of PLGA, free vortioxetine, and vortioxetine microspheres were scanned by the IRSpirit FTIR Spectrometer (Shimadzu Co., Ltd, Japan) using dried power samples directly. The background signal was scanned before running each sample to subtract any residual peaks from the instrument and the environment. FTIR spectra were scanned by transmittance mode from 500 cm^{-1} to 3500 cm^{-1} with a resolution of 0.9.

2.5 Analysis of drug loading efficiency

Ultra-performance liquid chromatography (ACQUITY UPLC System, Waters, USA) was used to detect the vortioxetine for the drug loading efficiency study. A photo diode array (PDA) detector was used and the PDA spectrum between 253 and 600 nm was used to quantify the concentration of the drug. The mass spectrometry detector was used to confirm the peak in the PDA spectrum belonging to vortioxetine. The calibration curve was built by preparing 1, 2, 4, 6, 8, and 10 µg/mL drug solutions. To investigate the loading efficiency, vortioxetine microspheres with five different weight ratios of drug to PLGA (1:2, 1:3, 1:4, 1:5, and 1:10) were prepared. The drug concentration in the dispersed phase was kept constant at 10 mg/mL, and the weight ratio was changed by adjusting the PLGA concentration in the dispersed phase. 1 mg of vortioxetine microspheres were weighed and dissolved in 1 mL acetonitrile and diluted to a suitable concentration within the linear range of the calibration curve. The drug loading efficiency was calculated by the following equation:

$$\%\ of\ loading\ efficiency = c_2/c_1 * 100\%$$

Equation 4-1. Where c_1 was the theoretical drug concentration in the samples. c_2 was the actual concentration in the samples.

2.6 Evaluation of *in vitro* drug release profiles

Pure PBS was used as the release medium to mimic physiological conditions. Vortioxetine microspheres (1:10 weight ratio of drug to PLGA) containing 50, 100, 300, or 500 µg drug were incubated in the incubator (Orbital Shanker-incubator, Grant-bio, UK) at 37°C with gentle shaking at 80 rpm. At each time-point, after centrifugation, 900 µL of supernatant was removed and stored, and replaced with fresh release medium. Microspheres were resuspended by vortex mixing. The samples were stored at -20°C for further investigation. At the end of the experiment, the concentration of drugs in all samples was detected by a fluorescence quenching method.(228) Briefly, 300 µL samples, 300 µL 0.15 mg/mL eosin Y, and 300 µL 0.2M acetic acid buffer at pH 3.7 were added into one 2 mL Eppendorf tube and mixed well by vortex mixer. The fluorescence intensity of eosin Y was read using excitation and emission wavelengths of 306 and 539 nm respectively. The calibration curve method was used to quantify the drug concentration (linear range 0.4 to 8 µg/mL). The cumulative amount of released drug could be calculated by the following equation.

$$m_n = \begin{cases} c_n * V_{Total} & (n = 1) \\ c_n * V_{Total} + V_{Replaced} * \sum_{i=1}^{n-1} c_i & (n > 1) \end{cases}$$

Equation 4-2: where m_n is the cumulative release amount of the nth time point (µg). c_n is the drug concentration of the nth time point (µg/mL). V_{Total} is the total volume of the release medium. $V_{Replaced}$ is the volume of the replaced release medium at each time point.

2.7 Cell culture

Patient-derived GBM stem cell lines (hGBM L0, L1, and L2) and primary human astrocytes were cultured and maintained as described in Chapter 2 section 2.9.

2.8 Cytocompatibility of empty PLGA microspheres

The cytocompatibility of empty PLGA microspheres was evaluated using primary human astrocytes. Cells were seeded in poly-L-lysine coated 48-well plates (Costar, 3548) at a density of 4,800 cells/well. After one day of incubation, empty PLGA microspheres were added to get a final concentration of 100 µg/mL. Images of cells were taken via a microscope camera (A35180U3, OMAX Microscope, South Korea) and the cell viability was tested using the PrestoBlue assay 1, 4, and 7 days after adding PLGA microspheres and normalizing to untreated control cells (background fluorescence was subtracted from experimental wells). Cells were incubated in PrestoBlue for 2

hours and the fluorescence intensity was read with an excitation wavelength of 560 nm and an emission wavelength of 590 nm by the bottom reading model.(233)

2.9 Cytotoxicity of free vortioxetine

To investigate the cytotoxicity of free vortioxetine, primary human astrocytes were plated in poly-L-lysine coated 96-well plates (Costar, 3595) at a density of 1,600 cells/well, and hGBM cell lines were plated in Geltrex coated 96-well plates at a density of 5,000 cells/well. After one day of incubation, vortioxetine solution was added, which was prepared by serial dilution from 5 mg/mL stock solution in pure DMSO using complete culture medium. The cell viability was tested using the PrestoBlue assay 1, 4, and 7 days after adding the drugs to the cells.

2.10 Antitumor efficacy of vortioxetine microspheres in 2D cell culture models

The hGBM L0, L1, and L2 cells were cultured in Geltrex-coated 48-well plates as adherent cells to investigate the *in vitro* antitumor efficacy. Cells at a density of 15,000 cells/well were cultured for one day, and then drugs were added to get a final concentration of 100 µg/mL for empty PLGA microspheres control; 0.625, 1.25, 2.5, 5, and 10 µg/mL for vortioxetine microspheres; and 1.25 µg/mL for the free drug control. 1, 4, or 7 days after adding the microspheres/drug, the cells were imaged, and the cell viability was analysed using the PrestoBlue assay.

2.11 Analyzing the efficacy of vortioxetine microspheres against 3D GBM spheroids

Ultra-low attachment 96-well plates (Costar, 7007) were used to establish the 3D spheroid model. Briefly, hGBM L0 and L2 cells were seeded at a density of 1,000 cells/well. Well plates were centrifuged at 300 g for 5 minutes. The spheroids were incubated for 4 days before adding the experimental groups, and then treated with 1.25, 2.5, 5, 10 µg/mL vortioxetine microspheres or 1.25 µg/mL of free drug. Images of spheroids were taken on Day 4, 5, 6, 7, 8, 11, 13, 15, and 18. The size of the spheroids was measured using ImageJ. On Day 5, 8, 11, and 18, additional cultures of the spheroids were incubated with PrestoBlue for 3 hours before reading the fluorescence intensity. To investigate the efficacy of vortioxetine microspheres against larger, pre-established spheroids, hGBM L0 and L2 spheroids were cultured for 7 days before adding the experimental groups. The size of the spheroids was monitored on Day 7, 8, 10, 12, 14, and 16, and the cell viability was evaluated on Day 12 and 16.

2.12 Statistical analysis

Statistical analysis was conducted as described in Chapter 2 Section 2.16.

3. Results and Discussion

3.1 Preparation and characterization of PLGA microspheres

At present, emulsion-solvent evaporation still dominates the preparation of PLGA microspheres either in laboratories or in commercial products. A single oil-in-water (O/W) emulsion is commonly used to encapsulate hydrophobic drugs in PLGA,(317) while hydrophilic drugs including proteins loaded into PLGA microspheres are usually prepared by a water-in-oil-in-water (W/O/W) double emulsion.(328) Although relatively good control of size distribution has been achieved, it is still challenging to produce high consistency in product sizes. Many factors can affect the production of PLGA microspheres by these methods, including physical parameters such as stirring rate and volume ratio of two phases, physicochemical parameters such as viscosity and density, and chemical parameters such as surfactant and solvent.(329) Droplet-based microfluidics is an emerging technology to prepare microspheres.(330-332) The generation of the droplets can be monitored in real-time, and the size and the morphology of microspheres can be precisely controlled by the geometry of the microfluidic device, flow rate ratio, and viscosity of the two phases. One of the drawbacks of microfluidics is the low production efficiency. Using multiple devices or multiple microchannel devices is a simple way to increase production efficiency.(333) However, a typical PLGA microsphere synthesis protocol using organic solvents such as dichloromethane is unsuitable for adaptation to use in a commonly used microfluidic device made from polydimethylsiloxane (PDMS). The solvent can cause the PDMS to swell, thus changing channel dimensions if not ruining the device. Glass microfluidic devices could potentially be used, but at a high cost, further hampering scale-up for production.

Cyclic olefin copolymers (COC) are a novel class of polymeric materials. The strengths of COC include high transparency, rigidity, strength, hardness, biocompatibility, and very good resistance to acids, alkalis, and polar solvents.(190) We therefore used microfluidic chips made from COCs to prepare PLGA microspheres. However, these are still not resistant to dichloromethane, so another solvent with a low boiling point (for ease of removal post-synthesis) was sought for use with the devices. The requirements to prepare PLGA microspheres by microfluidics included 1) two immiscible solvents; 2) devices resistant to both solvents; 3) a solvent with high solubility of PLGA and the drug; 4) a suitable method to remove the dispersed phase solvent; 5) a suitable surfactant to be dissolved in either of these two solvents. In our previous research, HFE-7500 oil was used as the continuous phase solvent to prepare W/O emulsion by COC microfluidics chips.(278)

Meanwhile, 008 Fluoro Surfactant was the corresponding surfactant soluble in the HFE oil for emulsion preparation. To use this combination as the continuous phase, we needed another solvent for the dispersed phase that would be immiscible with HFE but not affect COC yet have high solubility of PLGA and the drug. We found that acetonitrile could meet all these requirements. The solubility of PLGA and vortioxetine in the acetonitrile was more than 100 mg/mL and 10 mg/mL, respectively. Using a high concentration of PLGA could increase production efficiency, reduce the extent of shape deformation, and ensure good drug distribution. The high drug solubility could keep the drug ratio in the microspheres at a high level when using a high concentration of PLGA. The latent heat of vaporization of HFE and acetonitrile is stated as 88.5 and 729 kJ/kg, and the densities are 1614 and 786 kg/m^3, respectively (manufacturers information). Although HFE evaporates faster than acetonitrile, the acetonitrile is in the upper layer when mixed with HFE, meaning the acetonitrile could be evaporated before the HFE. The evaporation order of solvents was critical because the droplets needed to be solidified whilst an emulsion was in the continuous phase.

In order to achieve monodisperse droplets via microfluidics (**Figure 4-1 (A)**), a dripping regime was used as shown in **Figure 4-1 (B)**.(334, 335) The high viscosity of the dispersed phase when using high molecular weight PLGA led to unstable droplet generation (**Figure 4-2**), so PLGA (L:G 75:25) of molecular weight 4,000-15,000 Da was used. The schematic diagram (**Figure 4-1 (C)**) depicts the structure of the droplets. The perfluoropolyether/poly (ethylene glycol) (PFPE-PEG-PFPE) triblock copolymer surfactant gave remarkable stability to the formed droplets allowing ease of handling during purification etc. Furthermore, it was removed easily due to its high solubility in the PFO. The procedure for solidification of the droplets and the purification of PLGA microspheres is shown in **Figure 4-1 (D)**. **Figure 4-1 (E)** and **(F)** show the morphology of the droplets and the purified vortioxetine microspheres that were resuspended in PBS. The size of the vortioxetine microspheres was slightly decreased compared to the droplets due to the evaporation of acetonitrile. SEM images (**Figure 4-1 (G)**) show that microspheres were a regular spherical shape with a smooth surface. Three batches of vortioxetine microspheres were prepared to evaluate reproducibility. All batches of microspheres had a similar size with a narrow size distribution (Batch 1: 36.80 ± 1.96 µm, batch 2: 35.41 ± 1.05 µm, batch 3: 34.49 ± 2.15 µm; n=300 for each batch; **Figure 4-1 (H)**). Empty PLGA microspheres were also prepared by keeping the concentration of PLGA constant. The size of empty PLGA microspheres was 33.44 ± 1.86 µm (n=300), slightly smaller than vortioxetine microspheres (The size distribution of empty PLGA microspheres is shown in **Figure 4-3**).

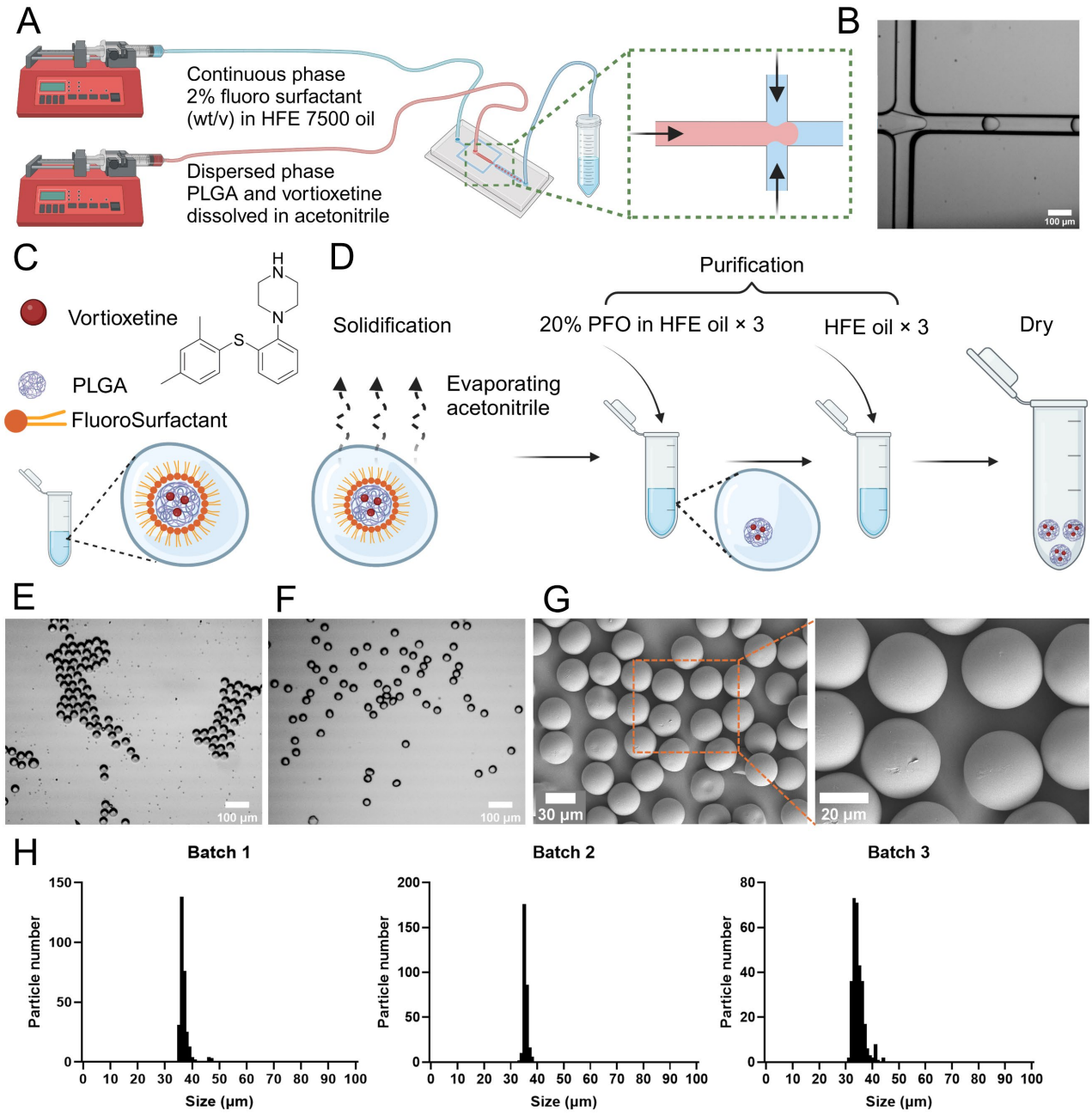

Figure 4-1 Preparation and characterization of vortioxetine microspheres.

(A) Schematic diagram showed the preparation of O/O (acetonitrile in HFE oil) emulsion by microfluidic techniques. **(B)** A photo showed the droplet generation as a dripping regime at the crossing junction. **(C)** The structure of the droplets. **(D)** The schematic diagram shows the procedure of the purification. Droplets were solidified by evaporating acetonitrile. Fluoro Surfactant was removed by PFO. Dry powder microspheres were produced after the HFE oil was evaporated. Representative bright field microscope images of **(E)** droplets and **(F)** vortioxetine microspheres after purification. **(G)** SEM pictures and a component of the zoomed-in portion of vortioxetine microspheres. **(H)** showed the size distribution of vortioxetine microspheres from three batches (n=300 per batch). **Figure (A)**, **(C)**, and **(D)** were generated with Biorender.com.

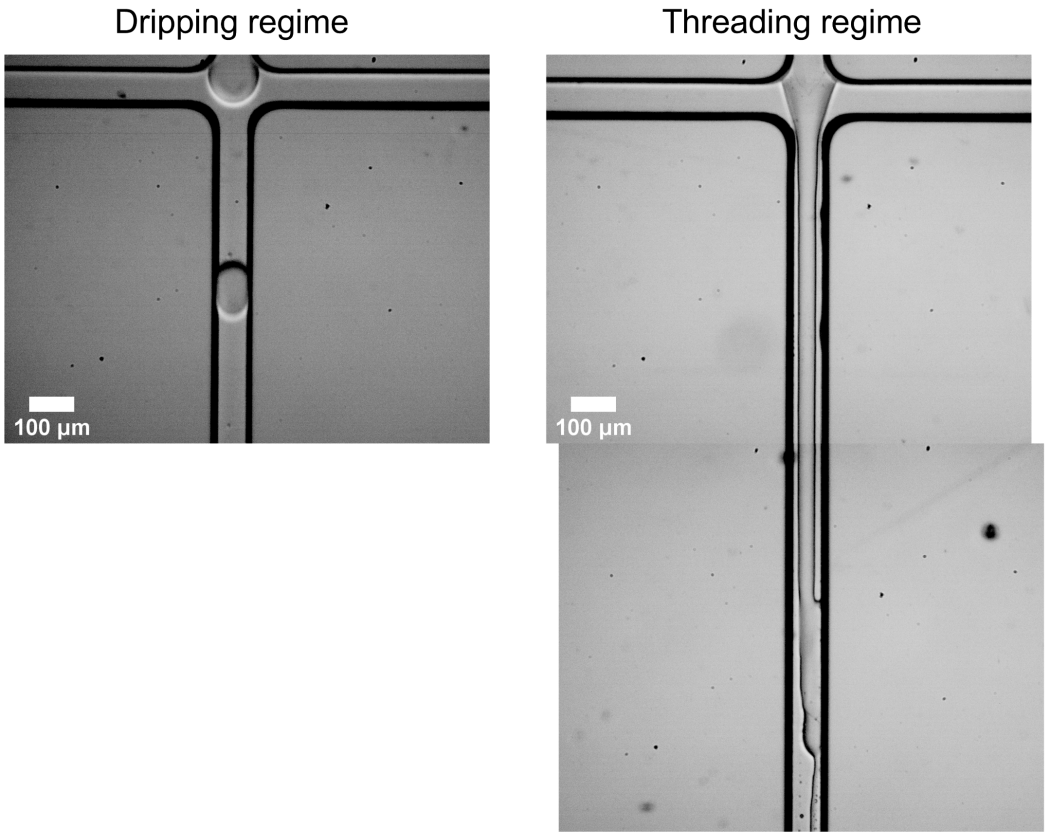

Figure 4-2 The droplet generation was unstable when using higher molecular weight PLGA (molecular weight range: 76,000-115,000) at a concentration of 100 µg/mL.

The dripping regime would switch to the threading regime.

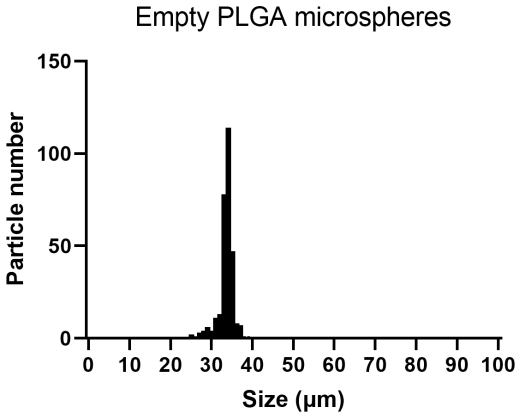

Figure 4-3 The size distribution of empty PLGA microspheres (n=300).

Figure 4-4 (A) shows the FTIR spectra of PLGA, vortioxetine, vortioxetine microspheres, and the physical mixture of vortioxetine and PLGA. The peaks of vortioxetine microspheres and the physical mixture did not change in comparison to the PLGA material, indicating no chemical interactions between vortioxetine and PLGA. The proportion of vortioxetine in the physical mixture affected the

intensity of the signature peaks of vortioxetine (**Figure 4-4 (B)**). The characteristic peaks of vortioxetine related to N-H stretching at 3240 cm^{-1}, =C-H stretching in aromatic at 3050 cm^{-1}, and C=C stretching in an aromatic ring at 1580, and 1470 cm^{-1} presented in the 1:1 weight ratio physical mixture without shifts, further confirming no chemical interactions.

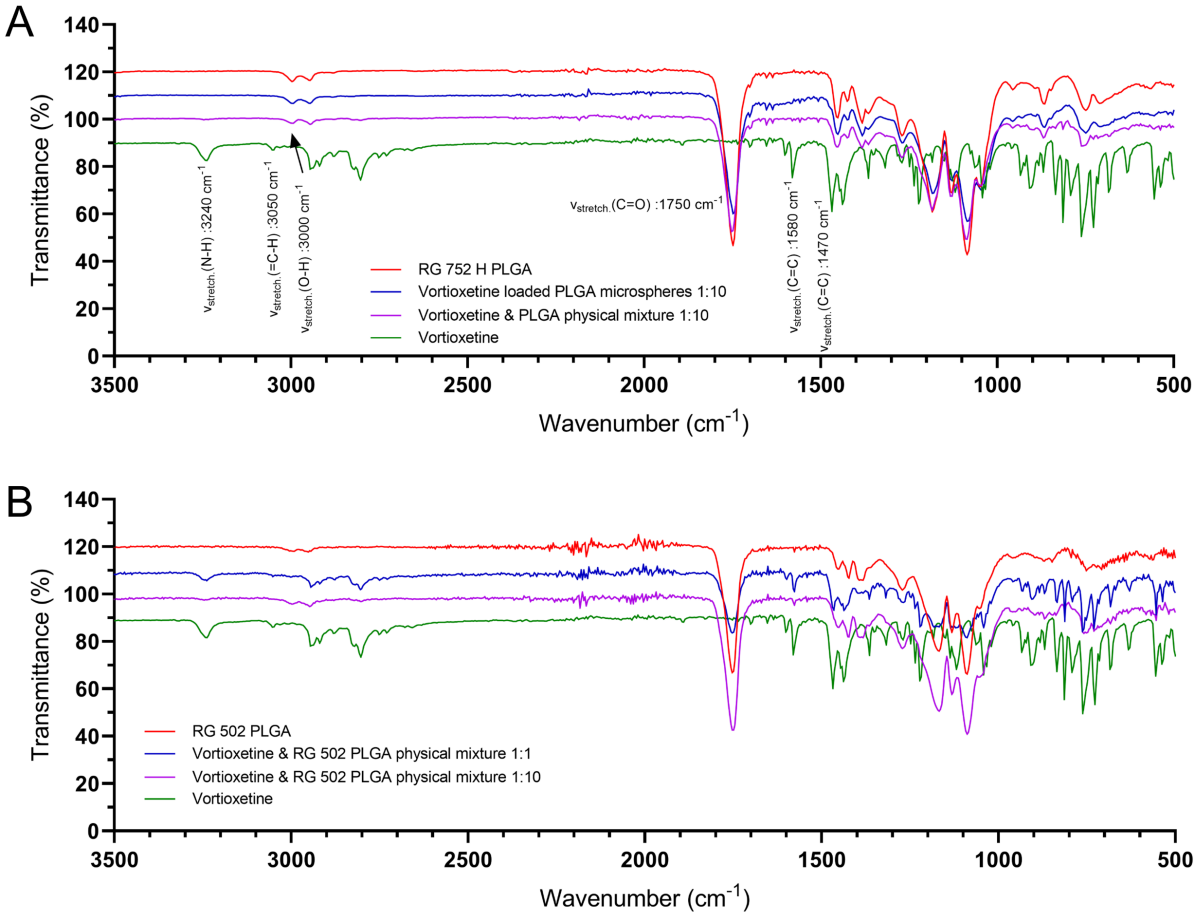

Figure 4-4 FTIR spectra of vortioxetine microspheres, a physical mixture of PLGA and vortioxetine, PLGA materials, and drug powder.

(A) shows the FTIR spectra of vortioxetine microspheres and a physical mixture with the same weight ratio. **(B)** shows the effect of the vortioxetine proportion in the physical mixture on the intensity of peaks, showing a large reduction in the peaks when only a small amount of the drug is present.

3.3 High vortioxetine loading efficiency is achieved in microspheres

To investigate the drug loading efficiency, vortioxetine microspheres with different weight ratios of drugs to PLGA were prepared. As shown in **Figure 4-5 (A)**, a 1:10 drug-to-polymer ratio showed the highest loading efficiency, with 90.06% ± 8.27% (n=3) of the drug being entrapped in the microspheres. As expected, the loading efficiency decreased when the ratio of drug to PLGA

increased, as drug molecules might leak from the droplets during solidification due to the reduced PLGA concentration. Therefore, a 1:10 ratio was used for the subsequent experiments (the percentage of drug loading: 9.1% (wt/wt)).

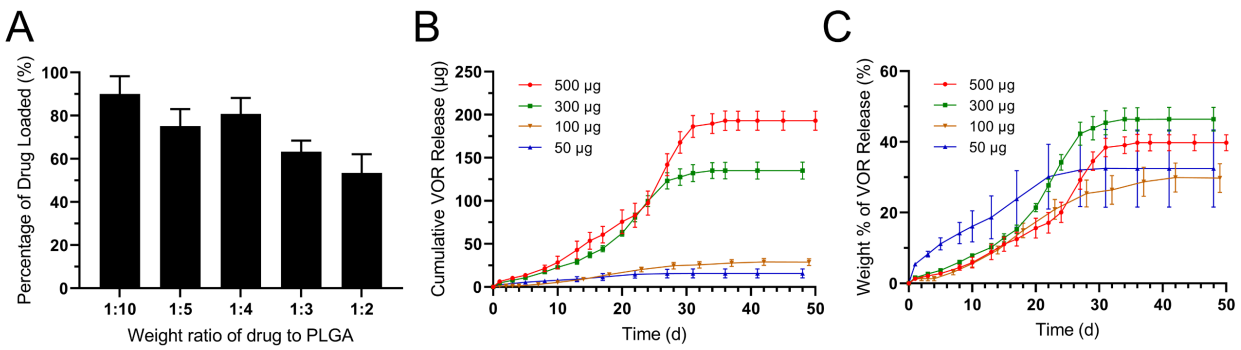

Figure 4-5 High drug loading efficiency and sustained drug release can be achieved with vortioxetine microspheres.

(A) shows the drug loading efficiency of vortioxetine microspheres at various weight ratios of drug to PLGA (n=3, error bars represent the mean ± SD). **(B)** and **(C)** show the amount and the weight percentage of cumulative drug release over time from the vortioxetine microspheres (1:10 weight ratio) (n=4, error bars represent the mean ± SD). The legend shows the amount of vortioxetine in release samples. Abbreviation: VOR: vortioxetine.

3.4 Vortioxetine is sustained released from the microspheres

The drug release study was conducted in pure PBS medium. As shown in **Figure 4-5 (B)** and **(C)**, vortioxetine microspheres did not show a burst release and could sustain drug release for more than one month. Samples with 300 and 500 µg of drug had an obvious bi-phasic drug release pattern, whilst 50 and 100 µg samples did not show a significant increase in release rate during the experiment. The drug release rate was nearly zero-order kinetics for the first phase. The release rate of the 300 and 500 µg samples increased between Day 27-31 and Day 20-27, respectively. Large microspheres usually have a tri-phase release profile.(336) The drug trapped on or close to the surface of the microspheres is released in the initial burst release.(337) PLGA microspheres with high porosity at the surface have previously exhibited a burst release pattern.(338) The sigmoidal shape of the drug release pattern was likely due to the degradation/erosion of PLGA, creating pores from which encapsulated drugs are released by diffusion. The absence of a burst release in these studies may be due to an even drug distribution in the polymer network and a smooth/low porosity surface for degradation/erosion to occur.

3.5 Cytocompatibility of empty microspheres

Astrocytes were used to evaluate the cytocompatibility of empty PLGA microspheres for their high prevalence and key support role in the central nervous system. 100 µg/mL empty PLGA microspheres were incubated with human astrocytes (hAstrocytes), to match the highest concentration of vortioxetine microspheres used in subsequent experiments. As shown in **Figure 4-6 (A)**, no changes in the morphology of hAstrocytes were observed when incubated with the microspheres, nor any reduction in viability at either Day 1, 4, or 7 (**Figure 4-6 (B)**). These results indicate that the new preparation method for PLGA microspheres does not incorporate any toxic compounds into the final product.

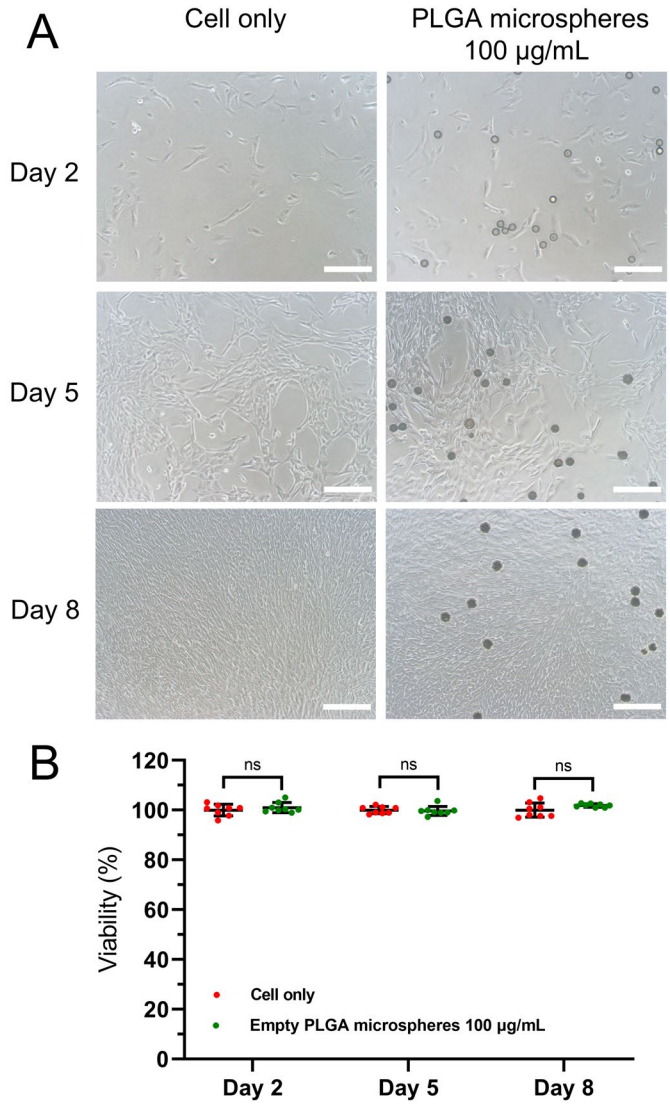

Figure 4-6 Empty PLGA microspheres cause no toxicity to primary human astrocytes.

(A) shows representative images of human astrocytes incubated with or without 100 µg/mL empty PLGA microspheres. Empty PLGA microspheres were added on Day 1. The dark circular shapes are

the microspheres. Images were taken on Day 2, 5, and 8(Scale bar = 200 µm). **(B)** shows the cell viability on Day 2, 5, and 8 (n=8, error bars represent the mean ± SD). Unpaired t-test Day 2 and Day 5, Welch's t-test Day 8, ns = no significant difference.

3.6 Cytotoxicity of free vortioxetine

The cytotoxicity of free vortioxetine was investigated on hAstrocytes and three patient-derived GBM cells (hGBM L0, L1, L2). The differences of protein expression among these three GBM cell lines included only hGBM L1 expressing OLIG2 and CD44 and hGBM L2 not expressing TOP2A and NF1.(232) The cytotoxicity of the vector was checked, and the results showed the cell viability was not affected (**Figure 4-7**). As shown in **Figure 4-8**, vortioxetine exhibited a time-dependent and dose-dependent toxicity. The IC_{50} values on all hGBM cell lines were around 1 µg/mL on Day 1 (**Table 4-3**). On Day 5, hGBM L2 was the most sensitive hGBM cell line to vortioxetine, whilst hGBM L0 was the most resistant cell line. However, the IC_{50} value of hAstrocytes was doubled even compared to hGBM L0 (1.48 µg/mL *vs* 0.75 µg/mL), which meant that there was potentially a decent therapeutic window to minimize the side effects to healthy/non-malignant cells. The IC_{50} values of free temozolomide, the first line chemotherapeutic in clinic for glioblastoma, on hAstrocytes and hGBM cell lines, were tens of times higher than that of the vortioxetine (e.g., 311.9 µg/mL on hAstrocytes and 23.09 µg/mL on hGBM L0 treated for 4 days; **Figure 4-9**, **Table 4-4**). Although temozolomide also had a therapeutic window, it was more toxic towards hAstrocytes on Day 8 compared to Day 5, indicating a delayed but substantial toxicity towards hAstrocytes.

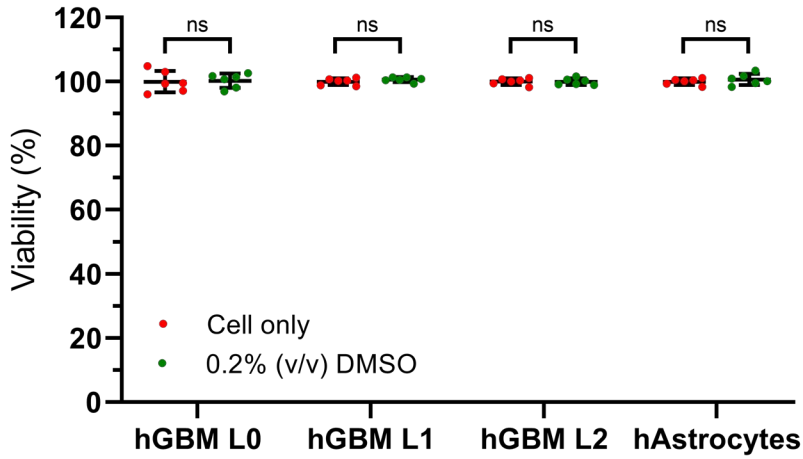

Figure 4-7 The DMSO concentration used does not affect cell viability.

0.2% (v/v) DMSO equalled the volume proportion at 10 µg/mL free vortioxetine diluted from the stock solution (5 mg/mL in pure DMSO). At this concentration, no significant reduction in the

viability of the three glioblastoma cell types and primary human astrocytes was observed (n=6, error bars represent the mean ± SD; unpaired t-test, ns = no significant difference).

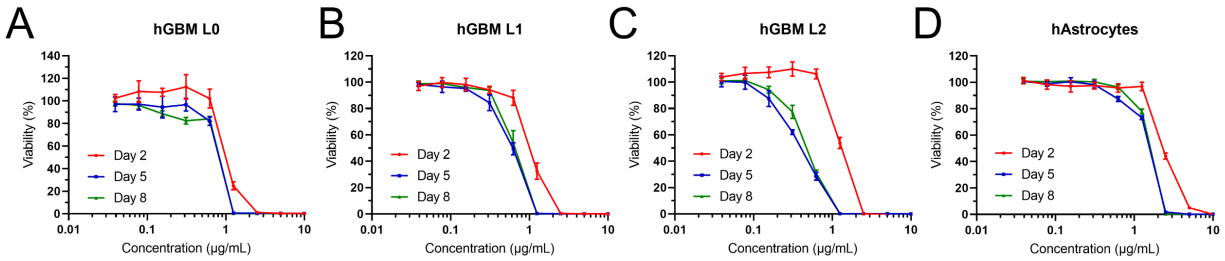

Figure 4-8 The dose-respond curves of free vortioxetine.

(A, B, and **C):** hGBM cell lines, **(D):** hAstrocytes (n=6, error bars represent the mean ± SD).

Table 4-3 IC_{50} values of free vortioxetine on hGBM cells and hAstrocytes (μg/mL)

	hGBM L0		**hGBM L1**		**hGBM L2**		**hAstrocytes**	
	IC_{50}	SD	IC_{50}	SD	IC_{50}	SD	IC_{50}	SD
Day 2	1.02	0.08	1.06	0.05	1.25	0.03	2.41	0.07
Day 5	0.75	0.13	0.62	0.03	0.39	0.02	1.48	0.08
Day 8	0.77	0.18	0.65	0.02	0.47	0.02	1.44	0.08

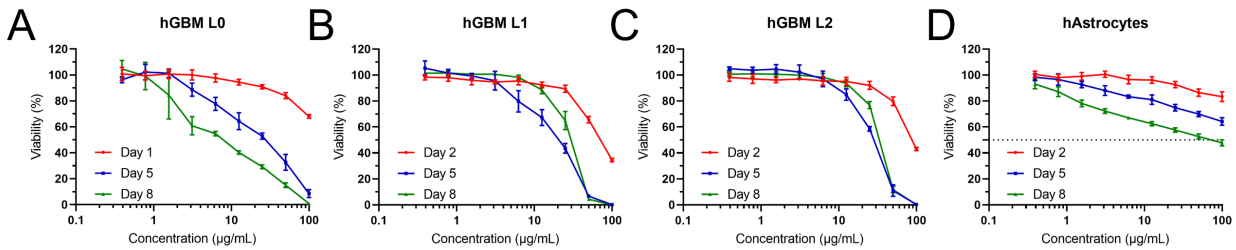

Figure 4-9 The dose-respond curves of free temozolomide.

(A, B, and **C):** hGBM cell lines, **(D):** hAstrocytes (n=6, error bars represent the mean ± SD).

Table 4-4 IC_{50} values of free temozolomide on hGBM cells and hAstrocytes (μg/mL)

	hGBM L0		**hGBM L1**		**hGBM L2**		**hAstrocytes**	
	IC_{50}	SD	IC_{50}	SD	IC_{50}	SD	IC_{50}	SD
Day 2	198.8	42.06	71.37	4.39	89.34	5.55	853.1	613.8
Day 5	23.09	2.67	18.21	1.81	26.78	1.58	311.9	116.0
Day 8	7.82	1.55	28.24	1.12	32.33	0.95	59.19	13.80

Previous research showed that the IC_{50} value of vortioxetine on the LN-229 GBM cell line was around 5 μM (1.5 μg/mL) and around 20 μM (6.0 μg/mL) for the ZH-161 cell line after 48 h treatment.(118) The *in vivo* dosage for these two types of tumour models was 10 mg/kg via intraperitoneal administration, which showed significant survival benefit compared to the negative

control. Based on the IC_{50} value on hGBM cell lines, the growth of these tumour models in animal studies should be effectively suppressed by vortioxetine.

3.7 Anti-GBM efficacy of vortioxetine microspheres

Geltrex basement membrane matrix was used to culture hGBM cell lines as adherent cells to investigate the *in vitro* antitumor efficacy of vortioxetine microspheres in 2D models. As shown in **Figure 4-10**, **4-11**, and **4-12**, empty PLGA microspheres did not reduce the viability of hGBM cells after 7 days of incubation (hGBM L0: 98.78% ± 7.86%; hGBM L1: 99.51% ± 2.38%; hGBM L2: 97.80% ± 5.55%; n=5 for each cell line). 1.25 μg/mL free drug killed nearly all tumour cells after one day of incubation (hGBM L0: 5.28% ± 0.36%; hGBM L1: 12.15% ± 3.73%; hGBM L2: 1.68% ± 0.17%; n=4 for each cell line). Vortioxetine microspheres showed a time- and dose-dependent efficacy. Compared with cells treated with 1.25 μg/mL free drug, the cell viability of 10 μg/mL vortioxetine microspheres on Day 2 (hGBM L0: 76.97% ± 10.54%; hGBM L1: 86.34% ± 10.08%; hGBM L2: 65.17% ± 16.89%; n=5 for each cell line) was significantly higher, which confirmed that microspheres did not exhibit a burst release of the drug. The sensitivity of three hGBM cell lines to vortioxetine also matched with the previous IC_{50} experiment (**Figure 4-8**). This can be concluded because the drug release data showed about 6%, 15% and 20% payload release after 1, 4, and 7 days of the incubation, respectively which fits with the microsphere efficacy data (**Figure 4-10**, **4-11**, and **4-12**) and with the dose-response curve of free vortioxetine (**Figure 4-8**). The cytotoxicity of vortioxetine microspheres was also evaluated on hAstrocytes (**Figure 4-13**). The cell viability was 58.63% ± 11.53% (n=5) after being treated with 10 μg/mL vortioxetine microspheres for 7 days, which was much higher than that of hGBM cell lines. 5 μg/mL vortioxetine microspheres did not significantly reduce the cell viability of hAstrocytes (87.50% ± 7.51%, n=5) compared to the negative control (p=0.1831) on Day 8, but this concentration was not enough to kill the resistant tumour cells such as hGBM L0. So, 5-10 μg/mL is the optimal dose range for vortioxetine microspheres to eradicate GBM cells, depending on the resistance of the cell lines.

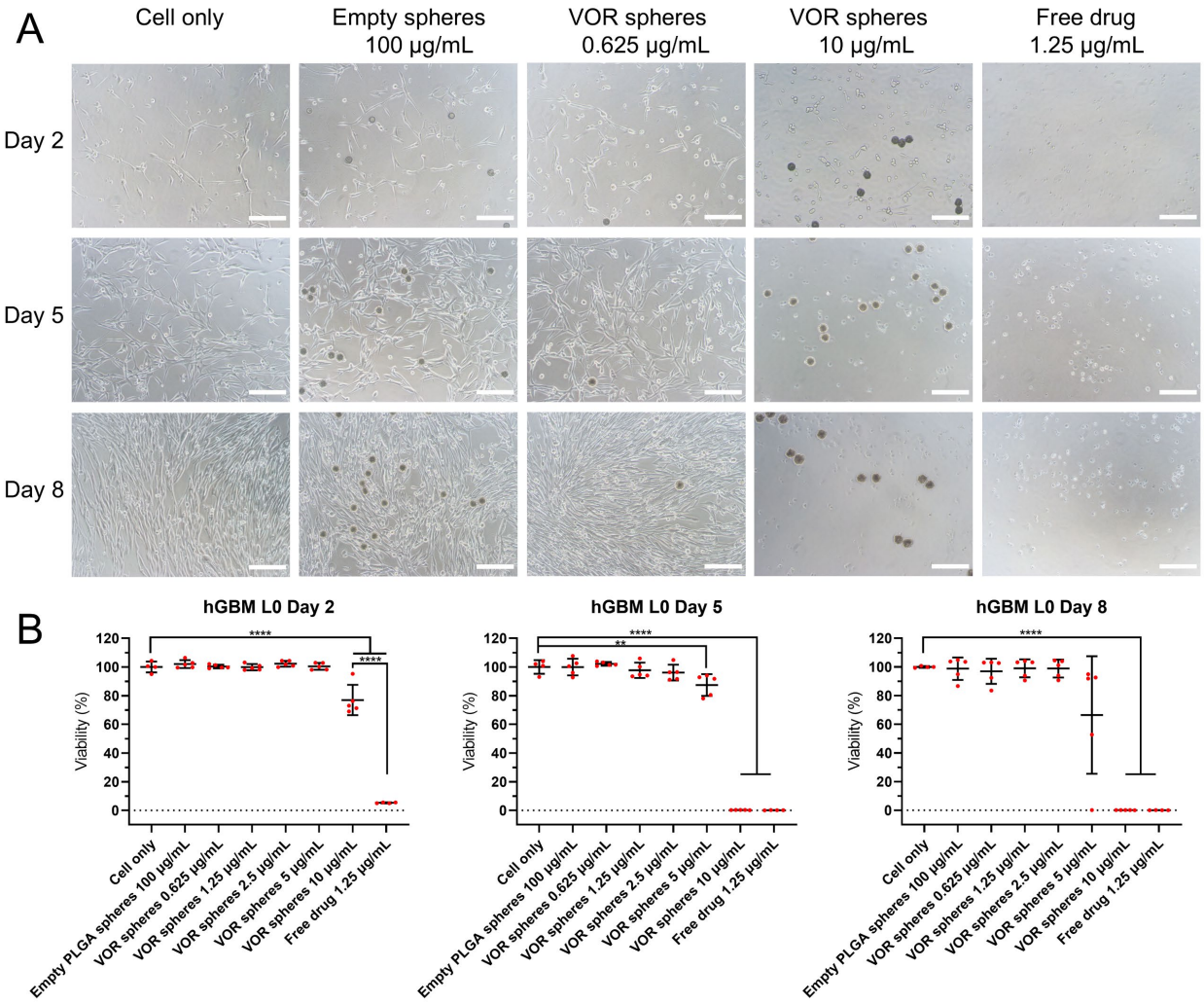

Figure 4-10 Vortioxetine microspheres reduce the viability of hGBM L0 cells.

(A) shows representative bright field images of hGBM L0 cells incubated with culture medium only, empty PLGA microspheres 100 µg/mL, vortioxetine microspheres 10 or 0.625 µg/mL and free vortioxetine 1.25 µg/mL. PLGA microspheres were added on Day 1. Images were taken on Day 2, 5, and 8 (Scale bar = 200 µm). The dark circular shapes are the microspheres. **(B)** shows the cell viability on Day 2, 5, and 8 (Empty PLGA microspheres and vortioxetine microspheres, n=5; cell only and free drug, n=4; mean ± SD). Ordinary one-way ANOVA test for all time points, for ** $p \leq 0.01$, **** $p \leq 0.001$. Abbreviation: VOR: vortioxetine.

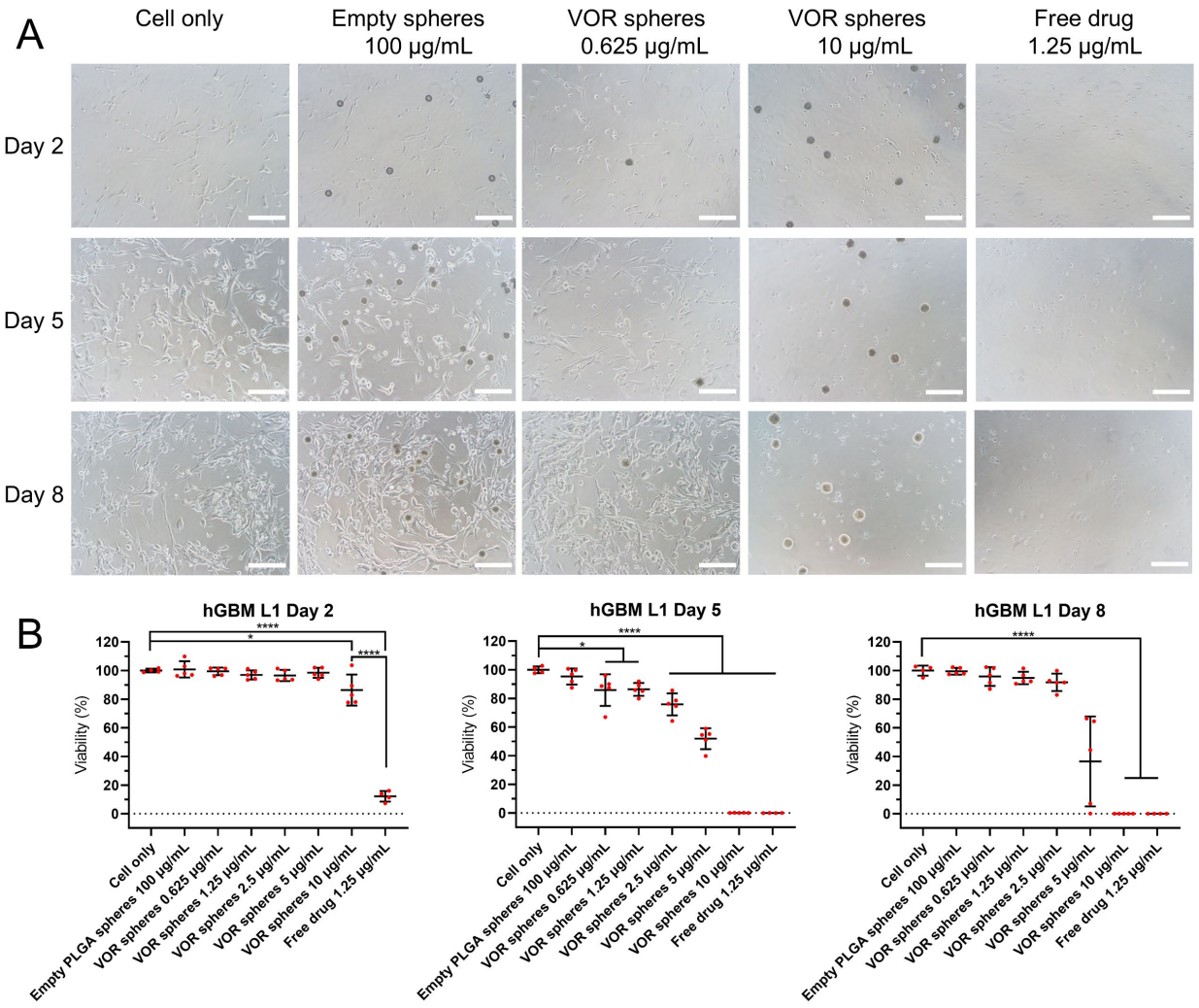

Figure 4-11 Vortioxetine microspheres reduce the viability of hGBM L1 cells.

(A) shows representative bright field images of hGBM L1 cells incubated with culture medium only, empty PLGA microspheres 100 µg/mL, vortioxetine microspheres 10 or 0.625 µg/mL, and free vortioxetine 1.25 µg/mL. PLGA microspheres were added on Day 1. Images were taken on Day 2, 5, and 8 (Scale bar = 200 µm). The dark circular shapes are the microspheres. **(B)** shows the cell viability on Day 2, 5, and 8 (Empty PLGA microspheres and vortioxetine microspheres, n=5; cell only and free drug, n=4; mean ± SD). Ordinary one-way ANOVA test: Day 2 and Day 5, Welch ANOVA test: Day 8, for * $p \leq 0.05$, **** $p \leq 0.001$. Abbreviation: VOR: vortioxetine.

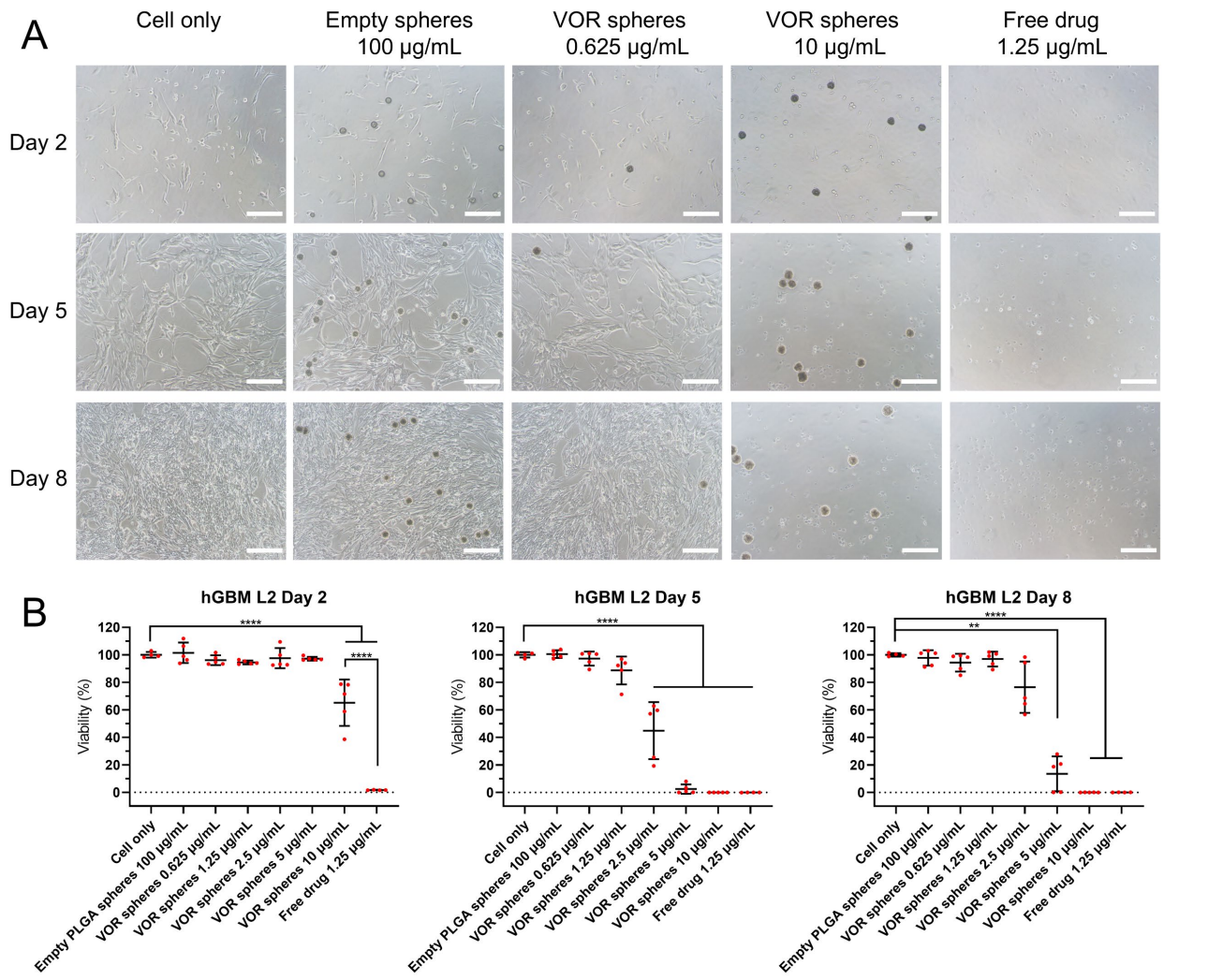

Figure 4-12 Vortioxetine microspheres reduce the viability of hGBM L2 cells.

(A) shows representative bright field images of hGBM L2 cells incubated with culture medium only, empty PLGA microspheres 100 µg/mL, vortioxetine microspheres 10 or 0.625 µg/mL, and free vortioxetine 1.25 µg/mL. PLGA microspheres were added on Day 1. Images were taken on Day 2, 5, and 8 (Scale bar = 200 µm). The dark circular shapes are the microspheres. **(B)** shows the cell viability on Day 2, 5, and 8 (Empty PLGA microspheres and vortioxetine microspheres, n=5; cell only and free drug, n=4; mean ± SD). Ordinary one-way ANOVA test: Day 2 and Day 5, Welch ANOVA test: Day 8, for ** $p \leq 0.01$, **** $p \leq 0.001$. Abbreviation: VOR: vortioxetine.

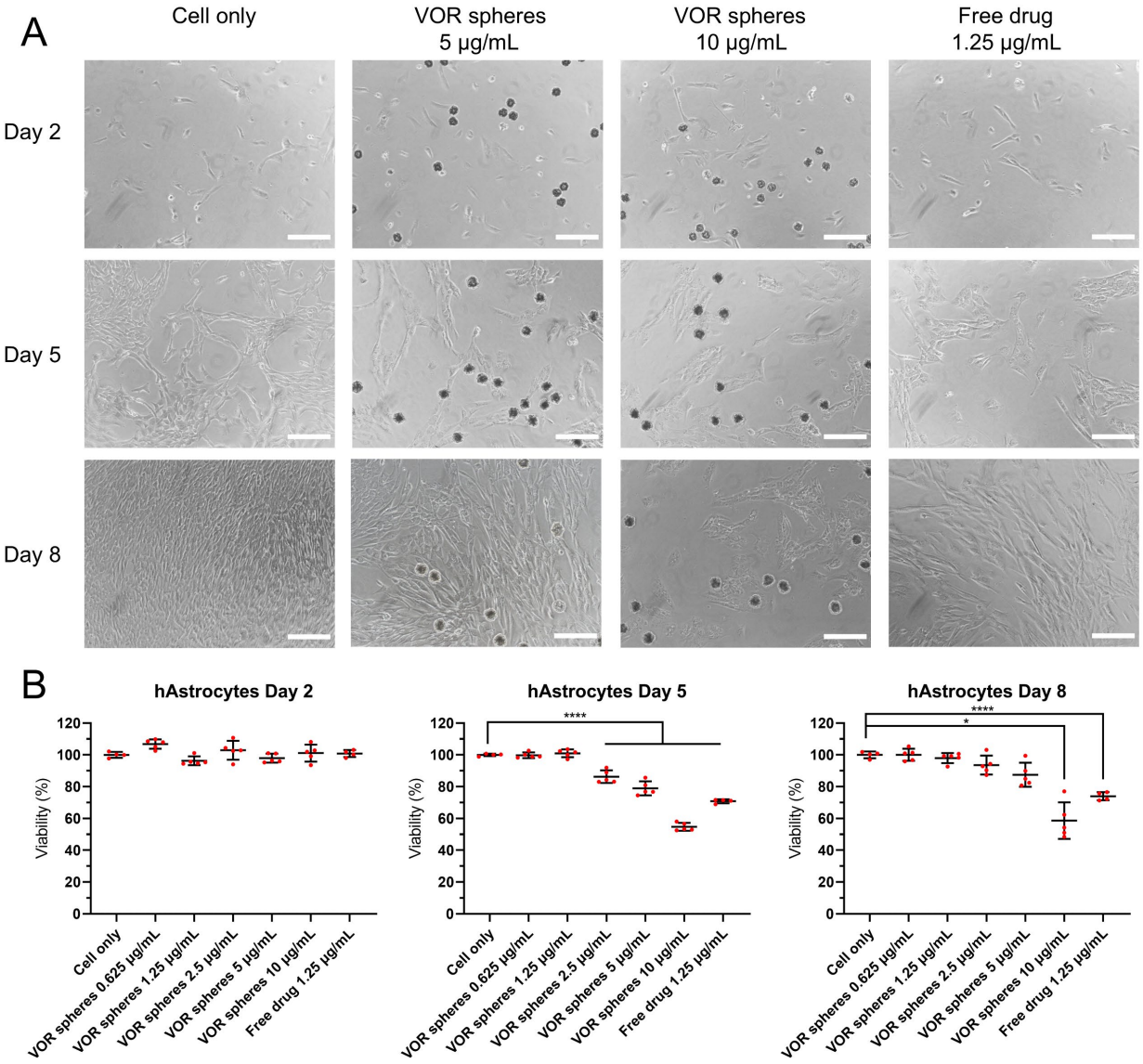

Figure 4-13 The cytotoxicity of vortioxetine microspheres on primary human astrocytes.

(A) shows representative bright field images of primary human astrocytes during the treatment. **(B)** shows the cell viability on Day 2, Day 5 and Day 8 (Vortioxetine microspheres, n=5; cell only and free drug, n=4; error bars represent the mean ± SD. Ordinary one-way ANOVA test: Day 2 and Day5, Welch ANOVA test: Day 7, for * $p \leq 0.05$, **** $p \leq 0.001$). PLGA microspheres were added on Day 1. Abbreviation: VOR: vortioxetine.

3.8 Vortioxetine microspheres effectively destroy the hGBM 3D tumour spheroids

Monolayer cell cultures lack physiological relevance to the *in vivo* environment, perhaps contributing to the high failure rate of drug candidates entering phase I trials.(296) 3D cell culture models have gained more attraction in drug discovery because they better mimic the *in vivo* situation in terms of cell proliferation, cell-cell interaction, and protein expression.(339) 3D cultured hepatocellular carcinoma cells showed organoid-like features which mimicked the *in vivo*

conditions of glandular epithelium, such as acinar morphogenesis and expression of progenitor cell markers.(340) Oskarsson et al. found that 3D tumour spheroids upregulated the expression of embryonic stem cell markers while they downregulated the expression of differentiation markers compared to monolayer cell culture, which suggested the correlation to the *in vivo* microenvironment in stem cell niches.(341) 3D model also increased the expression of drug resistance-related genes.(342) Furthermore, 3D cell culture models showed an enhancement of GBM stemness and chemotherapy resistance compared to 2D cell culture models.(343) Ma et al. found that the gene expression of GBM cells dramatically changed when comparing 2D and 3D cell culture models,(344) and indicated that a 3D cell culture model was a more relevant platform for drug screening. We used round bottom ultra-low attachment well plates to culture hGBM L0 and L2 as 3D spheroids via the forced floating method.

Figure 4-14 shows the representative images of hGBM L2 spheroids cultured with 1.25 or 10 µg/mL vortioxetine microspheres, 1.25 µg/mL free drug or without treatment. The alive spheroids had a clear edge and became less transparent during the experiment. Dead spheroids lost cell attachments and broke off, resulting in a larger area of dead cells than the spheroid. Comparing the images on Day 4 and Day 6, the size of the PLGA microspheres grew through swelling in aqueous medium (the dark circles scattered throughout the image are the microspheres). The PLGA microspheres kept the integrated structure even after 14 days of incubation. Compared to the cell-only control, vortioxetine microspheres suppressed the growth of cell spheroids in a dose-dependent manner (**Figure 4-15 (A)**, the size of cell spheroids on Day 18: cell-only control: 997,243 ± 20,954 μm^2, n=6; 1.25 µg/mL vortioxetine microspheres: 890,154 ± 207,720 μm^2, n=8; 2.5 µg/mL vortioxetine microspheres: 740,423 ± 108,214 μm^2, n=8; 5 µg/mL vortioxetine microspheres: 371,084 ± 245,057 μm^2, n=8; 10 µg/mL vortioxetine microspheres: 106,660 ± 12,100 μm^2, n=8; 1.25 µg/mL free drug: 90,434 ± 38,988 μm^2, n=6). 1.25 µg/mL vortioxetine microspheres could not reduce the growth of cell spheroids during the 14-day period. However, when the concentration reached 2.5 µg/mL, cell spheroids were significantly smaller than the no treatment group. 5 µg/mL vortioxetine microspheres killed 5 of 8 cell spheroids during the 14 days (**Figure 4-15 (B)**). 10 µg/mL vortioxetine microspheres resulted in complete destruction of all the spheroids after 4 days. Directly adding 1.25 µg/mL free vortioxetine resulted in the rapid killing of the spheroids after only 1 day (cell viability: 0.73% ± 0.21%, n=6). Together, these results confirm that vortioxetine microspheres exhibited no initial burst release, which could have compromised their safety.

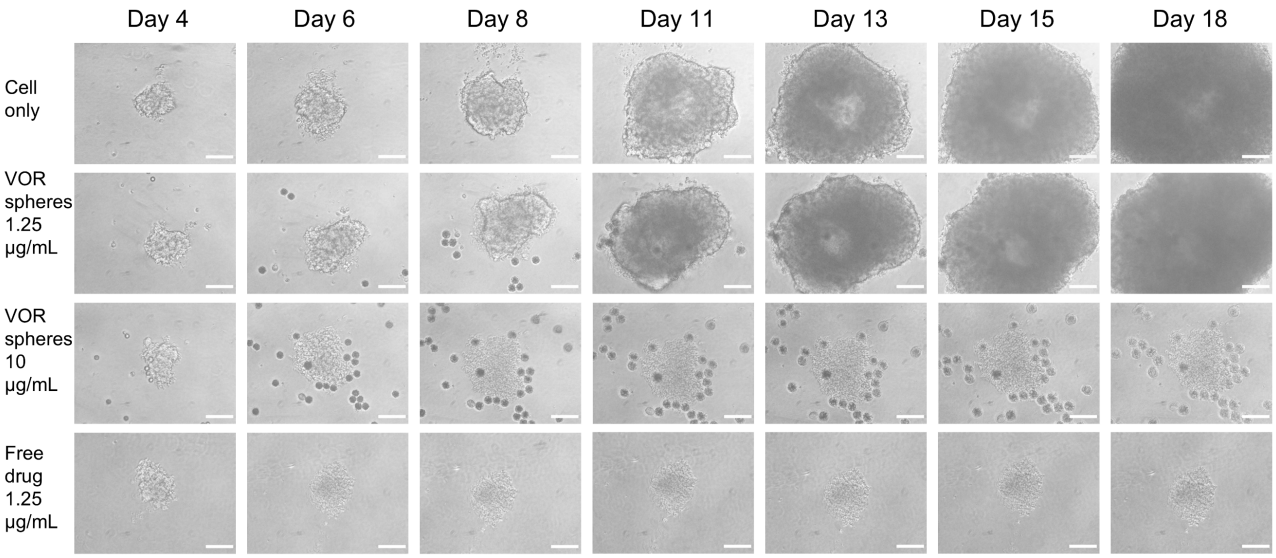

Figure 4-14 Vortioxetine microspheres suppress the growth of hGBM L2 spheroids.

Representative bright field images of hGBM L2 3D spheroids incubated with culture medium only, vortioxetine microspheres 10 or 1.25 µg/mL, and free vortioxetine 1.25 µg/mL (Scale bar = 200 µm). PLGA microspheres were added on Day 4 and can be seen as dark circular shapes. Abbreviation: VOR: vortioxetine.

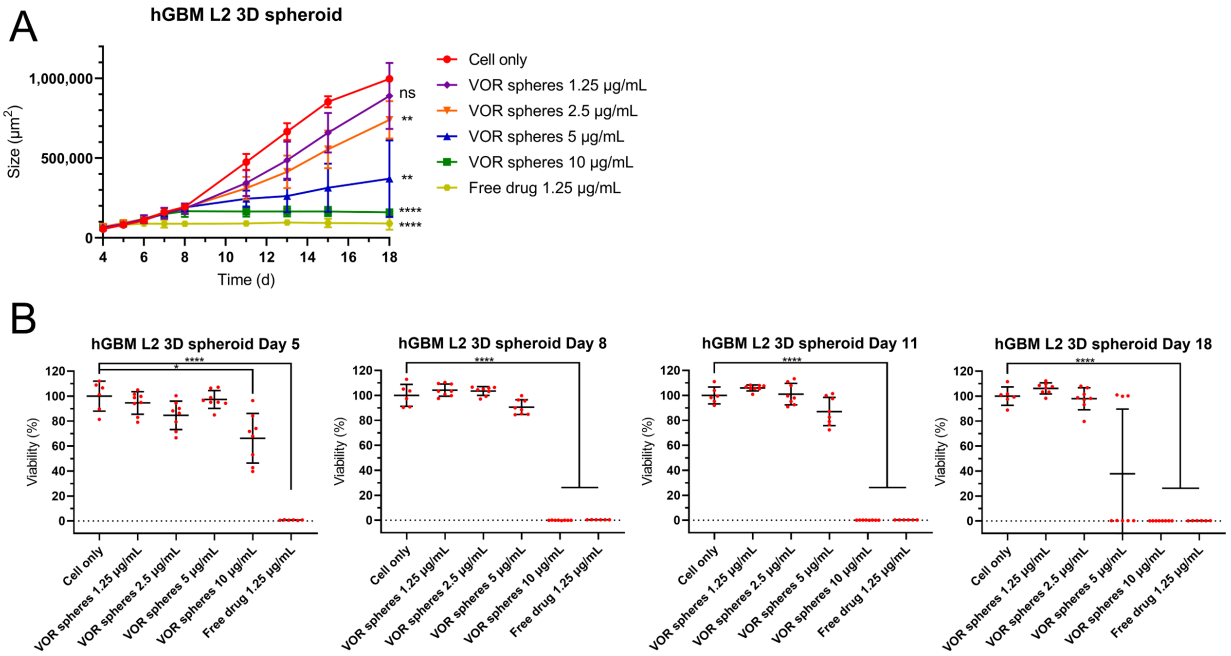

Figure 4-15 Vortioxetine microspheres reduce cell viability of hGBM L2 spheroids.

(A) shows the size of hGBM L2 3D spheroids incubated with vortioxetine microspheres (Cell only and free drug, n=6; vortioxetine microspheres, n=8; mean ± SD). **(B)** shows the cell viability on Day 5, 8, 11, and 18 (Cell only and free drug, n=6; vortioxetine microspheres, n=8; mean ± SD). **(A)** Two-way ANOVA test. The statistically significant difference compared to cell only. **(B)** Welch ANOVA

test. For ns = no significant difference, * $p \leq 0.05$, ** $p \leq 0.01$, **** $p \leq 0.001$ Abbreviation: VOR: vortioxetine.

Although the cell viability of cell spheroids cultured with 2.5 and 5 µg/mL vortioxetine microspheres was not significantly different from the non-treatment group, these concentrations could effectively suppress the growth of hGBM cell spheroids. 5 µg/mL vortioxetine microspheres significantly decreased the cell viability of hGBM L2 2D culture model by Day 8, but not in the 3D culture model indicating higher drug resistance in the 3D culture model. This could potentially be due to differences in cell proliferation, metabolism, and communication, between 2D and 3D cultures. In the most resistant hGBM L0 model, 10 µg/mL vortioxetine microspheres killed the spheroids in the early stage of spheroid development with the dead cells separating over a larger area than the viable spheroids, but 5 µg/mL vortioxetine microspheres did not suppress the cell growth (**Figure 4-16** and **4-17**). Next, the efficacy of vortioxetine microspheres against a grown 3D spheroid was evaluated by postponing the starting date of the treatment to Day 7. 10 µg/mL vortioxetine microspheres significantly decreased the size of the hGBM L0 spheroids compared to the negative control on Day 16 (932,034 ± 151,200 μm^2 *vs* 1,269,770 ± 71,657μm^2, n=8, **Figure 4-18** and **4-19**). The no significant difference in the cell viability between the vortioxetine microsphere treatment and control group on Day 16 (**Figure 4-19 (C)**) might be because of the limited penetration of the 3D spheroids for PrestoBlue reagent. Similar results were observed on hGBM L2 spheroids (**Figure 4-20** and **4-21**). These results further proved the efficacy of vortioxetine against GBM in all experimental parameters tested, providing a rationale for further analysis as a new therapeutic strategy for glioblastoma.

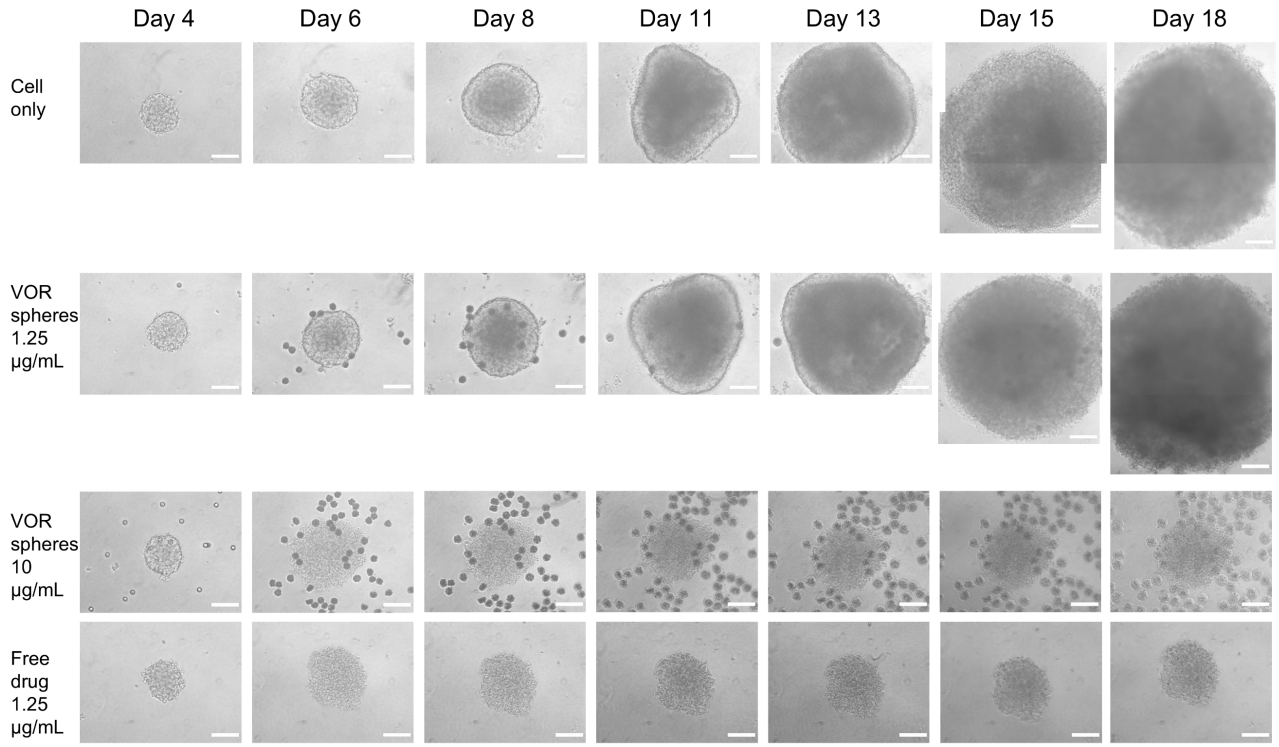

Figure 4-16 Representative bright field images of hGBM L0 3D spheroids during treatment with vortioxetine-loaded spheres and free drug (Scale bar = 200 µm).

PLGA microspheres were added on Day 4, and the high concentration resulted in a reduction in spheroid growth. Abbreviation: VOR: vortioxetine.

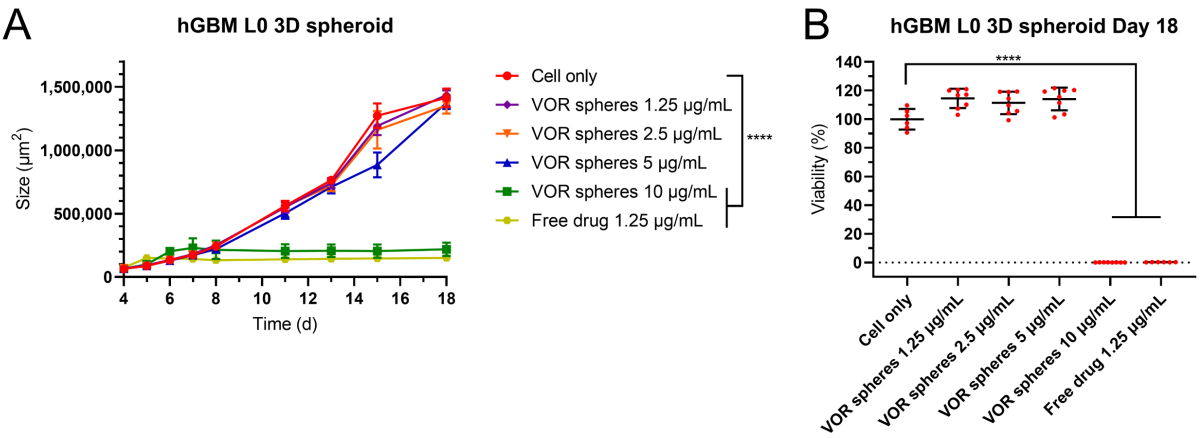

Figure 4-17 Vortioxetine microspheres eradicate the more resistant hGBM L0 3D spheroids at the higher concentration.

(A) shows the size of the hGBM L0 3D spheroids during the treatment (Cell only and free drug, n=6; vortioxetine microspheres, n=8. Asterisks represent the statistically significant difference compared to cell only control on Day 18 (Two-way ANOVA test, for **** $p \leq 0.0001$). **(B)** shows the

corresponding cell viability at the end of the experiment (Welch ANOVA test). Abbreviation: VOR: vortioxetine. Error bars represent the mean ± SD.

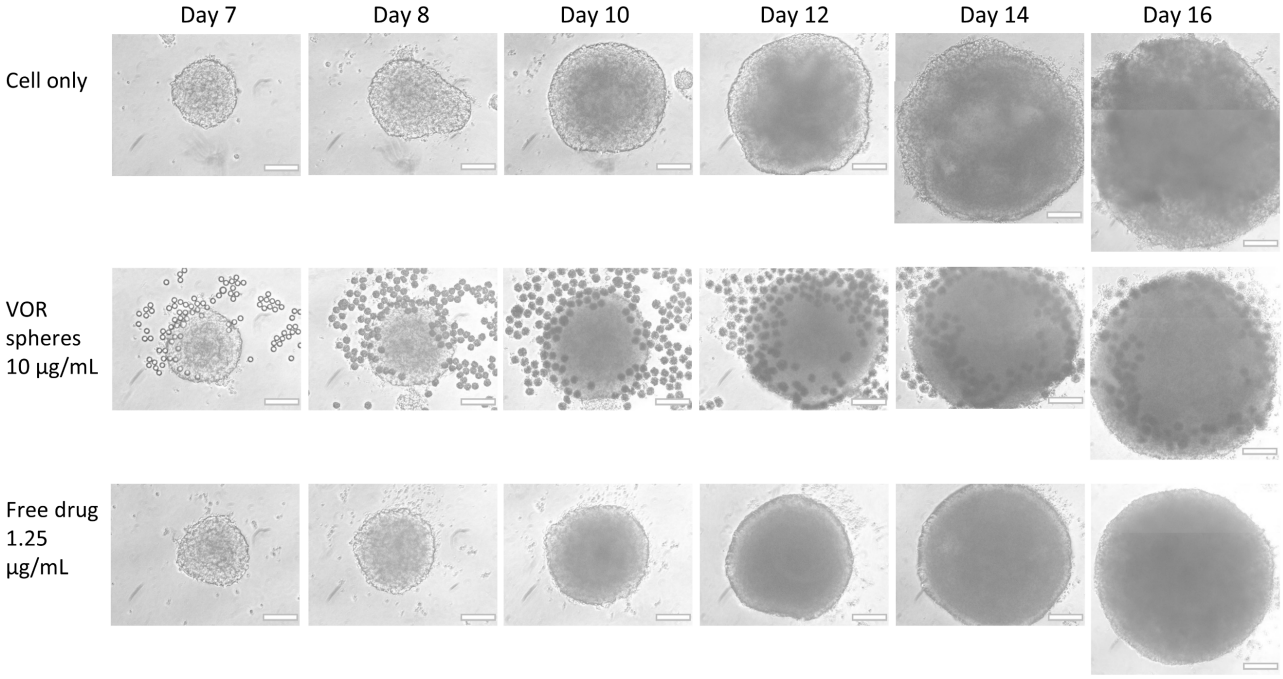

Figure 4-18 Representative bright field images show vortioxetine microspheres against the pre-established (grown) hGBM L0 3D spheroids (Scale bar = 200 µm).

PLGA microspheres were added on Day 7. Abbreviation: VOR: vortioxetine.

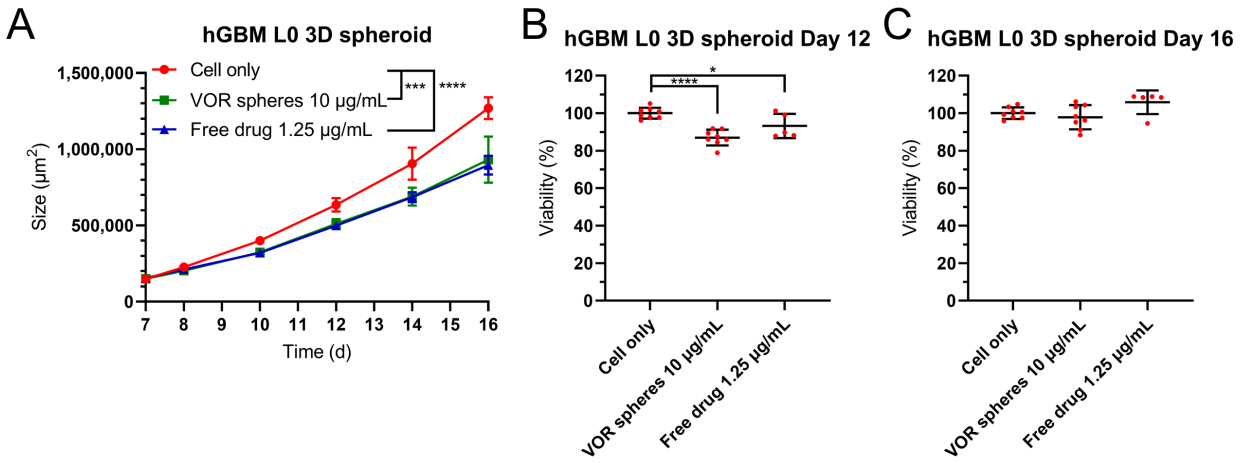

Figure 4-19 Vortioxetine microspheres reduce the size of the pre-established (grown) hGBM L0 3D spheroids.

(A) shows the size changes during the treatment. Asterisks represent the statistically significant on Day 16 (Two-way ANOVA test, cell only and vortioxetine microspheres: n=8; free drug: n=5. **(B)** and **(C)** show the cell viability on Day 12 and Day 16, respectively. **(B)**: Ordinary one-way ANOVA test. **(C)**: Nonparametric Kruskal-Wallis test. For * $p \leq 0.05$, *** $p \leq 0.001$, **** $p \leq 0.0001$. PLGA

microspheres were added on Day 7. Abbreviation: VOR: vortioxetine. Error bars represent the mean ± SD.

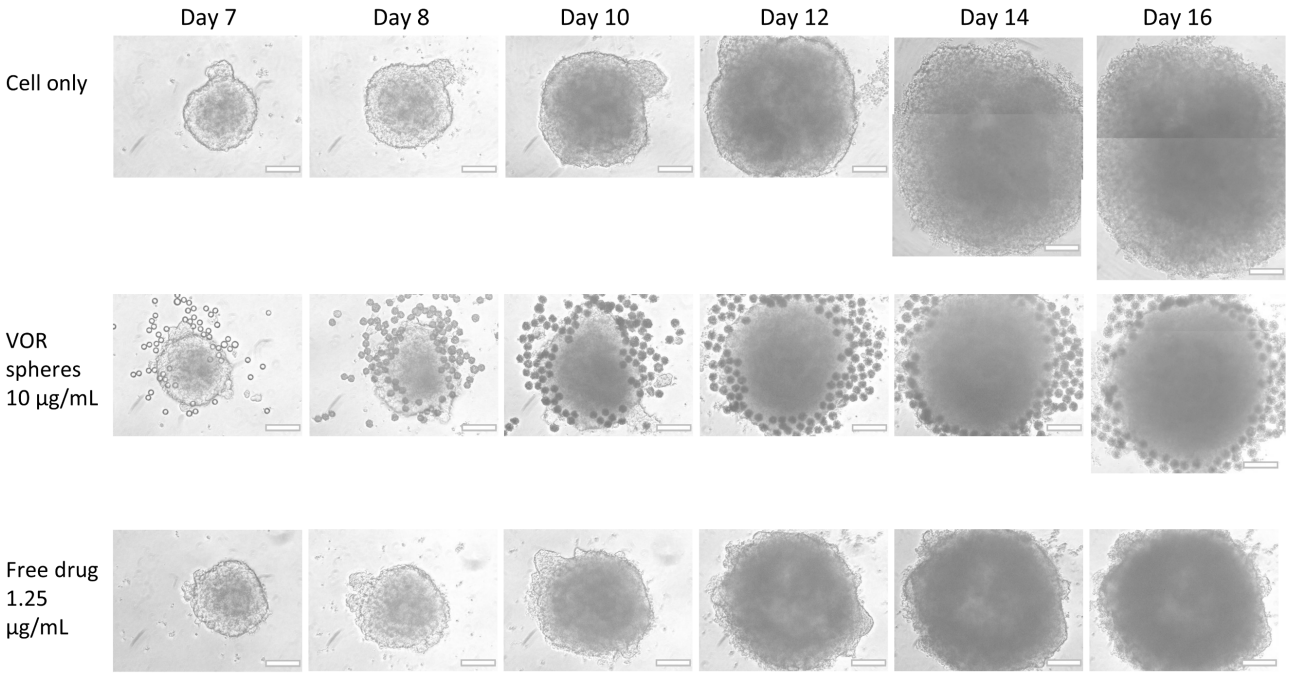

Figure 4-20 Representative bright field images show vortioxetine microspheres against the pre-established (grown) hGBM L2 3D spheroids (Scale bar = 200 µm).

PLGA microspheres were added on Day 7. Abbreviation: VOR: vortioxetine.

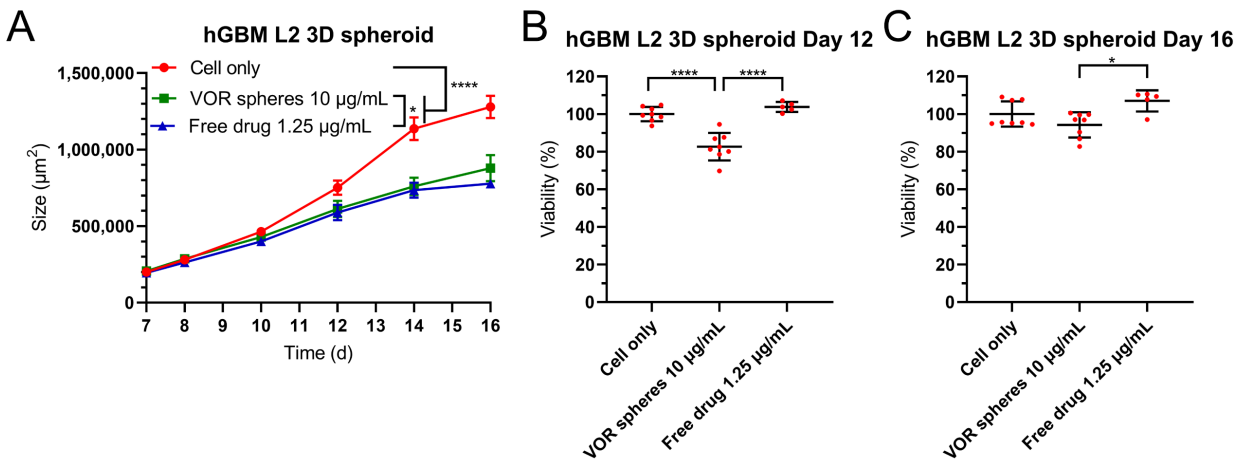

Figure 4-21 Vortioxetine microspheres reduce the size of the pre-established (grown) hGBM L2 3D spheroids.

(A) shows the size changes during the treatment. Asterisks represent the statistically significant on Day 16 (Two-way ANOVA test, cell only and vortioxetine microspheres: n=8; free drug: n=5). **(B)** and **(C)** show the cell viability on Day 12 and Day 16, respectively. **(B)**: Ordinary one-way ANOVA

test. **(C)**: Nonparametric Kruskal-Wallis test. For * $p \leq 0.05$, **** $p \leq 0.0001$. PLGA microspheres were added on Day 7. Abbreviation: VOR: vortioxetine. Error bars represent the mean ± SD.

4. Conclusions

In summary, we developed a new method to prepare PLGA microspheres by droplet-based microfluidics with a new oil-in-oil emulsion formula. Vortioxetine, the drug proposed to be repurposed as a GBM therapy, was loaded into the PLGA microspheres with high loading efficiency. Drug release patterns showed that PLGA microspheres released drugs in a bi-phasic manner, and no initial burst release was observed. Drugs were released with near zero-order for around three weeks, followed by one week of faster degradation-controlled release. Empty PLGA microspheres exhibited good cytocompatibility towards astrocytes. The IC_{50} value of the free vortioxetine on astrocytes *vs* glioblastoma cells suggested that there is a therapeutic window, minimizing the toxicity to healthy cells. Vortioxetine microspheres showed efficacy against hGBM cells as 2D monolayer cell culture models and as a 3D spheroid cell culture model. The optimal dose range for vortioxetine microspheres is 5-10 µg/mL, depending on the therapeutic resistance of the GBM cells. These results have shown that vortioxetine could have therapeutic potential for GBM and be delivered in a controlled and sustained manner from microspheres.

Chapter 5: Summary discussion and future directions

1. Summary discussion

The overall objective of this project was to develop local DDSs to treat GBM. We selected some repurposed drugs for GBM treatment because this strategy has the advantage of reducing drug development time and investment, proven safety of drug candidates, and overcoming drug resistance.

In the literature review, I systematically searched for publications that researched the therapeutic efficacy of DDS via direct intracranial injection using unresected GBM animal models. The results of the *meta*-analysis suggested a clear rationale to continue developing local DDS for GBM therapeutics in which the local treatment of DDSs prolonged the MS compared to the negative control groups, local or systemic treatment of the free drug. Local treatment could enhance the therapeutic efficacy by increasing the drug concentration at the tumour sites. However, these preclinical studies also have crucial flaws such as the lack of activity of immune systems for immunodeficient animals, using unaggressive GBM cell lines, and rapid drug release profiles of DDSs. These might be the reasons for the clinical translation difficulty. Furthermore, the time point of treatment, the drug dose, and the injection volume have a huge difference between animal studies and clinical studies. So, developing the GBM model mimicking the real nature of GBM and using multiple GBM models with different growth patterns is critical to validating the therapeutic efficacy of the DDS.

Up to now, Gliadel® is still the only FDA-approved local DDS for GBM treatment. The drawbacks such as stiff structure, rapid release, and using an alkylating agent limit the therapeutic efficiency.(53) So, in the first objective, I designed and created a soft cylindrical-shaped cryogel as an implant into the GBM resection cavity in a mouse model to deliver a repurposed drug, clemastine. The interconnected macropores scaffold of this cryogel provides soft mechanical properties to match the brain tissue. Clemastine showed a therapeutic window between the astrocytes and GBM cells, indicating the advantage of the treatment. Cryogels showed good biocompatibility when implanted into the surgical resection cavity in an orthotopic GBM mouse model. Although local treatment did not show better efficacy than systemic administration, the drug dosage used for the local treatment was much lower, suggesting higher drug delivery efficiency. Furthermore, local treatment avoided any delay in starting the treatment post-surgery, which might be another reason for achieving a similar therapeutic efficacy with a lower dose.

However, clemastine did not suppress the growth of the bulk primary tumour, limiting the translational applications of clemastine monotherapy.

The cylindrical-shaped cryogel was designed exclusively to fit the surgical resection of a mouse model. However, the size of the resection cavity varies in clinics and is hard to predict. So, it is critical to develop a versatile DDS to facilitate the administration procedure. In the third objective, I developed microscale cryogels to resolve this problem. Leveraging shape memory and robust structure characteristics, MCs are injectable DDS suitable for irregular-shaped cavities and non-resectable GBM. The electrostatic interactions for drug loading stimulate the improvement of drug loading capacity. Theoretically, one negative charge group in the MCs could bind with one drug molecule. With the high charge density, MCs achieved a weight ratio of drug to materials above 1:1. This advantage accelerates the drug delivery efficiency in comparison to drugs incorporated in the DDS such as liposomes and nanoparticles, which usually only load with 10-20% drugs.(345-347) MCs are also suitable for large resection cavities because the remaining space could be filled with empty MCs. Two repurposed drugs (brexpiprazole and vortioxetine) and two chemotherapeutics (venetoclax and DOX) were tested for drug loading and drug release. DOX showed good loading capacity and efficiency, but the release pattern dramatically changed when reducing the amount of drug to 5 μg, the *in vivo* dose for animal studies. It revealed the shortcomings of the drug loading via electrostatic interactions, in which the required drug concentration gradient of the drug binding with charged groups in the material dominated the drug loading and drug release. Additionally, the drug concentration gradient was irrelevant to the amount of drugs already bound with the material. So, this effect could be magnified when loading or delivering a small amount of drug. Specifically, the drug loading efficiency dramatically decreases when MCs are incubated with low drug concentrations. In contrast, the drug release rate (in percentage) boosts for MCs only loaded with a small amount of drugs. Therefore, a drug that requires a low dose might not be suitable to be delivered by MCs. However, it also should be kept in mind that the circulation of cerebrospinal fluid was slow. It is difficult to mimic the real drug release environment *in vitro*. Brexpiprazole showed the best drug loading efficiency and release profiles among the above-mentioned four model drugs. So, brexpiprazole MCs were selected for evaluating the anti-GBM efficacy *in vitro*. The results showed that brexpiprazole MCs effectively reduced cell viability on 2D monolayer and 3D spheroid cell culture models. However, an *in vivo* study is needed to evaluate the anti-GBM efficacy, especially compared to the systemic administration of free brexpiprazole.

To overcome the shortage of MCs delivering a small amount of drug, I hypothesized that polymeric microspheres could better manipulate the drug release profiles. The conventional preparation method lacks control of the size distribution and reproducibility. So, I leveraged my knowledge of microfluidics to develop a novel methodology for preparing monodisperse polymeric microspheres. I used PLGA to encapsulate vortioxetine, which had a rapid release pattern in MCs. The optimized protocol had good reproducibility and generated narrow-size distribution microspheres. This protocol also has the potential to scale up production. As a novel preparation method, the cytocompatibility of the product was crucial. The results showed that empty PLGA microspheres did not cause any toxicity on primary human astrocytes. The sustained drug release pattern of vortioxetine microspheres was validated by *in vitro* anti-GBM efficacy. These promising preliminary results provide the foundation for further animal studies. This preparation method could also encapsulate other drugs and create microspheres with different polymer materials.

2. Future directions

This project develops three drug delivery systems for local treatment of GBM. However, further studies need to be done to pave the way for clinical translation. For example, the mechanism of action of clemastine is still unclear. The lysosomal membrane damage might be a reason for the disruption of cell invasion. However, the signalling pathways regulating the lysosomal membrane integrity have not been validated. So, further studies, especially in molecular biology, need to be done to uncover the mechanism of action of clemastine. Additionally, studies have shown that lysosomal membrane disruption rescued the multidrug resistance of cancer cells and effectively killed the apoptosis-resistant cancer cells.(348, 349) So, targeting the lysosomal membrane disruption might be a strategy against GBM. On the other hand, clemastine treatment was poor against the bulk primary tumour, which suggested that clemastine monotherapy was not enough to cure GBM. By providing critical insights into the mechanism of action of clemastine, a chemotherapeutic with a synergistic effect could be discovered, which has the potential to transform glioblastoma treatment paradigms.

Brexpiprazole MCs showed promise against GBM cells in 2D and 3D *in vitro* models. This finding should lead to an evaluation of the anti-GBM efficacy in animal models. *In vivo* studies are also important to understand the real drug release patterns, especially for the initial burst release in the first few hours, because the burst-released drug could limit the drug dose. The *in vitro* drug release model lacks the mimicking of the tumour microenvironment, so, the *in vivo* drug release patterns

might be different. Since most GBM patients undergo surgical tumour resection, we aim to administer the MCs into cavities post-surgery. If the sustained drug release long enough allows us only to perform one treatment without any other intervention such as additional intracerebral injection, the less invasive treatment strategy could improve patient compliance, increase effectiveness, and potentially reduce adverse effects and healthcare costs.

PLGA microspheres are a general vehicle to deliver various drugs and are suitable for non-charged drugs and drugs with poor loading and release results in the cryogel system. Vortioxetine was found to have promising anti-GBM efficacy in recent years,(118) but the dosage of local treatment is still unknown. Further studies are needed to compare the *in vivo* efficacy of local treatment to systemic treatment. Since PLGA is an out-of-fashion material, other novel biodegradable materials such as poly(beta-amino ester)s (PBAE) are more attractive to create microspheres. PBAEs are a type of polymer material synthesized from diacrylate and amine molecules.(350) These positively charged materials have wide applications in DNA delivery.(351) Some pilot studies have shown that PBAE microspheres can be created by the same microfluidics method as PLGA microspheres. These results suggest that this preparation method has versatile applications in polymeric microsphere preparation.

Future research will explore several hypotheses stemming from the tuneable nature of PBAE microspheres and their integration into cryogel-based delivery systems. First, I hypothesize that the degradation rate of PBAE microspheres can be predictably controlled by varying molecular weight and monomer composition, enabling precise modulation of drug release kinetics. This can be falsified by demonstrating a lack of consistent correlation between polymer structure and drug release profiles in *in vitro* drug release studies. Second, I propose that tailoring drug release profiles will enhance therapeutic efficacy. This can be tested by comparing treatment outcomes/adverse effects in preclinical models using microspheres with various release patterns (rapid/long-term). Third, I hypothesize that positively charged PBAE microspheres will exhibit enhanced drug distribution during the treatment if incorporated within the negatively charged cryogel. This hypothesis is falsifiable through imaging-based spatial analysis showing no improvement compared to administering microspheres only. Finally, I propose that embedding stiff PBAE microspheres into cryogels improves the mechanical property of the scaffold, which can be falsified through comparative mechanical testing by showing negligible enhancement.

The cryogel used in this project is made of a non-biodegradable material, which means it would be permanently in the brain after the treatment. Although animal studies showed that cryogel

implantation did not cause host response and affect the mice's behaviour, developing biodegradable cryogel should be more attractive for clinical applications.

References:

1. Shergalis A, Bankhead A, 3rd, Luesakul U, Muangsin N, Neamati N. Current challenges and opportunities in treating glioblastoma. Pharmacol Rev. 2018;70(3):412-45. doi: 10.1124/pr.117.014944

2. Stupp R, Taillibert S, Kanner A, Read W, Steinberg D, Lhermitte B, et al. Effect of tumor-treating fields plus maintenance temozolomide vs maintenance temozolomide alone on survival in patients with glioblastoma: a randomized clinical trial. JAMA. 2017;318(23):2306-16. doi: 10.1001/jama.2017.18718

3. Omuro A, DeAngelis LM. Glioblastoma and other malignant gliomas: a clinical review. JAMA. 2013;310(17):1842-50. doi: 10.1001/jama.2013.280319

4. Ostrom QT, Gittleman H, Truitt G, Boscia A, Kruchko C, Barnholtz-Sloan JS. CBTRUS statistical report: primary brain and other central nervous system tumors diagnosed in the United States in 2011–2015. Neuro-Oncology. 2018;20(suppl_4):iv1-iv86. doi: 10.1093/neuonc/noad149

5. Louis DN, Perry A, Reifenberger G, von Deimling A, Figarella-Branger D, Cavenee WK, et al. The 2016 World Health Organization classification of tumors of the central nervous system: a summary. Acta Neuropathol. 2016;131(6):803-20. doi: 10.1007/s00401-016-1545-1

6. Louis DN, Perry A, Wesseling P, Brat DJ, Cree IA, Figarella-Branger D, et al. The 2021 WHO classification of tumors of the central nervous system: a summary. Neuro Oncol. 2021;23(8):1231-51. doi: 10.1093/neuonc/noab106

7. Weller M, van den Bent M, Preusser M, Le Rhun E, Tonn JC, Minniti G, et al. EANO guidelines on the diagnosis and treatment of diffuse gliomas of adulthood. Nature Reviews Clinical Oncology. 2021;18(3):170-86. doi: 10.1038/s41571-020-00447-z

8. Wick W, Meisner C, Hentschel B, Platten M, Schilling A, Wiestler B, et al. Prognostic or predictive value of MGMT promoter methylation in gliomas depends on IDH1 mutation. Neurology. 2013;81(17):1515-22. doi: 10.1212/WNL.0b013e3182a95680

9. Athanassiou H, Synodinou M, Maragoudakis E, Paraskevaidis M, Verigos C, Misailidou D, et al. Randomized phase II study of temozolomide and radiotherapy compared with radiotherapy alone in newly diagnosed glioblastoma multiforme. J Clin Oncol. 2005;23(10):2372-7. doi: 10.1200/JCO.2005.00.331

10. Hegi ME, Diserens AC, Gorlia T, Hamou MF, de Tribolet N, Weller M, et al. MGMT gene silencing and benefit from temozolomide in glioblastoma. N Engl J Med. 2005;352(10):997-1003. doi: 10.1056/NEJMoa043331

11. Stupp R, Mason WP, van den Bent MJ, Weller M, Fisher B, Taphoorn MJ, et al. Radiotherapy plus concomitant and adjuvant temozolomide for glioblastoma. N Engl J Med. 2005;352(10):987-96. doi: 10.1056/NEJMoa043330

12. Lacroix M, Abi-Said D, Fourney DR, Gokaslan ZL, Shi W, DeMonte F, et al. A multivariate analysis of 416 patients with glioblastoma multiforme: prognosis, extent of resection, and survival. J Neurosurg. 2001;95(2):190-8. doi: 10.3171/jns.2001.95.2.0190

13. Yamahara T, Numa Y, Oishi T, Kawaguchi T, Seno T, Asai A, et al. Morphological and flow cytometric analysis of cell infiltration in glioblastoma: a comparison of autopsy brain and neuroimaging. Brain Tumor Pathol. 2010;27(2):81-7. doi: 10.1007/s10014-010-0275-7

14. Ganipineni LP, Danhier F, Preat V. Drug delivery challenges and future of chemotherapeutic nanomedicine for glioblastoma treatment. J Control Release. 2018;281:42-57. doi: 10.1016/j.jconrel.2018.05.008

15. Yabroff KR, Harlan L, Zeruto C, Abrams J, Mann B. Patterns of care and survival for patients with glioblastoma multiforme diagnosed during 2006. Neuro Oncol. 2012;14(3):351-9. doi: 10.1093/neuonc/nor218

16. Chang SM, Parney IF, Huang W, Anderson FA, Jr., Asher AL, Bernstein M, et al. Patterns of care for adults with newly diagnosed malignant glioma. JAMA. 2005;293(5):557-64. doi: 10.1001/jama.293.5.557

17. Scoccianti S, Magrini SM, Ricardi U, Detti B, Buglione M, Sotti G, et al. Patterns of care and survival in a retrospective analysis of 1059 patients with glioblastoma multiforme treated between 2002 and 2007: a multicenter study by the central nervous system study group of airo. Neurosurgery. 2010;67(2):446-58. doi: 10.1227/01.Neu.0000371990.86656.E8

18. Press RH, Shafer SL, Jiang R, Buchwald ZS, Abugideiri M, Tian S, et al. Optimal timing of chemoradiotherapy after surgical resection of glioblastoma: stratification by validated prognostic classification. Cancer. 2020;126(14):3255-64. doi: 10.1002/cncr.32797

19. Baumann M, DuBois W, Pu A, Freeman J, Suit HD. Response of xenografts of human malignant gliomas and squamous cell carcinomas to fractionated irradiation. Int J Radiat Oncol Biol Phys. 1992;23(4):803-9. doi: 10.1016/0360-3016(92)90653-y

20. Murat A, Migliavacca E, Gorlia T, Lambiv WL, Shay T, Hamou MF, et al. Stem cell-related "self-renewal" signature and high epidermal growth factor receptor expression associated with resistance to concomitant chemoradiotherapy in glioblastoma. J Clin Oncol. 2008;26(18):3015-24. doi: 10.1200/JCO.2007.15.7164

21. Pegg AE, Dolan ME, Moschel RC. Structure, function, and inhibition of O6-alkylguanine-DNA alkyltransferase. Prog Nucleic Acid Res Mol Biol. 1995;51:167-223. doi: 10.1016/s0079-6603(08)60879-x

22. Esteller M, Garcia-Foncillas J, Andion E, Goodman SN, Hidalgo OF, Vanaclocha V, et al. Inactivation of the DNA-repair gene MGMT and the clinical response of gliomas to alkylating agents. N Engl J Med. 2000;343(19):1350-4. doi: 10.1056/NEJM200011093431901

23. Perry JR, Laperriere N, O'Callaghan CJ, Brandes AA, Menten J, Phillips C, et al. Short-course radiation plus temozolomide in elderly patients with glioblastoma. N Engl J Med. 2017;376(11):1027-37. doi: 10.1056/NEJMoa1611977

24. Prados MD, Byron SA, Tran NL, Phillips JJ, Molinaro AM, Ligon KL, et al. Toward precision medicine in glioblastoma: the promise and the challenges. Neuro Oncol. 2015;17(8):1051-63. doi: 10.1093/neuonc/nov031

25. Barker FG, 2nd, Chang SM, Gutin PH, Malec MK, McDermott MW, Prados MD, et al. Survival and

functional status after resection of recurrent glioblastoma multiforme. Neurosurgery. 1998;42(4):709-20; discussion 20-3. doi: 10.1097/00006123-199804000-00013

26. Stupp R, Brada M, van den Bent MJ, Tonn JC, Pentheroudakis G, Group EGW. High-grade glioma: ESMO Clinical Practice Guidelines for diagnosis, treatment and follow-up. Ann Oncol. 2014;25 Suppl 3:iii93-101. doi: 10.1093/annonc/mdu050

27. Brada M, Stenning S, Gabe R, Thompson LC, Levy D, Rampling R, et al. Temozolomide versus procarbazine, lomustine, and vincristine in recurrent high-grade glioma. J Clin Oncol. 2010;28(30):4601-8. doi: 10.1200/JCO.2009.27.1932

28. Wick W, Puduvalli VK, Chamberlain MC, van den Bent MJ, Carpentier AF, Cher LM, et al. Phase III study of enzastaurin compared with lomustine in the treatment of recurrent intracranial glioblastoma. J Clin Oncol. 2010;28(7):1168-74. doi: 10.1200/JCO.2009.23.2595

29. Friedman HS, Prados MD, Wen PY, Mikkelsen T, Schiff D, Abrey LE, et al. Bevacizumab alone and in combination with irinotecan in recurrent glioblastoma. Journal of Clinical Oncology. 2009;27(28):4733-40. doi: 10.1200/Jco.2008.19.8721

30. Kreisl TN, Kim L, Moore K, Duic P, Royce C, Stroud I, et al. Phase II trial of single-agent bevacizumab fllowed by bevacizumab plus irinotecan at tumor progression in recurrent glioblastoma. Journal of Clinical Oncology. 2009;27(5):740-5. doi: 10.1200/Jco.2008.16.3055

31. Ameratunga M, Pavlakis N, Wheeler H, Grant R, Simes J, Khasraw M. Anti-angiogenic therapy for high-grade glioma. Cochrane Db Syst Rev. 2018(11) doi: 10.1002/14651858.CD008218.pub4

32. Wick W, Gorlia T, Bendszus M, Taphoorn M, Sahm F, Harting I, et al. Lomustine and bevacizumab in progressive glioblastoma. New England Journal of Medicine. 2017;377(20):1954-63. doi: 10.1056/NEJMoa1707358

33. Mikic N, Poulsen FR, Kristoffersen KB, Laursen RJ, Guldberg TL, Skjoth-Rasmussen J, et al. Study protocol for OptimalTTF-2: enhancing Tumor Treating Fields with skull remodeling surgery for first recurrence glioblastoma: a phase 2, multi-center, randomized, prospective, interventional trial. BMC Cancer. 2021;21(1):1010. doi: 10.1186/s12885-021-08709-4

34. Stupp R, Wong ET, Kanner AA, Steinberg D, Engelhard H, Heidecke V, et al. NovoTTF-100A versus physician's choice chemotherapy in recurrent glioblastoma: a randomised phase III trial of a novel treatment modality. Eur J Cancer. 2012;48(14):2192-202. doi: 10.1016/j.ejca.2012.04.011

35. Kesari S, Ram Z, Investigators EFT. Tumor-treating fields plus chemotherapy versus chemotherapy alone for glioblastoma at first recurrence: a post hoc analysis of the EF-14 trial. CNS Oncol. 2017;6(3):185-93. doi: 10.2217/cns-2016-0049

36. Stupp R, Wong ET, Kanner AA, Steinberg D, Engelhard H, Heidecke V, et al. NovoTTF-100A versus physician’s choice chemotherapy in recurrent glioblastoma: a randomised phase III trial of a novel treatment modality. European journal of cancer. 2012;48(14):2192-202. doi: 10.1016/j.ejca.2012.04.011

37. Patel AP, Tirosh I, Trombetta JJ, Shalek AK, Gillespie SM, Wakimoto H, et al. Single-cell RNA-seq

highlights intratumoral heterogeneity in primary glioblastoma. Science. 2014;344(6190):1396-401. doi: 10.1126/science.1254257

38. Nabilsi NH, Deleyrolle LP, Darst RP, Riva A, Reynolds BA, Kladde MP. Multiplex mapping of chromatin accessibility and DNA methylation within targeted single molecules identifies epigenetic heterogeneity in neural stem cells and glioblastoma. Genome Res. 2014;24(2):329-39. doi: 10.1101/gr.161737.113

39. Parker NR, Hudson AL, Khong P, Parkinson JF, Dwight T, Ikin RJ, et al. Intratumoral heterogeneity identified at the epigenetic, genetic and transcriptional level in glioblastoma. Sci Rep-Uk. 2016;6 doi: 10.1038/srep22477

40. Sharma P, Aaroe A, Liang J, Puduvalli VK. Tumor microenvironment in glioblastoma: Current and emerging concepts. Neuro-Oncology Advances. 2023;5(1) doi: 10.1093/noajnl/vdad009

41. Venkatesh HS, Morishita W, Geraghty AC, Silverbush D, Gillespie SM, Arzt M, et al. Electrical and synaptic integration of glioma into neural circuits. Nature. 2019;573(7775):539-45. doi: 10.1038/s41586-019-1563-y

42. Venkatesh HS, Tam LT, Woo PJ, Lennon J, Nagaraja S, Gillespie SM, et al. Targeting neuronal activity-regulated neuroligin-3 dependency in high-grade glioma. Nature. 2017;549(7673):533-7. doi: 10.1038/nature24014

43. Venkatesh Humsa S, Johung Tessa B, Caretti V, Noll A, Tang Y, Nagaraja S, et al. Neuronal activity promotes glioma growth through neuroligin-3 secretion. Cell. 2015;161(4):803-16. doi: 10.1016/j.cell.2015.04.012

44. Quail DF, Joyce JA. The microenvironmental landscape of brain tumors. Cancer Cell. 2017;31(3):326-41. doi: 10.1016/j.ccell.2017.02.009

45. Zuchero YJ, Chen X, Bien-Ly N, Bumbaca D, Tong RK, Gao X, et al. Discovery of novel blood-brain barrier targets to enhance brain uptake of therapeutic antibodies. Neuron. 2016;89(1):70-82. doi: 10.1016/j.neuron.2015.11.024

46. Wolbers JG. Novel strategies in glioblastoma surgery aim at safe, supra-maximum resection in conjunction with local therapies. Chin J Cancer. 2014;33(1):8-15. doi: 10.5732/cjc.013.10219

47. Vashist A, Vashist A, Gupta YK, Ahmad S. Recent advances in hydrogel based drug delivery systems for the human body. J Mater Chem B. 2014;2(2):147-66. doi: 10.1039/c3tb21016b

48. Westphal M, Hilt DC, Bortey E, Delavault P, Olivares R, Warnke PC, et al. A phase 3 trial of local chemotherapy with biodegradable carmustine (BCNU) wafers (Gliadel wafers) in patients with primary malignant glioma. Neuro Oncol. 2003;5(2):79-88. doi: 10.1093/neuonc/5.2.79

49. Juratli TA, Schackert G, Krex D. Current status of local therapy in malignant gliomas--a clinical review of three selected approaches. Pharmacol Ther. 2013;139(3):341-58. doi: 10.1016/j.pharmthera.2013.05.003

50. Brem H, Piantadosi S, Burger PC, Walker M, Selker R, Vick NA, et al. Placebo-controlled trial of safety and efficacy of intraoperative controlled delivery by biodegradable polymers of chemotherapy for recurrent gliomas. The Polymer-brain Tumor Treatment Group. Lancet. 1995;345(8956):1008-12. doi: 10.1016/s0140-

6736(95)90755-6

51. Valtonen S, Timonen U, Toivanen P, Kalimo H, Kivipelto L, Heiskanen O, et al. Interstitial chemotherapy with carmustine-loaded polymers for high-grade gliomas: a randomized double-blind study. Neurosurgery. 1997;41(1):44-8; discussion 8-9. doi: 10.1097/00006123-199707000-00011

52. Ashby LS, Smith KA, Stea B. Gliadel wafer implantation combined with standard radiotherapy and concurrent followed by adjuvant temozolomide for treatment of newly diagnosed high-grade glioma: a systematic literature review. World J Surg Oncol. 2016;14(1):225. doi: 10.1186/s12957-016-0975-5

53. Tabet A, Jensen MP, Parkins CC, Patil PG, Watts C, Scherman OA. Designing next-generation local drug delivery vehicles for glioblastoma adjuvant chemotherapy: lessons from the clinic. Adv Healthc Mater. 2019;8(3):e1801391. doi: 10.1002/adhm.201801391

54. McGovern PC, Lautenbach E, Brennan PJ, Lustig RA, Fishman NO. Risk factors for postcraniotomy surgical site infection after 1,3-bis (2-chloroethyl)-1-nitrosourea (Gliadel) wafer placement. Clin Infect Dis. 2003;36(6):759-65. doi: 10.1086/368082

55. Bota DA, Desjardins A, Quinn JA, Affronti ML, Friedman HS. Interstitial chemotherapy with biodegradable BCNU (Gliadel) wafers in the treatment of malignant gliomas. Ther Clin Risk Manag. 2007;3(5):707-15.

56. Bastiancich C, Bozzato E, Henley I, Newland B. Does local drug delivery still hold therapeutic promise for brain cancer? A systematic review. J Control Release. 2021;337:296-305. doi: 10.1016/j.jconrel.2021.07.031

57. Chaichana KL, Pinheiro L, Brem H. Delivery of local therapeutics to the brain: working toward advancing treatment for malignant gliomas. Ther Deliv. 2015;6(3):353-69. doi: 10.4155/tde.14.114

58. Hirst TC, Vesterinen HM, Sena ES, Egan KJ, Macleod MR, Whittle IR. Systematic review and meta-analysis of temozolomide in animal models of glioma: was clinical efficacy predicted? Brit J Cancer. 2013;108(1):64-71. doi: 10.1038/bjc.2012.504

59. Tierney JF, Stewart LA, Ghersi D, Burdett S, Sydes MR. Practical methods for incorporating summary time-to-event data into meta-analysis. Trials. 2007;8 doi: 10.1186/1745-6215-8-16

60. Simes RJ. Confronting publication bias: a cohort design for meta-analysis. Stat Med. 1987;6(1):11-29. doi: 10.1002/sim.4780060104

61. Higgins JPT LT, Deeks JJ (editors). Chapter 6: Choosing effect measures and computing estimates of effect. Cochrane Handbook for Systematic Reviews of Interventions version 62 (updated February 2021): Cochrane; 2021.

62. Menei P, Boisdron-Celle M, Croue A, Guy G, Benoit JP. Effect of stereotactic implantation of biodegradable 5-fluorouracil-loaded microspheres in healthy and C6 glioma-bearing rats. Neurosurgery. 1996;39(1):117-23; discussion 23-4. doi: 10.1097/00006123-199607000-00023

63. Fournier E, Passirani C, Montero-Menei C, Colin N, Breton P, Sagodira S, et al. Therapeutic effectiveness of novel 5-fluorouracil-loaded poly(methylidene malonate 2.1.2)-based microspheres on F98

glioma-bearing rats. Cancer. 2003;97(11):2822-9. doi: 10.1002/cncr.11388

64. Pang HH, Chen PY, Wei KC, Huang CW, Shiue YL, Huang CY, et al. Convection-enhanced delivery of a virus-like nanotherapeutic agent with dual-modal imaging for besiegement and eradication of brain tumors. Theranostics. 2019;9(6):1752-63. doi: 10.7150/thno.30977

65. Singleton WG, Collins AM, Bienemann AS, Killick-Cole CL, Haynes HR, Asby DJ, et al. Convection enhanced delivery of panobinostat (LBH589)-loaded pluronic nano-micelles prolongs survival in the F98 rat glioma model. Int J Nanomedicine. 2017;12:1385-99. doi: 10.2147/IJN.S125300

66. Stephen ZR, Kievit FM, Veiseh O, Chiarelli PA, Fang C, Wang K, et al. Redox-responsive magnetic nanoparticle for targeted convection-enhanced delivery of O-6-benzylguanine to brain tumors. Acs Nano. 2014;8(10):10383-95. doi: 10.1021/nn503735w

67. Vellimana AK, Recinos VR, Hwang L, Fowers KD, Li KW, Zhang YG, et al. Combination of paclitaxel thermal gel depot with temozolomide and radiotherapy significantly prolongs survival in an experimental rodent glioma model. J Neuro-Oncol. 2013;111(3):229-36. doi: 10.1007/s11060-012-1014-1

68. Tyler B, Fowers KD, Li KW, Recinos VR, Caplan JM, Hdeib A, et al. A thermal gel depot for local delivery of paclitaxel to treat experimental brain tumors in rats Laboratory investigation. J Neurosurg. 2010;113(2):210-7. doi: 10.3171/2009.11.Jns08162

69. Glage S, Lewis AL, Mertens P, Baltes S, Geigle P, Brinker T. Evaluation of biocompatibility and anti-glioma efficacy of doxorubicin and irinotecan drug-eluting bead suspensions in alginate. Clin Transl Oncol. 2012;14(1):50-9. doi: 10.1007/s12094-012-0761-y

70. Bernal GM, LaRiviere MJ, Mansour N, Pytel P, Cahill KE, Voce DJ, et al. Convection-enhanced delivery and in vivo imaging of polymeric nanoparticles for the treatment of malignant glioma. Nanomedicine. 2014;10(1):149-57. doi: 10.1016/j.nano.2013.07.003

71. Kikuchi T, Saito R, Sugiyama S, Yamashita Y, Kumabe T, Krauze M, et al. Convection-enhanced delivery of polyethylene glycol-coated liposomal doxorubicin: characterization and efficacy in rat intracranial glioma models. J Neurosurg. 2008;109(5):867-73. doi: 10.3171/JNS/2008/109/11/0867

72. Ozeki T, Kaneko D, Hashizawa K, Imai Y, Tagami T, Okada H. Combination therapy of surgical tumor resection with implantation of a hydrogel containing camptothecin-loaded poly(lactic-co-glycolic acid) microspheres in a C6 rat glioma model. Biol Pharm Bull. 2012;35(4):545-50. doi: 10.1248/bpb.35.545

73. Ozeki T, Hashizawa K, Kaneko D, Imai Y, Okada H. Treatment of rat brain tumors using sustained-release of camptothecin from poly(lactic-co-glycolic acid) microspheres in a thermoreversible hydrogel. Chemical and Pharmaceutical Bulletin. 2010;58(9):1142-7. doi: 10.1248/cpb.58.1142

74. Parkins CC, McAbee JH, Ruff L, Wendler A, Mair R, Gilbertson RJ, et al. Mechanically matching the rheological properties of brain tissue for drug-delivery in human glioblastoma models. Biomaterials. 2021;276:120919. doi: 10.1016/j.biomaterials.2021.120919

75. Allen J, Wang J, Zolotarskaya OY, Sule A, Mohammad S, Arslan S, et al. PEAMOtecan, a novel chronotherapeutic polymeric drug for brain cancer. J Control Release. 2020;321:36-48. doi:

10.1016/j.jconrel.2020.02.003

76. Wehbe M, Anantha M, Shi M, Leung AW, Dragowska WH, Sanche L, et al. Development and optimization of an injectable formulation of copper diethyldithiocarbamate, an active anticancer agent. Int J Nanomedicine. 2017;12:4129-46. doi: 10.2147/IJN.S137347

77. Zhang R, Saito R, Mano Y, Sumiyoshi A, Kanamori M, Sonoda Y, et al. Convection-enhanced delivery of SN-38-loaded polymeric micelles (NK012) enables consistent distribution of SN-38 and is effective against rodent intracranial brain tumor models. Drug Deliv. 2016;23(8):2780-6.

78. Zhou J, Patel TR, Sirianni RW, Strohbehn G, Zheng MQ, Duong N, et al. Highly penetrative, drug-loaded nanocarriers improve treatment of glioblastoma. Proc Natl Acad Sci U S A. 2013;110(29):11751-6. doi: 10.1073/pnas.1304504110

79. Allard E, Jarnet D, Vessieres A, Vinchon-Petit S, Jaouen G, Benoit JP, et al. Local delivery of ferrociphenol lipid nanocapsules followed by external radiotherapy as a synergistic treatment against intracranial 9L glioma xenograft. Pharmaceut Res. 2010;27(1):56-64. doi: 10.1007/s11095-009-0006-0

80. Grahn AY, Bankiewicz KS, Dugich-Djordjevic M, Bringas JR, Hadaczek P, Johnson GA, et al. Non-PEGylated liposomes for convection-enhanced delivery of topotecan and gadodiamide in malignant glioma: initial experience. J Neurooncol. 2009;95(2):185-97. doi: 10.1007/s11060-009-9917-1

81. Lollo G, Vincent M, Ullio-Gamboa G, Lemaire L, Franconi F, Couez D, et al. Development of multifunctional lipid nanocapsules for the co-delivery of paclitaxel and CpG-ODN in the treatment of glioblastoma. Int J Pharm. 2015;495(2):972-80. doi: 10.1016/j.ijpharm.2015.09.062

82. Barth RF, Wu G, Meisen WH, Nakkula RJ, Yang W, Huo T, et al. Design, synthesis, and evaluation of cisplatin-containing EGFR targeting bioconjugates as potential therapeutic agents for brain tumors. Oncotargets Ther. 2016;9:2769-81. doi: 10.2147/Ott.S99242

83. Xi G, Robinson E, Mania-Farnell B, Vanin EF, Shim KW, Takao T, et al. Convection-enhanced delivery of nanodiamond drug delivery platforms for intracranial tumor treatment. Nanomedicine. 2014;10(2):381-91. doi: 10.1016/j.nano.2013.07.013

84. Zhang J, Chen C, Li A, Jing W, Sun P, Huang X, et al. Immunostimulant hydrogel for the inhibition of malignant glioma relapse post-resection. Nat Nanotechnol. 2021;16(5):538-48. doi: 10.1038/s41565-020-00843-7

85. Yokosawa M, Sonoda Y, Sugiyama S, Saito R, Yamashita Y, Nishihara M, et al. Convection-enhanced delivery of a synthetic retinoid Am80, loaded into polymeric micelles, prolongs the survival of rats bearing intracranial glioblastoma xenografts. Tohoku J Exp Med. 2010;221(4):257-64. doi: 10.1620/tjem.221.257

86. Nordling-David MM, Yaffe R, Guez D, Meirow H, Last D, Grad E, et al. Liposomal temozolomide drug delivery using convection enhanced delivery. J Control Release. 2017;261:138-46. doi: 10.1016/j.jconrel.2017.06.028

87. Chen TJ, Gong T, Zhao T, Liu X, Fu Y, Zhang ZR, et al. Paclitaxel loaded phospholipid-based gel as a drug delivery system for local treatment of glioma. Int J Pharmaceut. 2017;528(1-2):127-32. doi:

10.1016/j.ijpharm.2017.06.013

88. Adhikari B, Li J, Brandel MG, Futalan D, Akers J, Deming T, et al. The use of TMZ embedded hydrogels for the treatment of orthotopic human glioma xenografts. J Clin Neurosci. 2017;45:288-92. doi: 10.1016/j.jocn.2017.07.027

89. Xu HL, Mao KL, Lu CT, Fan ZL, Yang JJ, Xu J, et al. An injectable acellular matrix scaffold with absorbable permeable nanoparticles improves the therapeutic effects of docetaxel on glioblastoma. Biomaterials. 2016;107:44-60. doi: 10.1016/j.biomaterials.2016.08.026

90. Gaudin A, Song E, King AR, Saucier-Sawyer JK, Bindra R, Desmaele D, et al. PEGylated squalenoyl-gemcitabine nanoparticles for the treatment of glioblastoma. Biomaterials. 2016;105:136-44. doi: 10.1016/j.biomaterials.2016.07.037

91. Kang C, Yuan X, Zhong Y, Pu P, Guo Y, Albadany A, et al. Growth inhibition against intracranial C6 glioma cells by stereotactic delivery of BCNU by controlled release from poly(D,L-lactic acid) nanoparticles. Technol Cancer Res Treat. 2009;8(1):61-70. doi: 10.1177/153303460900800108

92. Inoue T, Yamashita Y, Nishihara M, Sugiyama S, Sonoda Y, Kumabe T, et al. Therapeutic efficacy of a polymeric micellar doxorubicin infused by convection-enhanced delivery against intracranial 9L brain tumor models. Neuro Oncol. 2009;11(2):151-7. doi: 10.1215/15228517-2008-068

93. Zhou H, Chen D, Gong T, He Q, Guo C, Zhang P, et al. Chlorogenic acid sustained-release gel for treatment of glioma and hepatocellular carcinoma. Eur J Pharm Biopharm. 2021;166:103-10. doi: 10.1016/j.ejpb.2021.05.028

94. Xuan JJ, Balakrishnan P, Oh DH, Yeo WH, Park SM, Yong CS, et al. Rheological characterization and in vivo evaluation of thermosensitive poloxamer-based hydrogel for intramuscular injection of piroxicam. Int J Pharm. 2010;395(1-2):317-23. doi: 10.1016/j.ijpharm.2010.05.042

95. Lin CY, Li RJ, Huang CY, Wei KC, Chen PY. Controlled release of liposome-encapsulated temozolomide for brain tumour treatment by convection-enhanced delivery. J Drug Target. 2018;26(4):325-32. doi: 10.1080/1061186X.2017.1379526

96. Bastiancich C, Bianco J, Vanvarenberg K, Ucakar B, Joudiou N, Gallez B, et al. Injectable nanomedicine hydrogel for local chemotherapy of glioblastoma after surgical resection. J Control Release. 2017;264:45-54. doi: 10.1016/j.jconrel.2017.08.019

97. Chen PY, Ozawa T, Drummond DC, Kalra A, Fitzgerald JB, Kirpotin DB, et al. Comparing routes of delivery for nanoliposomal irinotecan shows superior anti-tumor activity of local administration in treating intracranial glioblastoma xenografts. Neuro-Oncology. 2013;15(2):189-97. doi: 10.1093/neuonc/nos305

98. Zhang YH, Zhang H, Liu JM, Yue ZJ. Temozolomide/PLGA microparticles: a new protocol for treatment of glioma in rats. Med Oncol. 2011;28(3):901-6. doi: 10.1007/s12032-010-9531-2

99. Laine AL, Huynh NT, Clavreul A, Balzeau J, Bejaud J, Vessieres A, et al. Brain tumour targeting strategies via coated ferrociphenol lipid nanocapsules. Eur J Pharm Biopharm. 2012;81(3):690-3. doi: 10.1016/j.ejpb.2012.04.012

100. Sasso MS, Lollo G, Pitorre M, Solito S, Pinton L, Valpione S, et al. Low dose gemcitabine-loaded lipid nanocapsules target monocytic myeloid-derived suppressor cells and potentiate cancer immunotherapy. Biomaterials. 2016;96:47-62. doi: 10.1016/j.biomaterials.2016.04.010

101. Bastiancich C, Malfanti A, Preat V, Rahman R. Rationally designed drug delivery systems for the local treatment of resected glioblastoma. Adv Drug Deliv Rev. 2021;177:113951. doi: 10.1016/j.addr.2021.113951

102. Zalles M, Towner RA. Pre-clinical models and potential novel therapies for glioblastomas. In: Debinski W, editor. Gliomas. Brisbane (AU); 2021.

103. McCrorie P, Rowlinson J, Scurr DJ, Marlow M, Rahman R. Detection of label-free drugs within brain tissue using orbitrap secondary ion mass spectrometry as a complement to neuro-oncological drug delivery. Pharmaceutics. 2022;14(3) doi: 10.3390/pharmaceutics14030571

104. Fu L, Jin W, Zhang J, Zhu L, Lu J, Zhen Y, et al. Repurposing non-oncology small-molecule drugs to improve cancer therapy: current situation and future directions. Acta Pharm Sin B. 2022;12(2):532-57. doi: 10.1016/j.apsb.2021.09.006

105. Aggarwal S, Verma SS, Aggarwal S, Gupta SC. Drug repurposing for breast cancer therapy: old weapon for new battle. Semin Cancer Biol. 2021;68:8-20. doi: 10.1016/j.semcancer.2019.09.012

106. Sleigh SH, Barton CL. Repurposing strategies for therapeutics. Pharmaceutical Medicine. 2010;24(3):151-9. doi: 10.1007/BF03256811

107. Prasad V, Mailankody S. Research and development spending to bring a single cancer drug to market and revenues after approval. JAMA internal medicine. 2017;177(11):1569-75. doi: 10.1001/jamainternmed.2017.3601

108. Fu L, Jin W, Zhang J, Zhu L, Lu J, Zhen Y, et al. Repurposing non-oncology small-molecule drugs to improve cancer therapy: current situation and future directions. Acta Pharmaceutica Sinica B. 2022;12(2):532-57. doi: 10.1016/j.apsb.2021.09.006

109. Ashburn TT, Thor KB. Drug repositioning: identifying and developing new uses for existing drugs. Nature reviews Drug discovery. 2004;3(8):673-83. doi: 10.1038/nrd1468

110. Yadavalli S, Yenugonda VM, Kesari S. Repurposed drugs in treating glioblastoma multiforme: clinical trials update. Cancer J. 2019;25(2):139-46. doi: 10.1097/PPO.0000000000000365

111. Hosseinalizadeh H, Ebrahimi A, Tavakoli A, Monavari SH. Glioblastoma as a novel drug repositioning target: updated state. Anticancer Agents Med Chem. 2023;23(11):1253-64. doi: 10.2174/1871520623666230202163112

112. Alomari S, Zhang I, Hernandez A, Kraft CY, Raj D, Kedda J, et al. Drug repurposing for glioblastoma and current advances in drug delivery-a comprehensive review of the literature. Biomolecules. 2021;11(12) doi: 10.3390/biom11121870

113. Basso J, Miranda A, Sousa J, Pais A, Vitorino C. Repurposing drugs for glioblastoma: from bench to bedside. Cancer Lett. 2018;428:173-83. doi: 10.1016/j.canlet.2018.04.039

114. Zhao Y, Cao J, Melamed A, Worley M, Gockley A, Jones D, et al. Losartan treatment enhances

chemotherapy efficacy and reduces ascites in ovarian cancer models by normalizing the tumor stroma. Proceedings of the National Academy of Sciences. 2019;116(6):2210-9. doi: 10.1073/pnas.1818357116

115. Jones HM, Fang Z, Sun W, Clark LH, Stine JE, Tran AQ, et al. Atorvastatin exhibits anti-tumorigenic and anti-metastatic effects in ovarian cancer in vitro. Am J Cancer Res. 2017;7(12):2478-90.

116. Altwairgi AK, Alnajjar F, Alhussain H, Alsaeed E, Balbaid A, Aldandan S, et al. 53P - Phase II study of atorvastatin in combination with radiotherapy and temozolomide in patients with glioblastoma (ART): final analysis report. Annals of Oncology. 2019;30:ix20. doi: 10.1093/annonc/mdz419

117. Sotelo J, Briceño E, López-González MA. Adding chloroquine to conventional treatment for glioblastoma multiforme: a randomized, double-blind, placebo-controlled trial. Annals of internal medicine. 2006;144(5):337-43. doi: 10.7326/0003-4819-144-5-200603070-00008

118. Lee S, Weiss T, Bühler M, Mena J, Lottenbach Z, Wegmann R, et al. High-throughput identification of repurposable neuroactive drugs with potent anti-glioblastoma activity. Nature Medicine. 2024 doi: 10.1038/s41591-024-03224-y

119. Zhu J, Ma R, Li G. Drug repurposing: clemastine fumarate and neurodegeneration. Biomedicine & Pharmacotherapy. 2023;157:113904. doi: 10.1016/j.biopha.2022.113904

120. Chung JH, deTineo ML, Naclerio RM, Sorrentino JV, Winslow CM, Baroody FM. Low dose clemastine inhibits sneezing and rhinorrhea during the early nasal allergic reaction. Annals of Allergy, Asthma & Immunology. 1997;78(3):307-12. doi: 10.1016/S1081-1206(10)63187-0

121. Nogrady S, Hartley J, Handslip P, Hurst N. Bronchodilatation after inhalation of the antihistamine clemastine. Thorax. 1978;33(4):479-82. doi: 10.1136/thx.33.4.479

122. Akdis CA, Simons FER. Histamine receptors are hot in immunopharmacology. European journal of pharmacology. 2006;533(1-3):69-76. doi: 10.1016/j.ejphar.2005.12.044

123. Chen J, Liu G, Wang X, Hong H, Li T, Li L, et al. Glioblastoma stem cell-specific histamine secretion drives pro-angiogenic tumor microenvironment remodeling. Cell Stem Cell. 2022;29(11):1531-46.e7. doi: 10.1016/j.stem.2022.09.009

124. Lin J-J, Zhao T-Z, Cai W-K, Yang Y-X, Sun C, Zhang Z, et al. Inhibition of histamine receptor 3 suppresses glioblastoma tumor growth, invasion, and epithelial-to-mesenchymal transition. Oncotarget. 2015;6(19) doi: 10.18632/oncotarget.3672

125. Le Joncour V, Filppu P, Hyvonen M, Holopainen M, Turunen SP, Sihto H, et al. Vulnerability of invasive glioblastoma cells to lysosomal membrane destabilization. EMBO Mol Med. 2019;11(6) doi: 10.15252/emmm.201809034

126. Nakamura Y, Adachi J, Hirota N, Iba K, Shimizu K, Nakai M, et al. Brexpiprazole treatment for agitation in Alzheimer's dementia: a randomized study. Alzheimer's & Dementia.n/a(n/a) doi: 10.1002/alz.14282

127. Maeda K, Sugino H, Akazawa H, Amada N, Shimada J, Futamura T, et al. Brexpiprazole I: in vitro and in vivo characterization of a novel serotonin-dopamine activity modulator. J Pharmacol Exp Ther. 2014;350(3):589-604. doi: 10.1124/jpet.114.213793

128. Zhong K, Cummings J. A critical review of brexpiprazole oral tablets as the first drug approved to treat agitation symptoms associated with dementia due to Alzheimer's disease. Expert Review of Neurotherapeutics.1-9. doi: 10.1080/14737175.2024.2407836

129. Kane JM, Skuban A, Ouyang J, Hobart M, Pfister S, McQuade RD, et al. A multicenter, randomized, double-blind, controlled phase 3 trial of fixed-dose brexpiprazole for the treatment of adults with acute schizophrenia. Schizophrenia research. 2015;164(1-3):127-35. doi: 10.1016/j.schres.2015.01.038

130. Correll CU, Skuban A, Ouyang J, Hobart M, Pfister S, McQuade RD, et al. Efficacy and safety of brexpiprazole for the treatment of acute schizophrenia: a 6-week randomized, double-blind, placebo-controlled trial. American Journal of Psychiatry. 2015;172(9):870-80. doi: 10.1176/appi.ajp.2015.14101275

131. Marder SR, Hakala MJ, Josiassen MK, Zhang P, Ouyang J, Weiller E, et al. Brexpiprazole in patients with schizophrenia: overview of short-and long-term phase 3 controlled studies. Acta neuropsychiatrica. 2017;29(5):278-90. doi: 10.1017/neu.2016.57

132. Weiss C, MacKenzie E, Therrien F, Zhang P, Meehan S. T50. symptomatic and functional response to brexpip razole treatment in patients with acute schizophrenia by age. Schizophrenia Bulletin. 2018;44(Suppl 1):S133. doi: 10.1093/schbul/sby016.326

133. Suzuki S, Yamamoto M, Togashi K, Sanomachi T, Sugai A, Seino S, et al. In vitro and in vivo anti-tumor effects of brexpiprazole, a newly-developed serotonin-dopamine activity modulator with an improved safety profile. Oncotarget. 2019;10(37) doi: 10.18632/oncotarget.26949

134. Bang-Andersen B, Ruhland T, Jørgensen M, Smith G, Frederiksen K, Jensen KG, et al. Discovery of 1-[2-(2,4-dimethylphenylsulfanyl)phenyl]piperazine (Lu AA21004): a novel multimodal compound for the treatment of major depressive disorder. J Med Chem. 2011;54(9):3206-21. doi: 10.1021/jm101459g

135. Mørk A, Pehrson A, Brennum LT, Nielsen SM, Zhong H, Lassen AB, et al. Pharmacological effects of Lu AA21004: a novel multimodal compound for the treatment of major depressive disorder. J Pharmacol Exp Ther. 2012;340(3):666-75. doi: 10.1124/jpet.111.189068

136. Pehrson AL, Cremers T, Bétry C, van der Hart MG, Jørgensen L, Madsen M, et al. Lu AA21004, a novel multimodal antidepressant, produces regionally selective increases of multiple neurotransmitters--a rat microdialysis and electrophysiology study. Eur Neuropsychopharmacol. 2013;23(2):133-45. doi: 10.1016/j.euroneuro.2012.04.006

137. Thase ME, Mahableshwarkar AR, Dragheim M, Loft H, Vieta E. A meta-analysis of randomized, placebo-controlled trials of vortioxetine for the treatment of major depressive disorder in adults. European Neuropsychopharmacology. 2016;26(6):979-93. doi: 10.1016/j.euroneuro.2016.03.007

138. Cipriani A, Furukawa TA, Salanti G, Chaimani A, Atkinson LZ, Ogawa Y, et al. Comparative efficacy and acceptability of 21 antidepressant drugs for the acute treatment of adults with major depressive disorder: a systematic review and network meta-analysis. The Lancet. 2018;391(10128):1357-66. doi: 10.1016/S0140-6736(17)32802-7

139. Kanno T, Uyama H. Unique ivy-like morphology composed of poly(lactic acid) and bacterial cellulose

cryogel. ACS Omega. 2018;3(1):631-5. doi: 10.1021/acsomega.7b01968

140. Lozinsky VI, Kolosova OY, Michurov DA, Dubovik AS, Vasil'ev VG, Grinberg VY. Cryostructuring of polymeric systems. 49. Unexpected "Kosmotropic-Like" impact of organic chaotropes on freeze–thaw-induced gelation of PVA in DMSO. Gels. 2018;4(4):81. doi: 10.3390/gels4040081

141. Razavi M, Qiao Y, Thakor AS. Three-dimensional cryogels for biomedical applications. J Biomed Mater Res A. 2019;107(12):2736-55. doi: 10.1002/jbm.a.36777

142. Liu W, Li Y, Zeng Y, Zhang X, Wang J, Xie L, et al. Microcryogels as injectable 3-D cellular microniches for site-directed and augmented cell delivery. Acta Biomater. 2014;10(5):1864-75. doi: 10.1016/j.actbio.2013.12.008

143. Bencherif SA, Sands RW, Bhatta D, Arany P, Verbeke CS, Edwards DA, et al. Injectable preformed scaffolds with shape-memory properties. Proc Natl Acad Sci U S A. 2012;109(48):19590-5. doi: 10.1073/pnas.1211516109

144. Koshy ST, Zhang DKY, Grolman JM, Stafford AG, Mooney DJ. Injectable nanocomposite cryogels for versatile protein drug delivery. Acta Biomaterialia. 2018;65:36-43. doi: 10.1016/j.actbio.2017.11.024

145. Koshy ST, Ferrante TC, Lewin SA, Mooney DJ. Injectable, porous, and cell-responsive gelatin cryogels. Biomaterials. 2014;35(8):2477-87. doi: 10.1016/j.biomaterials.2013.11.044

146. Villard P, Rezaeeyazdi M, Colombani T, Joshi-Navare K, Rana D, Memic A, et al. Autoclavable and injectable cyogels for biomedical applications. Adv Healthc Mater. 2019;8(17):e1900679. doi: 10.1002/adhm.201900679

147. Hwang YS, Sangaj N, Varghese S. Interconnected macroporous poly(ethylene glycol) cryogels as a cell scaffold for cartilage tissue engineering. Tissue Eng Pt A. 2010;16(10):3033-41. doi: 10.1089/ten.tea.2010.0045

148. Plieva FM, Galaev IY, Noppe W, Mattiasson B. Cryogel applications in microbiology. Trends Microbiol. 2008;16(11):543-51. doi: 10.1016/j.tim.2008.08.005

149. Henderson TMA, Ladewig K, Haylock DN, McLean KM, O'Connor AJ. Cryogels for biomedical applications. J Mater Chem B. 2013;1(21):2682-95. doi: 10.1039/c3tb20280a

150. Dragan ES, Cocarta AI. Smart macroporous IPN hydrogels responsive to pH, temperature, and Ionic strength: synthesis, characterization, and evaluation of controlled release of drugs. ACS Appl Mater Interfaces. 2016;8(19):12018-30. doi: 10.1021/acsami.6b02264

151. Koshy ST, Zhang DKY, Grolman JM, Stafford AG, Mooney DJ. Injectable nanocomposite cryogels for versatile protein drug delivery. Acta Biomater. 2018;65:36-43. doi: 10.1016/j.actbio.2017.11.024

152. Kahveci MU, Beyazkilic Z, Yagci Y. Polyacrylamide cryogels by photoinitiated free radical polymerization. Journal of Polymer Science Part A: Polymer Chemistry. 2010;48(22):4989-94. doi: 10.1002/pola.24295

153. Reichelt S, Abe C, Hainich S, Knolle W, Decker U, Prager A, et al. Electron-beam derived polymeric cryogels. Soft Matter. 2013;9(8):2484-92. doi: 10.1039/C2SM27517A

154. Ahmad Z, Li Y, Huang C, Gou X, Fan Y, Chen J. Underwater suspended bifunctionalized polyethyleneimine-based sponge for selective removal of anionic pollutants from aqueous solution. Journal of Hazardous Materials. 2021;412:125284. doi: 10.1016/j.jhazmat.2021.125284

155. Kirsebom H, Elowsson L, Berillo D, Cozzi S, Inci I, Piskin E, et al. Enzyme-catalyzed crosslinking in a partly frozen state: a new way to produce supermacroporous protein structures. Macromolecular Bioscience. 2013;13(1):67-76. doi: 10.1002/mabi.201200343

156. Berillo D, Mattiasson B, Galaev IY, Kirsebom H. Formation of macroporous self-assembled hydrogels through cryogelation of Fmoc–Phe–Phe. Journal of Colloid and Interface Science. 2012;368(1):226-30. doi: 10.1016/j.jcis.2011.11.006

157. Hasirci V, Yilgor P, Endogan T, Eke G, Hasirci N. 1.121 - Polymer Fundamentals: Polymer Synthesis. In: Ducheyne P, editor. Comprehensive Biomaterials. Oxford: Elsevier; 2011. p. 349-71.

158. Arcaute K, Mann BK, Wicker RB. Stereolithography of three-dimensional bioactive poly(ethylene glycol) constructs with encapsulated cells. Annals of Biomedical Engineering. 2006;34(9):1429-41. doi: 10.1007/s10439-006-9156-y

159. Rizzo R, Ruetsche D, Liu H, Zenobi-Wong M. Optimized photoclick (bio)resins for fast volumetric bioprinting. Adv Mater. 2021;33(49):e2102900. doi: 10.1002/adma.202102900

160. Ström A, Larsson A, Okay O. Preparation and physical properties of hyaluronic acid-based cryogels. J Appl Polym Sci. 2015;132(29) doi: 10.1002/app.42194

161. Gun'ko VM, Savina IN, Mikhalovsky SV. Cryogels: morphological, structural and adsorption characterisation. Advances in Colloid and Interface Science. 2013;187-188:1-46. doi: 10.1016/j.cis.2012.11.001

162. Memic A, Colombani T, Eggermont LJ, Rezaeeyazdi M, Steingold J, Rogers ZJ, et al. Latest advances in cryogel technology for biomedical applications. Adv Ther-Germany. 2019;2(4) doi: 10.1002/adtp.201800114

163. Feng S, Yi J, Ma Y, Bi J. Influence of starch with different degrees and order of gelatinization on the microstructural and mechanical properties of pectin cryogels: a potential pore morphology regulator. International Journal of Biological Macromolecules. 2022;222:533-45. doi: 10.1016/j.ijbiomac.2022.09.199

164. Bencherif SA, Warren Sands R, Ali OA, Li WA, Lewin SA, Braschler TM, et al. Injectable cryogel-based whole-cell cancer vaccines. Nat Commun. 2015;6:7556. doi: 10.1038/ncomms8556

165. Yetiskin B, Okay O. High-strength silk fibroin scaffolds with anisotropic mechanical properties. Polymer. 2017;112:61-70. doi: 10.1016/j.polymer.2017.01.079

166. Wu X, Liu Y, Li X, Wen P, Zhang Y, Long Y, et al. Preparation of aligned porous gelatin scaffolds by unidirectional freeze-drying method. Acta Biomater. 2010;6(3):1167-77. doi: 10.1016/j.actbio.2009.08.041

167. Ciolacu D, Rudaz C, Vasilescu M, Budtova T. Physically and chemically cross-linked cellulose cryogels: Structure, properties and application for controlled release. Carbohydr Polym. 2016;151:392-400. doi: 10.1016/j.carbpol.2016.05.084

168. Backer A, Goppert B, Sturm S, Abaffy P, Sollich T, Gruhl FJ. Impact of adjustable cryogel properties on

the performance of prostate cancer cells in 3D. Springerplus. 2016;5(1):902. doi: 10.1186/s40064-016-2629-z

169. Conoscenti G, Schneider T, Stoelzel K, Carfi Pavia F, Brucato V, Goegele C, et al. PLLA scaffolds produced by thermally induced phase separation (TIPS) allow human chondrocyte growth and extracellular matrix formation dependent on pore size. Mater Sci Eng C Mater Biol Appl. 2017;80:449-59. doi: 10.1016/j.msec.2017.06.011

170. Ceylan S, Gokturk D, Bolgen N. Effect of crosslinking methods on the structure and biocompatibility of polyvinyl alcohol/gelatin cryogels. Biomed Mater Eng. 2016;27(4):327-40. doi: 10.3233/BME-161589

171. Krukiewicz K, Zak JK. Biomaterial-based regional chemotherapy: Local anticancer drug delivery to enhance chemotherapy and minimize its side-effects. Mater Sci Eng C Mater Biol Appl. 2016;62:927-42. doi: 10.1016/j.msec.2016.01.063

172. Baimenov A, Berillo D, Abylgazina L, Poulopoulos SG, Inglezakis VJ. Novel amphoteric cryogels for Cd2+ ions removal from aqueous solutions. Key Engineering Materials. 2018;775:376-82. doi: 10.4028/www.scientific.net/KEM.775.376

173. Ozmen MM, Okay O. Superfast responsive ionic hydrogels with controllable pore size. Polymer. 2005;46(19):8119-27. doi: 10.1016/j.polymer.2005.06.102

174. Wahlberg LU, Lind G, Almqvist PM, Kusk P, Tornøe J, Juliusson B, et al. Targeted delivery of nerve growth factor via encapsulated cell biodelivery in Alzheimer disease: a technology platform for restorative neurosurgery: Clinical article. Journal of Neurosurgery JNS. 2012;117(2):340-7. doi: 10.3171/2012.2.JNS11714

175. Bauleth-Ramos T, Shih T-Y, Shahbazi M-A, Najibi AJ, Mao AS, Liu D, et al. Acetalated dextran nanoparticles loaded into an injectable alginate cryogel for combined chemotherapy and cancer vaccination. Advanced Functional Materials. 2019;29(35):1903686. doi: 10.1002/adfm.201903686

176. Männel MJ, Selzer L, Bernhardt R, Thiele J. Optimizing process parameters in commercial micro-stereolithography for forming emulsions and polymer microparticles in nonplanar microfluidic devices. Advanced Materials Technologies. 2019;4(1):1800408. doi: 10.1002/admt.201800408

177. Whitesides GM. The origins and the future of microfluidics. Nature. 2006;442(7101):368-73. doi: 10.1038/nature05058

178. Squires TM, Quake SR. Microfluidics: fluid physics at the nanoliter scale. Reviews of Modern Physics. 2005;77(3):977-1026. doi: 10.1103/RevModPhys.77.977

179. Christopher GF, Anna SL. Microfluidic methods for generating continuous droplet streams. Journal of Physics D: Applied Physics. 2007;40(19):R319. doi: 10.1088/0022-3727/40/19/R01

180. Teh SY, Lin R, Hung LH, Lee AP. Droplet microfluidics. Lab Chip. 2008;8(2):198-220. doi: 10.1039/b715524g

181. Hua J, Zhang B, Lou J. Numerical simulation of microdroplet formation in coflowing immiscible liquids. AIChE Journal. 2007;53(10):2534-48. doi: 10.1002/aic.11287

182. Chen JM, Kuo M-C, Liu C-P. Control of droplet generation in flow-focusing microfluidic device with a converging-diverging nozzle-shaped section. Japanese Journal of Applied Physics. 2011;50(10R):107301. doi: 10.1143/JJAP.50.107301

183. De Menech M, Garstecki P, Jousse F, Stone HA. Transition from squeezing to dripping in a microfluidic T-shaped junction. Journal of Fluid Mechanics. 2008;595:141-61. doi: 10.1017/S002211200700910X

184. Liu Z, Chai M, Chen X, Hejazi SH, Li Y. Emulsification in a microfluidic flow-focusing device: effect of the dispersed phase viscosity. Fuel. 2021;283:119229. doi: 10.1016/j.fuel.2020.119229

185. Utada AS, Lorenceau E, Link DR, Kaplan PD, Stone HA, Weitz DA. Monodisperse double emulsions generated from a microcapillary device. Science. 2005;308(5721):537-41. doi: 10.1126/science.1109164

186. Zhang J, Yang Z, Liu L, Zhang T, Hu L, Hu C, et al. Ultrafast nucleic acid detection equipment with silicon-based microfluidic chip. Biosensors. 2023;13(2):234. doi: 10.3390/bios13020234

187. Friend J, Yeo L. Fabrication of microfluidic devices using polydimethylsiloxane. Biomicrofluidics. 2010;4(2) doi: 10.1063/1.3259624

188. Daridon A, Fascio V, Lichtenberg J, Wütrich R, Langen H, Verpoorte E, et al. Multi-layer microfluidic glass chips for microanalytical applications. Fresenius' Journal of Analytical Chemistry. 2001;371(2):261-9. doi: 10.1007/s002160101004

189. Chen Y, Zhang L, Chen G. Fabrication, modification, and application of poly(methyl methacrylate) microfluidic chips. Electrophoresis. 2008;29(9):1801-14. doi: 10.1002/elps.200700552

190. Agha A, Waheed W, Alamoodi N, Mathew B, Alnaimat F, Abu-Nada E, et al. A review of cyclic olefin copolymer applications in microfluidics and microdevices. Macromolecular Materials and Engineering. 2022;307(8):2200053. doi: 10.1002/mame.202200053

191. Whitesides GM. The origins and the future of microfluidics. Nature. 2006;442(7101):368-73. doi: 10.1038/nature05058

192. Daliri K, Pfannkuche K, Garipcan B. Effects of physicochemical properties of polyacrylamide (PAA) and (polydimethylsiloxane) PDMS on cardiac cell behavior. Soft Matter. 2021;17(5):1156-72. doi: 10.1039/D0SM01986K

193. Vladisavljevic GT, Khalid N, Neves MA, Kuroiwa T, Nakajima M, Uemura K, et al. Industrial lab-on-a-chip: design, applications and scale-up for drug discovery and delivery. Adv Drug Deliv Rev. 2013;65(11-12):1626-63. doi: 10.1016/j.addr.2013.07.017

194. Bandulasena MV, Vladisavljević GT, Benyahia B. Versatile reconfigurable glass capillary microfluidic devices with Lego® inspired blocks for drop generation and micromixing. Journal of Colloid and Interface Science. 2019;542:23-32. doi: 10.1016/j.jcis.2019.01.119

195. Chen H, Jia F, Zhu C, Xu J, Hua X, Xi Z, et al. Controllable preparation of SB-3CT loaded PLGA microcapsules for traumatic-brain-injury pharmaco-therapy. Chemical Engineering Journal. 2018;339:346-58. doi: 10.1016/j.cej.2018.01.140

196. Huang R, Zhang H, Lv L, Zhang Y, Li J, Wang H, et al. Design of gefitinib-loaded PLGA microspheres via

microfluidics for lung cancer. Materials & Design. 2023;234:112336. doi: 10.1016/j.matdes.2023.112336
197. Aboelela SS, Ibrahim M, Badruddoza AZM, Tran V, Ferri JK, Roper TD. Encapsulation of a highly hydrophilic drug in polymeric particles: a comparative study of batch and microfluidic processes. Int J Pharmaceut. 2021;606:120906. doi: 10.1016/j.ijpharm.2021.120906
198. Iliescu C, Taylor H, Avram M, Miao J, Franssila S. A practical guide for the fabrication of microfluidic devices using glass and silicon. Biomicrofluidics. 2012;6(1):16505-1650516. doi: 10.1063/1.3689939
199. Tang Z, Reynolds DE, Lv C, Zhang D, Ko J, Wang Y. A versatile microchannel array device for portable and parallel droplet generation. Small Science. 2024;4(5):2400005. doi: 10.1002/smsc.202400005
200. Kong KS, Choi JH, Kim GM. Microfluidic array chip with parallel channels for fast preparation of sample droplet array. Journal of Nanoscience and Nanotechnology. 2016;16(6):6294-8. doi: 10.1166/jnn.2016.12120
201. Sollier E, Murray C, Maoddi P, Di Carlo D. Rapid prototyping polymers for microfluidic devices and high pressure injections. Lab on a Chip. 2011;11(22):3752-65. doi: 10.1039/C1LC20514E
202. Yang C-H, Huang K-S, Grumezescu AM, Wang C-Y, Tzeng S-C, Chen S-Y, et al. Synthesis of uniform poly(d,l-lactide) and poly(d,l-lactide-co-glycolide) microspheres using a microfluidic chip for comparison. ELECTROPHORESIS. 2014;35(2-3):316-22. doi: 10.1002/elps.201300185
203. Oe Y, Kobayashi M, Yoshida T, Kojima H, Terukina T, Kondo H. Injectable testosterone PLGA microsphere with different characteristics: effect of preparation method (paddle mixing versus microfluidic device). Pharmaceutical Development and Technology. 2024;29(5):482-91. doi: 10.1080/10837450.2024.2348580
204. Wu J, Kong T, Yeung KWK, Shum HC, Cheung KMC, Wang L, et al. Fabrication and characterization of monodisperse PLGA–alginate core–shell microspheres with monodisperse size and homogeneous shells for controlled drug release. Acta Biomaterialia. 2013;9(7):7410-9. doi: 10.1016/j.actbio.2013.03.022
205. Brown TJ, Brennan MC, Li M, Church EW, Brandmeir NJ, Rakszawski KL, et al. Association of the extent of resection with survival in glioblastoma: A systematic review and meta-analysis. JAMA Oncol. 2016;2(11):1460-9. doi: 10.1001/jamaoncol.2016.1373
206. McGovern PC, Lautenbach E, Brennan PJ, Lustig RA, Fishman NO. Risk factors for postcraniotomy surgical site infection after 1,3-bis (2-Chloroethyl)-1-nitrosourea (Gliadel) wafer placement. Clinical Infectious Diseases. 2003;36(6):759-65. doi: 10.1086/368082
207. Baimenov A, Berillo DA, Poulopoulos SG, Inglezakis VJ. A review of cryogels synthesis, characterization and applications on the removal of heavy metals from aqueous solutions. Advances in Colloid and Interface Science. 2020;276:102088. doi: 10.1016/j.cis.2019.102088
208. Eigel D, Schuster R, Männel MJ, Thiele J, Panasiuk MJ, Andreae LC, et al. Sulfonated cryogel scaffolds for focal delivery in ex-vivo brain tissue cultures. Biomaterials. 2021;271:120712. doi: 10.1016/j.biomaterials.2021.120712
209. Plieva FM, Karlsson M, Aguilar M-R, Gomez D, Mikhalovsky S, Galaev' IY. Pore structure in supermacroporous polyacrylamide based cryogels. Soft Matter. 2005;1(4):303-9. doi: 10.1039/B510010K

210. Zhang Y, Wang C, Jiang W, Zuo W, Han G. Influence of stage cooling method on pore architecture of biomimetic alginate scaffolds. Sci Rep-Uk. 2017;7(1):16150. doi: 10.1038/s41598-017-16024-x

211. Sahiner N, Demirci S, Sahiner M, Yilmaz S, Al-Lohedan H. The use of superporous p(3-acrylamidopropyl)trimethyl ammonium chloride cryogels for removal of toxic arsenate anions. Journal of Environmental Management. 2015;152:66-74. doi: 10.1016/j.jenvman.2015.01.023

212. Baimenov AZ, Berillo DA, Inglezakis VJ. Cryogel-based Ag°/Ag2O nanocomposites for iodide removal from water. Journal of Molecular Liquids. 2020;299:112134. doi: 10.1016/j.molliq.2019.112134

213. Johnson-Arbor K, Dubey R. Doxorubicin. StatPearls. Treasure Island (FL); 2022.

214. Nitiss JL. Targeting DNA topoisomerase II in cancer chemotherapy. Nature Reviews Cancer. 2009;9(5):338-50. doi: 10.1038/nrc2607

215. Rivankar S. An overview of doxorubicin formulations in cancer therapy. Journal of cancer research and therapeutics. 2014;10(4):853-8. doi: 10.4103/0973-1482.139267

216. Chatterjee K, Zhang J, Honbo N, Karliner JS. Doxorubicin cardiomyopathy. Cardiology. 2009;115(2):155-62. doi: 10.1159/000265166

217. Pecoraro M, Del Pizzo M, Marzocco S, Sorrentino R, Ciccarelli M, Iaccarino G, et al. Inflammatory mediators in a short-time mouse model of doxorubicin-induced cardiotoxicity. Toxicology and applied pharmacology. 2016;293:44-52. doi: 10.1016/j.taap.2016.01.006

218. Singal P, Li T, Kumar D, Danelisen I, Iliskovic N. Adriamycin-induced heart failure: mechanisms and modulation. Molecular and cellular biochemistry. 2000;207:77-86. doi: 10.1023/a:1007094214460

219. Tang H, Tao A, Song J, Liu Q, Wang H, Rui T. Doxorubicin-induced cardiomyocyte apoptosis: Role of mitofusin 2. The international journal of biochemistry & cell biology. 2017;88:55-9. doi: 10.1016/j.biocel.2017.05.006

220. Barenholz Y. Doxil® — The first FDA-approved nano-drug: lessons learned. J Control Release. 2012;160(2):117-34. doi: 10.1016/j.jconrel.2012.03.020

221. Liu J, Dupree JL, Gacias M, Frawley R, Sikder T, Naik P, et al. Clemastine enhances myelination in the prefrontal cortex and rescues behavioral changes in socially isolated mice. J Neurosci. 2016;36(3):957-62. doi: 10.1523/JNEUROSCI.3608-15.2016

222. Ellegaard AM, Dehlendorff C, Vind AC, Anand A, Cederkvist L, Petersen NHT, et al. Repurposing cationic amphiphilic antihistamines for cancer treatment. EBioMedicine. 2016;9:130-9. doi: 10.1016/j.ebiom.2016.06.013

223. Aits S, Jaattela M. Lysosomal cell death at a glance. J Cell Sci. 2013;126(9):1905-12. doi: 10.1242/jcs.091181

224. Sun MA, Yang R, Liu H, Wang W, Song X, Hu B, et al. Repurposing clemastine to target glioblastoma cell stemness. Cancers (Basel). 2023;15(18) doi: 10.3390/cancers15184619

225. Lathia JD, Mack SC, Mulkearns-Hubert EE, Valentim CL, Rich JN. Cancer stem cells in glioblastoma. Genes Dev. 2015;29(12):1203-17. doi: 10.1101/gad.261982.115

226. Chen R, Nishimura MC, Bumbaca SM, Kharbanda S, Forrest WF, Kasman IM, et al. A hierarchy of self-renewing tumor-initiating cell types in glioblastoma. Cancer Cell. 2010;17(4):362-75. doi: 10.1016/j.ccr.2009.12.049

227. Bianco J, Bastiancich C, Joudiou N, Gallez B, des Rieux A, Danhier F. Novel model of orthotopic U-87 MG glioblastoma resection in athymic nude mice. J Neurosci Methods. 2017;284:96-102. doi: 10.1016/j.jneumeth.2017.04.019

228. Kaur K, Malik AK. Study on the fluorescence quenching reaction of amitriptyline and clomipramine hydrochlorides with eosin Y and its analytical application. J Fluoresc. 2013;23(3):533-42. doi: 10.1007/s10895-013-1185-y

229. Breiner A, Moher D, Brooks J, Cheng W, Hegen H, Deisenhammer F, et al. Adult CSF total protein upper reference limits should be age-partitioned and significantly higher than 0.45 g/L: a systematic review. Journal of neurology. 2019;266:616-24. doi: 10.1007/s00415-018-09174-z

230. Sanchez-Perez JA, Gallardo-Moreno AM, González-Martín ML, Vadillo-Rodriguez V. BSA adsorption onto nanospheres: Influence of surface curvature as probed by electrophoretic light scattering and UV/vis spectroscopy. Applied Surface Science. 2015;353:1095-102. doi: 10.1016/j.apsusc.2015.06.198

231. Piccirillo SG, Reynolds BA, Zanetti N, Lamorte G, Binda E, Broggi G, et al. Bone morphogenetic proteins inhibit the tumorigenic potential of human brain tumour-initiating cells. Nature. 2006;444(7120):761-5. doi: 10.1038/nature05349

232. Siebzehnrubl FA, Silver DJ, Tugertimur B, Deleyrolle LP, Siebzehnrubl D, Sarkisian MR, et al. The ZEB1 pathway links glioblastoma initiation, invasion and chemoresistance. EMBO Mol Med. 2013;5(8):1196-212. doi: 10.1002/emmm.201302827

233. Alghamdi M, Chierchini F, Eigel D, Taplan C, Miles T, Pette D, et al. Poly(ethylene glycol) based nanotubes for tuneable drug delivery to glioblastoma multiforme. Nanoscale Advances. 2020;2(10):4498-509. doi: 10.1039/D0NA00471E

234. Taylor Z, Miller K. Reassessment of brain elasticity for analysis of biomechanisms of hydrocephalus. J Biomech. 2004;37(8):1263-9. doi: 10.1016/j.jbiomech.2003.11.027

235. Liang Y, Deng X, Zhang L, Peng X, Gao W, Cao J, et al. Terminal modification of polymeric micelles with π-conjugated moieties for efficient anticancer drug delivery. Biomaterials. 2015;71:1-10. doi: 10.1016/j.biomaterials.2015.08.032

236. Cui P-F, Zhuang W-R, Hu X, Xing L, Yu R-Y, Qiao J-B, et al. A new strategy for hydrophobic drug delivery using a hydrophilic polymer equipped with stacking units. Chemical Communications. 2018;54(59):8218-21. doi: 10.1039/C8CC04363A

237. Lee J, Kotliarova S, Kotliarov Y, Li A, Su Q, Donin NM, et al. Tumor stem cells derived from glioblastomas cultured in bFGF and EGF more closely mirror the phenotype and genotype of primary tumors than do serum-cultured cell lines. Cancer Cell. 2006;9(5):391-403. doi: 10.1016/j.ccr.2006.03.030

238. Diaz-Arrastia R, Wang KK, Papa L, Sorani MD, Yue JK, Puccio AM, et al. Acute biomarkers of traumatic

brain injury: relationship between plasma levels of ubiquitin C-terminal hydrolase-L1 and glial fibrillary acidic protein. Journal of neurotrauma. 2014;31(1):19-25. doi: 10.1089/neu.2013.3040

239. Foerch C, Niessner M, Back T, Bauerle M, De Marchis GM, Ferbert A, et al. Diagnostic accuracy of plasma glial fibrillary acidic protein for differentiating intracerebral hemorrhage and cerebral ischemia in patients with symptoms of acute stroke. Clinical Chemistry. 2012;58(1):237-45. doi: 10.1373/clinchem.2011.172676

240. Hunt CPJ, Penna V, Gantner CW, Moriarty N, Wang Y, Franks S, et al. Tissue programmed hydrogels functionalized with GDNF improve human neural grafts in Parkinson's disease. Advanced Functional Materials. 2021;31(47):2105301. doi: 10.1002/adfm.202105301

241. Gállego Pérez-Larraya J, Paris S, Idbaih A, Dehais C, Laigle-Donadey F, Navarro S, et al. Diagnostic and prognostic value of preoperative combined GFAP, IGFBP-2, and YKL-40 plasma levels in patients with glioblastoma. Cancer. 2014;120(24):3972-80. doi: 10.1002/cncr.28949

242. Tichy J, Spechtmeyer S, Mittelbronn M, Hattingen E, Rieger J, Senft C, et al. Prospective evaluation of serum glial fibrillary acidic protein (GFAP) as a diagnostic marker for glioblastoma. J Neuro-Oncol. 2016;126:361-9. doi: 10.1007/s11060-015-1978-8

243. Abdelhak A, Foschi M, Abu-Rumeileh S, Yue JK, D'Anna L, Huss A, et al. Blood GFAP as an emerging biomarker in brain and spinal cord disorders. Nature Reviews Neurology. 2022;18(3):158-72. doi: 10.1038/s41582-021-00616-3

244. Ahmadipour Y, Gembruch O, Pierscianek D, Sure U, Jabbarli R. Does the expression of glial fibrillary acid protein (GFAP) stain in glioblastoma tissue have a prognostic impact on survival? Neurochirurgie. 2020;66(3):150-4. doi: 10.1016/j.neuchi.2019.12.012

245. Kiviniemi A, Gardberg M, Frantzén J, Parkkola R, Vuorinen V, Pesola M, et al. Serum levels of GFAP and EGFR in primary and recurrent high-grade gliomas: correlation to tumor volume, molecular markers, and progression-free survival. J Neuro-Oncol. 2015;124:237-45. doi: 10.1007/s11060-015-1829-7

246. Shih C-C, Lee T-S, Tsuang F-Y, Lin P-L, Cheng Y-J, Cheng H-L, et al. Pretreatment serum lactate level as a prognostic biomarker in patients undergoing supratentorial primary brain tumor resection. Oncotarget. 2017;8(38):63715. doi: 10.18632/oncotarget.18891

247. Vietheer J-M, Rieger J, Wagner M, Senft C, Tichy J, Foerch C. Serum concentrations of glial fibrillary acidic protein (GFAP) do not indicate tumor recurrence in patients with glioblastoma. J Neuro-Oncol. 2017;135:193-9. doi: 10.1007/s11060-017-2565-y

248. Ito D, Imai Y, Ohsawa K, Nakajima K, Fukuuchi Y, Kohsaka S. Microglia-specific localisation of a novel calcium binding protein, Iba1. Brain Res Mol Brain Res. 1998;57(1):1-9. doi: 10.1016/s0169-328x(98)00040-0

249. Siddiqui TA, Lively S, Vincent C, Schlichter LC. Regulation of podosome formation, microglial migration and invasion by Ca(2+)-signaling molecules expressed in podosomes. J Neuroinflammation. 2012;9:250. doi: 10.1186/1742-2094-9-250

250. Sasaki Y, Ohsawa K, Kanazawa H, Kohsaka S, Imai Y. Iba1 is an actin-cross-linking protein in macrophages/microglia. Biochem Biophys Res Commun. 2001;286(2):292-7. doi: 10.1006/bbrc.2001.5388

251. Poon CC, Sarkar S, Yong VW, Kelly JJ. Glioblastoma-associated microglia and macrophages: targets for therapies to improve prognosis. Brain. 2017;140(6):1548-60. doi: 10.1093/brain/aww355

252. Bettinger I, Thanos S, Paulus W. Microglia promote glioma migration. Acta neuropathologica. 2002;103:351-5. doi: 10.1007/s00401-001-0472-x

253. Markovic DS, Glass R, Synowitz M, Rooijen Nv, Kettenmann H. Microglia stimulate the invasiveness of glioma cells by increasing the activity of metalloprotease-2. Journal of Neuropathology & Experimental Neurology. 2005;64(9):754-62. doi: 10.1097/01.jnen.0000178445.33972.a9

254. Papageorgiou IE, Lewen A, Galow LV, Cesetti T, Scheffel J, Regen T, et al. TLR4-activated microglia require IFN-γ to induce severe neuronal dysfunction and death in situ. Proceedings of the National Academy of Sciences. 2016;113(1):212-7. doi: 10.1073/pnas.1513853113

255. Liddelow SA, Guttenplan KA, Clarke LE, Bennett FC, Bohlen CJ, Schirmer L, et al. Neurotoxic reactive astrocytes are induced by activated microglia. Nature. 2017;541(7638):481-7. doi: 10.1038/nature21029

256. de Luzy IR, Law KCL, Moriarty N, Hunt CPJ, Durnall JC, Thompson LH, et al. Human stem cells harboring a suicide gene improve the safety and standardisation of neural transplants in Parkinsonian rats. Nature Communications. 2021;12(1):3275. doi: 10.1038/s41467-021-23125-9

257. Patel DM, Agarwal N, Tomei KL, Hansberry DR, Goldstein IM. Optimal timing of whole-brain radiation therapy following craniotomy for cerebral malignancies. World Neurosurgery. 2015;84(2):412-9. doi: 10.1016/j.wneu.2015.03.052

258. Kumar A, Rodríguez-Caballero A, Plieva FM, Galaev IY, Nandakumar KS, Kamihira M, et al. Affinity binding of cells to cryogel adsorbents with immobilized specific ligands: effect of ligand coupling and matrix architecture. Journal of Molecular Recognition: An Interdisciplinary Journal. 2005;18(1):84-93. doi: 10.1002/jmr.693

259. Kemençe N, Bölgen N. Gelatin-and hydroxyapatite-based cryogels for bone tissue engineering: synthesis, characterization, in vitro and in vivo biocompatibility. Journal of tissue engineering and regenerative medicine. 2017;11(1):20-33. doi: 10.1002/term.1813

260. Kumari J, Kumar A. Development of polymer based cryogel matrix for transportation and storage of mammalian cells. Sci Rep-Uk. 2017;7(1):41551. doi: 10.1038/srep41551

261. Takei T, Danjo S, Sakoguchi S, Tanaka S, Yoshinaga T, Nishimata H, et al. Autoclavable physically-crosslinked chitosan cryogel as a wound dressing. Journal of Bioscience and Bioengineering. 2018;125(4):490-5. doi: 10.1016/j.jbiosc.2017.10.015

262. Lee SB, Kim YH, Chong MS, Hong SH, Lee YM. Study of gelatin-containing artificial skin V: fabrication of gelatin scaffolds using a salt-leaching method. Biomaterials. 2005;26(14):1961-8. doi: 10.1016/j.biomaterials.2004.06.032

263. Tokuyama H, Kanehara A. Novel synthesis of macroporous poly(N-isopropylacrylamide) hydrogels using oil-in-water emulsions. Langmuir. 2007;23(22):11246-51. doi: 10.1021/la701492u

264. Henderson TMA, Ladewig K, Haylock DN, McLean KM, O'Connor AJ. Cryogels for biomedical applications. Journal of Materials Chemistry B. 2013;1(21):2682-95. doi: 10.1039/C3TB20280A

265. Vladimir IL. Cryogels on the basis of natural and synthetic polymers: preparation, properties and application. Russian Chemical Reviews. 2002;71(6):489. doi: 10.1070/RC2002v071n06ABEH000720

266. Bencherif SA, Sands RW, Bhatta D, Arany P, Verbeke CS, Edwards DA, et al. Injectable preformed scaffolds with shape-memory properties. Proceedings of the National Academy of Sciences. 2012;109(48):19590-5. doi: 10.1073/pnas.1211516109

267. Eggermont LJ, Rogers ZJ, Colombani T, Memic A, Bencherif SA. Injectable Cryogels for Biomedical Applications. Trends Biotechnol. 2020;38(4):418-31. doi: 10.1016/j.tibtech.2019.09.008

268. Langer R. Drug delivery and targeting. Nature. 1998;392(6679 Suppl):5-10. doi: 10.1007/978-3-031-52864-4

269. Shi L, Hodges M, Yurgin N, Boye KS. Impact of dose frequency on compliance and health outcomes: a literature review (1966–2006). Expert Review of Pharmacoeconomics & Outcomes Research. 2007;7(2):187-202. doi: 10.1586/14737167.7.2.187

270. Cheng MM, Alfonso R, Best JH, Garrison LP, Bruhn D, Veenstra DL. The economic value of reducing medication dosing frequency with drug delivery technologies: an evidence assessment. Journal of Medical Economics. 2010;13(2):193-202. doi: 10.3111/13696991003757500

271. Vulic K, Shoichet MS. Affinity-based drug delivery systems for tissue repair and regeneration. Biomacromolecules. 2014;15(11):3867-80. doi: 10.1021/bm501084u

272. Wang NX, von Recum HA. Affinity-based drug delivery. Macromolecular Bioscience. 2011;11(3):321-32. doi: 10.1002/mabi.201000206

273. Thatiparti TR, Shoffstall AJ, von Recum HA. Cyclodextrin-based device coatings for affinity-based release of antibiotics. Biomaterials. 2010;31(8):2335-47. doi: 10.1016/j.biomaterials.2009.11.087

274. Acharya P, Chattopadhyaya J. Electrostatic cross-modulation of the pseudoaromatic character in single-stranded RNA by nearest-neighbor interactions. Pure and Applied Chemistry. 2005;77(1):291-311. doi: 10.1351/pac200577010291

275. Liu Z, Fan AC, Rakhra K, Sherlock S, Goodwin A, Chen X, et al. Supramolecular stacking of doxorubicin on carbon nanotubes for in vivo cancer therapy. Angewandte Chemie International Edition. 2009;48(41):7668-72. doi: 10.1002/anie.200902612

276. Liu N, Han J, Zhang X, Yang Y, Liu Y, Wang Y, et al. pH-responsive zwitterionic polypeptide as a platform for anti-tumor drug delivery. Colloids and Surfaces B: Biointerfaces. 2016;145:401-9. doi: 10.1016/j.colsurfb.2016.05.027

277. Shah NJ, Hyder MN, Quadir MA, Dorval Courchesne N-M, Seeherman HJ, Nevins M, et al. Adaptive growth factor delivery from a polyelectrolyte coating promotes synergistic bone tissue repair and

reconstruction. Proceedings of the National Academy of Sciences. 2014;111(35):12847-52. doi: 10.1073/pnas.1408035111

278. Hakami A, Narasimhan K, Comini G, Thiele J, Werner C, Dowd E, et al. Cryogel microcarriers for sustained local delivery of growth factors to the brain. J Control Release. 2024;369:404-19. doi: 10.1016/j.jconrel.2024.03.023

279. Souers AJ, Leverson JD, Boghaert ER, Ackler SL, Catron ND, Chen J, et al. ABT-199, a potent and selective BCL-2 inhibitor, achieves antitumor activity while sparing platelets. Nat Med. 2013;19(2):202-8. doi: 10.1038/nm.3048

280. Moore VDG, Brown JR, Certo M, Love TM, Novina CD, Letai A. Chronic lymphocytic leukemia requires BCL2 to sequester prodeath BIM, explaining sensitivity to BCL2 antagonist ABT-737. The Journal of clinical investigation. 2007;117(1):112-21. doi: 10.1172/JCI28281

281. Vogler M, Dinsdale D, Dyer MJ, Cohen GM. ABT-199 selectively inhibits BCL2 but not BCL2 L1 and efficiently induces apoptosis of chronic lymphocytic leukaemic cells but not platelets. British journal of haematology. 2013;163(1) doi: 10.1111/bjh.12457

282. Fischer U, Forster M, Rinaldi A, Risch T, Sungalee S, Warnatz HJ, et al. Genomics and drug profiling of fatal TCF3-HLF-positive acute lymphoblastic leukemia identifies recurrent mutation patterns and therapeutic options. Nat Genet. 2015;47(9):1020-9. doi: 10.1038/ng.3362

283. Jones J, Choi MY, Mato AR, Furman RR, Davids MS, Heffner LT, et al. Venetoclax (VEN) monotherapy for patients with chronic lymphocytic leukemia (CLL) who relapsed after or were refractory to irutinib or idelalisib. Blood. 2016;128(22):637. doi: 10.1182/blood.V128.22.637.637

284. Beltzig L, Christmann M, Kaina B. Abrogation of cellular senescence induced by temozolomide in glioblastoma cells: search for senolytics. Cells. 2022;11(16):2588. doi: 10.3390/cells11162588

285. Karpel-Massler G, Ishida CT, Bianchetti E, Zhang Y, Shu C, Tsujiuchi T, et al. Induction of synthetic lethality in IDH1-mutated gliomas through inhibition of Bcl-xL. Nature Communications. 2017;8(1):1067. doi: 10.1038/s41467-017-00984-9

286. Rahman M, Olson I, Mansour M, Carlstrom LP, Sutiwisesak R, Saber R, et al. Selective vulnerability of senescent glioblastoma cells to BCL-XL inhibition. Molecular Cancer Research. 2022;20(6):938-48. doi: 10.1158/1541-7786.Mcr-21-0029

287. Derayea SM, Omar MA, Abu-hassan AA. Studying the association complex formation of atomoxetine and fluvoxamine with eosin Y and its application in their fluorimetric determination. Royal Society Open Science. 2018;5(3):170943. doi: doi:10.1098/rsos.170943

288. Koshy ST, Ferrante TC, Lewin SA, Mooney DJ. Injectable, porous, and cell-responsive gelatin cryogels. Biomaterials. 2014;35(8):2477-87. doi: 10.1016/j.biomaterials.2013.11.044

289. Fairbanks BD, Schwartz MP, Bowman CN, Anseth KS. Photoinitiated polymerization of PEG-diacrylate with lithium phenyl-2,4,6-trimethylbenzoylphosphinate: polymerization rate and cytocompatibility. Biomaterials. 2009;30(35):6702-7. doi: 10.1016/j.biomaterials.2009.08.055

290. Murphy CA, Lim KS, Woodfield TBF. Next evolution in organ-scale biofabrication: bioresin design for rapid high-resolution vat polymerization. Adv Mater. 2022;34(20):2107759. doi: 10.1002/adma.202107759

291. Nguyen AK, Goering PL, Elespuru RK, Sarkar Das S, Narayan RJ. The photoinitiator lithium phenyl (2,4,6-trimethylbenzoyl) phosphinate with exposure to 405 nm light is cytotoxic to mammalian cells but not mutagenic in bacterial reverse mutation assays. Polymers. 2020;12(7):1489. doi: 10.3390/polym12071489

292. Monteiro N, Thrivikraman G, Athirasala A, Tahayeri A, França CM, Ferracane JL, et al. Photopolymerization of cell-laden gelatin methacryloyl hydrogels using a dental curing light for regenerative dentistry. Dental Materials. 2018;34(3):389-99. doi: 10.1016/j.dental.2017.11.020

293. Lai YL, Smith PM, Lamm WJ, Hildebrandt J. Sampling and analysis of cerebrospinal fluid for chronic studies in awake rats. J Appl Physiol Respir Environ Exerc Physiol. 1983;54(6):1754-7. doi: 10.1152/jappl.1983.54.6.1754

294. Pegg CC, He C, Stroink AR, Kattner KA, Wang CX. Technique for collection of cerebrospinal fluid from the cisterna magna in rat. J Neurosci Methods. 2010;187(1):8-12. doi: 10.1016/j.jneumeth.2009.12.002

295. Newland B, Varricchio C, Körner Y, Hoppe F, Taplan C, Newland H, et al. Focal drug administration via heparin-containing cryogel microcarriers reduces cancer growth and metastasis. Carbohydrate Polymers. 2020;245:116504. doi: 10.1016/j.carbpol.2020.116504

296. Pampaloni F, Reynaud EG, Stelzer EHK. The third dimension bridges the gap between cell culture and live tissue. Nature Reviews Molecular Cell Biology. 2007;8(10):839-45. doi: 10.1038/nrm2236

297. Weigelt B, Ghajar CM, Bissell MJ. The need for complex 3D culture models to unravel novel pathways and identify accurate biomarkers in breast cancer. Adv Drug Deliv Rev. 2014;69-70:42-51. doi: 10.1016/j.addr.2014.01.001

298. Carvalho MR, Lima D, Reis RL, Correlo VM, Oliveira JM. Evaluating biomaterial- and microfluidic-based 3D tumor models. Trends in Biotechnology. 2015;33(11):667-78. doi: 10.1016/j.tibtech.2015.09.009

299. Bahcecioglu G, Basara G, Ellis BW, Ren X, Zorlutuna P. Breast cancer models: engineering the tumor microenvironment. Acta Biomaterialia. 2020;106:1-21. doi: 10.1016/j.actbio.2020.02.006

300. Lukas RV, Wainwright DA, Ladomersky E, Sachdev S, Sonabend AM, Stupp R. Newly diagnosed glioblastoma: a review on clinical management. Oncology (Williston Park). 2019;33(3):91-100.

301. Liau LM, Ashkan K, Brem S, Campian JL, Trusheim JE, Iwamoto FM, et al. Association of autologous tumor lysate-loaded dendritic cell vaccination with extension of survival among patients with newly diagnosed and recurrent glioblastoma: a phase 3 prospective externally controlled cohort trial. JAMA Oncology. 2023;9(1):112-21. doi: 10.1001/jamaoncol.2022.5370

302. Wick W, Meisner C, Hentschel B, Platten M, Schilling A, Wiestler B, et al. Prognostic or predictive value of MGMT promoter methylation in gliomas depends on IDH1 mutation. Neurology. 2013;81(17):1515-22. doi: 10.1212/WNL.0b013e3182a95680

303. Cohen MH, Shen YL, Keegan P, Pazdur R. FDA drug approval summary: bevacizumab (Avastin) as treatment of recurrent glioblastoma multiforme. Oncologist. 2009;14(11):1131-8. doi:

10.1634/theoncologist.2009-0121

304. Chinot OL, Wick W, Mason W, Henriksson R, Saran F, Nishikawa R, et al. Bevacizumab plus radiotherapy-temozolomide for newly diagnosed glioblastoma. N Engl J Med. 2014;370(8):709-22. doi: 10.1056/NEJMoa1308345

305. Herrlinger U, Rieger J, Koch D, Loeser S, Blaschke B, Kortmann RD, et al. Phase II trial of lomustine plus temozolomide chemotherapy in addition to radiotherapy in newly diagnosed glioblastoma: UKT-03. J Clin Oncol. 2006;24(27):4412-7. doi: 10.1200/JCO.2006.06.9104

306. Glas M, Happold C, Rieger J, Wiewrodt D, Bahr O, Steinbach JP, et al. Long-term survival of patients with glioblastoma treated with radiotherapy and lomustine plus temozolomide. J Clin Oncol. 2009;27(8):1257-61. doi: 10.1200/JCO.2008.19.2195

307. Weller M, Le Rhun E. How did lomustine become standard of care in recurrent glioblastoma? Cancer Treat Rev. 2020;87:102029. doi: 10.1016/j.ctrv.2020.102029

308. Sanchez C, Asin KE, Artigas F. Vortioxetine, a novel antidepressant with multimodal activity: review of preclinical and clinical data. Pharmacology & Therapeutics. 2015;145:43-57. doi: 10.1016/j.pharmthera.2014.07.001

309. Chen G, Højer A-M, Areberg J, Nomikos G. Vortioxetine: clinical pharmacokinetics and drug interactions. Clinical Pharmacokinetics. 2018;57(6):673-86. doi: 10.1007/s40262-017-0612-7

310. De Bonis P, Anile C, Pompucci A, Fiorentino A, Balducci M, Chiesa S, et al. Safety and efficacy of Gliadel wafers for newly diagnosed and recurrent glioblastoma. Acta Neurochirurgica. 2012;154(8):1371-8. doi: 10.1007/s00701-012-1413-2

311. Singleton WG, Bienemann AS, Woolley M, Johnson D, Lewis O, Wyatt MJ, et al. The distribution, clearance, and brainstem toxicity of panobinostat administered by convection-enhanced delivery. Journal of Neurosurgery: Pediatrics. 2018;22(3):288-96. doi: 10.3171/2018.2.PEDS17663

312. Wang Y, Bastiancich C, Newland B. Injectable local drug delivery systems for glioblastoma: a systematic review and meta-analysis of progress to date. Biomaterials Science. 2023;11(5):1553-66. doi: 10.1039/D2BM01534J

313. Blasi P. Poly(lactic acid)/poly(lactic-co-glycolic acid)-based microparticles: an overview. Journal of Pharmaceutical Investigation. 2019;49(4):337-46. doi: 10.1007/s40005-019-00453-z

314. Tice TR, Tabibi SE. Parenteral drug delivery: injectables. Treatise on controlled drug delivery: CRC Press; 2017. p. 315-39.

315. Wan B, Bao Q, Burgess D. Long-acting PLGA microspheres: advances in excipient and product analysis toward improved product understanding. Adv Drug Deliv Rev. 2023;198:114857. doi: 10.1016/j.addr.2023.114857

316. Lu Y, Cheng D, Niu B, Wang X, Wu X, Wang A. Properties of poly(lactic-co-glycolic acid) and progress of poly(lactic-co-glycolic acid)-based biodegradable materials in biomedical research. Pharmaceuticals. 2023;16(3):454. doi: 10.3390/ph16030454

317. Wu B, Wu L, He Y, Yin Z, Deng L. Engineered PLGA microspheres for extended release of brexpiprazole: in vitro and in vivo studies. Drug Dev Ind Pharm. 2021;47(6):1001-10. doi: 10.1080/03639045.2021.1934859

318. Casagrande S, Tiribuzi R, Cassetti E, Selmin F, Gervasi GL, Barberini L, et al. Biodegradable composite porous poly(dl-lactide-co-glycolide) scaffold supports mesenchymal stem cell differentiation and calcium phosphate deposition. Artif Cells Nanomed Biotechnol. 2018;46(sup1):219-29. doi: 10.1080/21691401.2017.1417866

319. Tracy MA. Development and scale-up of a microsphere protein delivery system. Biotechnol Prog. 1998;14(1):108-15. doi: 10.1021/bp9701271

320. Im HY, Sah H. Ammonolysis-based microencapsulation technique using isopropyl formate as dispersed solvent. Int J Pharm. 2009;382(1-2):130-8. doi: 10.1016/j.ijpharm.2009.08.020

321. Thomasin C, Merkle HP, Gander B. Drug microencapsulation by PLA/PLGA coacervation in the light of thermodynamics. 2. Parameters determining microsphere formation. J Pharm Sci. 1998;87(3):269-75. doi: 10.1021/js970048j

322. O'Connor G, Krishnan N, Fagan-Murphy A, Cassidy J, O'Leary S, Robertson BD, et al. Inhalable poly(lactic-co-glycolic acid) (PLGA) microparticles encapsulating all-trans-Retinoic acid (ATRA) as a host-directed, adjunctive treatment for mycobacterium tuberculosis infection. Eur J Pharm Biopharm. 2019;134:153-65. doi: 10.1016/j.ejpb.2018.10.020

323. Han FY, Whittaker AK, Howdle SM, Naylor A, Shabir-Ahmed A, Zhang C, et al. Formulation of bioerodible ketamine microparticles as an analgesic adjuvant treatment produced by supercritical fluid polymer encapsulation. Pharmaceutics. 2018;10(4) doi: 10.3390/pharmaceutics10040264

324. Liang YJ, Yu H, Feng G, Zhuang L, Xi W, Ma M, et al. High-performance poly(lactic-co-glycolic acid)-magnetic microspheres prepared by rotating membrane emulsification for transcatheter arterial embolization and magnetic ablation in VX(2) liver tumors. ACS Appl Mater Interfaces. 2017;9(50):43478-89. doi: 10.1021/acsami.7b14330

325. Bianchi JRO, de la Torre LG, Costa ALR. Droplet-based microfluidics as a platform to design food-grade delivery systems based on the entrapped compound type. Foods. 2023;12(18) doi: 10.3390/foods12183385

326. Berkland C, Kim K, Pack DW. PLG microsphere size controls drug release rate through several competing factors. Pharm Res. 2003;20(7):1055-62. doi: 10.1023/a:1024466407849

327. Kang J, Schwendeman SP. Determination of diffusion coefficient of a small hydrophobic probe in poly(lactide-co-glycolide) microparticles by laser scanning confocal microscopy. Macromolecules. 2003;36(4):1324-30. doi: 10.1021/ma021036+

328. Park H. Exploring the effects of process parameters during W/O/W emulsion preparation and supercritical fluid extraction on the protein encapsulation and release properties of PLGA microspheres. Pharmaceutics. 2024;16(3):302. doi: 10.3390/pharmaceutics16030302

329. Lu Y, Park K. Microencapsulation: methods and pharmaceutical applications. Encyclopedia of pharmaceutical science and technology, 4th edn Informa Healthcare, USA. 2012 doi:

10.3109/9781841848204.000

330. Hauck N, Neuendorf TA, Männel MJ, Vogel L, Liu P, Stündel E, et al. Processing of fast-gelling hydrogel precursors in microfluidics by electrocoalescence of reactive species. Soft Matter. 2021;17(45):10312-21. doi: 10.1039/D1SM01176F

331. Heida T, Neubauer JW, Seuss M, Hauck N, Thiele J, Fery A. Mechanically defined microgels by droplet microfluidics. Macromolecular Chemistry and Physics. 2017;218(2):1600418. doi: 10.1002/macp.201600418

332. Jiang QR, Pu XQ, Deng CF, Wang W, Liu Z, Xie R, et al. Microfluidic controllable preparation of iodine-131-labeled microspheres for radioembolization therapy of liver tumors. Adv Healthc Mater. 2023;12(21):e2300873. doi: 10.1002/adhm.202300873

333. Liu Y, Yang G, Hui Y, Ranaweera S, Zhao CX. Microfluidic nanoparticles for drug delivery. Small. 2022;18(36):e2106580. doi: 10.1002/smll.202106580

334. Fu T, Wu Y, Ma Y, Li HZ. Droplet formation and breakup dynamics in microfluidic flow-focusing devices: from dripping to jetting. Chemical Engineering Science. 2012;84:207-17. doi: 10.1016/j.ces.2012.08.039

335. Nie Z, Seo M, Xu S, Lewis PC, Mok M, Kumacheva E, et al. Emulsification in a microfluidic flow-focusing device: effect of the viscosities of the liquids. Microfluidics and Nanofluidics. 2008;5(5):585-94. doi: 10.1007/s10404-008-0271-y

336. Berchane NS, Carson KH, Rice-Ficht AC, Andrews MJ. Effect of mean diameter and polydispersity of PLG microspheres on drug release: experiment and theory. Int J Pharm. 2007;337(1-2):118-26. doi: 10.1016/j.ijpharm.2006.12.037

337. Huang X, Brazel CS. On the importance and mechanisms of burst release in matrix-controlled drug delivery systems. J Control Release. 2001;73(2-3):121-36. doi: 10.1016/s0168-3659(01)00248-6

338. Kang J, Schwendeman SP. Pore closing and opening in biodegradable polymers and their effect on the controlled release of proteins. Molecular pharmaceutics. 2007;4(1):104-18. doi: 10.1021/mp060041n

339. Chaicharoenaudomrung N, Kunhorm P, Noisa P. Three-dimensional cell culture systems as an in vitro platform for cancer and stem cell modeling. World J Stem Cells. 2019;11(12):1065-83. doi: 10.4252/wjsc.v11.i12.1065

340. Takai A, Fako V, Dang H, Forgues M, Yu Z, Budhu A, et al. Three-dimensional organotypic culture models of human hepatocellular carcinoma. Sci Rep. 2016;6:21174. doi: 10.1038/srep21174

341. Oskarsson T, Acharyya S, Zhang XHF, Vanharanta S, Tavazoie SF, Morris PG, et al. Breast cancer cells produce tenascin C as a metastatic niche component to colonize the lungs. Nature Medicine. 2011;17(7):867-74. doi: 10.1038/nm.2379

342. Tang M, Tiwari SK, Agrawal K, Tan M, Dang J, Tam T, et al. Rapid 3D bioprinting of glioblastoma model mimicking native biophysical heterogeneity. Small. 2021;17(15):2006050. doi: 10.1002/smll.202006050

343. Lv D, Yu SC, Ping YF, Wu H, Zhao X, Zhang H, et al. A three-dimensional collagen scaffold cell culture system for screening anti-glioma therapeutics. Oncotarget. 2016;7(35):56904-14. doi: 10.18632/oncotarget.10885

344. Ma L, Zhang B, Zhou C, Li Y, Li B, Yu M, et al. The comparison genomics analysis with glioblastoma multiforme (GBM) cells under 3D and 2D cell culture conditions. Colloids and Surfaces B: Biointerfaces. 2018;172:665-73. doi: 10.1016/j.colsurfb.2018.09.034

345. Maritim S, Boulas P, Lin Y. Comprehensive analysis of liposome formulation parameters and their influence on encapsulation, stability and drug release in glibenclamide liposomes. Int J Pharmaceut. 2021;592:120051. doi: 10.1016/j.ijpharm.2020.120051

346. Tamam H, Park J, Gadalla HH, Masters AR, Abdel-Aleem JA, Abdelrahman SI, et al. Development of liposomal gemcitabine with high drug loading capacity. Molecular Pharmaceutics. 2019;16(7):2858-71. doi: 10.1021/acs.molpharmaceut.8b01284

347. Gómez-Gaete C, Tsapis N, Besnard M, Bochot A, Fattal E. Encapsulation of dexamethasone into biodegradable polymeric nanoparticles. Int J Pharmaceut. 2007;331(2):153-9. doi: 10.1016/j.ijpharm.2006.11.028

348. Groth-Pedersen L, Jäättelä M. Combating apoptosis and multidrug resistant cancers by targeting lysosomes. Cancer Letters. 2013;332(2):265-74. doi: 10.1016/j.canlet.2010.05.021

349. Ellegaard A-M, Groth-Pedersen L, Oorschot V, Klumperman J, Kirkegaard T, Nylandsted J, et al. Sunitinib and SU11652 inhibit acid sphingomyelinase, destabilize lysosomes, and inhibit multidrug resistance. Molecular cancer therapeutics. 2013;12(10):2018-30. doi: 10.1158/1535-7163.MCT-13-0084

350. Lynn DM, Langer R. Degradable poly (β-amino esters): synthesis, characterization, and self-assembly with plasmid DNA. Journal of the American Chemical Society. 2000;122(44):10761-8. doi: 10.1021/ja0015388

351. Anderson DG, Peng W, Akinc A, Hossain N, Kohn A, Padera R, et al. A polymer library approach to suicide gene therapy for cancer. Proceedings of the National Academy of Sciences. 2004;101(45):16028-33. doi: 10.1073/pnas.0407218101